

Mircea Radeş

MĂŞINI ROTATIVE

Editura Printech
2005

UNIVERSITATEA POLITEHNICA BUCURESTI
CATEDRA REZISTENTA MATERIALELOR
LABORATORUL INTEGRITATEA MASINILOR

Mircea Radeş

Rotating Machinery

Design Features and
Dynamics of Rotors

2003

FOREWORD

This book contains much of the illustrative material used in the *Dynamics of Machinery* lecture course given to the fourth year students in the Department of Engineering Sciences (now F.I.L.S.), English Stream, University Politehnica of Bucharest, since 1993.

It is complementary to the book *Dynamics of Machinery* which grew up from the lecture notes of several series of students and was written to facilitate that course, giving basic information on subjects taught later. The focus is on the presentation of the basic principles and design features of rotating machines, with emphasis on the rotor-bearing-seals system. No reference is made to the vibrations of discs, impellers and blades treated elsewhere.

The book is a concise compilation of English texts on turbines, compressors, pumps, fans and generators. The source is mentioned for each figure and it is understood that the corresponding comment is reproduced from the same source.

The author has no claims for the originality of the content. It has been considered that, for students learning in a foreign language, it is useful to read authentic texts written by native speakers of the respective language, or at least translated by such persons.

May 2003

Contents

Foreword	1
Contents	2
1. Centrifugal Pumps	5
1.1 Introduction.	5
1.2 Rotordynamic Analysis	5
1.3 Basic Principles	7
1.4 Design Characteristics	10
1.5 Forces Acting upon Pump Rotors	17
1.6 Annular Seals	19
1.7 Impeller-Volute Interaction	30
1.8 Shroud Forces	34
1.9 Final Remarks	35
References	37
2. Centrifugal Compressors	39
2.1 Introduction	39
2.2 Basic Principles	41
2.3 Design Characteristics	43
2.4 Typical Applications	50
2.5 Annular Gas Seals	52
2.6 Floating Contact Seals	56
2.7 Squeeze Film Dampers	65
2.8 Aerodynamic Cross-Coupling at Impellers	72
2.9 Rotordynamic Considerations	72
References	77
3. Fans and Blowers	79
3.1 Introduction	79
3.2 Basic Principles	80

3.3 Design Characteristics	83
3.4 Calculation Example	91
3.5 Guidelines for Vibration Levels	93
References	94
4. Hydraulic Turbines	95
4.1 Introduction	95
4.2 Hydraulic Turbine Parameters	96
4.3 Pelton Turbines	99
4.4 Francis Turbines	104
4.5 Kaplan Turbines	112
4.6 Bulb and Straflo Turbines	118
4.7 Condition Monitoring of Hydropower Machines	120
4.8 Guidelines for Vibration Limits	122
4.9 Stator Supports for Vertical Generators	125
References	127
5. Axial Compressors	129
5.1 Introduction	129
5.2 Basic Principles	130
5.3 Design Characteristics	135
5.4 Axial vs. Centrifugal Compressor Considerations	140
References	142
6. Gas Turbines	143
6.1 Introduction	143
6.2 Basic Principles	143
6.3 Stationary Turbines for Power Generation	146
6.4 Gas Turbines for Aero-Engines	153
6.5 Exhaust Gas Turbochargers	161
6.6 Gas Turbine Rotor Designs	165
6.7 Numerical Example	171

6.8 Guidelines for Vibration Limits	175
6.9 Final Remarks	178
References	179
7. Steam Turbines	181
7.1 Introduction	181
7.2 Basic Principles	181
7.3 Design Characteristics	184
7.4 Turbine Rotor Designs	196
7.5 Rotordynamic Computations	216
7.6 Condition Monitoring of Steam Turbines	220
7.7 Guidelines for Shaft Vibrations	221
7.8 Rotor Modelling	222
References	223
8. Turbo-Generators	225
8.1 Introduction	225
8.2 Design Characteristics	226
8.3 Precession of Non-Symmetric Rotors	233
8.4 Guidelines for Vibration Limits	235
8.5 Torsional Vibrations	237
References	244
Bibliography	245
Index	247

1. CENTRIFUGAL PUMPS

1.1 Introduction

Centrifugal pumps are used in services involving boiler feed, water injection, reactor charge, etc. Present techniques for the design of pumps rely heavily on empiricism and previous designs. In recent years, pumps have been extended to higher capacities, heads, and overall efficiencies. In many cases, designs for these larger pumps are proportionally larger versions of smaller older pumps. As a result, any problems with smaller pumps are magnified and new problems sometimes arise.

Instability problems encountered in the space shuttle hydrogen fuel turbopumps and safety requirements of nuclear main coolant pumps have prompted new research interest in annular seals. It is now widely recognized that in high-energy centrifugal pumps, the rotordynamic behaviour is affected by the fluid dynamic phenomena arising in the gaps between rotating and stationary parts.

1.2 Rotordynamic Analysis

Until recently, the dynamic analysis of centrifugal pumps concentrated on the calculation of critical speeds to comply with requirements of user specifications. For example, in *API Standard 610* [1.1] the critical speed is required to be at least 20% greater or 15% less than any operating speed.

The goal of earlier dynamic analyses was to calculate *dry critical speeds*, assuming that fluid dynamic phenomena specific to the close clearance running fits do not affect the rotordynamic behaviour of centrifugal pumps.

Later research has proved that this assumption is untenable and the computation of dry critical speeds is irrelevant. So-called *wet critical speeds* have to be calculated, including the fluid dynamic effects in sealing rings. First, only the Lomakin effect [1.2] has been

considered, which introduces a relatively large hydrostatic force, hence a large direct stiffness, raising the rotor critical speeds.

In recent studies, the focus is shifting towards prediction of response amplitudes and rotor instability. Such calculations include dynamic coefficients at wear rings, interstage rings, balancing rings and impeller/casing clearance, quantification of hydraulic forces generated by the impeller, and between the impeller shroud and stator.

It is now recognized that turbulent flow annular seals in multi-stage pumps and in straddle-mounted single-stage pumps have a dramatic effect on the dynamics of the machine. Stiffness and damping properties provided by seals represent the dominant forces exerted on pump shafts, excluding the fluid forces of flow through the impellers, particularly at part-flow operating conditions. For these systems, the hydrodynamics of oil-lubricated journal bearings is dominated by seal properties [1.3, 1.4].

Typical multi-stage centrifugal pumps have more inter-stage fluid annuli than they have journal bearings. The fluid annuli are distributed between the journal bearings where precession amplitudes are highest and can therefore be 'exercised' more as dampers than can be the bearings.

In typical applications, shaft resonant critical speeds are rarely observed at centrifugal pumps because of the high damping capability afforded by seals. Problems encountered with boiler feed pumps have been produced by excessive wear in seals, yielding a decrease in the dynamic forces exerted by the seals.

Recent interest in seal rotordynamic properties has been prompted by nuclear reactor main coolant pumps. In most designs, the impeller is cantilevered from the pump shaft bearing. The two annular seals, one at the impeller suction, and the other between the impeller and the pump shaft bearing, exert dynamic forces that critically affect the dynamic behaviour of the lower portion of the pump shaft.

A resurgence of interest in seals also occurred because of instability problems encountered in the space shuttle engine high pressure hydrogen fuel turbopumps [1.3]. Rotordynamic analysis indicated that improved stability could be achieved by redesign of the interstage seals to produce increased stiffness and damping, thereby

increasing the natural frequency of the unstable mode and more effectively damp the unstable excitations. In addition to rekindling analytic research interest, this particular problem has led to further experimental programs motivated by the extremely high Reynolds numbers (of order 500,000) occurring with liquid hydrogen flows.

1.3 Basic Principles

Centrifugal pumps are radial flow machines. A centrifugal pump impeller is shown schematically in figure 1.1.

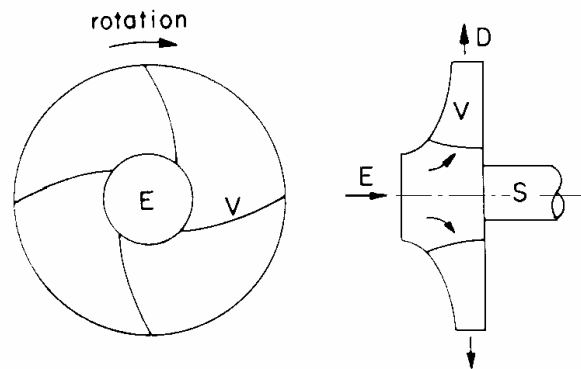


Fig. 1.1 (from [1.5])

Liquid enters the eye *E* of the impeller, moving in an axial direction and then turns to a radial direction to finally emerge at the discharge *D* having both a radial and a tangential component of velocity. The vanes *V* impart a curvilinear motion to the fluid particles, thus setting up a radial centrifugal force which is responsible for the outward flow of fluid against the resistance of wall friction and pressure forces.

Different impeller designs are shown in figure 1.2. The radial wheel *a* is for slow running pumps ($n_q=10-30$); the diagonal-radial wheel *b* is for medium speed pumps ($n_q=30-60$); the diagonal (half-axial) wheel *c* is for high speed pumps ($n_q=50-150$); and the axial wheel/propeller *d* is for the highest speeds ($n_q=110-500$).

The characteristic speed n_q is constant for geometrically similar impellers:

$$n_q = n \frac{Q^{1/2}}{H^{3/4}} \quad (1.1)$$

where Q is the flow rate, m^3/s , H is the pump head, m, and n is the rotational speed, rpm.

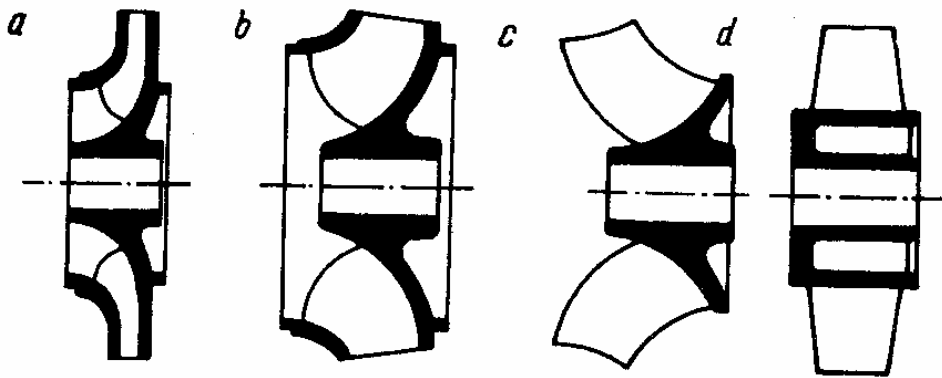


Fig. 1.2 (from [1.6])

The outer cover in *a* and *b* is the shroud. The wheel *c* is unshrouded. The wheel *d* is like a propeller.

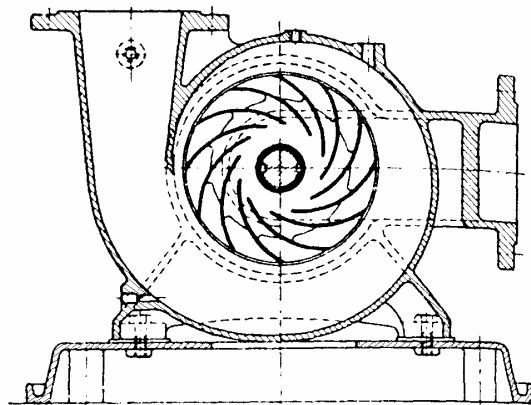


Fig. 1.3

An end view of an impeller is shown in figure 1.3. The vanes shown are curved backwards. Fluid next to the pressure face of the vane is forced to rotate at blade speed. The optimum number of vanes for pumps lies in the range of 5 to 12.

The fluid exits the impeller with tangential and radial components of absolute velocity. It is collected and conducted to the discharge of the pump by the volute or scroll portion of the casing. The volute is usually in the form of a channel of increasing cross-sectional area (Fig.1.4,*a*). The volute begins at the tongue with negligible sectional area and ends at the discharge nozzle. The so-called discharge nozzle, which is really a diffuser, joins the volute to the discharge flange of the pump.

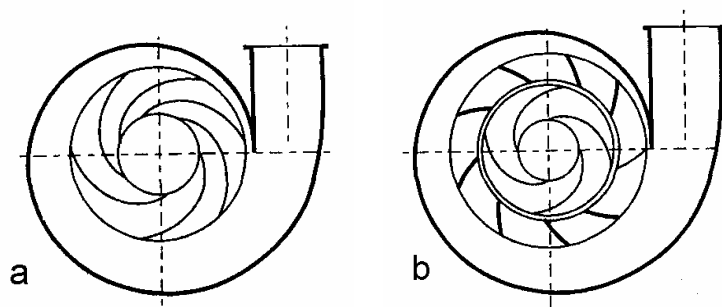


Fig. 1.4

A radial diffuser may be added between the impeller and the volute for high-pressure pumps. This may take the form of a space of constant width without vanes (vaneless diffuser) or it may include vanes forming diverging passages aligned with the absolute velocity vector (Fig.1.4,*b*).

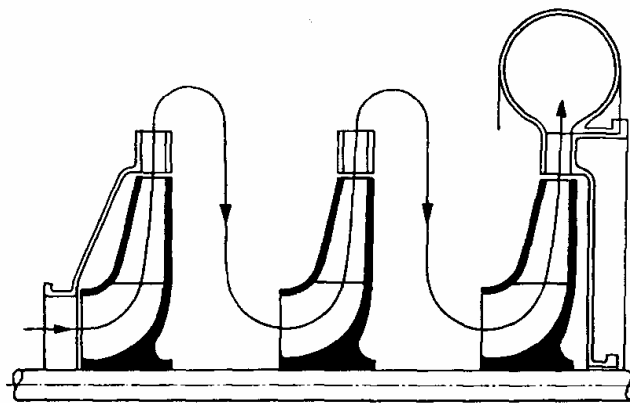


Fig. 1.5 (from [1.6])

Multi-stage pumps have several impellers mounted on the same shaft. The fluid discharging from one is conducted to the inlet of the neighbouring impeller (Fig.1.5), thus making the overall pressure rise of the pump the sum of the individual-stage pressure rises.

1.4 Design Characteristics

Centrifugal pumps have comparatively slender shafts and relatively flexible cantilevered bearing housings (Figs. 1.6 and 1.7).

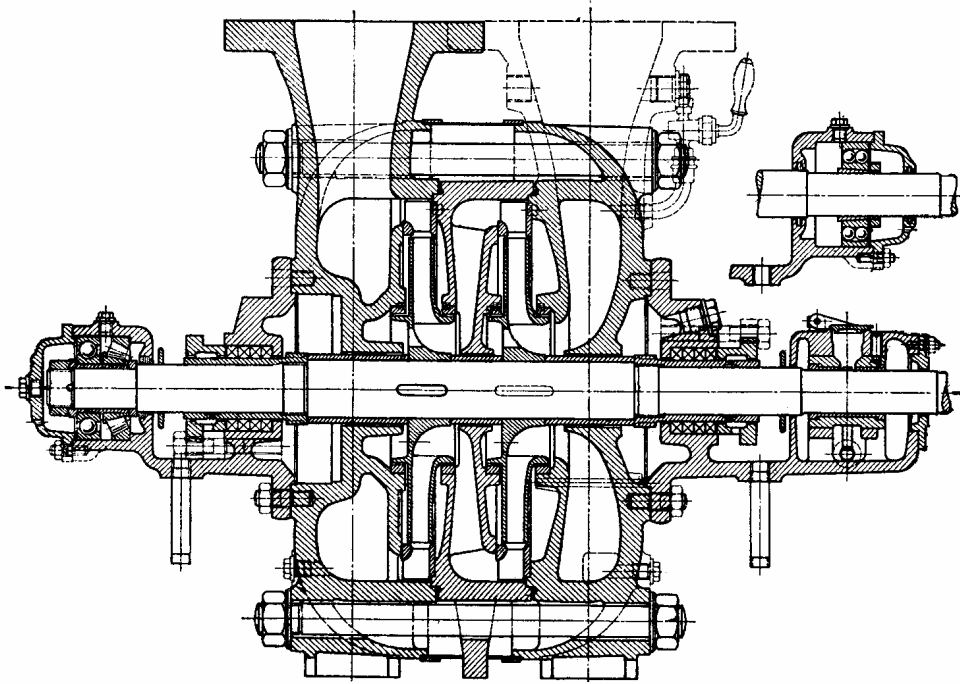


Fig. 1.6 (from [1.6])

Pump shafts are supported on a variety of bearing types, including rolling element, hydrodynamic and hydrostatic.

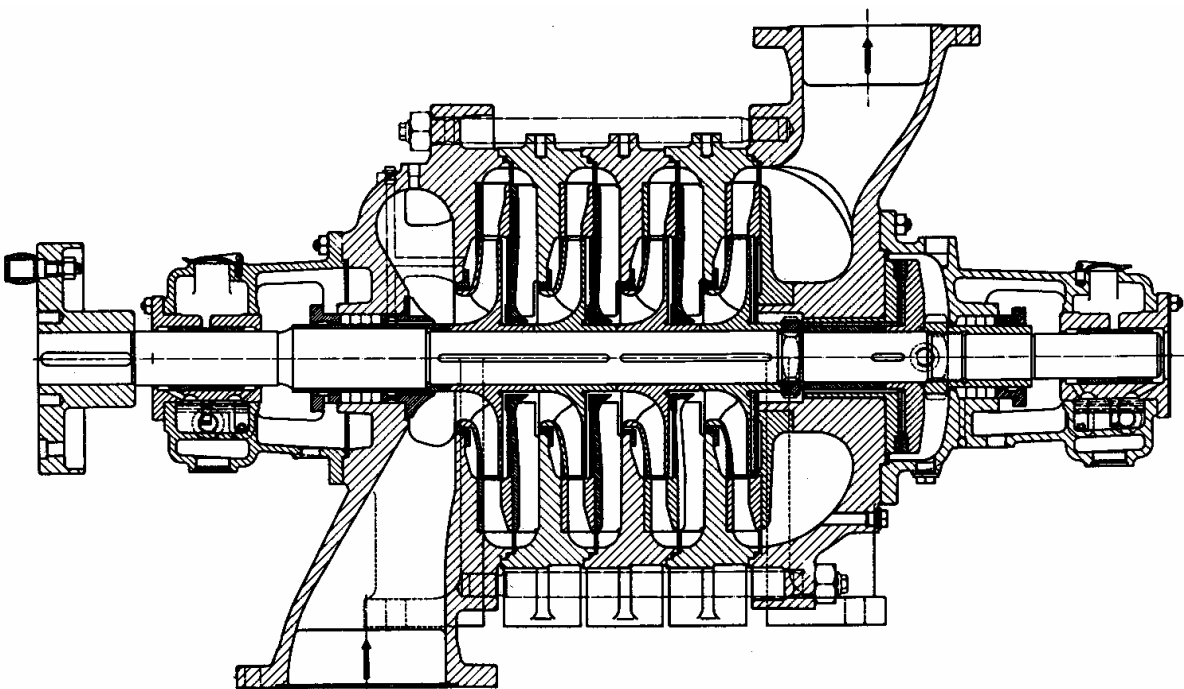


Fig. 1.7 (from [1.7])

Dynamic coefficients of hydrodynamic bearings depend on rotor speed and static bearing loads. The static bearing load is a resultant of rotor deadweight and all static fluid forces. The static impeller forces depend on flow rate, impeller hydraulic design, and type of pump casing. Each flow condition of the pump creates different static impeller forces and therefore different bearing force coefficients in terms of stiffness and damping.

Fine clearance annular seals are used in pumps primarily to prevent leakage between regions of different pressure within the pump. The rotordynamic behaviour of pumps is critically dependent on forces developed by annular seals. Two of the most typical arrangements are shown in figure 1.8.

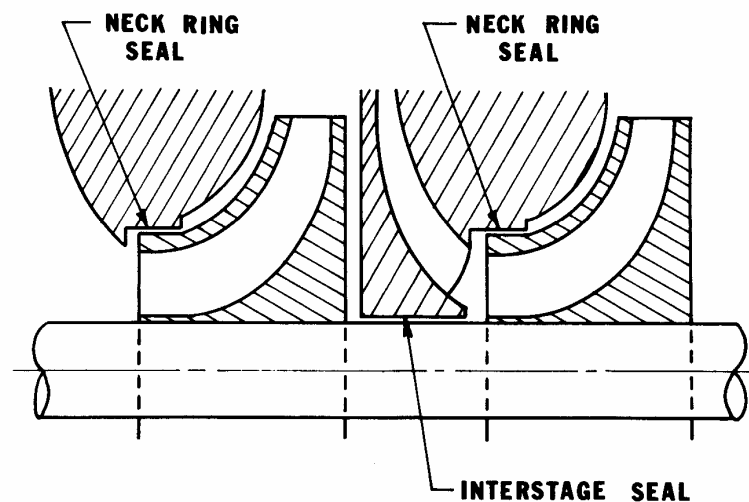


Fig. 1.8 (from [1.3])

The neck ring (or wearing ring) seal *A* is located at the suction region of a shrouded centrifugal impeller (Fig. 1.9). It is used to restrict leakage flow along impeller shroud, from impeller discharge to impeller inlet. The interstage seal *B* restricts flow along the shaft between stages. Although similar in appearance, there can be significant differences between the seals due to different lengths, radii, pressure drops across them, and velocity conditions of the fluid at the entrance.

Other close-clearance running fits are *C* - the balance-piston seal and *D* - the throttle bushings, breakdown bushings, or packing glands. In figure 1.9, *E* are the radial bearings, *F* the thrust bearing.

The stator/impeller interaction is denoted G , and the shroud/fluid interaction by H .

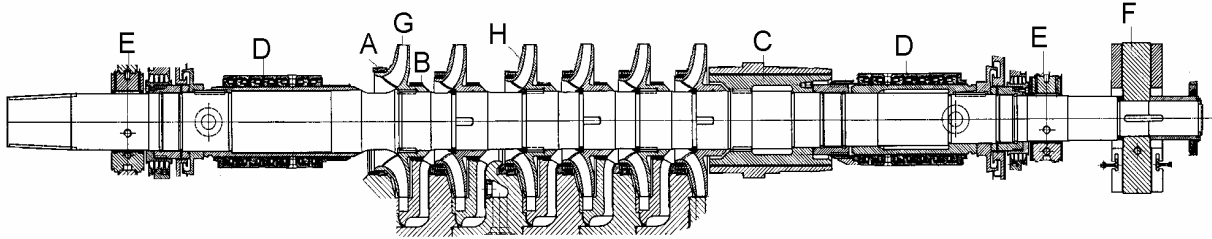


Fig. 1.9

The single-stage pump from figure 1.10 and the two-stage pump from figure 1.6 have annular seals on the back of the impellers and holes to balance the axial pressure drop. Modern designs have balance pistons as C in figure 1.9.

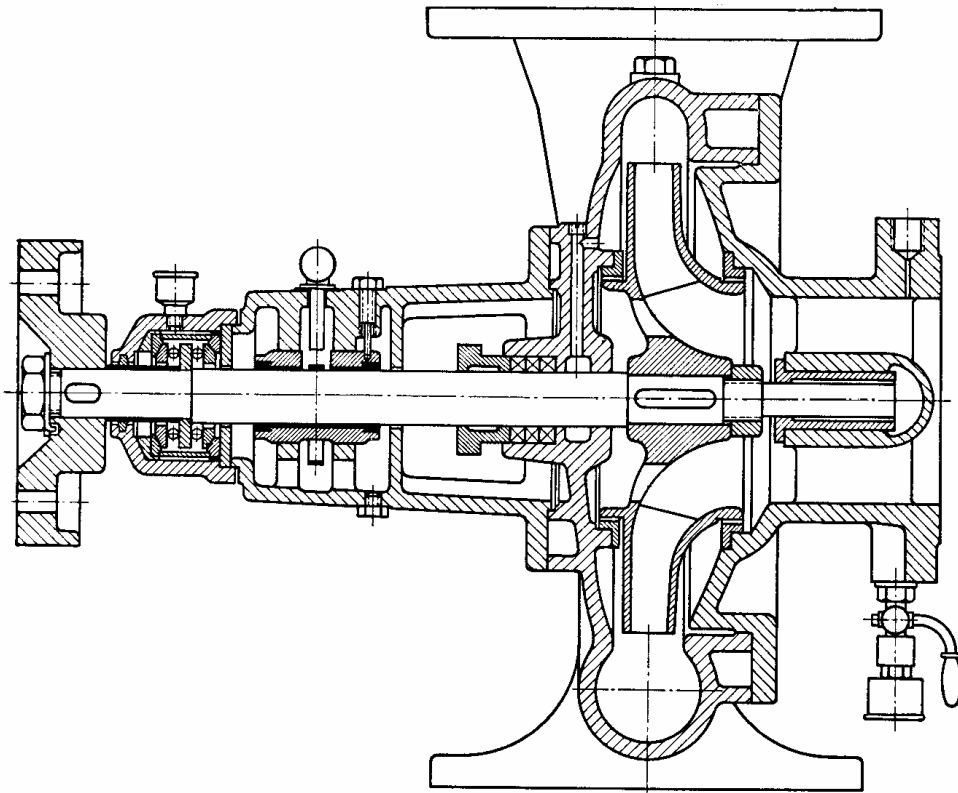


Fig. 1.10 (from [1.6])

A horizontal single-stage pump with a cantilevered impeller is presented in figure 1.11.

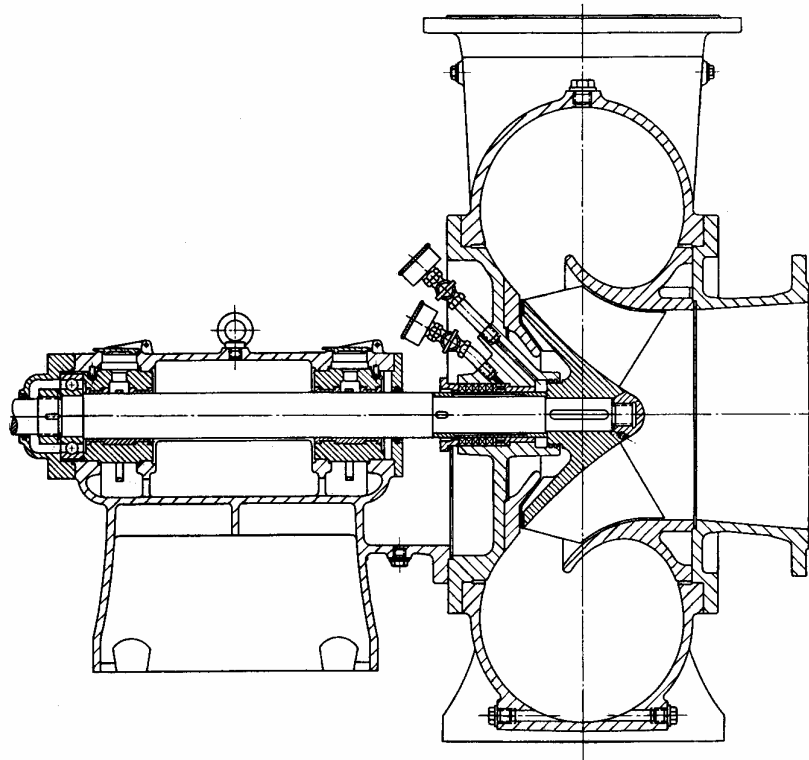


Fig. 1.11 (from [1.7])

Figure 1.12 shows a pump with a double suction impeller.

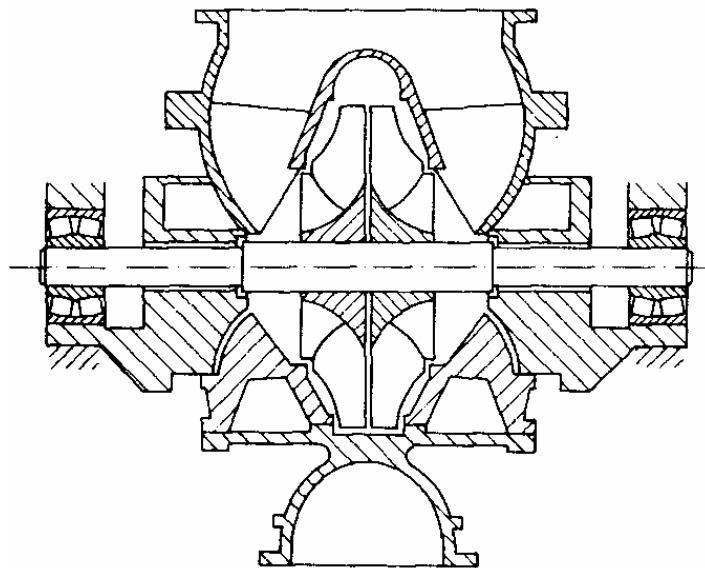


Fig. 1.12 (from [1.8])

Figure 1.13 illustrates the main components of a vertical nuclear reactor main coolant pump [1.9]. The pump impeller is not

mounted between bearings, but is cantilevered from the pump shaft bearing. The motor has two tilting-pad oil-lubricated journal bearings. They are sufficiently removed from the impeller so that their effects on the dynamics of the pump shaft are limited due to motor and pump shaft flexibility and coupling flexibility. The turbulent hydrostatic pump shaft bearing is generally pressure fed with water from the impeller. Unlike multi-stage horizontal pumps, there are only two annular seals, one at the impeller suction and one between the impeller and the pump shaft bearing. Shaft seals are provided between the coupling and the pump bearing.

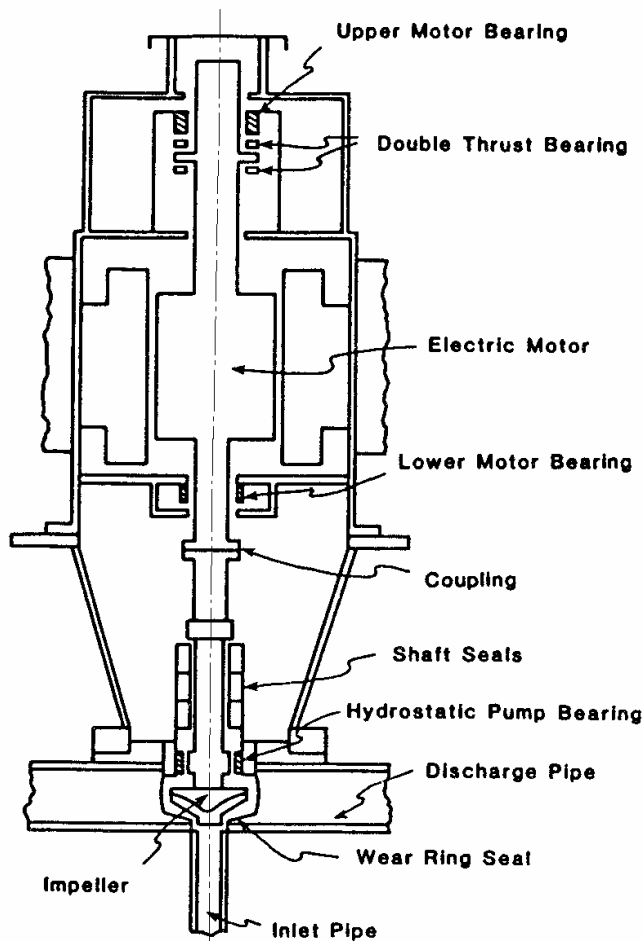


Fig. 1.13 (from [1.9])

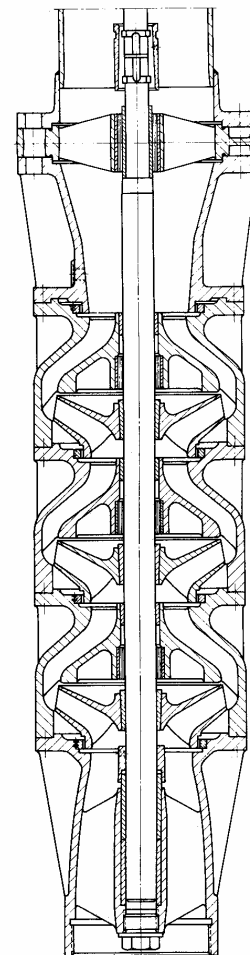


Fig. 1.14 [1.7]

A three-stage vertical extraction pump for drill holes, with $H=13$ m, $Q=220$ m³/h, $n=1450$ rpm, is shown in figure 1.14 [1.7]. Multi-stage horizontal pumps are shown in figures 1.15 [1.10] and 1.16 [1.11].

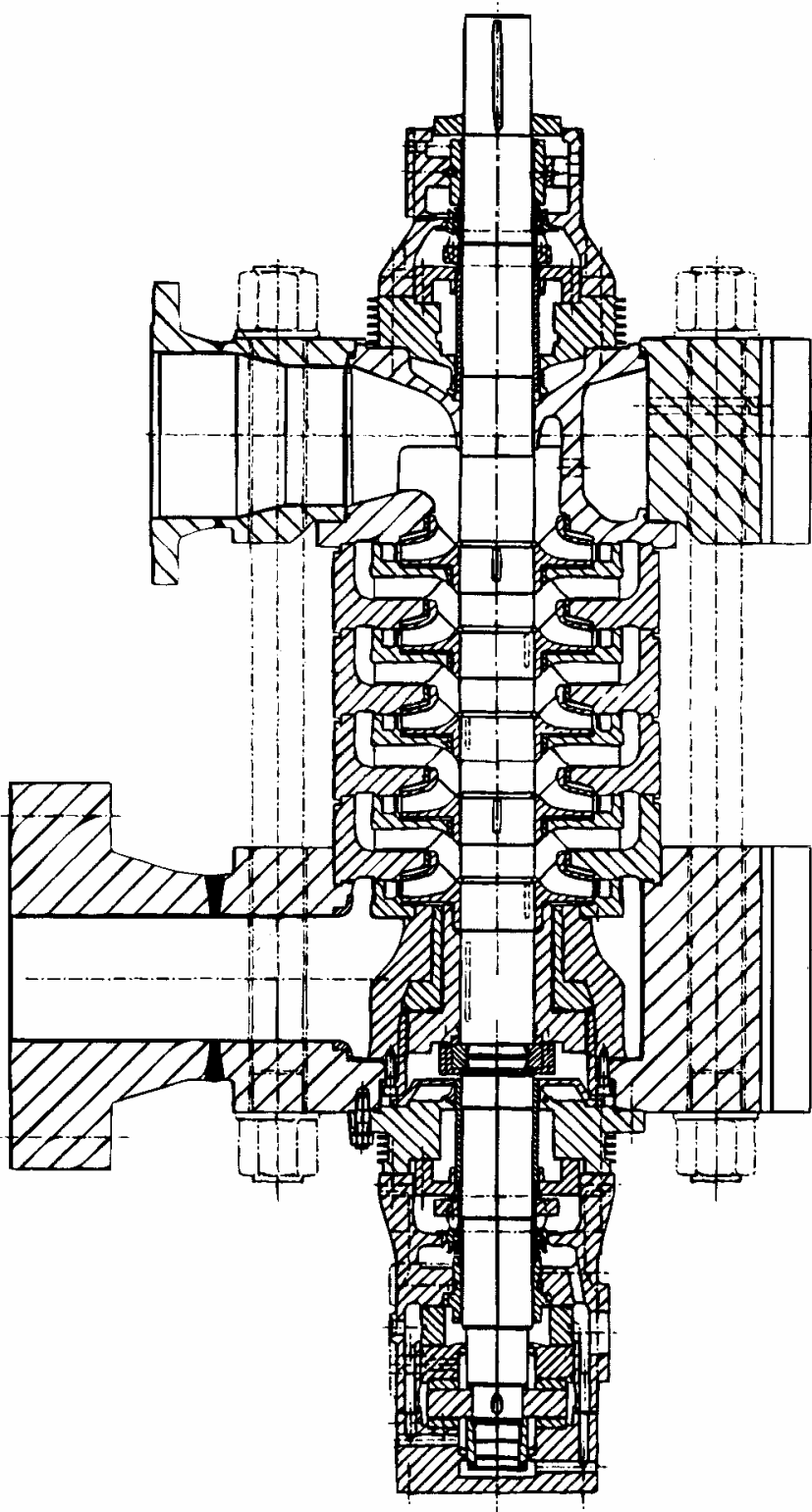


Fig.1.15 (from [1.10])

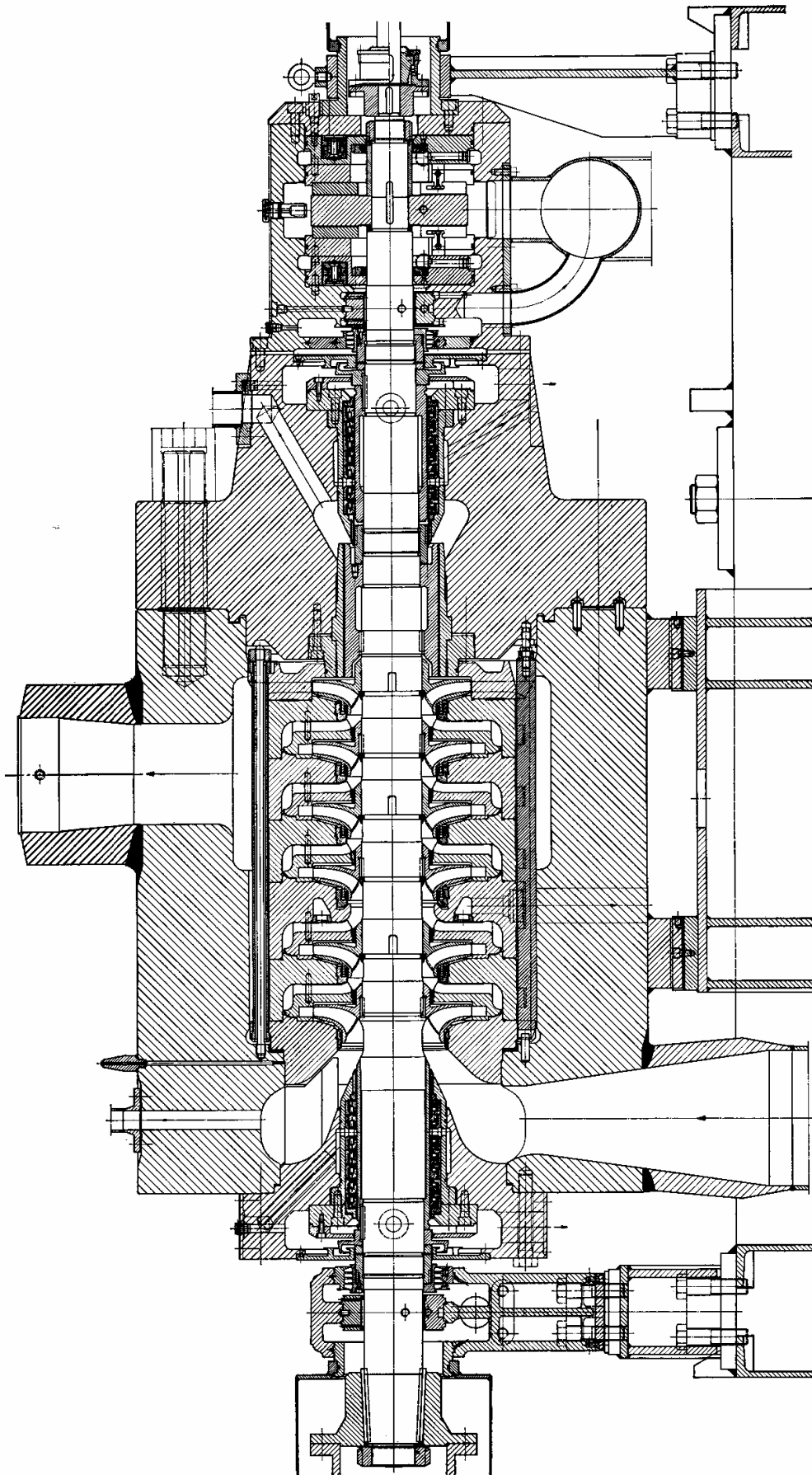


Fig.1.16 (from [1.11])

The six-stage boiler feed pump from figure 1.16, built by Sulzer in 1971, has the following parameters: flow rate 1370 t/h, head 4015 m, absorbed power 18.45 MW, operating temperature 216°C, speed 5770 rpm. A separate view of the rotor is shown in figure 1.9.

Figure 1.17 depicts the location of annular seals (numbered) in the high-pressure fuel turbopump of the space shuttle main engine. The turbine stages develop 57 MW at 37,000 rpm. Pump impeller diameters are about 150 mm. Axial thrust is absorbed by a balance piston arrangement at the backside of the third impeller stage. The rolling-element bearings have radial "dead-band" clearances between the outer bearing races and the housings to allow relative axial slip and limit the axial load carried by the bearings.

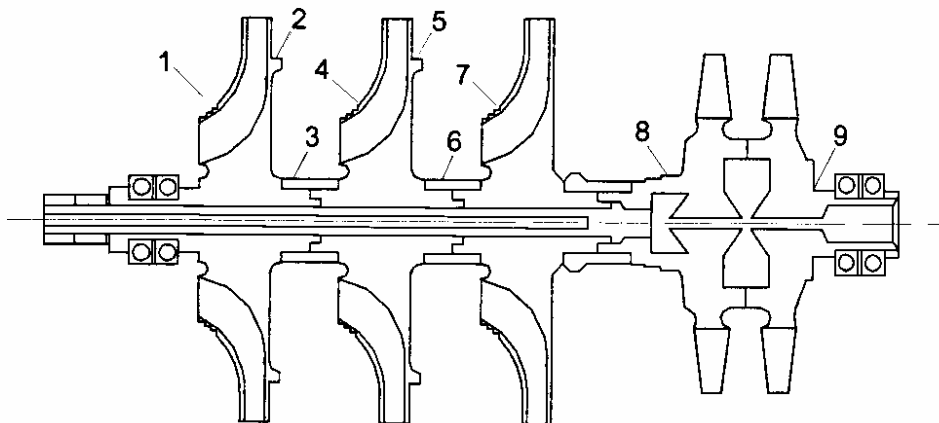


Fig. 1.17

1.5 Forces Acting upon Pump Rotors

The forces that act upon a pump rotor result from mechanical and hydraulic actions. Mechanical forces are mainly due to unbalance and coupling misalignment.

Hydraulic forces arise in two different ways. First, when the shaft centre is fixed, radial forces occur as a result of distribution of static pressure and fluid momenta. These forces are termed *steady excitation forces*. Second, when the shaft centre also moves as a result

of precession, additional forces are generated due to the interaction of impeller and surrounding fluid. These are *dynamic forces* and are described by dynamic coefficients.

Steady excitation forces are fairly well understood and well quantified when a pump operates at its best efficiency point. At off-design conditions, the flow field can become very complex and analytical predictions become impossible. In addition, the effect of geometrical tolerances appears to be significant.

As the rotor moves excentrically within the pump, significant forces are developed a) in the annular seals; b) between the impeller shroud and the stator; c) between the impeller back disc and the stator; and d) between impeller and diffuser. When a shaft is displaced laterally in a ring seal, a strong restoring force is set up in the clearance space. This *hydrostatic force* increases with the pressure drop and the amplitude of shaft lateral motion. In effect, the clearance acts as a spring. The phenomenon is known as the *Lomakin effect*.

For a whirling shaft, a *destabilizing tangential force* appears normal to the shaft radial displacement, yielding a cross-coupled stiffness. This is approximately proportional to the average tangential velocity of the fluid. Wide variations occur in the inlet swirl velocity, depending upon where annular seals are located in the pump. Swirl brakes are commonly used upstream of seals to sharply reduce this velocity. A deliberately roughened stator also reduces the average tangential velocity.

Damping forces also arise from drag mechanisms.

Recent research revealed that impeller shrouds develop significant destabilizing forces. Conservation of momentum considerations for leakage flow inward, along the impeller shroud, can generate high tangential velocities for the flow entering the neck ring and balance piston seals. Enlarged clearances of the exit seal, due to wear or damage, increase the tangential velocity over the shroud and into the seal. Lateral forces on pump impellers can also have a significant dynamic effect.

Forces are exerted on the impeller as a result of the asymmetry of flow caused by the volute or diffuser and the motion of the impeller. *Supersynchronous forces* are generated in volute pumps at

the vane passing frequency. In turn, the diffuser pumps can generate greater forces in the subsynchronous range, depending on the casing tip clearance. *Subsynchronous forces* with frequency components from 30% to 80% of running speed can be attributed to partial flows or associated with destabilizing forces.

The impeller/casing interaction can be described with dynamic force coefficients. Other volute effects as well as the shed vorticity from the vane trailing edges generate instationary forces. Impeller offsets and nonuniformities in the impeller manufacturing process generate *synchronous forces*.

1.6 Annular Seals

Plain (ungrooved) annular seals are joints with the inner cylinder (the rotor) rotating in a tight fluid annulus with respect to the outer cylinder (the stator). For a centred seal, there is an axial velocity due to the axial pressure gradient (leakage flow) and a circumferential velocity due to the shaft rotation and shaft-fluid friction. In the "bulk-flow" model [1.3], these velocities are constant across the film, and shear stresses are accounted for only at the boundaries, at the shaft and the seal stator.

For an eccentric seal, the difference between the pressure gradient on the tight and loose sides provides a restoring force, which opposes the shaft displacement, yielding a large direct stiffness. This is the *Lomakin effect*.

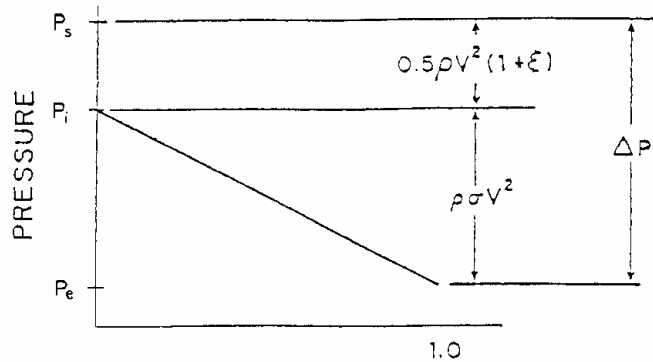
For a whirling shaft, a tangential force will appear normal to the shaft radial displacement, yielding a cross-coupled stiffness.

In the "short seal" solution, the pressure-induced tangential velocity is neglected. An improved treatment accounts for the development of circumferential flow due to the shear forces along the seal.

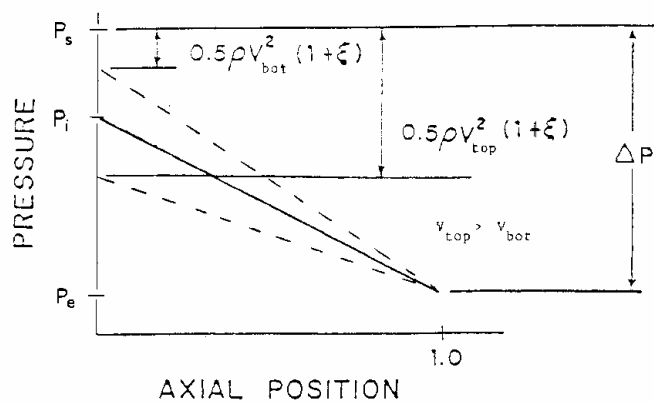
In the following, the short seal solutions of Black and Childs are presented.

1.6.1 Hydrostatic Reaction. Lomakin Effect

The steady-state axial pressure distribution at any circumferential location within a plain non-serrated seal is shown in figure 1.18 for a simple case without shaft rotation.



a. Steady Stage Axial Pressure Distribution



b. Pressure Drops at Seal Entrance

Fig. 1.18 (from [1.12])

The pressure at the inlet of the seal is p_s and that at the seal exit is p_e . As flow accelerates into the seal, a pressure drop occurs due to the Bernoulli effect. An additional decrease at the inlet region occurs due to the gradual growth of a turbulent flow velocity field into its fully developed form. The remainder of the pressure drop through the seal is very nearly linear.

The seal differential pressure can be calculated using Yamada's leakage relationship [1.13] for flow between concentric rotating cylinders

$$\Delta p = (1 + \xi + 2\sigma) \frac{\rho V^2}{2} \quad (1.2)$$

where ξ is the entrance loss factor, ρ is the fluid density, V is the average fluid velocity, and σ is a friction loss factor defined by

$$\sigma = \frac{\lambda L}{C_r} \quad (1.3)$$

In the above, L is the seal length, C_r is the radial clearance, and λ is a friction factor, defined by Yamada to be the following function of the axial and circumferential Reynolds numbers, R_a , R_c :

$$\lambda = 0.079 R_a^{-\frac{1}{4}} \left[1 + \left(\frac{7 R_c}{8 R_a} \right)^2 \right]^{\frac{3}{8}}, \quad (1.4)$$

$$R_a = \frac{2 V C_r}{\nu}, \quad R_c = \frac{R \omega C_r}{\nu}, \quad (1.5)$$

where ν is the fluid kinematic viscosity, R is the seal radius and ω is the rotor's angular speed, rad/s. The friction law definition of equation (1.4) fits the Blasius equation for pipe friction [1.3].

If the shaft moves downward within the seal, the velocity at the top of the shaft, V_{top} , increases, because of the larger gap through which the fluid flows. Flow velocity at the bottom, V_{bot} , decreases because of the smaller gap height there. Thus, pressure drops at the seal entrance are flow-velocity dependent and differ from top to bottom as shown in figure 1.18,b. At the top, the entrance pressure drop increases. At the bottom, the entrance pressure drop decreases. Therefore, a net increase in pressure at the bottom of the seal produces an *upward* force tending to restore the shaft to its original centred position.

A similar situation occurs when the lateral velocity of the shaft changes.

The combined effect of the inlet loss and axial-pressure gradient accounts for the large direct stiffness which can be developed by annular seals. This physical mechanism for the direct stiffness was first explained by Lomakin in 1958.

The actual pressure distributions shown in figures 1.18,*a* and *b* are modified by shaft rotation and geometric variations within the seal, but the underlying principles governing the pressure buildup within a seal remain the same.

The C_r/R ratio for seals is generally on the order of 0.003 versus 0.001 for bearings. These enlarged clearances, combined with a high pressure drop across the seal, mean that flow is highly turbulent.

Most analyses for pump seals have used "bulk-flow" models for the fluid within the seal. In such models, the variation of fluid velocity components across the clearance is neglected. Average (across the clearance) velocity components are used – hence the *bulk-flow* designation. Bulk-flow models neglect the shear stress variation for the fluid within the clearance and only account for shear stresses at the boundaries of the model [1.4].

1.6.2 Rotordynamic Coefficients

Dynamic seal forces are normally represented by a reaction force / seal motion model of the form:

$$\begin{Bmatrix} -F_y \\ -F_z \end{Bmatrix} = \begin{bmatrix} K & k \\ -k & K \end{bmatrix} \begin{Bmatrix} y \\ z \end{Bmatrix} + \begin{bmatrix} C & c \\ -c & C \end{bmatrix} \begin{Bmatrix} \dot{y} \\ \dot{z} \end{Bmatrix} + M \begin{Bmatrix} \ddot{y} \\ \ddot{z} \end{Bmatrix}, \quad (1.6)$$

where y and z are fixed coordinate displacements of the shaft and the dots are derivatives with respect to time. This model is valid for small motion about a centred position.

Short annular seals are usually considered isotropic. The diagonal terms of their stiffness and damping matrices are equal, while the off-diagonal terms are equal, but with reversed sign. The cross-coupled damping and the mass term arise primarily from inertial effects. Short seal solutions are obtained by neglecting the pressure-induced circumferential flow, while including the shear-induced flow.

Cross-coupled stiffnesses arise from fluid rotation, in the same way as in uncavitated plain journal bearings. For example, moving the seal rotor horizontally rightwards, a converging section is created in the lower half and a diverging section in the upper half of the seal (shaft rotates counterclockwise). The pressure is elevated in the converging section and depressed in the diverging section, yielding a reaction force upwards. This force acts normal to the radial displacement, having a destabilizing effect.

For long annular clearance seals, like those used to break down large pressure differences in multi-stage pumps, *angular dynamic coefficients* are introduced, because the rotor is acted upon by couples, and forces give rise to tilting shaft motions, and moments produce linear displacements.

The dynamic coefficients of equation (1.6) can be expressed in the following form:

Stiffness coefficients:

$$K = \mu_3 (\mu_0 - \mu_2 \omega^2 T^2 / 4), \quad k = \mu_3 \mu_1 \omega T / 2; \quad (1.7)$$

Damping coefficients:

$$C = \mu_3 \mu_1 T, \quad c = \mu_3 \mu_2 \omega T^2; \quad (1.8)$$

Inertia coefficients:

$$M = \mu_3 \mu_2 T^2; \quad (1.9)$$

where

$$\mu_3 = \frac{\pi R \Delta p}{\lambda} \quad (1.10)$$

and the mean passage time is

$$T = \frac{L}{V}. \quad (1.11)$$

The quantities μ_0 , μ_1 and μ_2 depend on the friction loss coefficient σ , and the entry loss coefficient ξ . Their formulae are given below for three slightly different annular seal models.

1. Black's model [1.14], [1.12]

$$\mu_0 = \frac{(1+\xi)\sigma^2}{(1+\xi+2\sigma)^2}, \quad (1.12)$$

$$\mu_1 = \frac{(1+\xi)^2\sigma + (1+\xi)(2.33+2\xi)\sigma^2 + 3.33(1+\xi)\sigma^3 + 1.33\sigma^4}{(1+\xi+2\sigma)^3},$$

$$\mu_2 = \frac{0.33(1+\xi)^2(2\xi-1)\sigma + (1+\xi)(1+2\xi)\sigma^2 + 2(1+\xi)\sigma^3 + 1.33\sigma^4}{(1+\xi+2\sigma)^4}.$$

For finite-length seals, Jenssen developed the following formulae to account for finite L/R ratios:

$$\bar{\mu}_0 = \mu_0 \left[1 + 0.28 \left(\frac{L}{R} \right)^2 \right]^{-1}, \quad \bar{\mu}_1 = \mu_1 \left[1 + 0.23 \left(\frac{L}{R} \right)^2 \right]^{-1},$$

$$\bar{\mu}_2 = \mu_2 \left[1 + 0.06 \left(\frac{L}{R} \right)^2 \right]^{-1},$$

where μ_0 , μ_1 and μ_2 are given by (1.12), and the "bar" quantities have to be used in equations (1.7) to (1.9) instead of those without bar over letter.

2. Jenssen's model [1.15]

In a further development, the coefficients μ_0 , μ_1 and μ_2 were defined in terms of the following additional parameter

$$\beta = \left(\frac{7R_c}{8R_a} \right)^2 \left[1 + \left(\frac{7R_c}{8R_a} \right)^2 \right]^{-1} \quad (1.13)$$

which accounts for a circumferential variation in λ due to a radial displacement perturbation from a centred position. They can be calculated as

$$\begin{aligned} \mu_0 &= \frac{1.25 A \sigma^2}{B D} , \\ \mu_1 &= \frac{\sigma A^2 + 2A \left[C \left(\frac{5}{6} + \frac{1}{3} \xi \right) - \frac{5}{8} \right] \sigma^2 + \frac{5}{6} E + \frac{1}{6} F}{B D^2} , \\ \mu_2 &= \frac{2A \left(\frac{1}{3} \xi - \frac{1}{6} \right) \sigma + A (1.25 + C \xi) \sigma^2 + \frac{1}{2} E + \frac{1}{6} F}{B D^3} , \end{aligned} \quad (1.14)$$

where

$$A = 1 + \xi , \quad B = 1 + \xi + 2\sigma , \quad C = 1.75 - 0.75 \beta ,$$

$$D = A + C \sigma , \quad E = A C^2 \sigma^3 , \quad F = C^3 \sigma^4 .$$

Plots of μ_0 , μ_1 and μ_2 from equations (1.14) are provided in figure 1.19 as a function of β and σ , for $\xi = 0.5$. These coefficients are comparatively insensible to anticipated variations of the entrance loss factor ξ .

Black also examined the influence of inlet swirl on seal coefficients. In previous analyses, a fluid element entering a seal was assumed to instantaneously achieve the half-speed tangential velocity $R \omega / 2$. In a later paper he demonstrates that a fluid element must travel a substantial distance axially along the seal before asymptotically approaching this limiting velocity. The practical consequence of this swirl effect is that predictions of the cross-coupling terms, k and c , may be substantially reduced. This applies especially for interstage seals, in which the inlet tangential velocity is negligible.

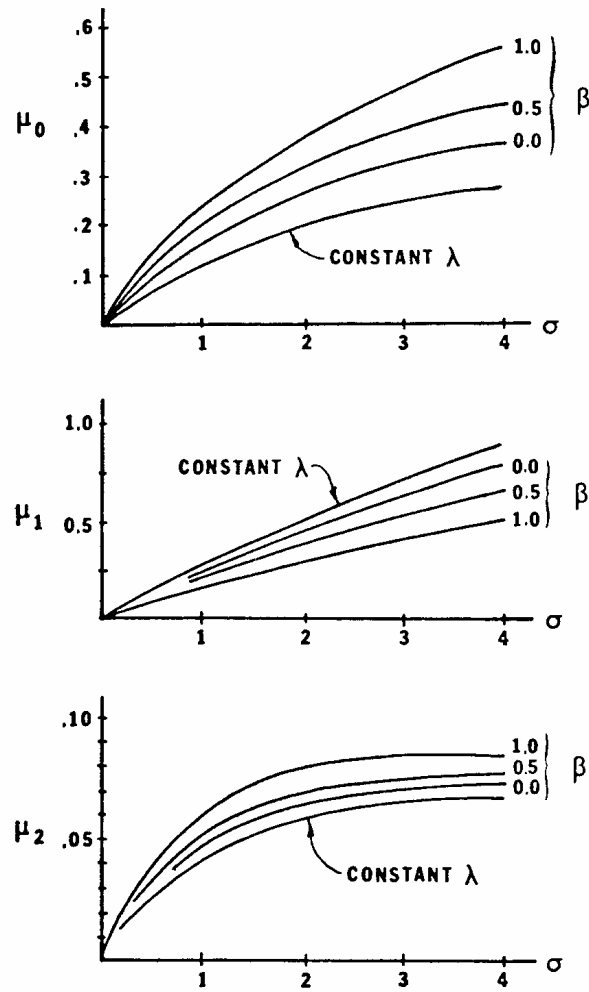


Fig. 1.19 (from [1.15])

3. Childs' model [1.16]

Childs completed a seal analysis based on Hirs' [1.17] turbulent lubrication model. In his analysis he assumed completely developed turbulent flow in both the circumferential and axial directions. The short seal dynamic coefficients derived by Childs are given by equations (1.7)-(1.9) but the coefficients μ_0 , μ_1 and μ_2 are

$$\mu_0 = \frac{2\sigma^2 E(1 - m_0)}{1 + \xi + 2\sigma},$$

$$\mu_1 = \frac{2\sigma^2}{1 + \xi + 2\sigma} \left[\frac{E}{\sigma} + \frac{B}{2} \left(\frac{1}{6} + E \right) \right], \quad (1.15)$$

$$\mu_2 = \frac{\sigma}{1 + \xi + 2\sigma} \left(\frac{1}{6} + E \right),$$

where

$$E = \frac{1 + \xi}{2(1 + \xi + B\sigma)}, \quad B = 1 + 4b^2\beta(1 + m_0),$$

$$\beta = \frac{1}{1 + 4b^2}, \quad b = \frac{R_a}{2R_c}, \quad (1.16)$$

and m_0 is an exponent entering the loss factor expression

$$\lambda = n_0 R_a^{m_0} \left(1 + \frac{1}{4b^2} \right)^{\frac{1+m_0}{2}}. \quad (1.17)$$

The short seal dynamic coefficients derived by Childs are similar to the previously mentioned solution by Black when an one-half shaft speed swirl velocity is assumed.

Childs considered the influence of the initial swirl V_0 . In this case, the seal dynamic coefficients are written in the following form

Stiffness coefficients:

$$K = \mu_3 \left[\mu_0 - \frac{\omega^2 T^2}{4} (\mu_2 + a_1) \right], \quad k = \mu_3 (\mu_1 + a_2) \frac{\omega T}{2}; \quad (1.18)$$

Damping coefficients:

$$C = \mu_3 \mu_1 T, \quad c = \mu_3 (\mu_2 + a_3) \omega T^2; \quad (1.19)$$

Inertia coefficients:

$$M = \mu_3 \mu_2 T^2, \quad (1.20)$$

where

$$a = \sigma [1 + \beta(1 + m_0)], \quad (1.21)$$

$$a_1 = \frac{2V_0}{a} \frac{2\sigma^2}{1+\xi+2\sigma} \left[\left(E + \frac{1}{a^2} \right) (1 - e^{-a}) - \left(\frac{1}{2} + \frac{1}{a} \right) e^{-a} \right],$$

$$a_2 = \frac{2V_0}{a} \frac{2\sigma^2}{1+\xi+2\sigma} \left\{ EB + \left(\frac{1}{\sigma} - \frac{B}{a} \right) \left[(1 - e^{-a}) \left(E + \frac{1}{2} + \frac{1}{a} \right) - 1 \right] \right\},$$

$$a_3 = \frac{2V_0}{a} \frac{\sigma}{1+\xi+2\sigma} \left[\left(E + \frac{1}{2} + \frac{1}{a^2} \right) (1 - e^{-a}) - \left(\frac{1}{2} + \frac{e^{-a}}{a} \right) \right].$$

For $V_0=0$, $a_1 = a_2 = a_3=0$, and one obtains eqs. (1.7)-(1.9).

From equation (1.6), a circular shaft orbit of radius A and precessional frequency ω yields radial and circumferential force components

$$F_r = -(K + c\omega - M\omega^2)A, \quad F_\theta = (k - C\omega)A.$$

The circumferential force can produce unstable operating regimes.

1.6.3 Example Calculation for a Short Seal

An annular neck ring seal has the following geometric properties: length $L=50$ mm, radius $R=75$ mm ($L/D=1/3$), radial clearance $C_r=0.25$ mm.

At operating conditions $N=1200$ rpm, the pressure difference across the axial length of the seal is $\Delta p=1.38 \cdot 10^6$ Pa. The water properties are: dynamic viscosity $\mu=4.14 \cdot 10^{-4}$ Ns/m², mass density $\rho=979$ kg/m³.

Assume initially that the flow velocity is $V=25$ m/s.

The initial axial Reynolds number is

$$R_a = \frac{2\rho VC_r}{\mu} = 29559.$$

The circumferential Reynolds number is

$$R_c = \frac{\omega \rho R C_r}{\mu} = 5572.$$

Solving for σ gives

$$\sigma = \frac{L}{C_r} \frac{0.079}{R_a^{1/4}} \left[1 + \left(\frac{7R_c}{8R_a} \right)^2 \right]^{3/8} = 1.217.$$

Considering $\xi=0.1$, from the equation for Δp a new value of V is obtained

$$V = \left(\frac{2\Delta p / \rho}{1 + \xi + 2\sigma} \right)^{1/2} = 26.77 \text{ m/s.}$$

The process is repeated iteratively until the mean flow velocity is obtained as $V=28.592$ m/s for which $\sigma = 1.174$.

The final value of the axial Reynolds number is $R_a = 33,807$ showing that the flow is fully turbulent.

Substituting $\xi=0.1$ and $\sigma=1.193$ into the equations (1.12) gives

$$\mu_0=0.1414, \quad \mu_1=0.35, \quad \mu_2=0.05287,$$

and also

$$\mu_3=5.6 \cdot 10^7.$$

The mean passage time is

$$T = \frac{L}{V} = 1.749 \cdot 10^{-3} \text{ s.}$$

The dynamic coefficients (1.7)-(1.9) have the following values

$$\begin{aligned} K &= 7.1139 \cdot 10^6 \text{ N/m}, & k &= 2.0604 \cdot 10^6 \text{ N/m}, \\ C &= 32,793 \text{ Ns/m}, & c &= 1153 \text{ Ns/m}, \\ M &= 9.176 \text{ Ns}^2/\text{m}. \end{aligned}$$

Note that $\frac{M\omega}{c}=1$, so that M and c tend to cancel for synchronous precession at the running speed and the radial reaction force component F_r is given only by the direct stiffness K .

The whirl frequency ratio is $\Omega_w = \frac{k}{C\omega} = 0.5$ corresponding to the average tangential velocity within the seal $R\omega/2$. The result is the same as for a plain journal bearing. For $\omega = \omega_n$, the rotor's first critical speed, the tangential reaction force component F_θ becomes destabilizing at the speed $\omega_s = \frac{\omega_n}{0.5} = 2\omega_n$. This shows that, theoretically, a seal becomes destabilizing at running speeds in excess of about twice the rotor's first critical speed. Because in seals Ω_w can be decreased, the on-set speed of instability ω_s is increased.

1.7 Impeller-Volute Interaction

The dynamic behaviour of centrifugal pump rotors is affected by the interaction between the flow exiting the impeller and entering a volute or a vaned diffuser (G in fig. 1.9)

At the design point, the flow field in the volute is characterized by a free vortex velocity distribution in the radial direction. In the circumferential direction, the velocity and static pressure are uniform, so that the relative flow in the impeller is steady.

If the impeller is displaced with respect to the geometric centre of the volute, the flow area in the direction of motion is decreased, and the tangential velocity is increased. At the diametrically opposite position, the flow area is increased and the flow velocity is decreased. Assuming no change in total head or losses, the difference in velocity on either side results in a difference of static pressure. In particular, the static pressure in the area in the direction of the displacement is reduced. Thus, a force is exerted in the same direction as the displacement. This force does not tend to restore the deflection. Hence the resulting direct stiffness is negative.

Further on, since the tangential velocities are different, integration of the momenta around the circumference will lead to a different value than when the impeller is centred. The difference in tangential moments will lead to a force normal to the deflection, generating cross-coupling stiffness.

For rotordynamic computations, the impeller-volute/diffuser interaction forces are generally modelled by an equation of the form

$$\begin{Bmatrix} -F_y \\ -F_z \end{Bmatrix} = \begin{bmatrix} K & k \\ -k & K \end{bmatrix} \begin{Bmatrix} y \\ z \end{Bmatrix} + \begin{bmatrix} C & c \\ -c & C \end{bmatrix} \begin{Bmatrix} \dot{y} \\ \dot{z} \end{Bmatrix} + \begin{bmatrix} M & m_c \\ -m_c & M \end{bmatrix} \begin{Bmatrix} \ddot{y} \\ \ddot{z} \end{Bmatrix}. \quad (1.22)$$

Note the presence of a cross-coupled mass coefficient m_c , in comparison to the liquid-seal model of equation (1.6).

Test results for impellers in a volute [1.3] confirm that the direct stiffness coefficient K is negative and could cause a reduction in a critical speed. The positive sign of k implies that a tangential force is developed in the direction of rotation, which would destabilize forward precession modes. The sign of m_c is negative, which implies that it is destabilizing for forward precession.

The model of equation (1.22), with identical diagonal elements and skew-symmetric off-diagonal elements, ensures radial isotropy. However, experimental data show slightly different values for both the diagonal and the off-diagonal coefficients [1.10].

From equation (1.22), a circular shaft orbit of radius A and precessional frequency ω yields radial and circumferential force components

$$F_r = -(K + c\omega - M\omega^2)A, \quad F_\theta = (k - C\omega - m_c\omega^2)A.$$

Impeller-volute interaction forces are considered to be relatively small with respect to forces generated in close clearance annular seals [1.3]. Note that the typical radial gap between the tongue of the volute and the impeller periphery is between 2 to 10 percent of the impeller radius, while the clearance-to-radius ratios of annular seals are of the order of 0.2 percent.

Numerical Example

Figure 1.20 shows the rotordynamics model of the double-flow radial pump from figure 1.12.

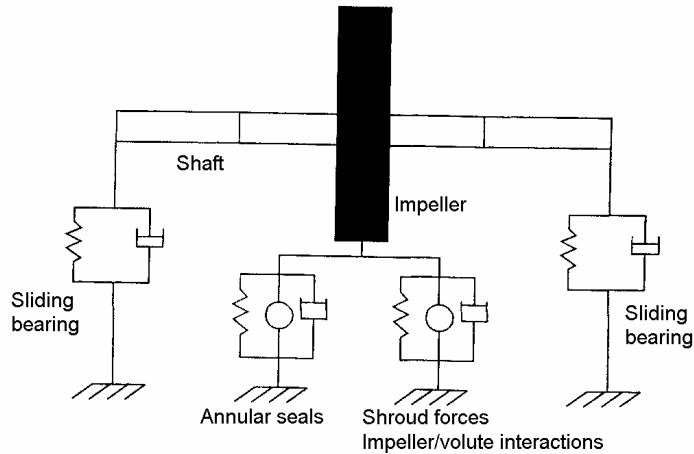


Fig. 1.20 (from [1.18])

Table 1.1

Shaft	Sliding bearing
Speed 6000 rpm	Length 40 mm
Length 2 m	Diameter 50 mm
Diameter 50 mm	Clearance 0.05 mm
Young's modulus 210 GPa	Dynamic viscosity 0.022 kg/ms
Mass density 7850 kg/m ³	L/D=0.8
Impeller/Volute	Annular seal
Impeller mass 25 kg	Length 15 mm
Outlet diameter 300 mm	Clearance 0.2 mm
Tongue radius 168.8 mm	Fluid density 1000 kg/m ³
Volute spiral angle 83°	Dynamic viscosity 0.8 g/ms
Inlet width 30 mm	Diameter 180 mm
Outlet angle 25°	Pressure drop 40 bar

The corresponding geometric and physical parameters are given in Table 1.1. The dynamic coefficients for fluid-structure interactions are given in Table 1.2. The stiffness, damping and mass coefficients are presented separately for the hydrodynamic bearings, for the plain annular neck seals and for the impeller-volute interaction [1.18].

The last column in Table 1.2 shows that the matrices are not skew-symmetrical and the diagonal elements are not equal as in equation (1.22).

Table 1.2

	Bearing	Annular seal	Impeller
$\begin{bmatrix} k_{yy} & k_{yz} \\ k_{zy} & k_{zz} \end{bmatrix} \frac{\text{N}}{\text{m}}$	$\begin{bmatrix} 14.2 & 172 \\ -157 & 43.6 \end{bmatrix} 10^6$	$\begin{bmatrix} 14.0 & 0.11 \\ -0.11 & 14.0 \end{bmatrix} 10^6$	$\begin{bmatrix} -0.55 & 0.17 \\ -0.25 & -0.45 \end{bmatrix} 10^6$
$\begin{bmatrix} c_{yy} & c_{yz} \\ c_{zy} & c_{zz} \end{bmatrix} \frac{\text{Ns}}{\text{m}}$	$\begin{bmatrix} 547 & -85 \\ -34 & 406 \end{bmatrix} 10^3$	$\begin{bmatrix} 7.6 & .048 \\ -.048 & 7.6 \end{bmatrix} 10^3$	$\begin{bmatrix} 1.2 & 5.2 \\ -5.4 & 1.1 \end{bmatrix} 10^3$
$\begin{bmatrix} m_{yy} & m_{yz} \\ m_{zy} & m_{zz} \end{bmatrix} \text{kg}$	$\begin{bmatrix} 0 & 0 \\ 0 & 0 \end{bmatrix}$	$\begin{bmatrix} 0.24 & -0.036 \\ 0.036 & 0.24 \end{bmatrix}$	$\begin{bmatrix} 7.78 & -0.69 \\ 0.71 & 7.84 \end{bmatrix}$

Black's model [1.19]

Working from the experimental results produced by Hergt and Krieger, a semi-empirical analysis by Black gave rotordynamic coefficients for impeller/diffuser interaction.

The tangential velocity at impeller outlet can be approximated from a velocity triangle with a slip factor of 0.8, i.e.

$$V_{\omega} = 0.8R_i \omega - u_m / \beta$$

where the impeller outlet angle β has been assumed small. If the mean outflow angle α is also assumed small,

$$u \approx \alpha V_{\omega}.$$

Assuming $u \approx V_\omega$, the pressure at impeller outlet is

$$p_i \approx \rho R_i \omega V_\omega - \rho V_\omega^2 / 2.$$

If the outflow angle α is allowed to change by a small amount δ , then a local pressure change Δp_i is obtained. A first order approximation gives

$$\Delta p_i = \frac{p_i (\alpha + 0.2 \beta) \delta}{(\alpha + 0.6 \beta)(\alpha + \beta)}.$$

The local pressure is integrated round the impeller assuming that, at part flow ratio Q , the diffuser loading alters the mean flow angle α locally in direct proportion to the local change in clearance.

The resulting rotordynamic coefficients are

$$K = \pi B_i p_i \frac{R_i}{C_r} \frac{(\alpha + 0.2 \beta)}{(\alpha + 0.6 \beta)(\alpha + \beta)} (1 - Q) \alpha_d,$$

$$k = \pi B_i \frac{p_i (\alpha + 0.2 \beta)}{(\alpha + 0.6 \beta)(\alpha + \beta)},$$

$$C = \frac{k}{\omega},$$

where B_i is the impeller width at outlet, α_d - diffuser inflow angle, Q - flow ratio, C_r - radial clearance, R_i - impeller radius, α - mean flow angle, β - impeller outlet angle, p_i - pressure change.

The dynamic coefficients are directly proportional to the pressure, and hence almost proportional to the square of speed.

1.8 Shroud Forces

Shroud forces arise due to the pressure fields produced by leakage paths in the forward and rear gaps at the front and back sides of a shroud impeller (H in Fig. 1.9).

The relatively small clearances suggested application of a bulk-flow analysis to calculate rotordynamic reaction forces on the impeller

shroud of the form (1.22). Large discrepancies between theoretical predictions and experiment are reported in [1.3].

It is generally accepted that in a pump impeller the shroud generates most of the destabilizing forces.

1.9 Final Remarks

The above seal analyses are restricted to a) plain seal surfaces; b) constant inlet loss coefficients, and c) fully developed inlet circumferential flow velocity.

The axial flow velocity is assumed to be much greater than the velocity in the circumferential direction. The predominant effect of variation in the inlet swirl velocity is to alter the cross-coupled stiffness coefficients. These coefficients are reduced in magnitude as the swirl velocity is reduced.

In fact, under proper values of seal geometry, axial pressure drops and inlet swirl velocity, the signs of the cross-coupled stiffness coefficients are reversed; cross-coupling promotes stability rather than instability. Experiments with spiral serrated seals, for axial Reynolds numbers ranging from 20,000 up to 40,000, revealed that long serrated seals possess negative direct stiffness. In calculations, correction factors on the seal length in a plain seal have to be used to account for grooving in serrated seals.

Dynamic coefficients in equation (1.6) are almost skew-symmetric, even for volute pumps, although such results would be expected only for rotationally symmetric configurations. In contrast to bearings, seals develop significant direct stiffness in the centred position, independent of rotation speed, from a hydrostatic mechanism.

Damping coefficients of seals are relatively large. As a result, the majority of centrifugal pumps operate with no evidence of rotor dynamic problems. For close clearance rings, hydrodynamic mass effects have been seen to be strong.

For synchronous rotor excitation and whirling, it was shown that the seal restoring force increases with the square of the speed. It has been thought of as being generated by a fictitious mass, called the Lomakin mass. However, a geometric mass correction is correct only for pure synchronous whirling. When the virtual mass is greater than the actual geometric mass the critical speed is suppressed. Such an approach would be correct only for systems in which the Lomakin mass and the geometric mass occur at the same locations. For systems in which this does not occur, the Lomakin effect should be treated as a stiffness and hence as a function of speed.

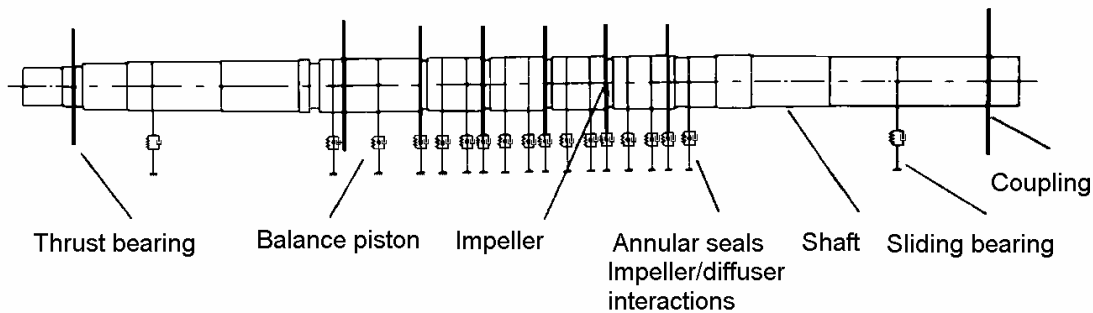


Fig. 1.21 (from [1.18])

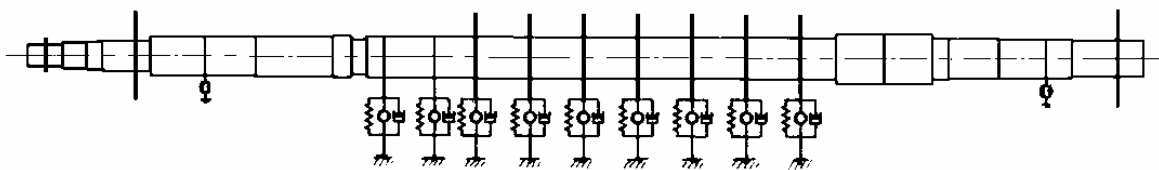


Fig. 1.22 (from [1.18])

The rotordynamics model of a five-stage pump rotor is shown in figure 1.21. Impellers are modelled as rigid discs. Around each disc there are three small elements of rotor-fluid interaction: one for the neck seal, one for the interstage seal, and one for the impeller/diffuser interaction. The balance piston seal is modelled separately.

A simplified model for a seven-stage centrifugal pump rotor is shown in figure 1.22 where all impeller-fluid interactions are modelled by a single mass-spring-damper element for each impeller.

Parametric studies, showing the influence of different factors upon the seal dynamic coefficients are presented in [1.18].

An overview of centrifugal pump design problems is given in [1.20].

References

- 1.1. **API Standard 610**, *Centrifugal Pumps for General Refinery Services*, American Petroleum Institute, 6th ed., Jan 1981.
- 1.2. Lomakin A.A., *Calculation of Critical Speeds and the Conditions Necessary for Dynamic Stability of Hydraulic High Pressure Pumps with Reference to Forces Arising in Seal Gaps*, *Energomashinostroenie*, vol.4, nr.1, p.1158, 1958 (in Russian).
- 1.3. Childs D., **Turbomachinery Rotordynamics: Phenomena, Modelling and Analysis**, Wiley, 1993.
- 1.4. Gasch R., Nordmann R., Pfützner H., **Rotordynamik**, 2.Auflage, Springer, 2002.
- 1.5. Logan E., **Turbomachinery. Basic Theory and Applications**, 2nd ed., Marcel Dekker Inc., New York, 1993.
- 1.6. Pfeleiderer C. and Petermann H., **Strömungsmaschinen**, 6.Aufl., Springer, 1990.
- 1.7. Raabe J., **Hydraulische Maschinen und Anlagen**, Teil 3, **Pumpen**, VDI Verlag, Düsseldorf, 1970.
- 1.8. Krämer E., **Dynamics of Rotors and Foundations**, Springer, 1993.
- 1.9. Flack R.D. and Allaire P.E., *Literature Review of Tilting Pad and Turbulent Hydrostatic Journal Bearings for Nuclear Main Coolant Pumps*, *Shock and Vibration Digest*, vol.16, nr.7, pp.3-12, 1984.
- 1.10. Fongang R., *Entwicklung eines Fluidmodells zur Berechnung der rotordynamischen Koeffizienten im Laufrad-Gehäuse-Bereich von Radialpumpen*, *Fortschritt-Berichte VDI*, Reihe 11: Schwingungstechnik, Nr.261, VDI Verlag, 1998.
- 1.11. Florjančič D., *L'evolution continue des pompes alimentaires et des grosses pompes multicellulaires pour alimentation en eau potable*, *Revue Technique Sulzer*, nr.4, pp.241-254, 1973.

- 1.12. Barrett L.E., *Turbulent Flow Annular Pump Seals: A Literature Review*, Shock and Vibration Digest, vol.16, nr.2, pp.3-13, 1984.
- 1.13. Yamada Y., *Resistance of Flow through an Annulus with an Inner Rotating Cylinder*, Bull. J.S.M.E., vol.5, nr.18, pp.302-310, 1962.
- 1.14. Black H.F., *Effects of Hydraulic Forces in Annular Pressure Seals on the Vibrations of Centrifugal Pump Rotors*, J.Mech.Eng.Sci., vol.11, nr.2, pp.206-213, 1969.
- 1.15. Black H.F. and Jenssen D.N., *Dynamic Hybrid Properties of Annular Pressure Seals*, J. Mech. Eng. Sci., Proc. Inst. Mech. Eng., vol.184, pp.92-100, 1970.
- 1.16. Childs D.W., *Dynamic Analysis of Turbulent Annular Seals Based on Hirs' Lubrication Equation*, J. of Lubrication Technology, Trans. ASME, vol.105, pp.437-444, 1983.
- 1.17. Hirs G.G., *A Bulk-Flow Theory for Turbulence in Lubricant Films*, J. of Lubrication Technology, Trans. ASME, pp.137-146, 1973.
- 1.18. Diewald W., *Das Biegeschwingsverhalten von Kreiselpumpen unter Berücksichtigung der Koppelwirkungen mit der Fluid*, Fortschritt-Berichte VDI, Reihe 11: Schwingungstechnik, Nr.121, VDI Verlag, 1989.
- 1.19. Brown R. D., *Vibration Phenomena in Boiler Feed Pumps Originating from Fluid Forces*, Proc. IFToMM Int. Conference on Rotordynamics, Rome, pp 497-506, 1982.
- 1.20. Stepanoff A.J., **Radial- und Axialpumpen**, Springer, 1959.

2. CENTRIFUGAL COMPRESSORS

2.1 Introduction

Although centrifugal compressors are slightly less efficient than axial-flow compressors, they are easier to manufacture and are thus preferred in applications where simplicity, ruggedness, and cheapness are primary requirements. Additionally, a single stage of a centrifugal compressor can produce a pressure ratio of 5 times that of a single stage of an axial-flow compressor [2.1]. Thus, centrifugal compressors find application in power station plants, petrochemical industry, gas injection and liquefaction, ground-vehicle turbochargers, locomotives, ships, auxiliary power units, etc.

A typical high-pressure compressor design is shown schematically in figure 2.1. Apart from shaft, impellers, bearings and coupling, modelled as for other machines, items of major concern in rotordynamic analyses are the *gas labyrinths*, the *oil ring seals* and the *aerodynamic cross coupling* at impellers. Furthermore, squeeze film dampers are used to stabilize compressors with problems.

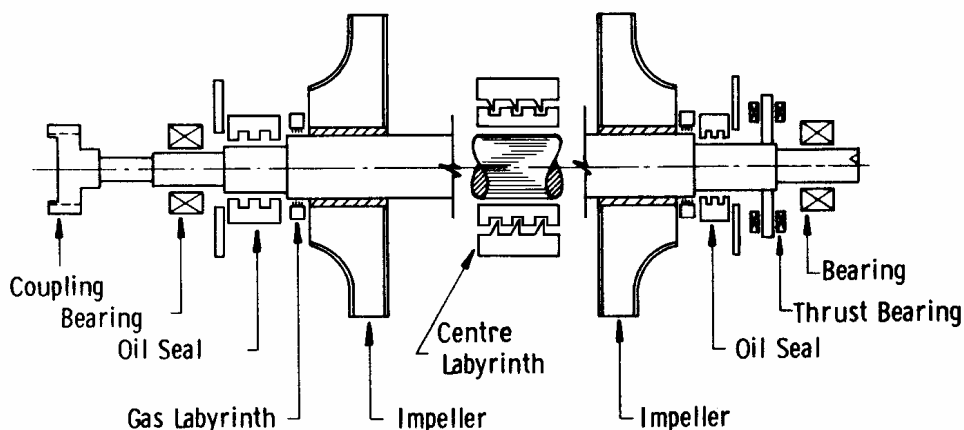


Fig. 2.1 (from [2.2])

Vibrations of a centrifugal compressor are controlled by: bearings, shaft geometry, gas seals and oil bushings, fluid forces on

impellers, and other factors. The purpose of this section is to present some of the mechanical features of the centrifugal compressors and to describe their influence on the rotordynamics behaviour of such machines.

Two distinct types of vibrations have been encountered: self-excited vibrations and forced vibrations.

Self-excited vibrations are common in high-pressure compressors, apparently with greater frequency in back-to-back designs and in high density and high-speed industrial units. Actually, a large percentage of industrial machines operating at high speed will sustain some low-level subharmonic vibrations even during normal operation. Some of these units develop instability problems. The vibration frequency observed is normally the fundamental bending natural frequency of the rotor.

Self-excited vibrations due to aerodynamic forces are twofold: a) vibrations where the destabilizing forces are function of the whirling motion of the rotor; they are produced by labyrinth seals and asymmetric blade loading of the impeller; and b) vibrations where the main flow is destabilized by hydrodynamic or viscous forces which are independent of the resulting mechanical vibration, such as those produced by rotating stall and/or surge.

Aerodynamic forces arising from the interaction of the impeller with the driven fluid introduce both direct and cross-coupled stiffnesses. In a radial flow machine, the change in force due to the clearance variations is negligible compared to that generated by the change in fluid momentum in an eccentric impeller, since the former is perpendicular to the main flow path.

Forced vibrations have been recorded in all high-density compressors. They have the following typical behaviors: a) they appear relatively near to surge and are very stable in amplitude; b) asynchronous frequency is very low (10 percent of rpm); and c) asynchronous amplitude depends on the tip speed and gas density.

Floating contact seals are components of major concern. Forces in this class of seals generally do not affect the natural frequency or the external damping of the system, so they are not usually involved in the rotordynamic design. But, under certain circumstances, e.g. when

the friction force in the contacting support face locks the seal in an eccentric position, significant destabilizing forces can be generated.

The use of flexible damped supports can help to eliminate instabilities or to alter the speed at which they occur. The *squeeze film damper* is one type of flexible support that is currently used for stabilization of centrifugal compressors.

2.2 Basic Principles

The parts of a single-stage centrifugal compressor are the same as those of a pump, namely, the impeller, the diffuser, and the volute (Fig.2.2).

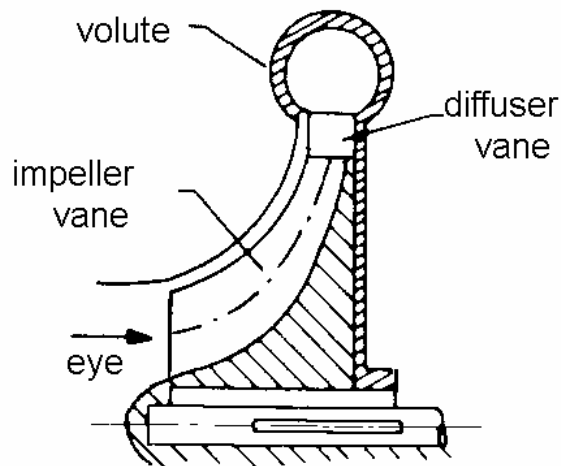


Fig. 2.2

In centrifugal compressors the air is turned through roughly 90° into a radially outward flow in an impeller, which imparts a high-speed spiral velocity to the fluid, as much as possible of which is converted to pressure by the diffuser which surrounds the periphery of the impeller.

A stage of a multi-stage compressor is shown in figure 2.3. In the velocity diagram at impeller exit c_2 is the absolute gas velocity, w_2 - relative gas velocity, and u_2 - transport velocity (tangential impeller velocity), AC - particle path in a fixed coordinate system, AB - particle path relative to the rotating impeller.

A vaneless diffuser, or empty space, between the leading edges of diffuser vanes and the impeller tip, allows some equalization of gas velocity and a rise in static pressure.

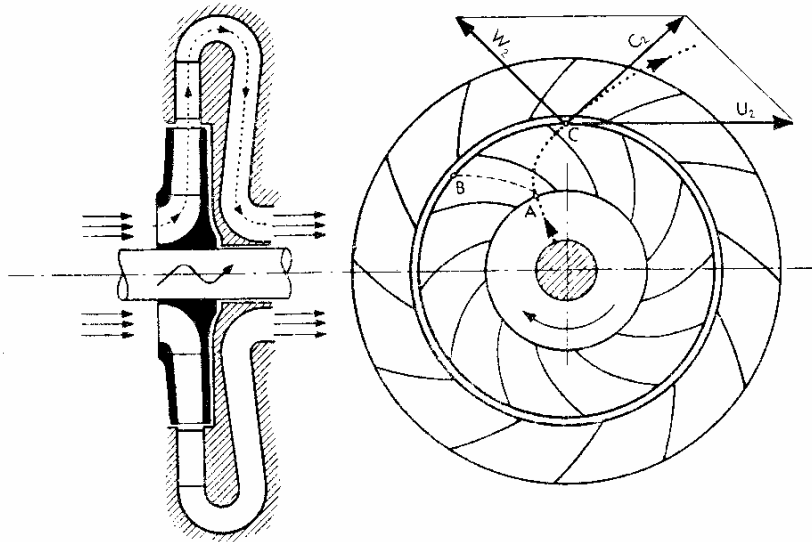


Fig. 2.3 (from [2.3])

The vaneless portion may have a width as large as 6 percent of the impeller diameter. The fluid path is approximately a logarithmic spiral. Diffuser vanes are set with the diffuser axes tangent to the spiral paths and with an angle of divergence between them not exceeding 12° . The wedge-shaped diffuser vanes are depicted in figure 2.4.

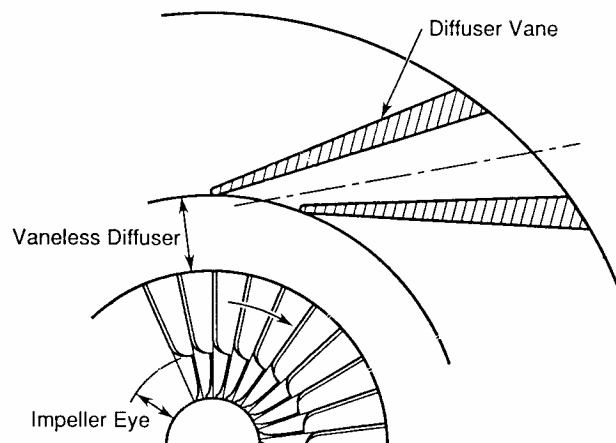


Fig. 2.4 (from [2.4])

Since the addition of a vaned portion in the diffusion system results in a small-diameter casing, vanes are preferred in instances where size limitations are imposed. On the other hand, a completely vaneless diffuser is more efficient. If vanes are used, then their number should generally be less than the number of impeller vanes to ensure uniformness of flow and high diffuser efficiency. Vibration problems have been experienced with designs in which the number of diffuser vanes was an integer multiple of the number of impeller vanes.

Difficult vibration problems arose during the development of centrifugal compressors for early aero-engines, owing to the buffeting which the impeller received from circumferential pressure variations originating in the diffuser. Failures were prevented by strengthening the tips of the impeller vanes, so minimising the deflections produced at this point as the impeller traversed the fluctuating pressure field, and reducing the amplitude of vibration throughout the impeller.

2.3 Design Characteristics

Two distinct types of centrifugal impeller are in use: unshrouded impellers (Fig. 2.5*a*) and shrouded impellers (Fig. 2.5*b*).

The unshrouded impeller vanes are mainly radial. Usually they are bent near the leading edge to conform to the direction of the relative gas velocity at the inlet [2.5].

The shrouded impeller vanes are "backward swept", i.e. the vanes are of a spiral form (Fig. 2.3), the sense of the spiral being that which would be traced out on the impeller disc by a point moving radially outward, while the impeller rotates in its normal direction. Improved efficiency is claimed for impellers with backward swept vanes, compared with the equivalent radial vaned component. A labyrinth seal fitted at the small diameter of the shroud can be used to reduce the "tip-leakage".

Backward swept vanes have little inherent strength to resist the very large radial bending forces developed during rotation, and it is necessary to support them from both sides of the fluid passage, which is achieved by the use of a shroud. Unlike the main impeller, the boss

of the shroud cannot be reduced to a small diameter in order to minimise the stress, but must have a large hole to provide the flow area required for the gas entering the compressor.

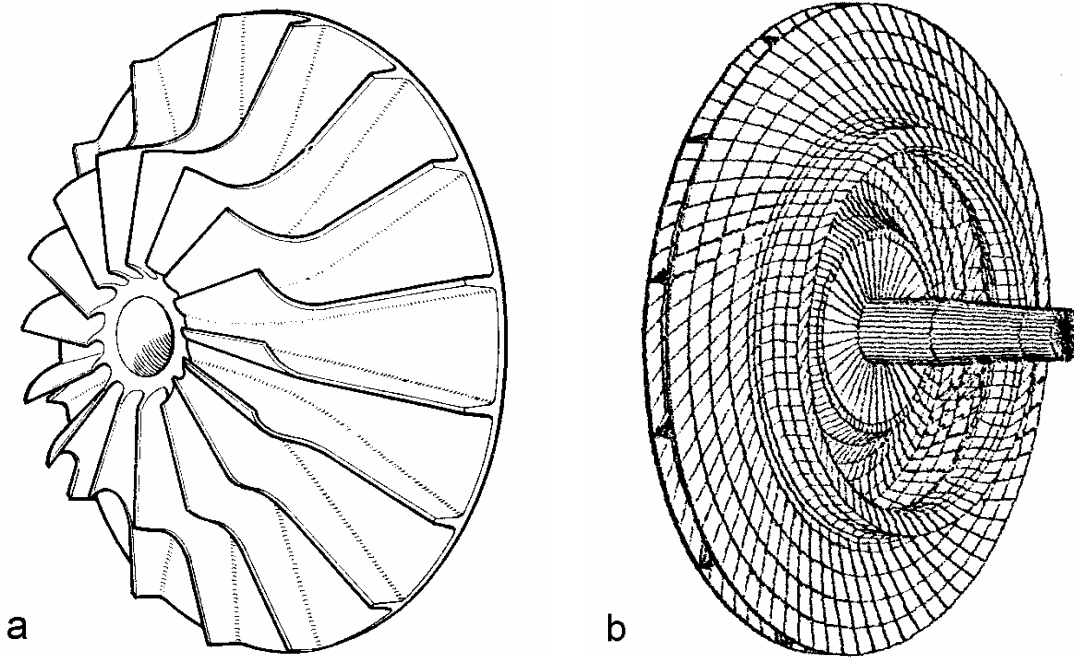


Fig. 2.5

Consequently, while the use of backward swept vanes and a shrouded impeller may result in some improvement in efficiency, stress considerations limit the compression ratio which can be produced in a single stage to about 2:1.

With radial vanes, however, there is no acute stress problem, as the centrifugal forces do not apply bending loads to the vanes, but are carried as tensile and shear stresses. Aluminium alloy impellers have been used in jet propulsion engines producing a compression ratio over 4:1 in a single stage. However, as their efficiency is so much lower than that of the equivalent axial compressor, their application in aero-engines is limited.

Different impeller designs are shown in figure 2.6. Type *a* is for very high tangential speeds, above 350 m/s, usually from Cr-Ni steels. Type *b* is for high speeds. Type *c* is for medium speeds, *d* and *e* for low speeds, all three of riveted sheet steel, 1 to 2.5 mm thickness.

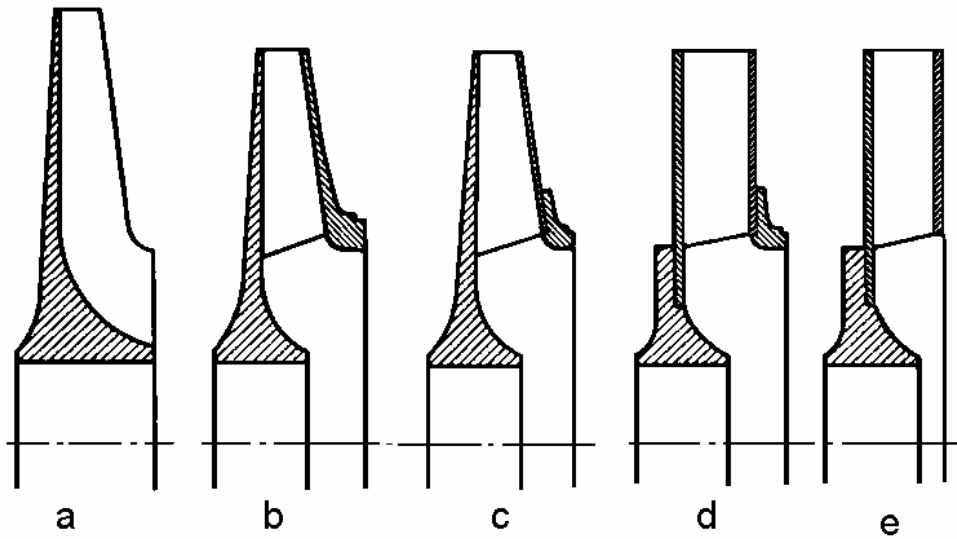


Fig. 2.6 (from [2.6])

With shrouded impellers, vibration problems are not often met, owing to the rigidity with which the impeller vanes are supported and the fact that considerable damping is introduced by the built-up construction usually adopted.

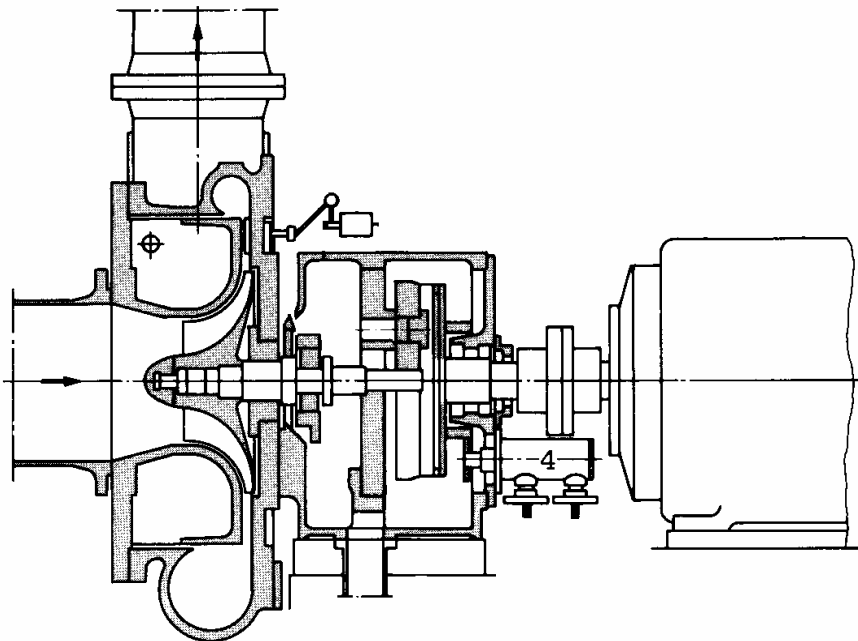


Fig. 2.7 (from [2.6])

A single-stage turbocompressor is shown in figure 2.7. When driven by electrical motors, a speed increasing gear is used. A four-stage compressor built by Sulzer is shown in figure 2.8.

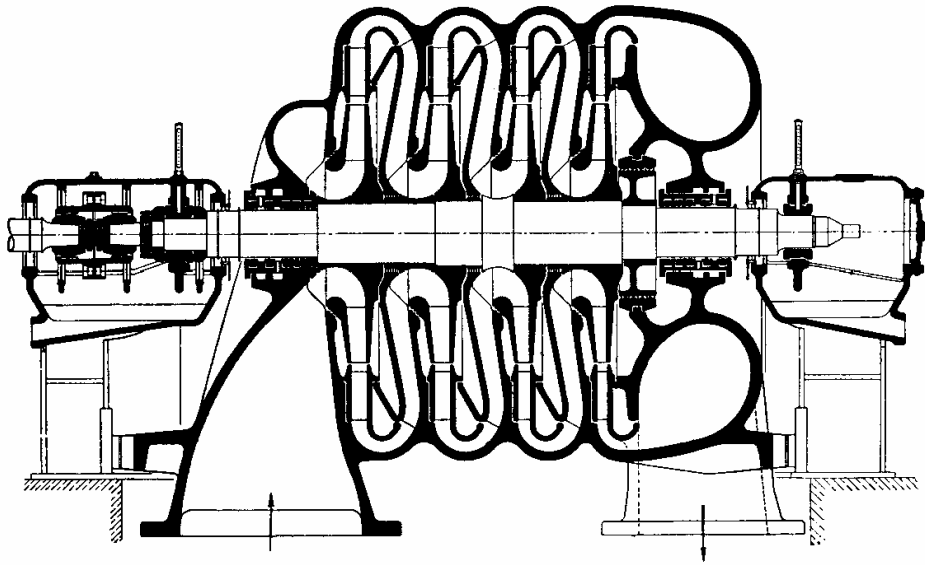


Fig. 2.8 (from [2.3])

High-pressure multi-stage compressors can use either the "series" (throughflow) or the "parallel" (back-to-back) designs.

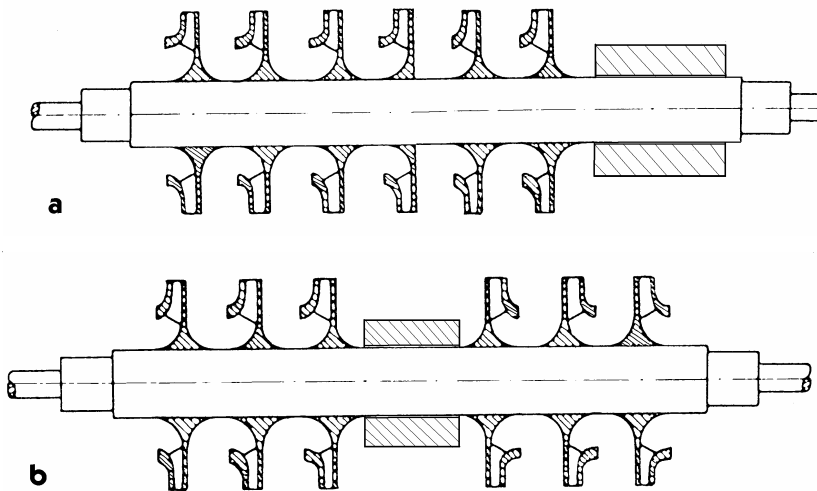


Fig. 2.9

In the throughflow design (Fig. 2.9a), flow enters from the left and proceeds directly from impeller to impeller, discharging on the right. For the back-to-back design (Fig. 2.9b), flow enters at the left and proceeds from left to right through the first three stages, then follows a crossover duct to the right-hand side of the compressor, and proceeds from right to left through the last three stages, discharging at the centre. Back-to-back designs obviously react with a smaller axial

thrust than series designs. In recent machines at the centre there is located the balance drum labyrinth.

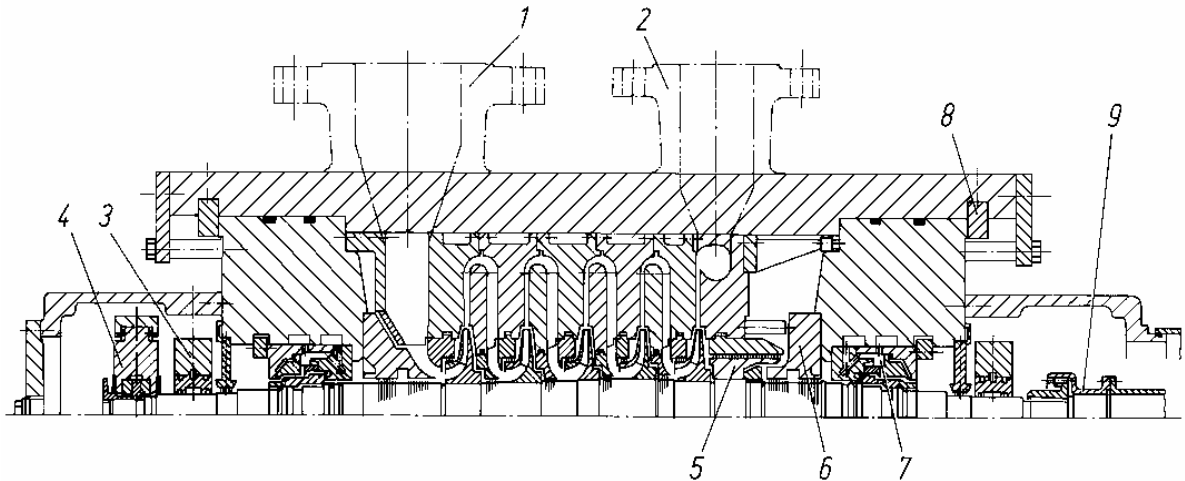


Fig. 2.10 (from [2.5])

Throughflow compressor designs are illustrated in figures 2.10 to 2.12. A five-stage high-pressure compressor built by Babcock-Borsig is shown in figure 2.10 where: 1 – intake duct, 2 – discharge duct, 3 – radial bearing, 4 – thrust bearing, 5 – balancing piston, 6 – labyrinth seal, 7 – contactless sealing oil packing, 8 – shear ring, 9 – coupling. The vertically split casing is for pressures up to 300 bar and flow rates up to 150,000 m³/h.

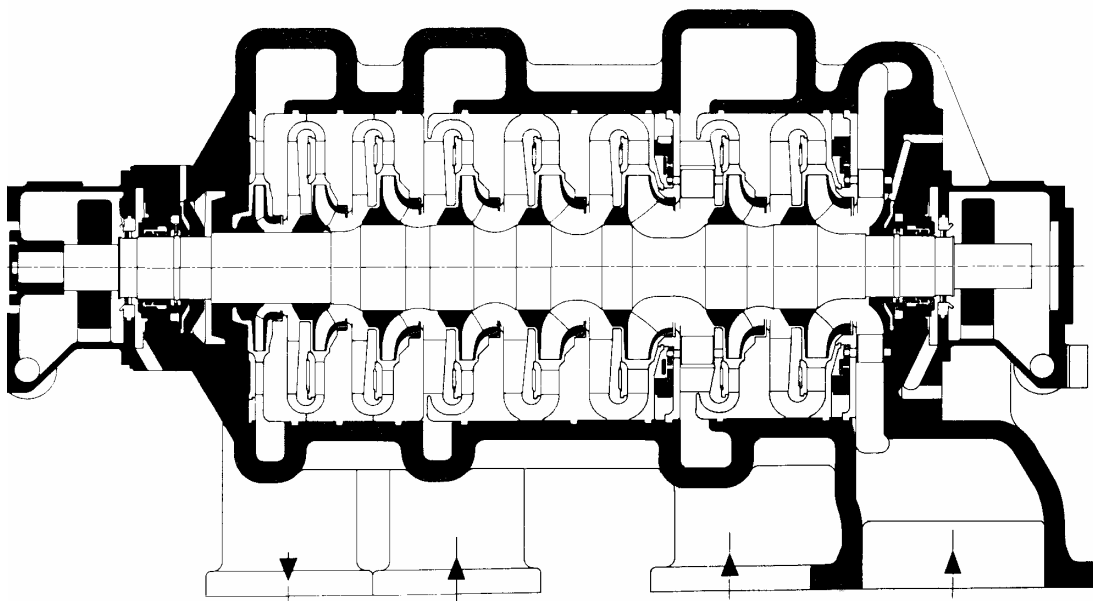


Fig. 2.11 (from [2.7])

The eight-stage compressor with two intermediate side streams from figure 2.11 is for a pressure ratio of about 15, with propane.

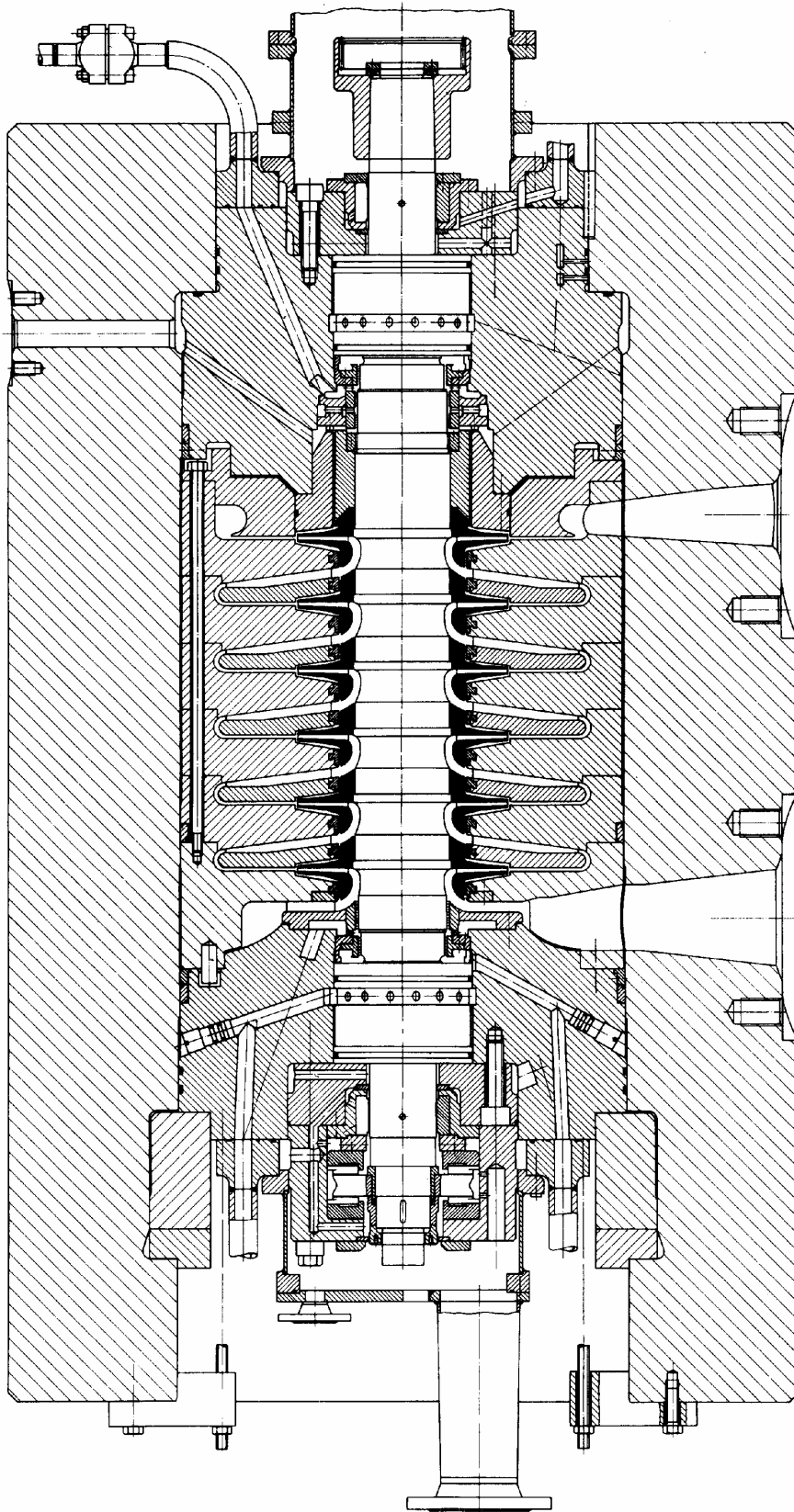


Fig.2.12 (from [2.8])

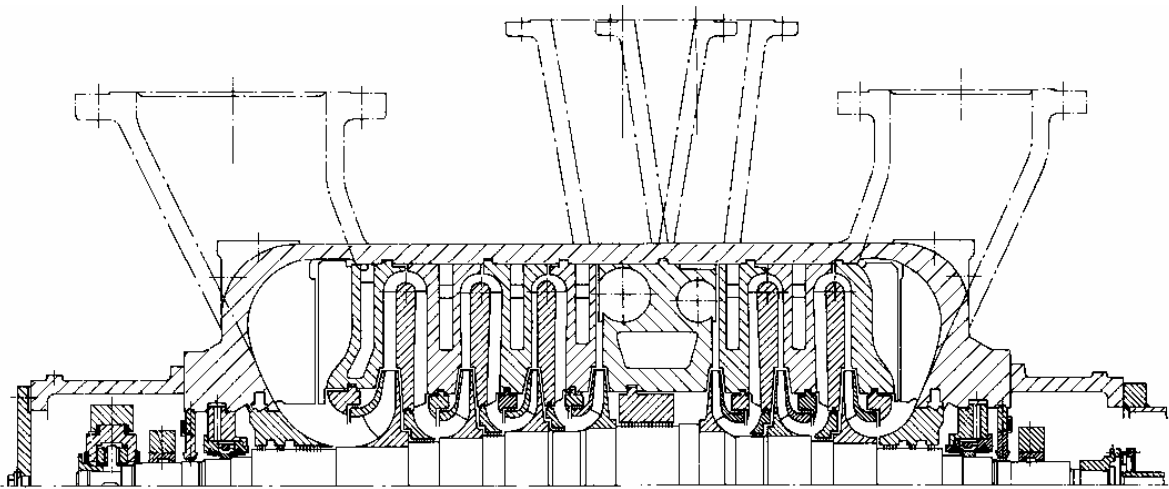


Fig. 2.13 (from [2.5])

A back-to-back seven-stage compressor with cooling after stage four is shown in figure 2.13. The design with the horizontally split casing is for pressures up to 70 bar and flow rates up to 250,000 m³/h.

A partial cross-section of an isolated multistage gas compressor rotor, indicating locations of dynamic rotor forces, is schematically shown in figure 2.14, where: *A* – fluid film bearings, *B* – buffer gas / oil seals, *C_n* – labyrinth seals at inlet, interstage, centre span, and balance piston, *D* – diffuser/impeller interaction, *E_n* – friction damping at long shrink fit, spline coupling, *F* – internal material damping.

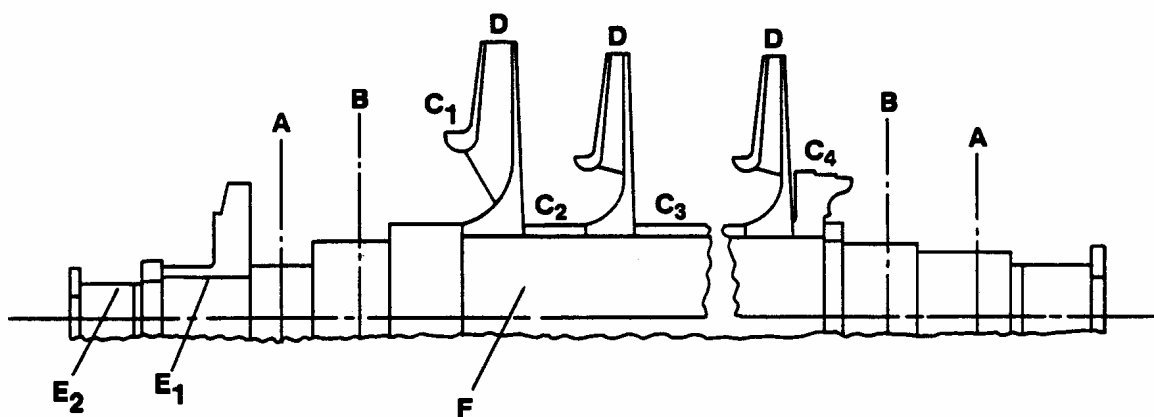


Fig. 2.14

All these forces have to be taken into account in a rotordynamic analysis. In the following, items specific for centrifugal compressors are considered in detail.

2.4 Typical Applications

There is a great variety of application areas for centrifugal compressors in energy technology, which may be characterized by the intake volume flow (as a measure for the size), the discharge pressure (as a measure for the design ruggedness) and the gas handled. Figure 2.15 provides a survey of the principal fields of application of both radial and axial compressors. A list of the eight application areas in energy technology, marked in figure 2.15, is given below.

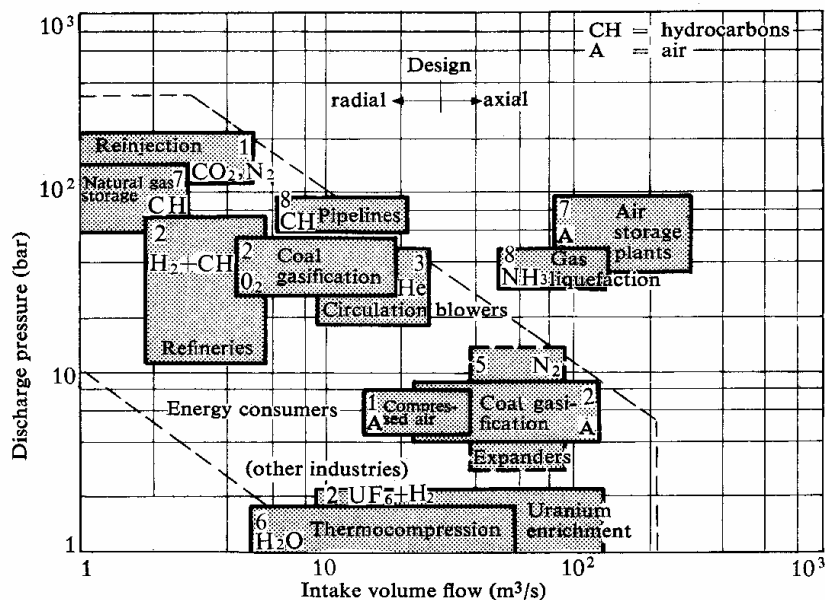


Fig. 2.15 (from [2.9])

1. *Production of energy carriers*: a) reinjection and gas lifting in the production of petroleum, requiring CO₂ or N₂ at high pressures; b) compressed air in coal mining.

2. *Processing*: a) refineries, H₂ and hydrocarbon recycle gas at medium pressures; b) coal gasification; air separation as primary stage, air, O₂, CO₂ and other gases, rising pressures; c) uranium enrichment, isotope separation plants, UF₆ and H₂, ranging from vacuum to slight overpressure.

3. *Energy production*: circulating blowers for gas cooled reactors, He, CO₂.

4. *Energy consumption*: all industrial compressors, in principle.

5. *Recovery*: compressors in combination with expanders in various industrial processes, primarily N_2 .

6. *Reconversion*: a) thermocompression (thermal upgrading of waste heat by compression), especially efficient with steam (water vapour), pressures often in the vacuum range; b) heat pump processes, only very small volume flows.

7. *Storage*: a) air storage (with gas turbine), highest volume flows and high pressures, air; b) natural gas storage, mainly CH_4 , for covering peak loads, high pressures.

8. *Transportation*: a) natural gas transportation by pipeline, medium pressures, gas turbine drive chiefly; b) natural gas liquefaction, refrigerant.

Special design arrangements comply with specific requirements. Barrel-type centrifugal compressors are used in petroleum refining, where pressures up to 400 bar are involved and absolute tightness is imposed by circulation and discharging of hydrogen and light hydrocarbon gases (Fig. 2.12).

Coal gasification involves the conversion of coal into hydrogen, carbon monoxide and other gases with oxygen and steam at high temperatures. The nitrogen resulting from air separation is used in downstream chemical processes. Special compressors are needed for leading off the gasification products. Combined axial and centrifugal compressors with integral intercooling are used in oxygen production. Decisive for operational security are the shaft seals, in conditions where some rotors run above the second critical speed and the pressure must be raised to 100 bar and higher. Since contact between stationary and rotating parts cannot be ruled out entirely, material pairs which preclude for certain any ignition if they touch are selected for the sealing elements, like nickel strips on the shaft and silver-plated copper bushes on the casing.

Small gas turbines designed for vehicle propulsion are coupled to centrifugal compressors, usually single-sided single-stage, with special diffuser designs.

In early aircraft applications, two-stage centrifugal compressors have been used with gas turbines (see Fig. 6.22 in **Gas Turbines**). In

order to save space and weight, the compressors have been pressed near to the limit of what is possible aerodynamically. Most solutions resulted by modifying turbocharger designs.

2.5 Annular Gas Seals

Annular gas seals, or labyrinth seals, have a leakage-control role in centrifugal compressors. Forces developed by gas seals are roughly proportional to the pressure drop across the seals and the fluid density within the seal. Because of the density dependence, gas seals have had a great impact on high-pressure compressors for gases with high molecular weight.

Several usual forms of labyrinths are shown in figure 2.16.

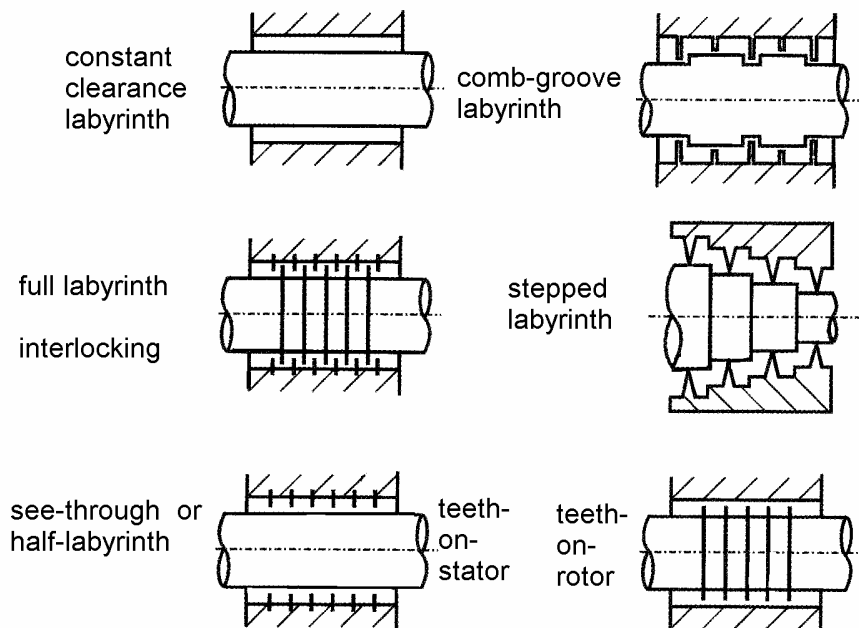


Fig. 2.16

Labyrinths can have a negative effect on the smooth running of compressor rotors. Two basically different mechanisms are possible.

1. The first case occurs if unbalance induced precession causes contact between labyrinth tabs and the shaft. Wherever a possible contact of the labyrinth leads to a marked heating and hence deformation of the rotor, it is advantageous to have the labyrinth strips

located on the shaft. The cooling induced by the strips protects the shaft against a local rise in temperature.

2. The second case is less apparent but more important. Any eccentricity causes a change of flow in the labyrinth and induces reaction forces that act back on the shaft and thus may diminish the rotor system damping. If this damping is sufficiently reduced, self-induced rotor vibrations occur that render the operation of the compressor impossible.

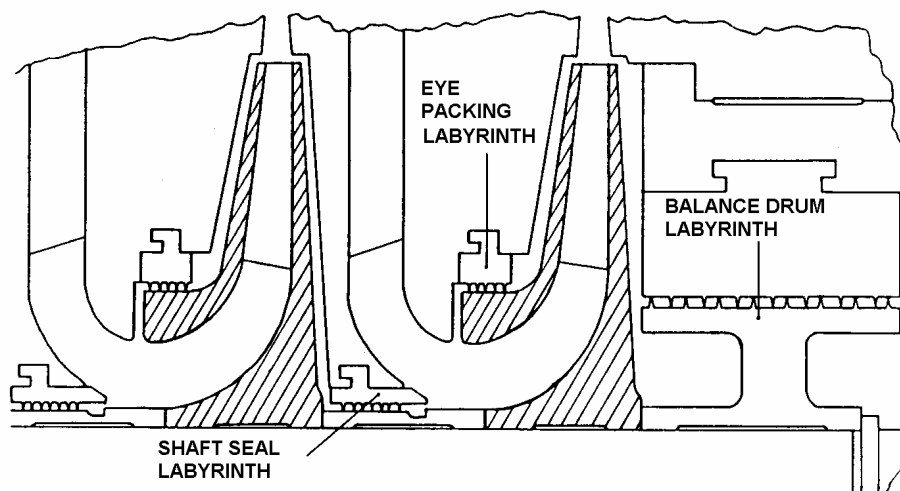


Fig. 2.17 (from [2.10])

Figure 2.17 illustrates a typical sealing arrangement for a last stage compressor impeller. The eye-packing seal limits return-flow leakages down the front of the impeller. The shaft seal restricts leakage along the shaft to the preceding stage. The eye packing and shaft seal configurations are called "see-through" or half-labyrinth seals (see Fig. 2.16).

In a throughflow compressor, leakage flow through the balance drum is returned to the inlet. The balance drum is a long seal which absorbs the full pressure differential of the compressor. The balance drum seal configuration is called an interlocking or full labyrinth (see Fig. 2.16).

For a back-to-back compressor, the balance drum absorbs the pressure drop between the last stage of the compressor and the last stage of the initial series of impellers, i.e., about one half of pressure drop per machine. For the same inlet and discharge pressures, the

average density is higher in the centre labyrinth of a back-to-back machine than in the balance drum labyrinth of a series machine.

Back-to-back compressors are more sensitive to the forces from the central labyrinth than are series machines to forces from the balance-drum labyrinth, and this is mainly because of the larger deflections at the middle span for the first critical mode.

The forces developed by compressor seal labyrinths are at least one order of magnitude lower than their liquid seal counterparts. They have negligible added-mass terms and are typically modeled by the following reaction force/motion model:

$$\begin{Bmatrix} -F_y \\ -F_z \end{Bmatrix} = \begin{bmatrix} K & k \\ -k & K \end{bmatrix} \begin{Bmatrix} y \\ z \end{Bmatrix} + \begin{bmatrix} C & c \\ -c & C \end{bmatrix} \begin{Bmatrix} \dot{y} \\ \dot{z} \end{Bmatrix}, \quad (2.1)$$

The diagonal terms of their stiffness and damping matrices are equal, while the off-diagonal terms are equal, but with reversed sign, which denotes isotropy. Unlike the pump seal model of equation (1.6), the direct stiffness term is typically negligible and is negative in many cases.

The coefficients in equation (2.1) are dependent on the gas density, giving rise to "load dependent" instabilities. This leads to an "onset power level of instability" instead of the known "onset speed of instability" encountered for rotors in hydrodynamic bearings, which exhibit speed-dependent instabilities.

Tests have shown that for "see-through" labyrinth seals: a) cross-coupled stiffness coefficients increase directly with increasing inlet tangential velocities; b) seal damping is small but must be accounted for to obtain reasonable rotordynamic predictions, and c) as clearances decrease, teeth-on-rotor seals become less stable and teeth-on-stator seals become more stable.

Stabilizing solutions include the *swirl brakes* or *swirl webs* at the entrance to labyrinth seals (Fig. 2.18). This device uses an array of axial vanes at the seal inlet to destroy or reduce the inlet tangential velocity.

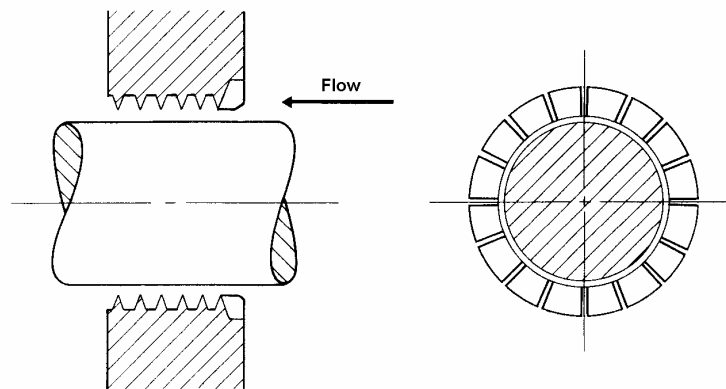


Fig. 2.18 (from [2.11])

Another approach for stabilizing compressors involves a "shunt line" and entails rerouting gas from the compressor discharge and injection flow into one of the early cavities in the balance-piston labyrinth (Fig. 2.19). Usually, the flow from the back side of the last stage impeller enters the labyrinth with a high tangential velocity which yields a high destabilizing force. The shunt flow forces the gas outward along the back face of the impeller, reducing the seal tangential velocity.

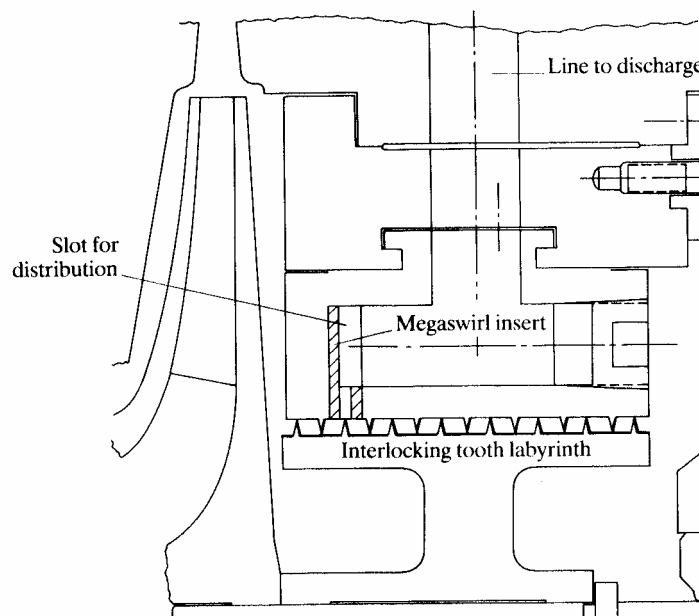


Fig. 2.19 (from [2.11])

Of all the labyrinth seals, the destabilizing forces are maximum for the balance piston labyrinth because it is the longest seal and has the highest pressure drop. For a throughflow machine it also has the highest gas density.

Some success has been obtained in improving the stability of compressors by replacing labyrinth seals with *honeycomb seals*. The latter develop larger destabilizing coefficients but much higher direct damping values. *Brush seals*, using wires in contact with a ceramic coating on the shaft, have a sharply reduced leakage flow as compared to a labyrinth or honeycomb seal.

2.6 Floating Contact Seals

Oil seals are frequently used in high speed multistage compressors to minimize the leakage of the process gas into the atmosphere. For hazardous gases, tightness is an important requirement. This is achieved with liquid seals in conjunction with floating ring seals (see Fig. 2.1).

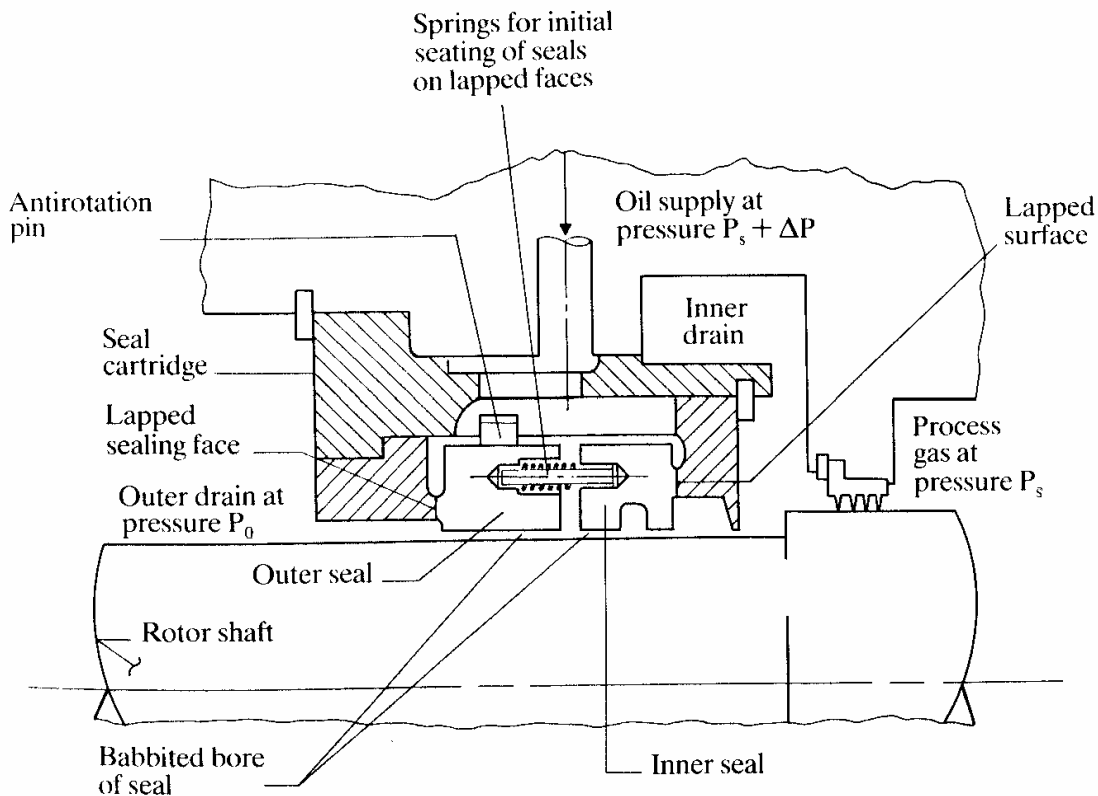


Fig. 2.20 (from [2.11])

2.6.1 Design Characteristics

If the desired pressure drop across the seal ring is adequate, only one seal ring is employed. Otherwise, a double floating ring combination is used, with sealing oil feed in the middle, as illustrated

in figure 2.20. The seal segments consist of outer and inner seals which are spring-loaded against each other. The preload of the spring causes the lapped external faces of the seal segments to be in contact with the seal cartridge housing. An antirotation pin is provided to prevent rotation of the seal segments. Oil is introduced between the rings at a pressure slightly above compressor suction pressure and then leaks axially along the shaft. The inner ring seals against process gas leakage, while the outer ring limits seal oil leakage to the outside. Most of the oil is recovered.

Heat dissipation is critical to the operational security of oil seals. This is ensured by the liquid flow in the relatively wide seal ring clearances, typically 50 to 80 μm , which entails high leak rates. These can be lowered providing the floating ring with a return thread.

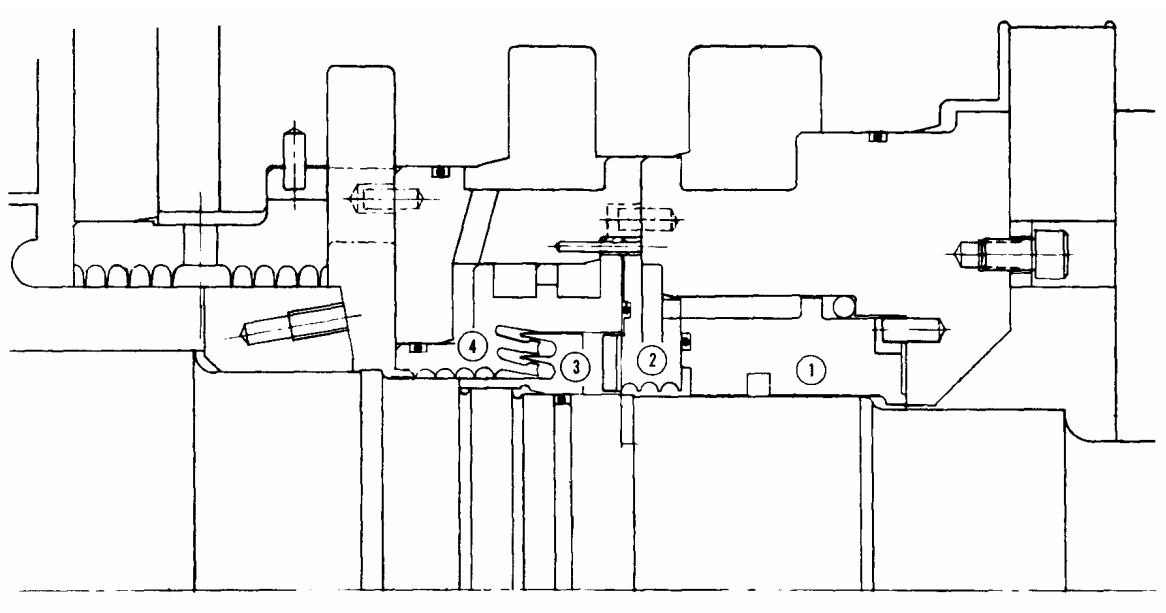


Fig. 2.21 (from [2.12])

A single ring seal arrangement, used in a 5-stage compressor for refinery service, is depicted in figure 2.21, where: 1 – oil bushing, 2 – diaphragm, 3 – sleeve (impeller), and 4 – stator.

The "trapped bushing seal", shown in figure 2.22, is a "dual" bushing which encompasses both the inner and outer seal in one ring. One can distinguish: 1 - shaft, 2 - sleeve with interference fit under

bushing, 3 – stator, 4 – stepped dual bushing, 5 – bushing cage, 6 – nut, 7 – shear ring, 8 – spacer ring.

The compact design allows shorter bearing spans for higher critical speeds. The sleeve 2 under bushing protects the shaft and simplifies assembly and disassembly. It requires only a jack/puller bolt ring. The spacer ring 8 is fitted at initial assembly, so there is no field fitting of parts.

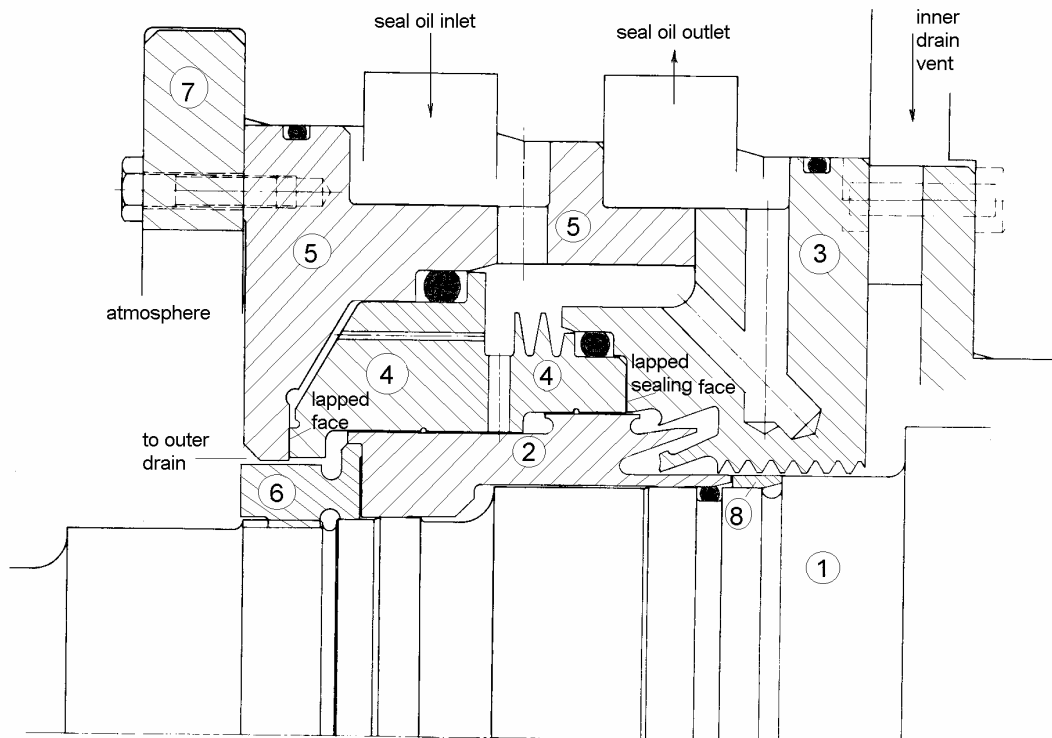


Fig. 2.22 (from [2.12])

This arrangement allows the bushing to freely track the shaft motion. Seal induced hydrodynamic forces are dissipated in seal motion and not applied to the shaft. The seal is also insensitive to wear on the axial faces [2.12].

Figure 2.23 shows a typical cone seal arrangement where *a* is the original design which experienced severe vibrations, and *b* is the improved design, obtained by reducing the sealing length and the width of the lapped face, and increasing the steady holding force of the springs.

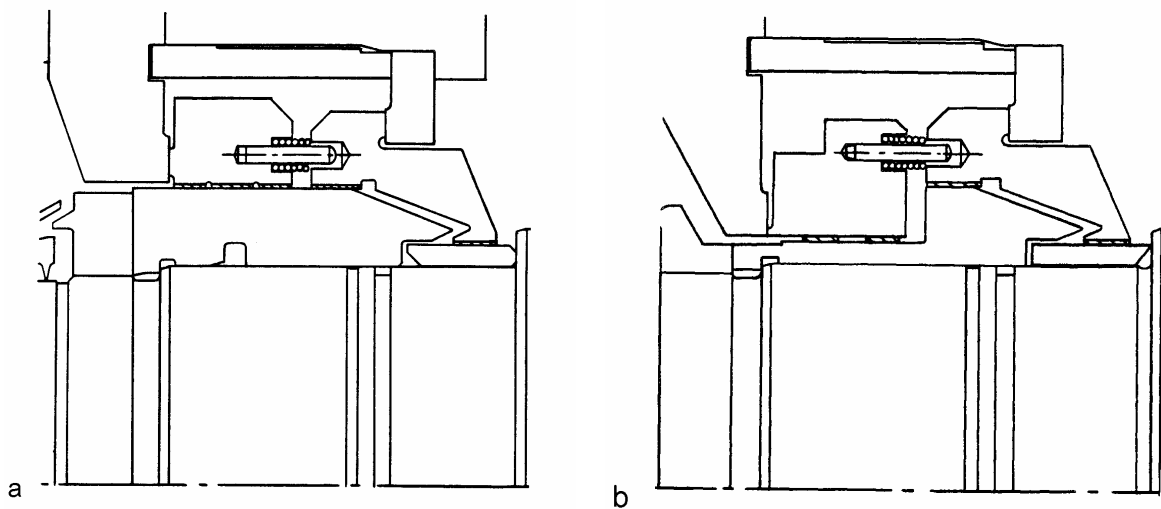


Fig. 2.23 (from [2.13])

An arrangement intended to solve the seal centering problem is shown in figure 2.24, where a tilting-pad bearing element is incorporated in the high-pressure seal ring.

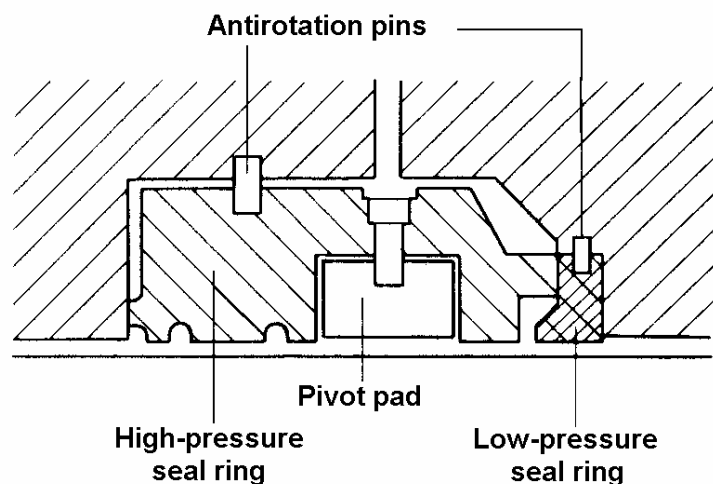


Fig. 2.24 (from [2.11])

Possible design improvements to the high-pressure ring are: a) decreasing the seal face area, in order to decrease the unbalanced axial force, hence the friction force; b) cutting circumferential grooves in the seal land region, to reduce the effective axial hydrodynamic length of the ring; and c) increasing the seal clearance.

2.6.2 Seal Ring Lockup

Compressors with oil seal rings are often subject to subsynchronous vibrations. The seal rings are designed to "float", in the sense that they orbit with the shaft as it vibrates (rotation is prevented by some pin or other device which still allows radial ring motion). If the seal ring orbits with the shaft, the oil film force, and thus the dynamic coefficients, between the shaft and ring are very small.

In certain circumstances, the seal rings may be prevented from moving. This is known as the "seal ring lockup". It causes large oil film forces to act between the shaft and ring, which may produce large stiffness and damping coefficients.

The building up of the cross-coupled stiffnesses by the seal ring lockup, in a machine with tilting pad bearings, can be described as follows [2.14]:

1. For a non-rotating shaft, the oil ring is resting on the top of the shaft. As the rotational speed increases, the oil seal fluid film supports the weight of the oil seal ring.

2. The pressure drop across the seal ring increases with the machine speed. This in turn increases the axial force due to unbalanced pressure, and correspondingly, the radial friction force acting on the seal ring (given by the coefficient of friction times the axial force). When the radial friction force acting on the seal exceeds the oil film radial force, the seal will lock up.

3. As the shaft speed continues to increase, the (tilting pad) bearing oil film forces tend to force the shaft upward in the bearing (the bearings are unloaded). The seal ring oil film forces tend to oppose this because the shaft is now taking an eccentric position within the fixed seal ring.

4. Unbalance forces inherent in rotor make the shaft undergo dynamic orbits. These dynamic forces in turn produce dynamic oil film forces in the lubricant between the shaft and fixed seal ring. If the combination of static and dynamic forces is larger than the radial friction force, the oil seal ring will move. If the dynamic forces are not large enough to overcome the available radial friction force at a given

speed, the seal ring is likely to lockup. This can happen at some speed well below running speed.

5. As the shaft increases in speed, the oil film forces in the bearings will lift the shaft in the bearing. This will create an eccentric position of the shaft relative to the locked up oil seal ring. This in turn will produce large cross-coupling stiffness terms acting on the shaft due to the oil film in the seal ring.

2.6.3 Locked-Up Oil Seal Rotordynamic Coefficients

In approximate calculations, it is assumed that the seal ring is locked up with the shaft centred and behaves as a non-cavitated concentric plain sleeve bearing, and there is no axial pressure gradient. Oil seal rings are short ($0.05 < L/D < 0.2$) and their flow is generally laminar, non-cavitating.

For this centric case, the cross-coupled stiffnesses are [2.12]

$$k_{yz} = -k_{zy} = \frac{\pi}{4} \omega D \mu \left(\frac{L}{C_r} \right)^3 = 2\pi \omega \mu L \left(\frac{R}{C_r} \right)^3 \left(\frac{L}{D} \right)^2 \quad (2.2)$$

where ω - shaft angular speed of rotation, rad/sec, D - shaft diameter, R - shaft radius, L - axial seal length, C_r - oil seal ring radial clearance, μ - fluid dynamic viscosity.

As coefficients are proportional to L^3 , a considerable reduction in destabilization can be achieved by providing the seal with circumferential grooves, as shown in figure 2.24.

For a concentric seal, the direct stiffnesses k_{yy} and k_{zz} are negligible. The direct damping coefficients are

$$c_{yy} = \frac{2}{\omega} k_{yz}, \quad c_{zz} = \frac{2}{\omega} k_{yz}, \quad (2.3)$$

Note that these properties are inversely proportional to C_r^3 , hence highly sensitive to variations in clearance. Thus, enlarged clearances at the seals would allow operation with low vibrations even when the seals are locked up.

The eccentric values of cross-coupled terms are known to be several times the value for the centred position.

There are more accurate calculation schemes to determine the seal dynamic coefficients, for various assumptions about the seal lockup eccentricity [2.10]. However, the results are sensitive to the assumptions about whether lockup results in increased or decreased journal loading in rotor bearings.

Stable operation of a rotor is possible even if the seal locks up and the seal clearances are abnormally large. Due to eccentric lock-up of the seal ring, direct stiffness terms are developed. Reduced journal loading will raise the natural frequencies of the rotor because the effective bearing span is reduced transferring the load to the seals. In this case, the frequency of the non-synchronous instability is higher than the calculated rigid bearing critical speed.

A quasi-steady method of determining the seal ring lockup conditions has been used with good results [2.14]. It involves matching the radial friction force to the seal ring weight, wherefrom the ring initial lockup speed is calculated first. As the shaft speed increases, it lifts off of the bottom pad of the tilting pad bearings. Based on known relationships for tilting pad bearings, the shaft position relative to the bearing centre line is determined, wherefrom the oil seal ring eccentricity and attitude angle can be calculated for a load capacity equal to the oil seal ring weight. Otherwise, because the static attitude angle depends on the friction force, it is, strictly speaking, indeterminate. Selection of the friction coefficient is a difficult task.

The subsequent calculation of rotordynamic coefficients can be done using the Ocvirk short-bearing model [2.10]. The relationship of the static eccentricity ratio ε_0 to the modified Sommerfeld number

$$S_s = \frac{\mu L D N}{W} \left(\frac{R}{C_r} \right)^2 \left(\frac{L}{D} \right)^2 = \frac{W_*}{W} \quad (2.4)$$

for a short bearing is illustrated in figure 2.25,*a*. Figure 2.25,*b* shows the rotordynamic coefficients for a short seal with an assumed attitude angle of 90° [2.11].

The seal has no direct stiffness for this attitude angle, and the cross-coupled stiffness and direct damping terms rise sharply with decreasing S_s , i.e. increasing static eccentricity ratio. The increase of c_{yy} and c_{zz} with ε_0 can be advantageous at low speeds, when the rotor is traversing a critical speed; however, the increase in k_{yz} and k_{zy} can lead to rotor instability at running speeds of the order of twice the critical speed.

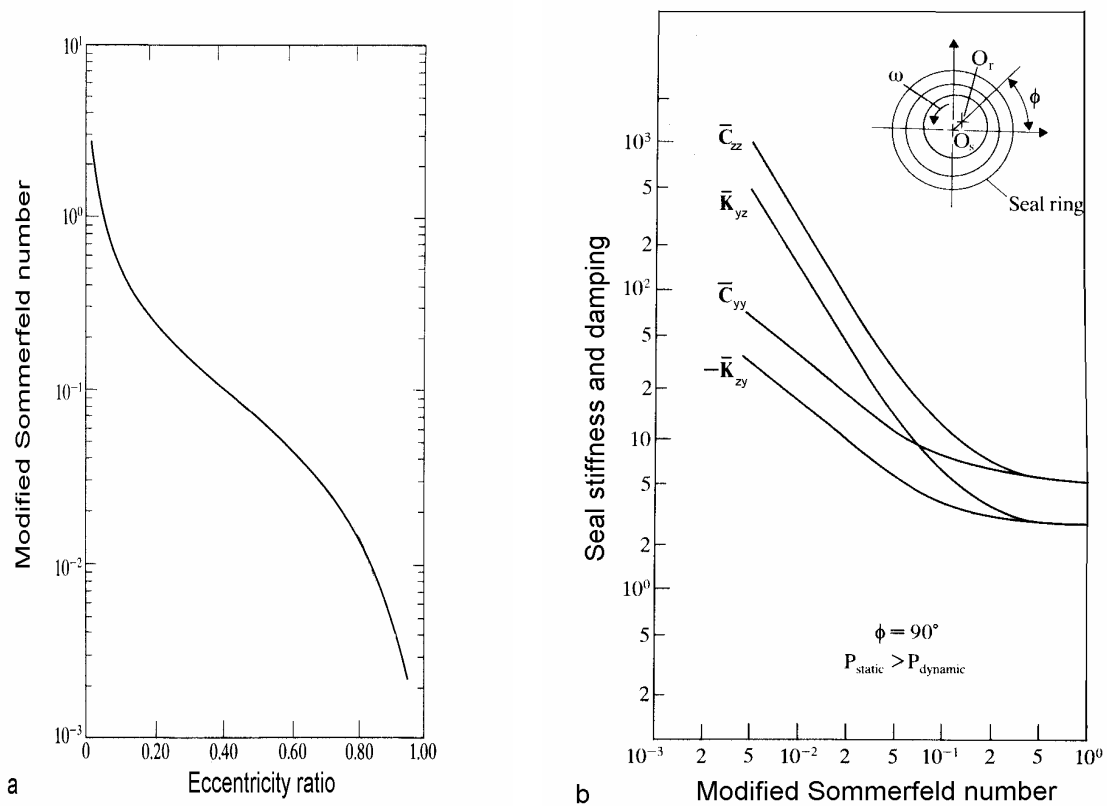


Fig. 2.25 (from [2.11])

For five values of the static eccentricity ratio ε_0 , the dimensionless oil seal coefficients are given in Table 2.1 [2.17].

The physical (dimensional) coefficients are then calculated as

$$k = \bar{K} \frac{W_*}{C_r}, \quad c = \bar{C} \frac{W_*}{\omega C_r} \quad (2.5)$$

where

$$W_* = \frac{\pi \mu R L^3 N}{60 C_r^2} = \mu \omega L D \left(\frac{R}{C_r} \right)^2 \left(\frac{L}{D} \right)^2 \quad (2.6)$$

and $\omega = 2\pi N/60$.

Table 2.1

ε_0	\bar{K}_{yz}	\bar{K}_{zy}	\bar{C}_{yy}	\bar{C}_{zz}
0.01	3.14	-3.14	6.28	6.28
0.1	3.28	-3.19	6.38	6.57
0.2	3.76	-3.33	6.67	7.51
0.5	9.67	-4.84	9.67	19.35
0.8	92.1	-14.54	29.1	184.2

Note that $\bar{K}_{yz} \neq -\bar{K}_{zy}$ and $\bar{C}_{yy} \neq \bar{C}_{zz}$ so that the locked-up eccentric seal is anisotropic.

The direct stiffness and damping coefficients are not as important as the cross-coupled coefficients because the seals are close to the bearings. Bearing direct stiffness and damping coefficients are much larger and tend to dominate the seal coefficients. Tilting pad bearings have no cross-coupled coefficients when symmetric loading occurs, so the oil seal cross-coupled coefficients are very significant.

A simple breakdown seal can have an axial force as high as $\frac{\pi}{2} D t \Delta p$. For a seal pressure drop $\Delta p = 6.89 \cdot 10^6$ Pa, a diameter $D = 165$ mm, and a face width $t = 6.35 \cdot 10^{-3}$ m, the axial locking force is approximately $1.11 \cdot 10^4$ N. For three seals and assuming a coefficient of friction of 0.1, the radial load capacity could be as high as $3.34 \cdot 10^3$ N, a value equal to a typical bearing load.

It is easy to see that, unless a special pressure-balanced ring seal is employed in medium-weight rotor, high-pressure machines, the bearings and seals will interact as rotor supports. In heavy rotor, lower pressure machines this interaction is less likely.

Thus, the high pressure can indirectly cause instability in otherwise stable machines, apart from influencing the gas density, by

locking oil breakdown seals axially such as to cause interaction with the stable rotor / tilting pad bearing system.

In *conclusion*, oil-buffered seals should be designed to act as sealing elements only and should not be part of the dynamic system of rotor and bearings. A pressure-balanced seal should be a design requirement, and means for causing seal lock-up should be eliminated from the compressor design.

2.7 Squeeze Film Dampers

Squeeze film dampers are used in centrifugal compressors to eliminate instabilities or to alter the speed at which they occur.

2.7.1. Basic Principle

Figure 2.26 shows the construction of a squeeze film damper.

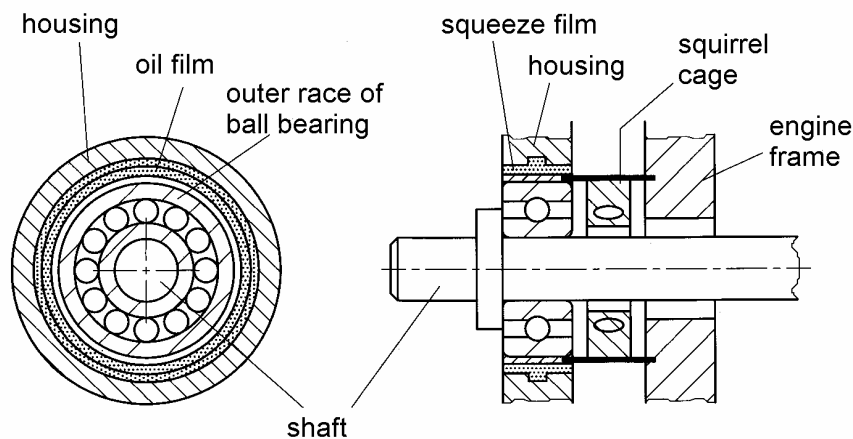


Fig. 2.26

It typically consists of an annulus with a clearance of 25 to 500 μm that contains the oil film and surrounds the outer race of the rolling element bearing. The squirrel cage constrains the rolling element bearing from rotating, preventing the shaft to reach the oil film. It also acts as a light retainer spring that centres the journal in the damper clearance.

Other designs of squeeze film dampers do not incorporate squirrel cages; they rely instead on a dog mechanism to constrain the

outer race of the rolling element from rotating. In such dampers the journal bottoms down in the damper clearance if no precession occurs.

The stationary oil film is the main characteristic of squeeze film dampers and is, in fact, the only difference between a squeeze film damper and a journal bearing, both of which are hydrodynamic bearings. The oil film in journal bearings rotates due to the rotation of the rotor even if there is no precession. The rotating oil creates the static load-carrying capacity of the journal bearing and contributes to its stiffness. But oil rotation also causes instabilities such as oil whirl and oil whip.

In contrast, in squeeze film dampers the oil does not rotate if the rotor is not precessing. These dampers therefore have no static load-carrying capacity and no stiffness. The oil film dampens motion only when the rotor whirls. If there is no precession (and no retainer spring) the journal would bottom down in a squeeze film damper. Because the oil film is stationary, oil whirl and oil whip do not occur in squeeze film dampers.

2.7.2 Design Configurations

A locally sealed damper with end hole feed/drain and radial piston rings is shown in figure 2.27,*a*. In such a damper, tightly sealed in the axial direction, the oil will flow circumferentially when squeezed.

An open-ended damper, sometimes referred to as a globally sealed damper, with end groove feed/drain and axial face seals is shown in figure 2.27,*b*. Because the damper is not sealed in the axial direction, the oil can flow axially when squeezed.

A different configuration for feeding oil is the central circumferential feed groove; it is most commonly found in dampers without end seals.

Other squeeze film damper designs are used with rolling element bearings, where the centering spring is generally eliminated, but antirotation tabs or keys are provided. Common end sealing

arrangements include a) radial O-ring seals, b) piston ring seals, and c) side O-ring seals.

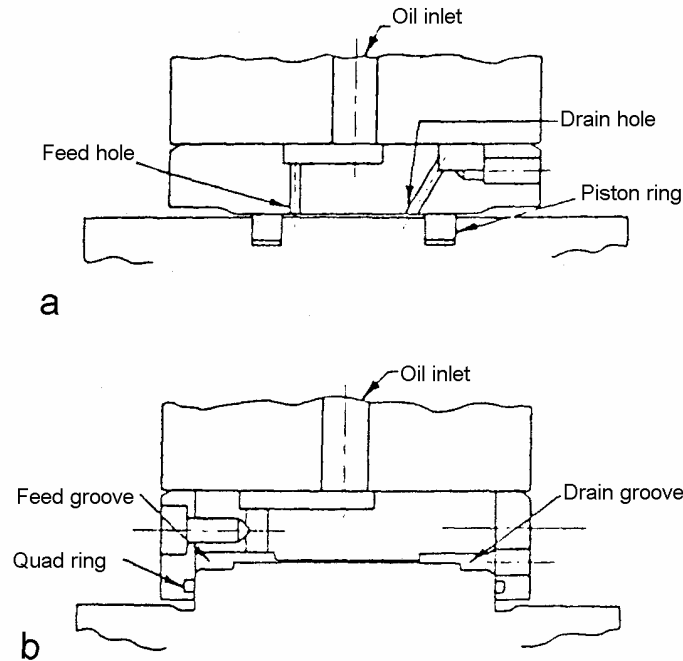


Fig. 2.27 (from [2.15])

2.7.3 Squeeze Film Stiffnes and Damping Coefficients

The stiffness K_{sf} and damping coefficient C_{sf} of the squeeze film damper can be derived from a solution of the Reynolds equation for a nonrotating journal bearing.

For a squeeze film with no end flow (Fig. 2.27a), assuming laminar flow, full cavitation, a circular synchronous precession orbit and an inertialess oil film, the stiffness and damping coefficient are found to be [2.16]

$$K_{sf} = \frac{24 \mu R^3 L \varepsilon \omega}{C_r^3 (2 + \varepsilon^2)(1 - \varepsilon^2)} \quad (2.7)$$

$$C_{sf} = \frac{12 \pi \mu R^3 L}{C_r^3 (2 + \varepsilon^2)(1 - \varepsilon^2)^{1/2}}, \quad (2.8)$$

where R - squeeze film radius, L - axial length of damper, C_r - radial clearance, μ - oil dynamic viscosity, ε - eccentricity ratio (orbit radius / radial clearance), ω - whirl speed.

For relatively short dampers ($L/D < 0.5$) with open ends, assuming unrestricted end flow (Fig. 2.27b), the damper stiffness is

$$K_{sf} = \frac{2\mu R L^3 \varepsilon \omega}{C_r^3 (1 - \varepsilon^2)^2} \quad (2.9)$$

and the damping coefficient is

$$C_{sf} = \frac{\pi \mu R L^3}{2 C_r^3 (1 - \varepsilon^2)^{3/2}} \quad (2.10)$$

For the uncavitated film, $K_{sf} = 0$ and

$$C_{sf} = \frac{\pi \mu R L^3}{C_r^3 (1 - \varepsilon^2)^{3/2}} \quad (2.11)$$

For pure radial squeeze motion, $K_{sf} = 0$ and

for cavitated film

$$C_{sf} = \frac{\mu R L^3 [\pi - \cos^{-1}(\varepsilon)](2\varepsilon^2 + 1)}{C_r^3 (1 - \varepsilon^2)^{5/2}} \quad ,$$

for uncavitated film

$$C_{sf} = \frac{\pi \mu R L^3 (2\varepsilon^2 + 1)}{C_r^3 (1 - \varepsilon^2)^{5/2}} \quad .$$

Note that the above stiffness and damping coefficients apply for a circular orbit of radius $C_r \varepsilon$. Dampers have no equilibrium position for an applied static load in the sense of a journal bearing. The "stiffness" developed by a damper results from its orbital motion due

to a rotating load and could more properly be defined with a cross-coupled damping coefficient.

For dampers operating at high speeds and high values of the squeeze-film Reynolds number

$$\text{Re} = \frac{\rho \omega C_r^2}{\mu},$$

where ρ is the oil density, fluid inertia forces become significant. Inertia or "added mass" coefficients can be obtained dividing the fluid inertia forces to the radial acceleration $\omega^2 C_r \varepsilon$. The direct inertia coefficient is

$$M_{sf} = -\frac{\pi \rho R L^3}{12 C_r} \frac{\beta - 1}{\beta \varepsilon^2} (2\beta - 1)$$

and the cross-coupled inertia coefficient is

$$m_{sf} = -\frac{\rho R L^3}{C_r} \left(\frac{27}{70\varepsilon} \right) \left(2 + \frac{1}{\varepsilon} \ln \frac{1-\varepsilon}{1+\varepsilon} \right),$$

where $\beta = (1 - \varepsilon^2)^{1/2}$.

2.7.4 Design of a Squeeze Film Damper

If a squeeze film damper is added to an existing compressor design to cure a subsynchronous vibration problem, a stability analysis is carried out based on a finite element model or a transfer matrix model of the rotor-bearing system.

Input parameters are damper radius, R , damper length, L , oil dynamic viscosity, μ , and rotational angular speed, ω . Usually, an aerodynamic cross-coupling stiffness is also considered. A practical highest level of cross-coupling for design studies is $1.75 \cdot 10^7$ N/m [2.16]. Output parameters are the radial clearance, C_r , and the eccentricity ratio, ε_0 , which produce support stiffness and damping coefficients able to eliminate the instability.

A computer program helps solving the damped eigenvalue problem and calculating the logarithmic decrement (or simply the real part of eigenvalues) as a function of design parameters.

A typical stability map is shown in figure 2.28, where the real part of the eigenvalue of the unstable mode is plotted as a function of support damping. Each curve corresponds to a given value of support stiffness. Separate maps are plotted for several assumed values of the aerodynamic cross-coupling stiffness K_p . The rotor and bearing characteristics remain unchanged.

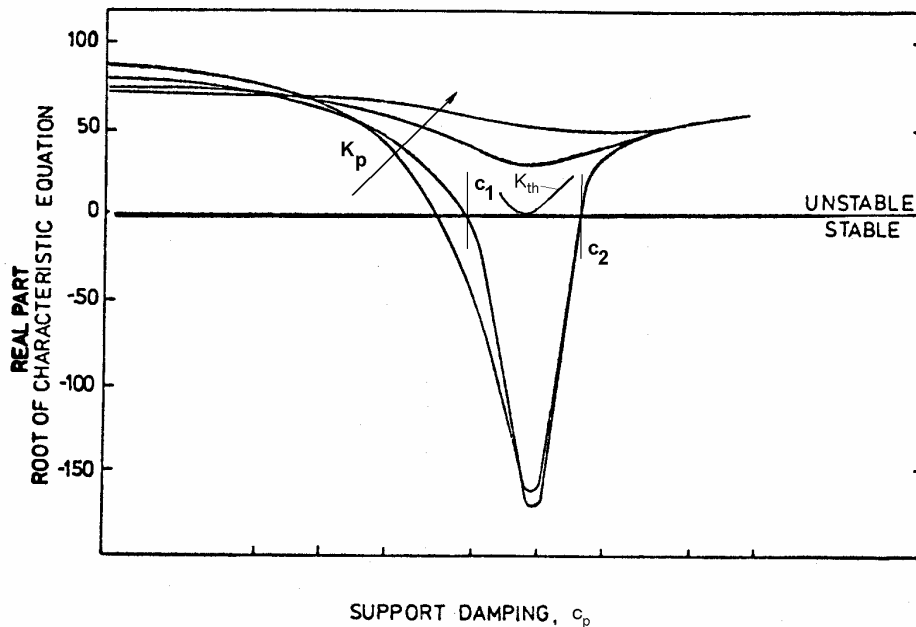


Fig. 2.28

Curves crossing the zero level of eigenvalue real part define stiffnesses for which the system can be stable. As the support stiffness is increased, the system becomes less stable, so that there is a threshold value K_{th} above which the system is always stable (the curves do not intersect the zero real part value).

On the other hand, for curves crossing the horizontal zero level axis, there is an intermediate range of support damping values for which the system is stable for a given value of support stiffness. For damping less than a certain value, c_1 , or larger than another value, c_2 , defined by the crossing points, the system is again unstable so that the

actual value of support damping has to be selected between the two limits.

Thus, linearized stability maps as that from figure 2.28 provide information on the support characteristics needed to promote stability in a given rotor-bearing system.

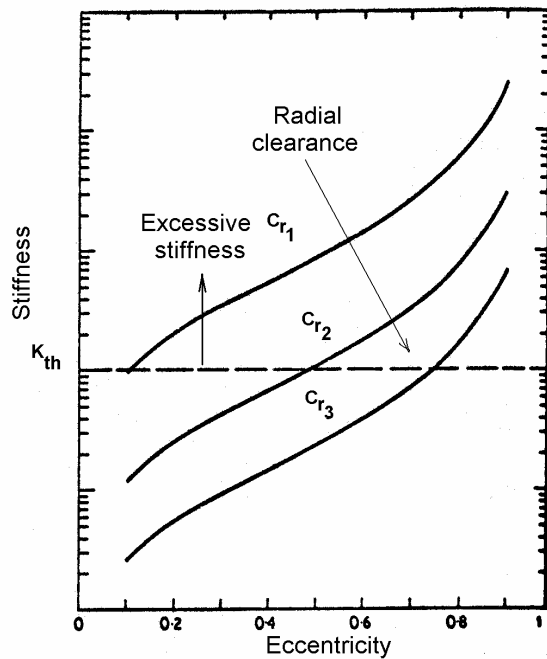


Fig. 2.29

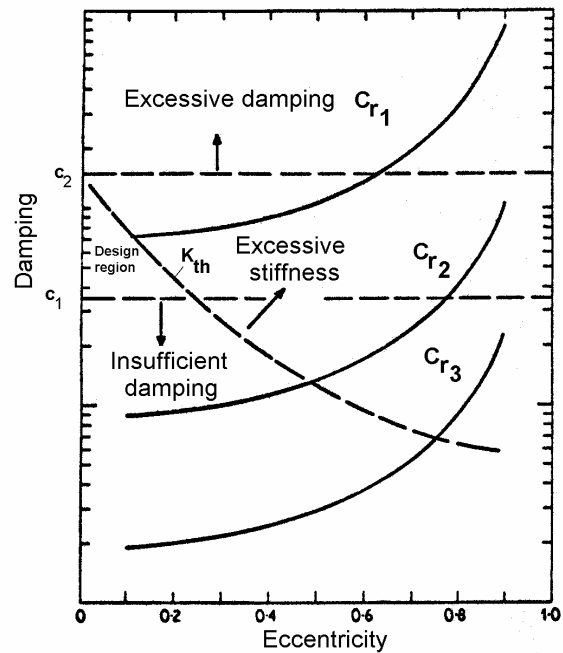


Fig. 2.30

In order to further determine the damper design parameters, two more diagrams are needed illustrating the support stiffness (Fig. 2.29) and damping (Fig. 2.30) versus eccentricity for different values of the radial clearance.

First, the diagram from figure 2.29 is used. Drawing a horizontal line for the value K_{th} , the values of ε_0 at the crossing points with curves $C_r = \text{const.}$ are determined.

Based on these values, the dotted line $K_{th} = \text{const.}$ is drawn in figure 2.30, which sets an upper border for the range of possible stable operation. Next, two horizontal lines are drawn in figure 2.30 corresponding to c_1 and c_2 , the limits of variation of the support damping for stable operation. The area between these two limits and below the K_{th} curve defines the *design region* of the damper. The

design parameters C_r and ε_0 are selected to correspond to points within this region.

2.8 Aerodynamic Cross-Coupling at Impellers

Wachel [2.2] developed an empirical formula for estimating the level of aerodynamic loading in centrifugal compressors.

The cross-coupling stiffness coefficients are given by

$$k_{yz} = -k_{zy} = 16 \frac{P M_w \rho_D}{D h f \rho_S} \quad (2.12)$$

where P - horsepower, kW, M_w - molecular weight, D - impeller diameter, m, h - restrictive dimension in flow path, m, f - frequency corresponding to rotational speed, Hz, ρ_D - gas density at discharge conditions, kg/m³, ρ_S - gas density at suction conditions, kg/m³.

When this formula was applied to several rotors that had instabilities, especially for gas reinjection compressors, it appeared to give overall levels of aerodynamic loading near that required to cause the logarithmic decrement to be negative. It corresponds to the observations that multistage centrifugal compressors become unstable as the horsepower and gas density increase. Units become unstable also when the ratio of running speed to first critical speed increases (f decreases).

2.9 Rotordynamic Considerations

A complete dynamic analysis of a turbomachine would involve such calculations as undamped natural frequencies, damped natural frequencies, linear stability and response of the system to exciting forces. In the case of centrifugal compressors, undamped critical speed maps are of little interest. For typical compressor precession modes which are heavily damped, second mode in particular, the damped natural frequency can be as much as 2 to 9 times lower than the expected peak response speed.

Shop testing, carried out after compressor is constructed but before it is commissioned, can reveal problems prior to start-up. Bode plots, obtained during run-up measurements, are used to check that the critical speeds are not within the operating speed range. Separation margins of the critical speeds from the intended operating speed range are defined in *API Standard 617*; resonances must be 20 percent above the maximum continuous speed and/or 15 percent below the operating speeds [2.18]. Compliance with present specifications requires calculation of deflections at each seal along the rotor, as a percentage of the total clearance.

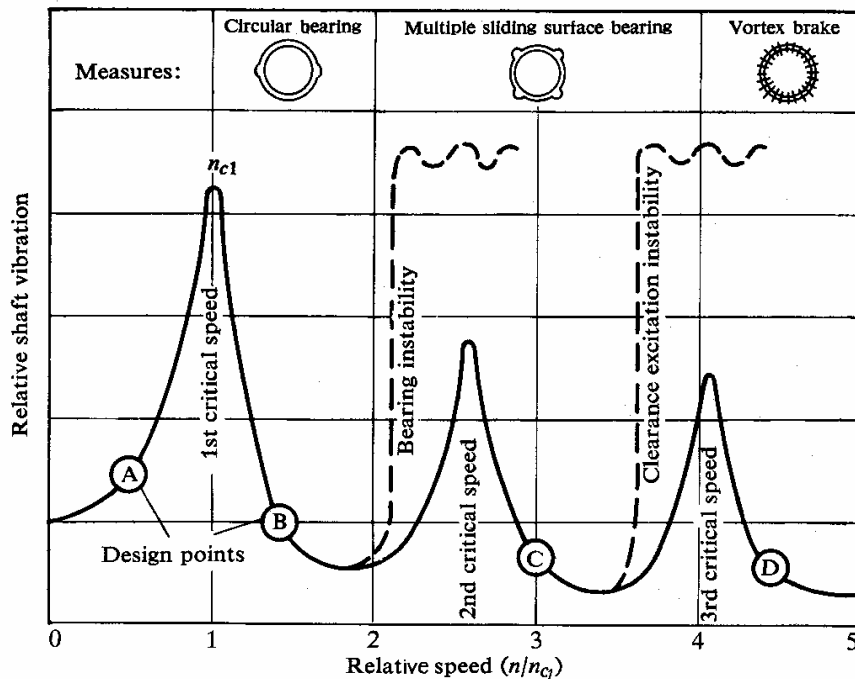


Fig. 2.31 (from [2.9])

Modern multistage compressors are typically designed to operate through and above several critical speeds so as to maximize the work done by a given size machine. For example, a 425 mm diameter impeller for an industrial centrifugal compressor can be designed for a work load well in excess of 2000 HP by running at speeds approaching 9000 rpm. Up to eight stages are used to obtain the required pressure rise. Process compressors and units used for natural gas injection can have discharge pressures of the order of 650 bar and can drive gases with high density. The result of this combination of supercritical speed, high pressure and high work load

has been an increasing tendency for such machines to exhibit problems of nonsynchronous rotor whirling. This is why *stability analysis* is of prime interest.

While many rotating machines operate below the first critical speed (point *A* in figure 2.31), turbomachinery operate above the first critical speed (point *B*). Until mid seventies any further shift of the resonance - and hence any increase in the maximum number of stages per casing - was precluded by the bearing stability limit. This was then raised by means of stronger bearing designs until operation above the second critical speed became possible (point *C*).

High pressure compressors operating on fixed lobe bearings could generate a violent shaft whip condition just above twice the first natural frequency. By going to tilting-pad bearings, that threshold speed can be raised to well over two times the first natural frequency. Attempts to raise speed further came up against another stability limit: rotor instability due to gap excitation. Using vortex brakes before labyrinths this boundary has been pushed back and the way is open in principle to still higher speed ratios (point *D*).

As can be seen from figures 2.10 to 2.13, multistage centrifugal compressors have relatively slender shafts. Usually, impellers are mounted on almost half of the rotor length, the other part being necessary for the centre seal, the balance drum, the oil seals, the radial bearings and the thrust bearing. The shaft diameter is kept small to increase the impeller eye. In comparison with the drum rotor of axial compressors, the shaft of centrifugal compressors is more flexible, having relatively low natural frequencies which favour instabilities.

Rotordynamic instability is characterized by whirling of the rotor-bearing system at frequencies other than shaft speed (non-synchronous). The cause is usually associated with the variation of some fluid dynamic pressure around the circumference of a rotor component, e.g. in gas seals, oil bushings, fluid pressures on impellers. The corresponding forces are "self-excited", that is, they are produced by the whirling motion itself. The rotor-bearing system tends to whirl at one of its natural frequencies. Because the shaft speed is faster than the whirl speed its motion is referred to as

"subsynchronous whirl". The destabilizing forces act tangentially to the shaft whirl orbit and thus feed energy into the whirling motion.

Operating experience with centrifugal compressors has shown the work-load dependence of instabilities. In many high pressure units, the vibration trip-out occurred when the suction pressure was increased, so that the design discharge pressure could not be reached. At a constant speed, the subsynchronous vibration is a function of the pressure ratio across the compressor. The non-synchronous vibration is also acceleration-dependent, so that slow run-up and slow pressure raise avoided the onset of instability.

Methods of eliminating the non-synchronous whirl condition could consist of one or more of the following: a) use of tilting pad bearings; b) raising the first critical speed to reduce the ratio operating speed vs. first critical speed; c) elimination of detrimental effects of oil seals; d) use of flexible damped supports to suppress fractional whirl conditions; and e) reduction of shrink fit contact area and residual stresses.

When evaluating a bearing design, a decision needs to be made on whether the problem is stability or the need for higher load capacity and better synchronous response. When higher load capacity and better synchronous response characteristics are needed, the load-between-pads (LBP) design is favored over the load-on-pad (LOP) configuration. The damping by the effective support area is larger on the LBP than LOP design. Consequently, heavy rotors operating at low speeds (low Sommerfeld numbers) characteristically have LBP configurations. Light rotors operating at high speeds do not require the load capacity of LBP designs. Typically, light rotors operating at high speeds (over 20,000 rpm) will have high aerodynamic cross-coupling forces, thus stability is more of a concern than synchronous response.

Preload is an important parameter. As preload increases, stiffness increases, however damping decreases. Change from LBP to LOP bearings increases the system stiffness depending on preload. Negative preload could cause pad lockup. The leading edge of the pad will dig into the shaft preventing a converging oil wedge. This could cause poor stiffness and damping coefficients.

Increasing the shaft diameter will raise the rotor stiffness and will improve stability.

One more point of interest. When modelling even simple rotors as those shown in figures 2.32 and 2.33, one has to consider the axial offset distance of the centre of gravity of the impellers to the point of attachment on the shaft. The offset distance of the impeller increases the total transverse moment of inertia of the impeller and thus also reduces the effective gyroscopic stiffening moment transmitted to the shaft.

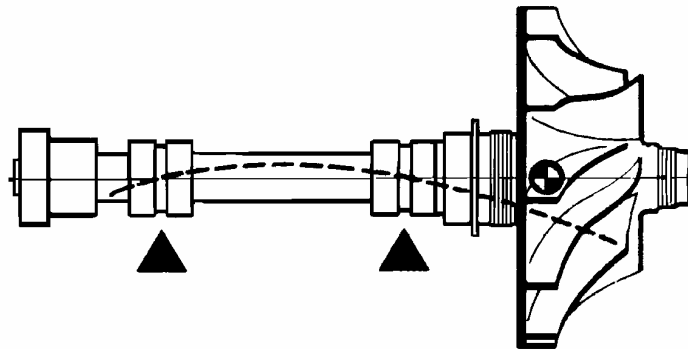


Fig. 2.32

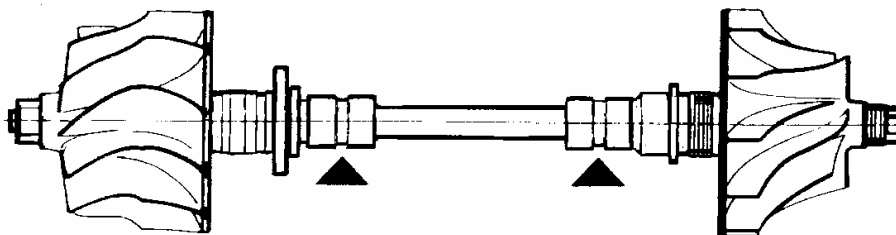


Fig. 2.33

Impeller hub and sleeves provide an additional stiffening effect to the shaft. This effect is usually handled by adding a fraction of the sleeve or hub stiffness to that of the corresponding shaft section. When the sleeve is shrunk to the shaft this fraction can be as high as 1. Otherwise, a value between 0.5 and 0.65 is used irrespective of fit.

References

- 2.1 Japikse D., **Centrifugal Compressor Design and Performance**, Concepts ETI & Oxford University Press, 1996.
- 2.2 Wachel J.C., *Rotordynamic Instability Field Problems*, NASA CP 2250, pp 1-19, 1982.
- 2.3 Agnet E., *Turboverdichter*, Sulzer Dampfkalender.
- 2.4 Logan E., **Turbomachinery. Basic Theory and Applications**, 2nd ed., Marcel Dekker Inc., New York, 1993.
- 2.5 Lüdtke K., *Turboverdichter*, in **Dubbel. Taschenbuch für den Maschinenbau**, 17. Auflage, Springer, pp R65-R75, 1990.
- 2.6 Pfeleiderer C. and Petermann H., **Strömungsmaschinen**, 6.Aufl., Springer, 1990.
- 2.7 Strub R.A., *Axial Compressors for Large LNG Plants or Other Applications*, Sulzer Technical Review, vol.62, nr.4, pp 134-142, 1980.
- 2.8 ** *Centrifugal Compressor for Ultra-High Pressures*, Druckschrift MA 25.69en/9.83, Mannesmann Demag.
- 2.9 Meiners K., *Compressors in Energy Technology*, Sulzer Technical Review, vol.62, nr.4, pp 143-148, 1980.
- 2.10 Childs D., **Turbomachinery Rotordynamics: Phenomena, Modelling and Analysis**, Wiley, 1993.
- 2.11 Ehrich F.F. (ed), **Handbook of Rotordynamics**, McGraw Hill, 1992.
- 2.12 Emerick M.F., *Vibration and Destabilizing Effects of Floating Ring Seals in Compressors*, NASA CP 2250, pp 187-204, 1982.
- 2.13 Kirk R.G. and Simpson M., *Full Load Shop Testing of 18000 HP Gas Turbine Driven Centrifugal Compressor for Offshore Platform Service: Evaluation of Rotor Dynamic Performance*, NASA CP 2409, pp 1-13, 1985.
- 2.14 Allaire P.E. and Kocur J.A.Jr., *Oil Seal Effects and Synchronous Vibrations in High-Speed Compressors*, NASA CP 2409, pp 205-223, 1985.
- 2.15 El-Shafei A., *Squeeze Film Dampers: Effective Damping Devices for Rotating Machinery*, *Vibrations*, vol.5, nr.3, pp 8-11, 1989.
- 2.16 Gunter E.J., Barrett L.E. and Allaire P.E., *Stabilization of Turbomachinery with Squeeze Film Dampers – Theory and Applications*, Proc. Conf. "Vibrations in Rotating Machinery", I. Mech. Eng., pp 291-300, 1976.
- 2.17 Kirk R.G., *The Impact of Rotor Dynamics Analysis on Advanced Turbo Compressor Design*, Proc. Conf. "Vibrations in Rotating Machinery", I. Mech. Eng., pp 139-150, 1976.

- 2.18 **API Standard 617**, *Centrifugal Compressors for General Refinery Services*, American Petroleum Institute, Washington, 1988.

3. FANS AND BLOWERS

3.1 Introduction

Fans are employed to move air or other gases. They may be classed in the group of machines prone to vibration. During operation their vibrational behaviour tends to worsen to a considerable degree and in some cases to a dangerous degree. The noticeable signs of this are a sudden or a gradual increase in the level of mechanical vibrations at the bearing locations, on housings and at the machine foundations. Similar behaviour is only encountered with very few other machines. Electric motors, compressors and pumps for example produce a vibration spectrum with almost constant amplitude over years of operation. In the case of fans and blowers, vibration-free running is frequently only achievable over a short period of operation or only for a certain operational condition. This peculiarity has three principal causes [3.1]:

1. *Impeller construction.* Most fan rotors are fabricated as a welded construction. The locked-in welding stresses can relieve themselves during operation under the influence of centrifugal forces or, in the case of hot air blowers, due to thermal effects and can cause deformations, i.e. unbalances. Unbalances however manifest themselves during rotation as vibration excitation.

2. *Effect of the transported gas.* In the case of exhaust gas fans, sintering blowers and air separators, deposits can form on the blades due to fly ash, stone impact can lead to rotor wear, and chemically aggressive media can cause partial corrosion of the impeller. All these phenomena cause new variable unbalances and hence new vibrations.

3. *Aerodynamic effects.* Aerodynamic effects cause, during operation, additional alternating forces and air vibrations, particularly at the blower housing but also at the bearing locations. Their amplitudes depend on the loading condition of the blower and frequently are amplified due to component resonances.

Examples from practical operations show that any of these causes can lead to dangerous vibrations. Residual shaft bending, broken off bearing pedestals, blade breakage, foundation damage, building cracking and costly sequential damages are the result if vibrations in fans are allowed to grow in an uncontrolled fashion. Such vibrational damage must be avoided in the interests of fault-free operation and the protection of the investment in plant.

3.2 Basic Principles

Fans can be either radial-flow or axial-flow machines. The ratio *discharge pressure vs. suction pressure* is defined as the *pressure ratio*, ε_c . The following classification is generally accepted [3.2]:

1. *Fans* are designed for pressure ratios, $\varepsilon_c \leq 1.1$. Centrifugal fans absorb powers between 0.05 kW and 1 MW, have flow rates up to $3 \cdot 10^5$ m³/h and discharge pressures up to 1000 mm H₂O ($\sim 10^4$ N/m²).

2. *Blowers* are single-stage uncooled compressors with pressure ratios, $\varepsilon_c = 1.1$ to 4, and discharge pressures up to $3.5 \cdot 10^5$ N/m².

3. *Compressors* have high pressure ratios, $\varepsilon_c > 4$, so they usually require interstage cooling.

The machine would be a compressor, blower or fan depending on the magnitude of the pressure rise occurring during transit from inlet to outlet. Fans produce very small pressure heads measured in millimeters of water pressure differential, so that the small changes of gas density are ignored. A compressor also handles gases, but with large enough pressure rises that significant fluid density changes occur. In some cases, if density is increased by 5 percent, then the turbomachine is called a compressor.

A centrifugal fan, as compared with a pump, requires a much smaller increase in impeller blade speed, i.e. a smaller ratio of outer to inner radius, R_2 / R_1 . It requires a volute, of course, but no diffuser is needed to enhance the pressure rise. The flow passages between impeller vanes are quite short, as shown in figure 3.1.

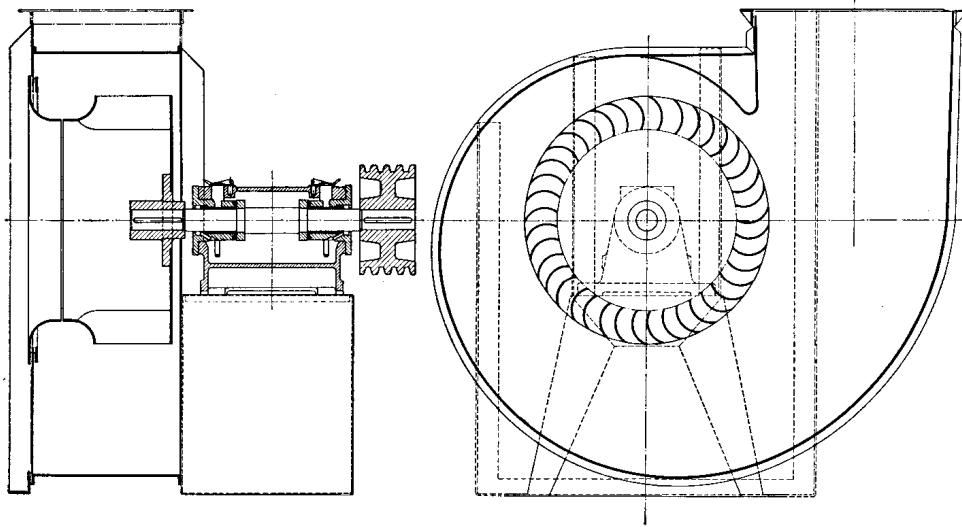


Fig. 3.1 (from [3.3])

The characteristic speed is defined as

$$n_q = n \frac{Q^{1/2}}{H^{3/4}} \quad (3.1)$$

where Q is the flow rate, m^3/s , H is the fan head, m, and n is the rotational speed, rpm. It is used in the fan design because it is independent of the gas density.

The specific speed σ , denoted V_S in (4.2), is defined as

$$\sigma = \frac{\Phi^{1/2}}{\Psi^{3/4}} = \frac{\omega}{\pi^{1/2}} \frac{Q^{1/2}}{(2gH)^{3/4}}, \quad (3.2)$$

where the flow coefficient

$$\Phi = \frac{4Q}{\pi D^2 U}$$

and the head coefficient

$$\Psi = \frac{2gH}{U^2}.$$

The specific speed σ , is related to the characteristic speed n_q by

$$\sigma = 0.00633 n_q, \quad n_q = 157.8 \sigma. \quad (3.3)$$

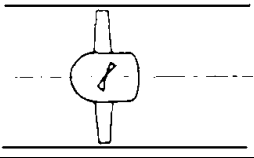
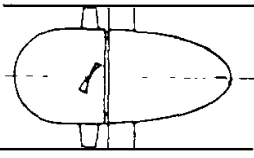
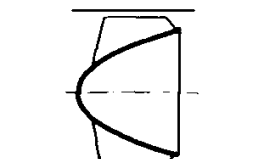
In table 3.1, the properties of different radial-flow fans are given as a function of the ratio of outer to inner radius.

Table 3.1

R_2 / R_1	Ψ	σ	n_q
0.9	2.1	0.4 - 0.5	63 - 79
0.7	0.6	0.657	104
0.5	1.0	0.283	44.7
0.3	1.1	0.162	26.6
0.15	1.1	0.04	6.3

For axial-flow fans these characteristics are given in Table 3.2.

Table 3.2

Fan	Ψ	σ	n_q
	0.05 - 0.1	1.6 - 3.8	250 - 600
	0.5	0.924	146
	0.7	0.715	113

3.3 Design Characteristics

The low-pressure fan from figure 3.1 has forward swept vanes and an overhung rotor. The design from figure 3.2 is a medium-pressure blower, with labyrinth seals, also overhung design.

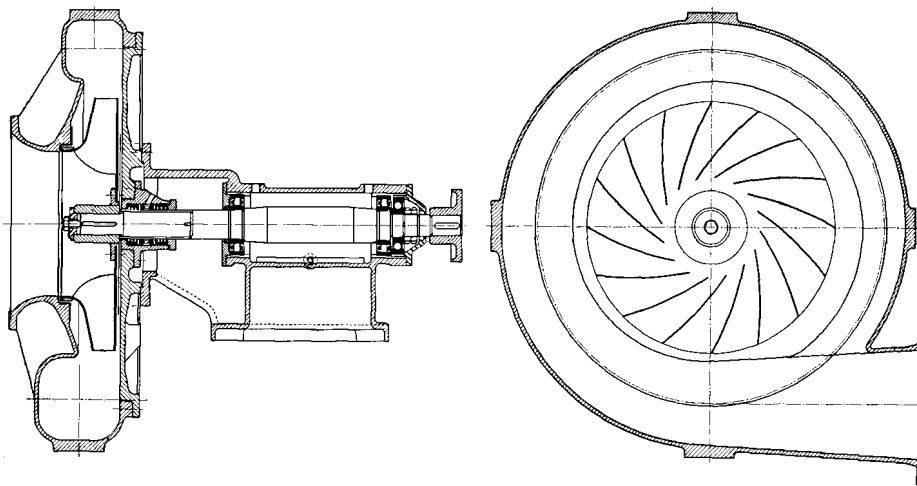


Fig. 3.2 (from [3.3])

The arrangement from figure 3.3 is a blower with backward swept vanes and centre-hung design.

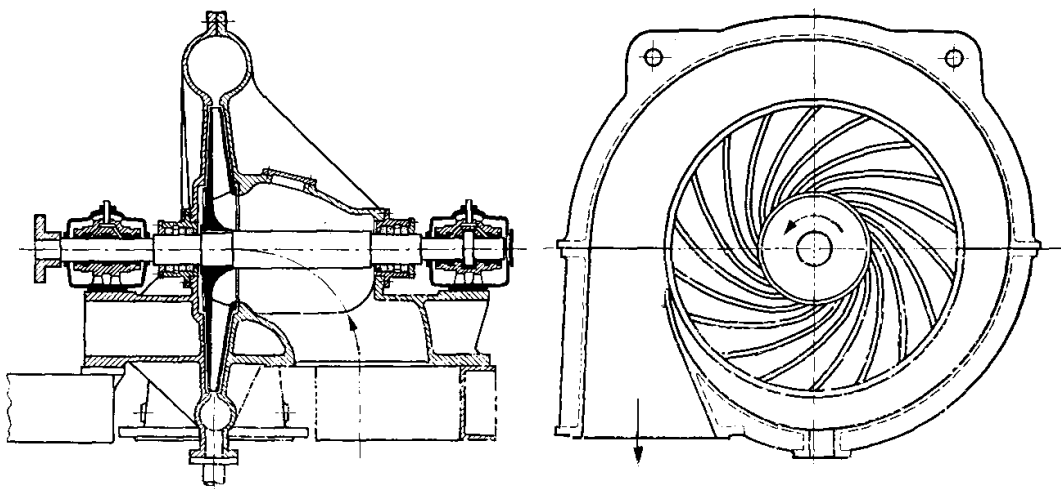


Fig. 3.3 (from [3.3])

The arrangement from figure 3.4 is with double suction and single exhaust.

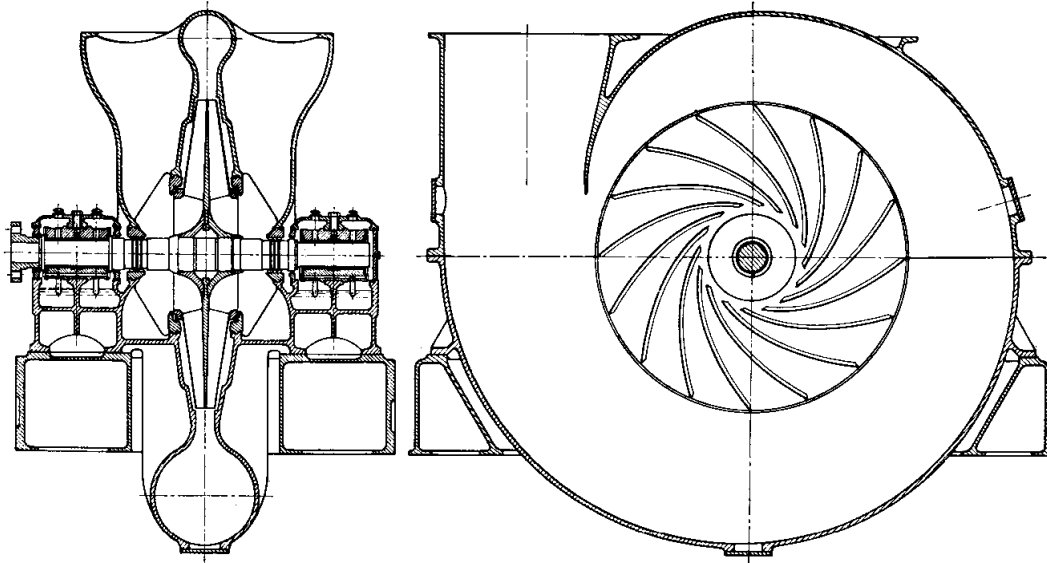


Fig. 3.4 (from [3.3])

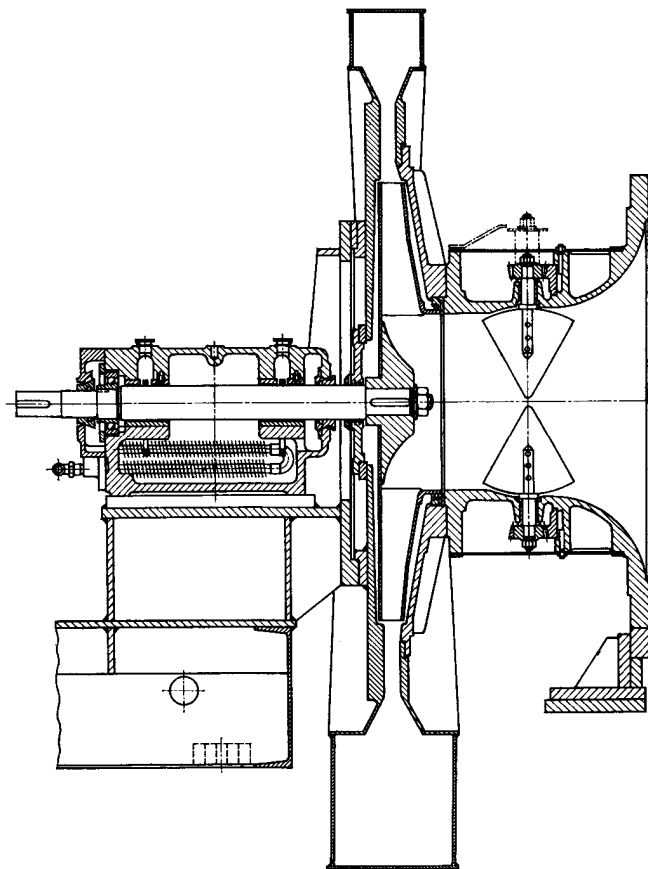


Fig. 3.5 (from [3.4])

The blower from figure 3.5 has adjustable guide blades.

Figure 3.6 shows an induced draft fan. Axial-flow fans move gases without significant effect on their density. They are like propellers in that power is supplied to produce axial motion of the fluid, but they are different in that the fluid being moved is enclosed by a casing. Like propellers, the vanes have small curvature and cause little deflection of the relative velocity vector of a fluid particle as it migrates through the moving passages. Generally, the vanes have shapes, or profiles, like that of an airfoil: they are thin, streamlined, and cambered.

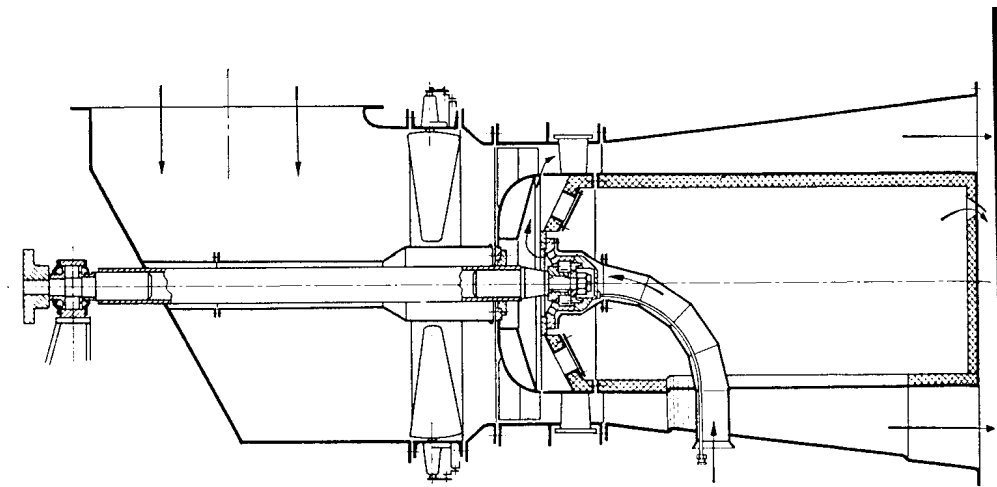


Fig. 3.6 (from [3.3])

Figure 3.7 represents a typical primary air fan on rolling element bearings. The fabricated overhung fan wheel is of welded construction, but it can also be bolted. The wheel has to be modeled as a flexible offset disc. Usually this is done considering a rigid disc, whose centre of gravity is assumed to be offset from the point of attachment of the shaft, and a rotational stiffness is introduced at the attachment point, based on a finite element analysis of the fan wheel.

An effective rotational spring stiffness may also be determined by finding the natural ringing frequency from a rap test. The first diametral ringing frequency of the disc is proportional to the square root of the ratio of the rotational stiffness divided by the diametral mass moment of inertia of the disc.

The two factors - a flexible fan disc and the axial offset distance of the centre of gravity of the fan - combine to reduce the first critical speed predicted by the centred disc model.

One important influence on the first critical speed of the rotor has the combined effective stiffness of pedestal and the bearing at the fan end. The first critical speed can be reduced by placing an elastomeric isolation pad under the rolling element bearing at the fan end. The difference in the horizontal and vertical stiffness values of the elastomeric pad in shear and compression can give rise to the so-called 'bifurcated' critical speed, and to two closely spaced peaks in the unbalance response diagram.

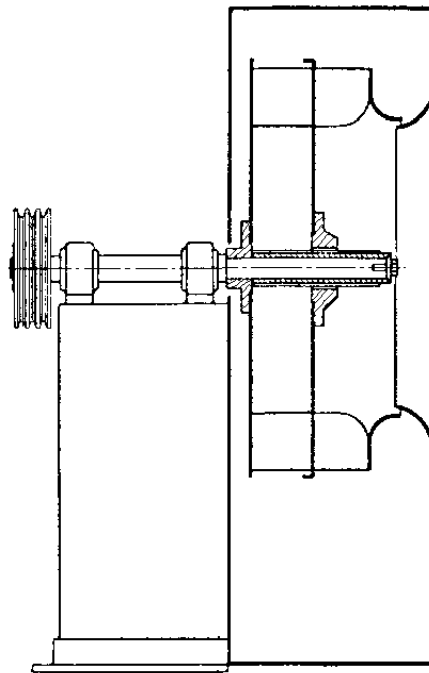


Fig. 3.7 (from [3.3])

Reduction of the critical speed below the operating speed greatly reduces the bearing forces transmitted, as well as the sensitivity of the system to unbalance. Balancing the overhung fan under operating conditions is much easier in this case, because little phase change occurs with small changes in speed.

Centrifugal fans used for forced- or induced-draft and primary-air service generally have large diameter rotors, operating from 500 to 900 rpm in pillow-block bearings, supported on structural steel or concrete foundations.

As a rule, the major problem with fans is unbalance caused by 1) uneven buildup or loss of deposited material; and 2) misalignment.

Both are characterized by changes in vibration at or near the rotational frequency.

Fan bearings are supported on either structural steel, or on stiff, reinforced-concrete pedestals. Several simple arrangements are shown in figures 3.8 to 3.10.

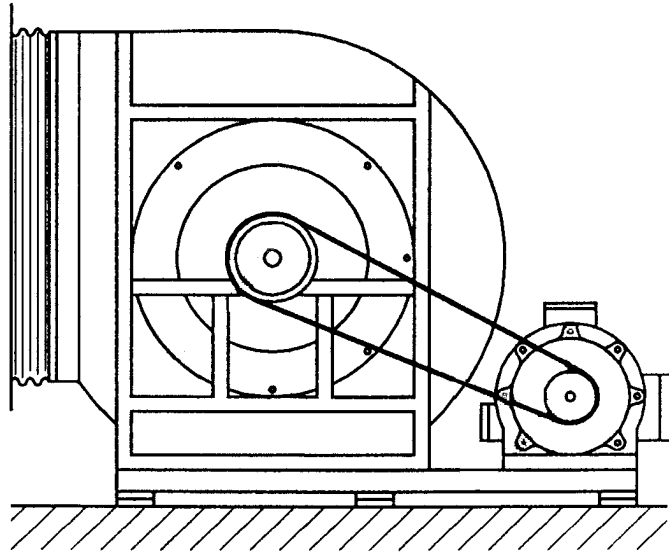


Fig. 3.8 (from [3.5])

Figure 3.8 shows a belt-driven fan mounted on the same steel skid as the electrical motor.

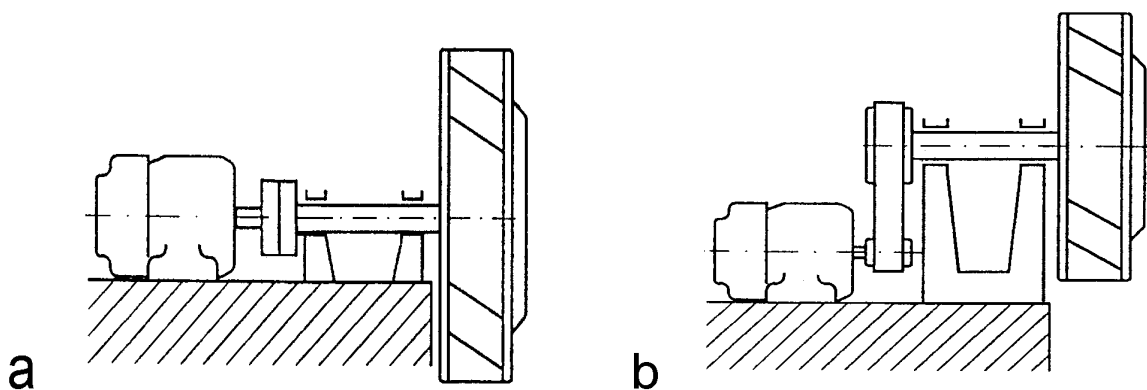


Fig. 3.9 (from [3.5])

Figure 3.9 illustrates a motor driven fan using: a) elastic coupling and low shaft; and b) belt-driven high shaft.

Figure 3.10 shows three types of driving from an electric motor: a) elastic coupling; b) belt drive; and c) direct drive.

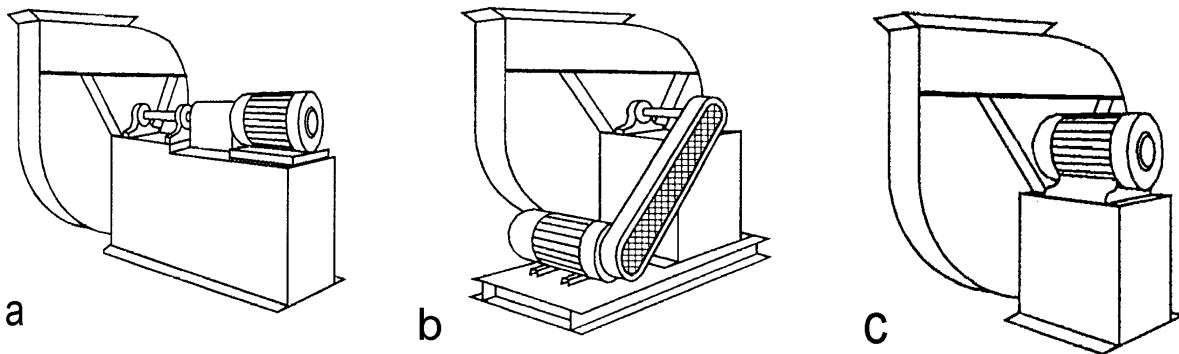


Fig. 3.10 (from [3.5])

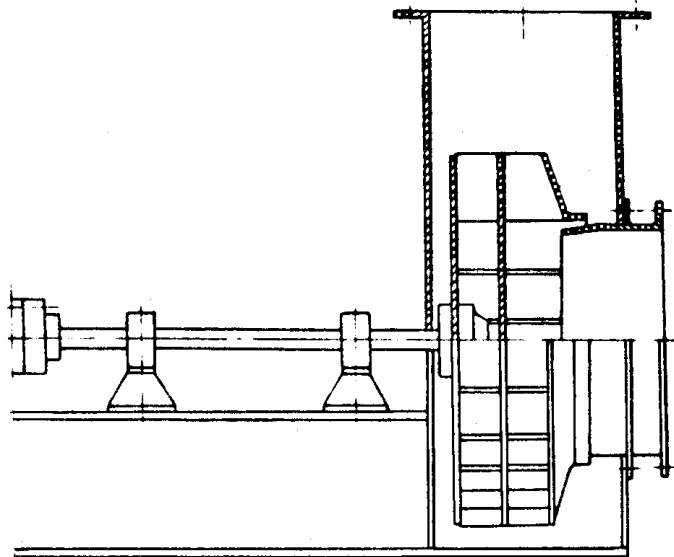


Fig. 3.11 (from [3.6])

Figure 3.11 shows a mine ventilator, type *SLM*, of nominal flow $320 \text{ m}^3/\text{min}$ and operating speed just below 1500 rpm . The overhung design implies large gyroscopic effects. Large amplitude synchronous vibrations have been recorded due to mass unbalance.

Figure 3.12 illustrates a universal ventilator, type *FKD-30*, with operating speed just below 1500 rpm . The bearing span is 0.677 m . Due to fabrication errors, the rotor had dissimilar principal moments of inertia giving rise to large subharmonic vibrations at angular speeds 138 rad/sec and 174 rad/sec . The first resonance corresponds to the operating speed.

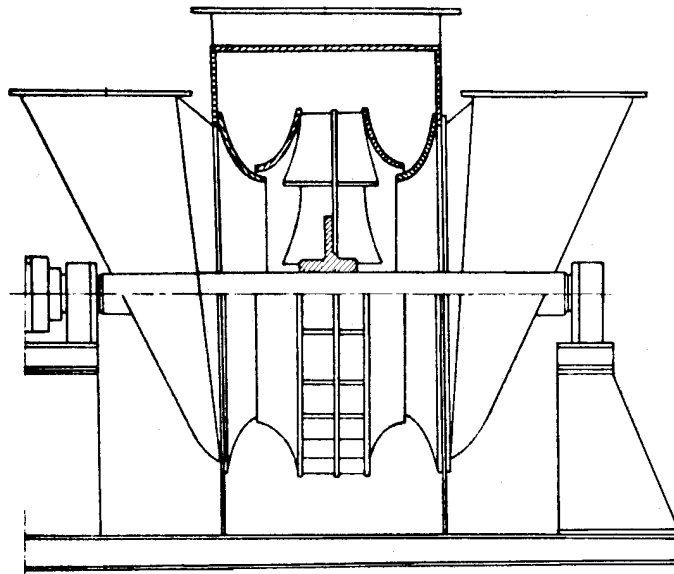


Fig. 3.12 (from [3.6])

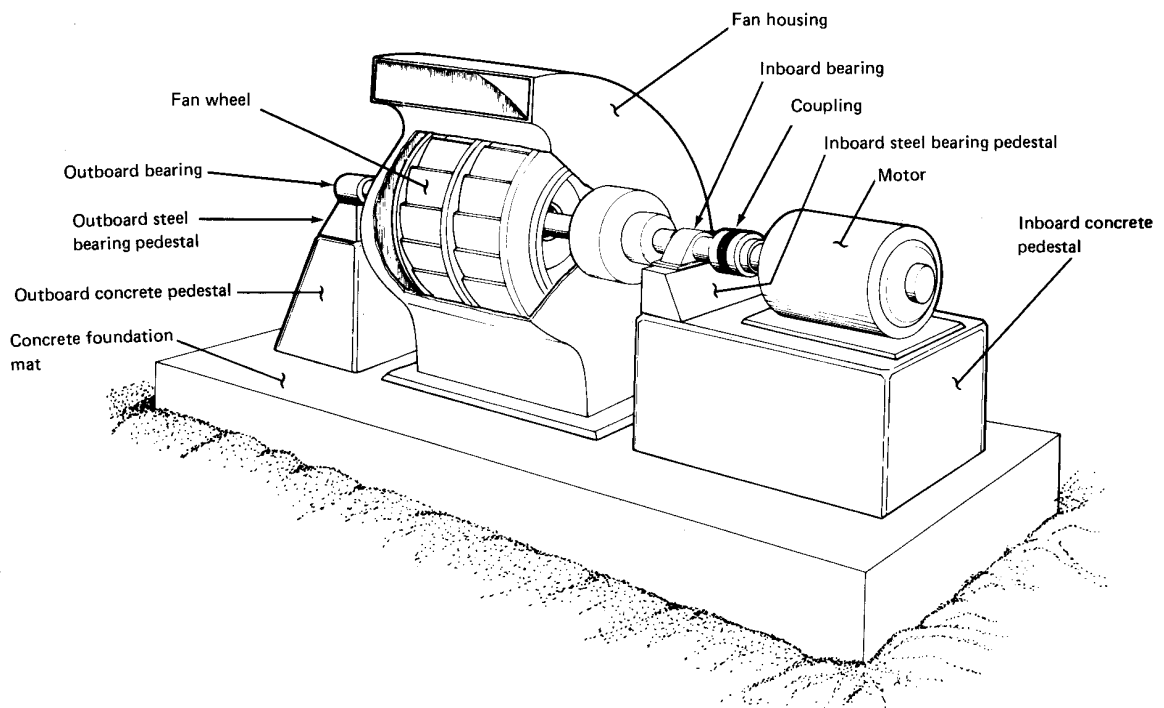


Fig. 3.13 (from [3.7])

Figure 3.13 illustrates the supporting structure of a large fan. The a double-inlet induced-draft fan is driven at 710 rpm by a 3000 HP motor. The fan wheel is 3.3 m in diameter and the total rotor weight, wheel plus shaft, is 18 tons. The rotor is supported by 254 mm diameter fluid film bearings. The bearings are mounted to steel

pedestals which are in turn mounted to concrete pedestals. The concrete pedestals are attached to a large concrete mat, $12.2 \times 7.6 \times 4.3$ m, which is supported by the soil.

The principal modes of vibration of the fan-foundation system are 1) the foundation slide mode, at 9.3 Hz, 2) the foundation rocking mode, at 26.0 Hz and 3) the rotor lateral mode, at 15.6 Hz. They are well designed to differ from the operating speed of 11.8 Hz.

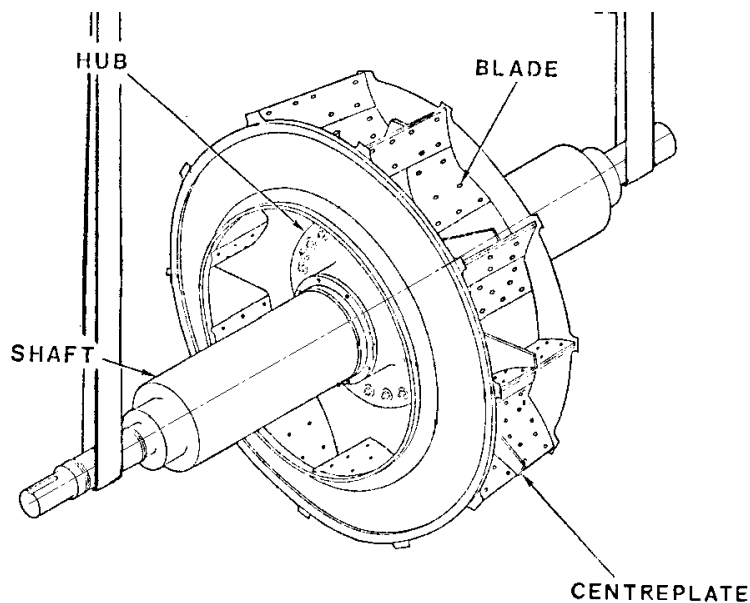


Fig. 3.14 (from [3.8])

Another large size fan rotor is shown in figure 3.14. The rotor has a double inlet wheel of 2.756 m diameter, with 10 airfoil blades on each side of a centre plate. It is important to determine the lowest few primary modes of vibration of the wheel, which has to be modeled as a flexible disc in a rotordynamic analysis. The wheel from figure 3.14 has the "disc-wobble" mode at 17.25 Hz and the "umbrella" mode at 29.9 Hz. Only the one-diameter mode is important for the calculation of lateral vibrations of the coupled shaft-wheel system.

3.4 Calculation Example

Results of a study of the critical speeds of several primary air fans in rolling element and fluid-film bearings were examined in [3.9].

A schematic cross section of the rotor with the fabricated overhung fan wheel is shown in figure 3.15. The fan assembly weighs about 680 kg and operates at 1,760 rpm. The shaft diameter at the bearing locations is 127 mm, the design bearing span is 0.56 m, and the overhang distance to the center of gravity of the fan is 0.56 m. The motor to motor end bearing distance is 0.394 m.

Designs of fabricated wheels using bolted or welded construction with either hollow or solid blades were tried. The hollow blade design collected coal dust and was impossible to balance. With the welded solid blade design, the weldment of the back plane of the impeller to the hub formed an annulus that collected coal dust. Maintaining rotor balance over a period of time was also difficult because coal dust built up on the back plane annulus.

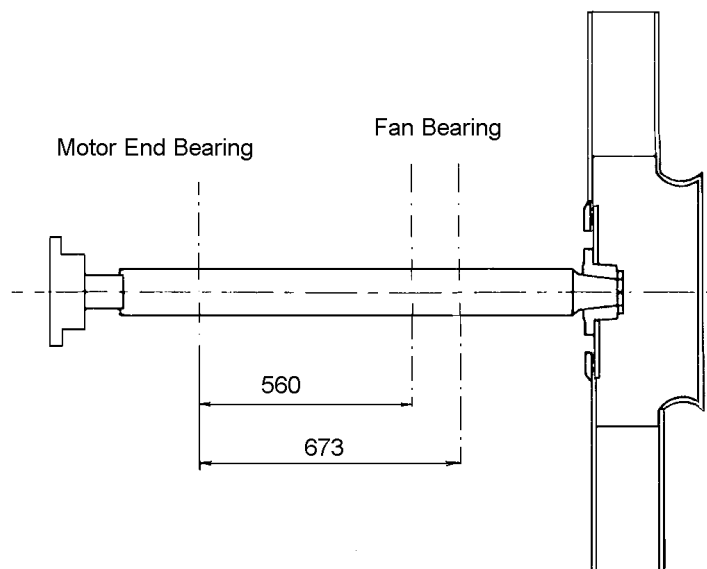


Fig. 3.15 (from [3.9])

The shaft was modeled with 17 beam finite elements, considering a steel density of $7,833 \text{ kg/m}^3$, and Young's modulus $2.068 \cdot 10^{11} \text{ Pa}$. The fan wheel was modelled as an offset disc with the centre of gravity 95 mm from the point of attachment to the shaft.

The rotational stiffness between disc and shaft was assumed to be $1.525 \cdot 10^6 \text{ Nm/rad}$, value based on a finite element analysis of the

fan wheel. The disc properties were: mass 458 kg, axial mass moment of inertia 170.6 kgm^2 , diametral mass moment of inertia 96.5 kgm^2 , outer diameter 838 mm, inner diameter 102 mm, width 190 mm.

The pedestal was included in the model by a stiffness of $2.63 \cdot 10^8 \text{ N/m}$ and an effective pedestal mass of 127 kg.

The calculated first critical speed of 1,662 rpm corresponds well with the value observed on start-up. For the first mode, the combined bearing/support strain energy for the fan bearing is 44% of the system strain energy, indicating that the bearing has a major influence on the value of the first critical speed. The influence of the pedestal mass and flexibility yields a combined (effective) bearing impedance of $1.313 \cdot 10^8 \text{ N/m}$, which is well below the rolling bearing stiffness $2.627 \cdot 10^8 \text{ N/m}$.

When the bearing span was increased to 0.673 m, the first critical speed increased to 2,185 rpm, which is 1.24 times the running speed. Calculations showed large forces transmitted from the bearing at the fan end. It was concluded that it is better for the fan with the 0.56 m span to operate above its first critical speed than for the fan with a span of 0.673 m to operate below its first critical speed, even with rolling element bearings.

When the bearing support stiffness was reduced to about $3.5 \cdot 10^7 \text{ N/m}$, the first critical speed of the fan rotor was around 1000 rpm. This was achieved by placing an elastomeric isolation pad under the rolling element bearing at the fan end. An isolation pad was not required under the bearing at the motor end.

The calculations showed that 70% of the strain energy of the system was associated with the bearing at the fan end, and 17% of this energy was associated with the shaft. The bearing at the motor end has become a nodal point.

Reduction of the fan rotor critical speed below the operating speed greatly reduced the bearing forces transmitted as well as the sensitivity of the system to unbalance.

3.5 Guidelines for Vibration Levels

For blowers with power greater than 300 kW, the standard *ISO 10816, Part 3* [3.10] provides specific guidance for assessing the severity of vibrations on bearings, bearing pedestals, or the housings, when measured *in situ*. Included are driving electrical machines with shaft heights over 315 mm.

Table 3.3

Support Class	Zone Boundary	Displacement, μm , RMS	Velocity, mm/s, RMS
Rigid	A/B	37	2.3
	B/C	72	4.5
	C/D	113	7.1
Flexible	A/B	56	3.5
	B/C	113	7.1
	C/D	175	11.0

Classification of the vibration severity zones is shown in Table 3.3 [3.10]. Zone *A* represents new machines that can be operated without restriction. Zone *B* is acceptable for long-term operation. Zone *C* represents machines that may be operated for a limited time until a suitable opportunity arises for remedial action to be taken. Zone *D* is identified as a trip level as these values are considered to be of sufficient severity to cause damage.

Table 3.4

Support Class	Zone Boundary	Displacement, μm , RMS	Velocity, mm/s, RMS
Rigid	A/B	22	1.4
	B/C	45	2.8
	C/D	71	4.5
Flexible	A/B	37	2.3
	B/C	71	4.5
	C/D	113	7.1

For machines with rated power between 30 and 300 kW, and driving electrical motors with shaft heights from 180 mm to 315 mm, the classification of the vibration severity zones is given in Table 3.4 [3.10]. The zone descriptions are the same as above.

References

- 3.1 Olsen U., *Vibrations in Blowers and Fans*, Schenck Technical Note C1207e.
- 3.2 Agnet E., *Turboverdichter*, Sulzer Dampfkalender.
- 3.3 Eck B., **Ventilatoren**, Springer, 1957.
- 3.4 Pfeleiderer C. and Petermann H., **Strömungsmaschinen**, 6.Aufl., Springer, 1990.
- 3.5 *** *Vorbeugende Maschineninstandhaltung*, Seminar 50C, Schenck, 1989.
- 3.6 Parszewski Z. and Krodkiewski J., *Parametric Instabilities of Rotor-Support Systems with Application to Industrial Ventilators*, NASA CP 2133, pp 383-400, 1980.
- 3.7 Ulm S.C., *Application of Modal Analysis to the Design of a Large Fan-Foundation System*, Proc. 2nd Int. Modal Analysis Conf., Orlando, Florida, pp 304-310, 1984.
- 3.8 Errett A.J., Solecki J.S. and Tuttle D.G., *Modal Analysis of Airfoil Fan Wheels*, Proc. 3rd Int. Modal Anal. Conf., Orlando, Florida, pp 198-204, 1985.
- 3.9 Gunter E.J. Jr., Spivey A.W. and Hobbs A., *Critical Speeds and Unbalance Response of an Overhung Primary Air Fan*, *Vibrations*, vol.5, no.4, pp 3-10, 1989.
- 3.10 **ISO 10816-3**, Mechanical Vibration - Evaluation of Machine Vibration by Measurements on Non-Rotating Parts - Part 3: *Industrial Machines with Normal Power above 30 kW and Nominal Speeds Between 120 and 15,000 rpm when Measured In Situ*, 1996.

4. HYDRAULIC TURBINES

4.1 Introduction

Hydraulic turbines have traditionally been used to convert hydraulic energy into electricity.

The first effective radial inward flow *reaction turbine* was developed around 1850 by Francis, in Lowell, Massachusetts. Around 1880 Pelton invented the split bucket with a central edge for *impulse turbines*. The modern Pelton turbine with a double elliptic bucket, a notch for the jet and a needle control for the nozzle was first used around 1900.

The *axial flow turbine*, with adjustable runner blades, was developed between 1910-1924 by Kaplan in Austria. The horizontal *bulb turbines* have a relatively straighter flow path through the intake and draft tube, with lower friction losses. In the *Straflo* (straight flow) design, the turbine and generator form an integral unit without a driving shaft.

Reversible machines, called *pump turbines*, are being used in pumped storage schemes, the most efficient large-scale technology available for the storage of electrical energy.

Modern hydroelectric power plant arrangements utilize a *reservoir* of water collected from a flowing river. The water flows into the hydraulic turbine through the *penstock* and leaves the turbine through the *draft tube*, entering a downstream reservoir known as the *tail race*. The available head is the vertical distance between the free water surface in the reservoir and the tail race.

The operating head H is the difference between the total pressure at turbine inlet and turbine outlet. Turbines are generally classified as low pressure, for $H < 20$ m, medium pressure, for $20 \text{ m} < H < 200$ m, and high pressure, for $200 \text{ m} < H < 2000$ m [4.1].

For hydraulic turbines the *degree of reaction* is defined as the ratio of the static pressure drop across the runner to the static pressure drop across the stage. In *reaction* stages such as Francis and Kaplan turbines a proportion of the pressure drop occurs in the rotor and a proportion in the stator. Typically, at their design points, a Kaplan turbine has a reaction around 90 percent, a Francis turbine of around 75 percent and a pump turbine of around 50 percent. At off-design operating points these values change. The Pelton turbine is an *impulse* stage and has zero reaction with all pressure drop occurring across the stationary components and no pressure drop across the runner.

Cavitation is a problem of main concern with hydraulic turbines. Cavitation occurs in the flow of water when, owing to regions of high-flow velocity, the local static pressure decreases below the vapour pressure and vapour bubbles appear. Cavitation may occur on the blade suction surface in regions of low pressure or at the runner leading edge at off-design operation. For low-head operation, cavitation will be located on the pressure side; for high-head operation it will be on the suction side.

Within vortices such as those induced by the tip leakage flow of Kaplan runners or those occurring in the blade passages of a Francis runner at extreme off-design operation and in the draft tube of Francis turbines, cavitation may also occur.

The effects of cavitation are harmful, both on performance and on erosion of material. Cavitation erosion is caused by the extremely high pressure peaks that occur during the implosion of cavitation bubbles in the vicinity of a solid surface. Cavitation imposes restrictions on blade loading and blade design.

4.2 Hydraulic Turbine Parameters

Basic hydraulic turbine parameters are the net head H , m, the flow rate Q , m³/s, and the rotational speed n , rpm.

Denote D - the rotor outer diameter, and $g = 9.81$ m/s². The flow coefficient Φ and the head coefficient Ψ , normalized with the

rotor blade speed $U = 0.5 D \omega$, where $\omega = \pi n / 30$ rad/s, can be written

$$\Phi = \frac{Q}{U \frac{\pi D^2}{4}}, \quad \Psi = \frac{H}{\frac{U^2}{2g}}. \quad (4.1)$$

A dimensionless specific speed V_s is defined as

$$V_s = \frac{\Phi^{1/2}}{\Psi^{3/4}} = \frac{\omega}{\pi^{1/2}} \frac{Q^{1/2}}{(2gH)^{3/4}}. \quad (4.2)$$

The specific (rotational) speed is defined as

$$n_s = n \frac{P^{1/2}}{H^{5/4}} \quad (4.3)$$

where P is the power output, in horse-power,

$$P = \frac{\rho Q H}{75} \quad (4.4)$$

and ρ is the water mass density ($\approx 1000 \text{ kg/m}^3$).

This specific speed is equal to that of the geometrically similar turbine when operating under a head of one meter of water, $H=1 \text{ m}$, and producing a horse-power, $P = 1 \text{ HP} = 736 \text{ W}$.

Denoting

$$n_q = n \frac{Q^{1/2}}{H^{3/4}}, \quad (4.5)$$

it can be shown that

$$n_s = \sqrt{\frac{\rho}{75}} n_q = 3.652 n_q \quad (4.6)$$

and

$$n_s = \sqrt{\frac{\rho}{75}} \frac{30}{\sqrt{\pi}} (2g)^{3/4} V_s \approx 576.4 V_s. \quad (4.7)$$

Hydraulic turbines have been conveniently classified with the aid of this parameter. It is possible to select the most desirable form of water turbine for a particular purpose by estimating the specific speed corresponding to the proposed operating conditions.

A diagram showing the best operating range of different turbines, marked by the picture of their runner, is given in figure 4.1 (head as a function of specific speed) [4.2].

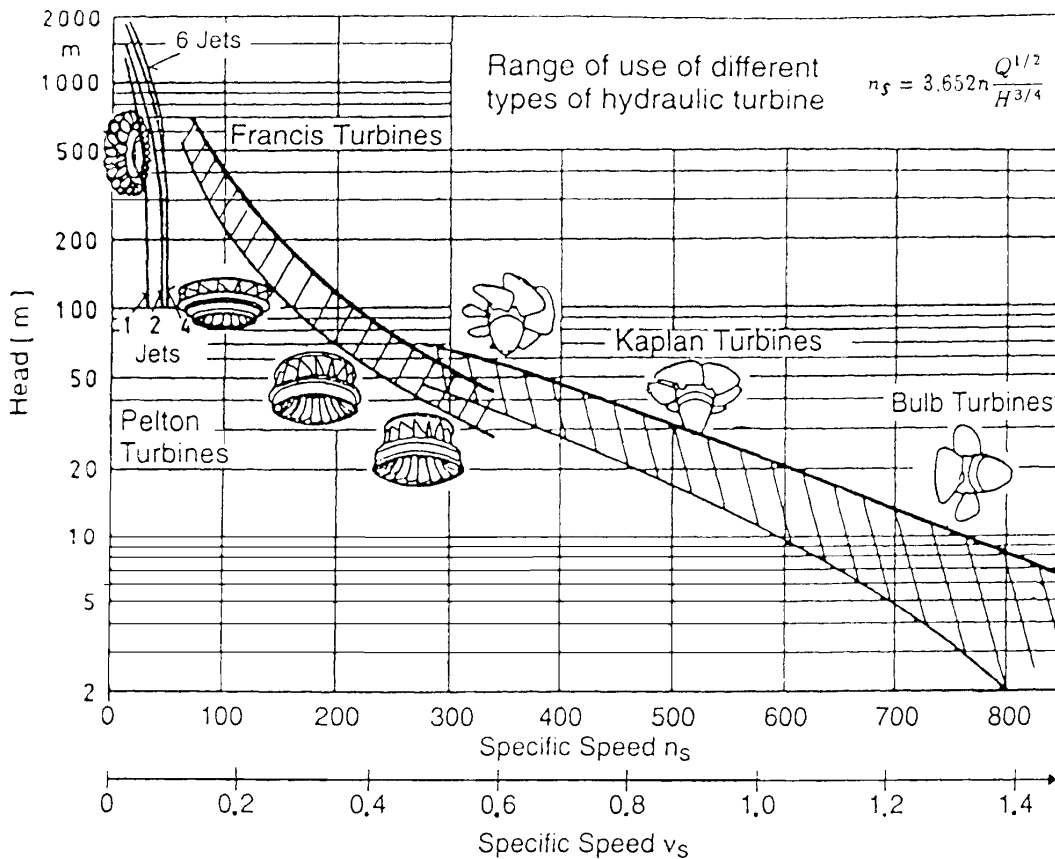


Fig. 4.1 (from [4.2])

In general, the number of runner vanes or buckets decreases with increasing specific speed, from about 26 to 18 in a Pelton wheel, from 19 to 11 in a Francis turbine, and from 7 to 3 in an axial turbine.

More details of the regimes of application of various hydraulic turbines are presented in figure 4.2. Apart from volume flows and head rise, this figure gives the generated absolute power output.

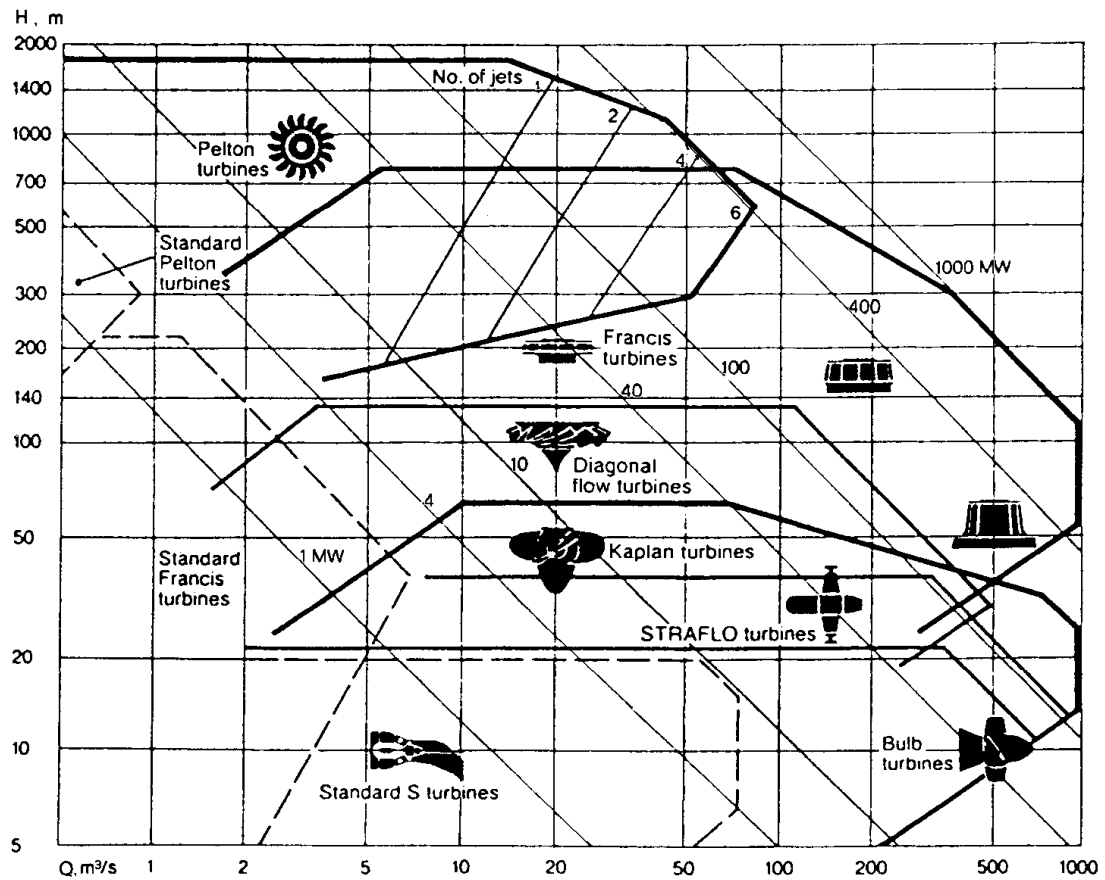


Fig. 4.2 (from [4.2])

4.3 Pelton Turbines

4.3.1 Design Features

The impulse turbine extracts energy from the water by first converting the available head into kinetic energy in the form of a high-speed jet discharged from the nozzle. The entire pressure drop occurs in the nozzle and the runner operates at constant static pressure. The Pelton turbine has zero reaction.

The jet is directed onto buckets fixed around the rim of a runner. Using more than one jet may increase the power of a given runner. The ratio of wheel diameter to jet diameter varies from 6 to 25. The buckets are positioned close together to avoid spillage, the number of buckets varying from 20 to 30 per wheel.

A cross-section through a typical vertical unit with six jets is shown in figure 4.3. Notice the deflecting mechanism and the jet used to brake the runner.

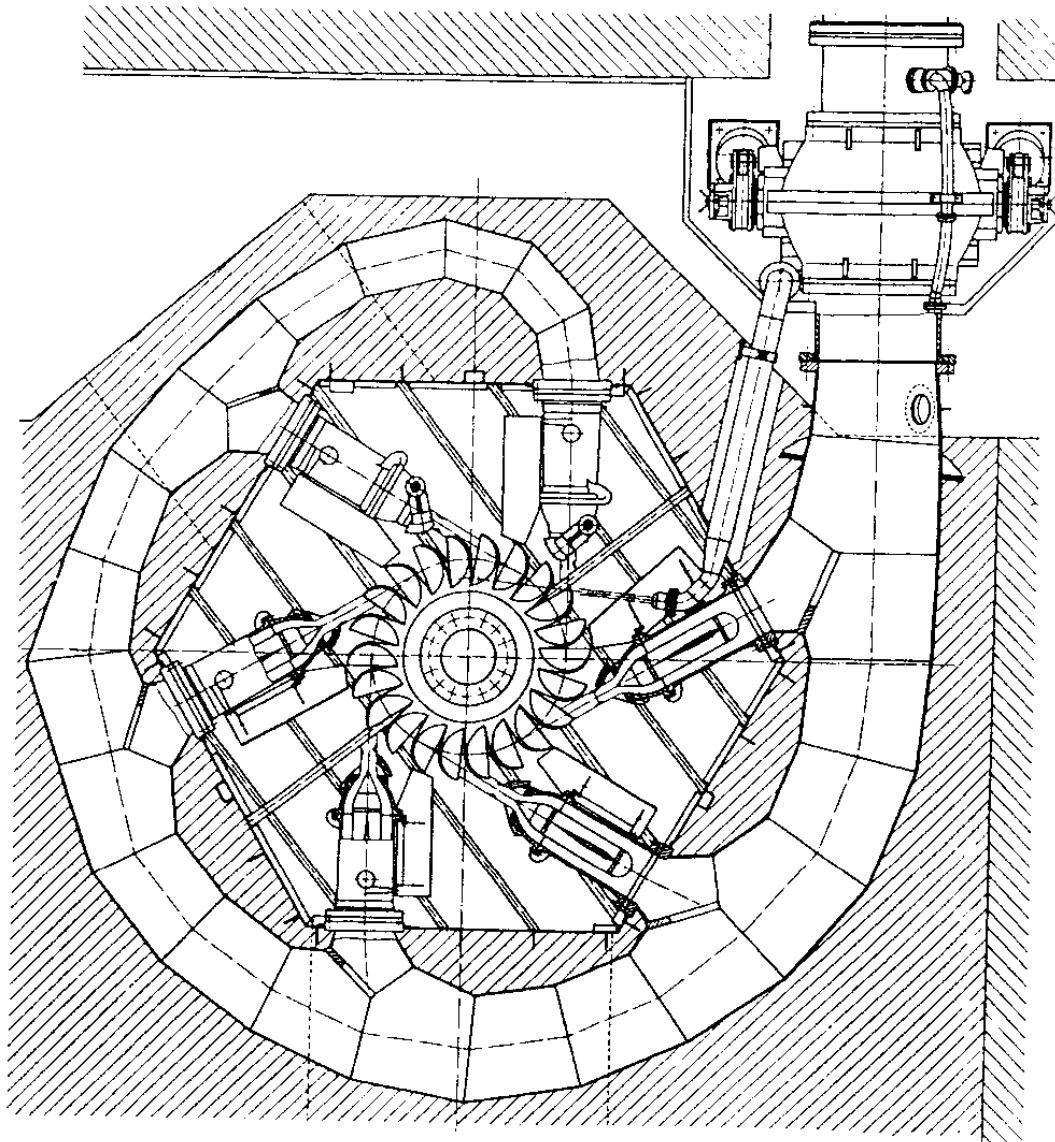


Fig. 4.3 (from [4.2])

Pelton turbines are used for large heads, $H = 2000$ to 300 m, small flow rates, specific speeds from 3 to 36 (60), with efficiencies of 92% and specific weights 30 N/kW.

In Romania, the Lotru Ciunget hydroelectric power plant has three Pelton turbines with six jets and 20 buckets, nominal speed 375 rpm, a gross head of 730 m, nominal water flow 26.6 m³/s and total rated power 174 MW.

4.3.2 Turbine-Generator Rotor Model

The underground Bieudron hydropower plant (Valais, Switzerland) has a maximum gross head of 1883 m (largest in the world), Pelton turbines of 420 MW and three-phase synchronous generators of 465 MVA. Having 14 poles, hence a per-pole rating of 33.2 MVA, they are also unique in the world [4.3].

The Pelton turbines have 5 nozzles, water flow $25 \text{ m}^3/\text{s}$, water velocity at nozzle outlet 690 km/h , weight 28 t, diameter 4.65 m, nominal speed 428.6 rpm, runaway speed 800 rpm.

A simplified model of the runner is shown in figure 4.4.

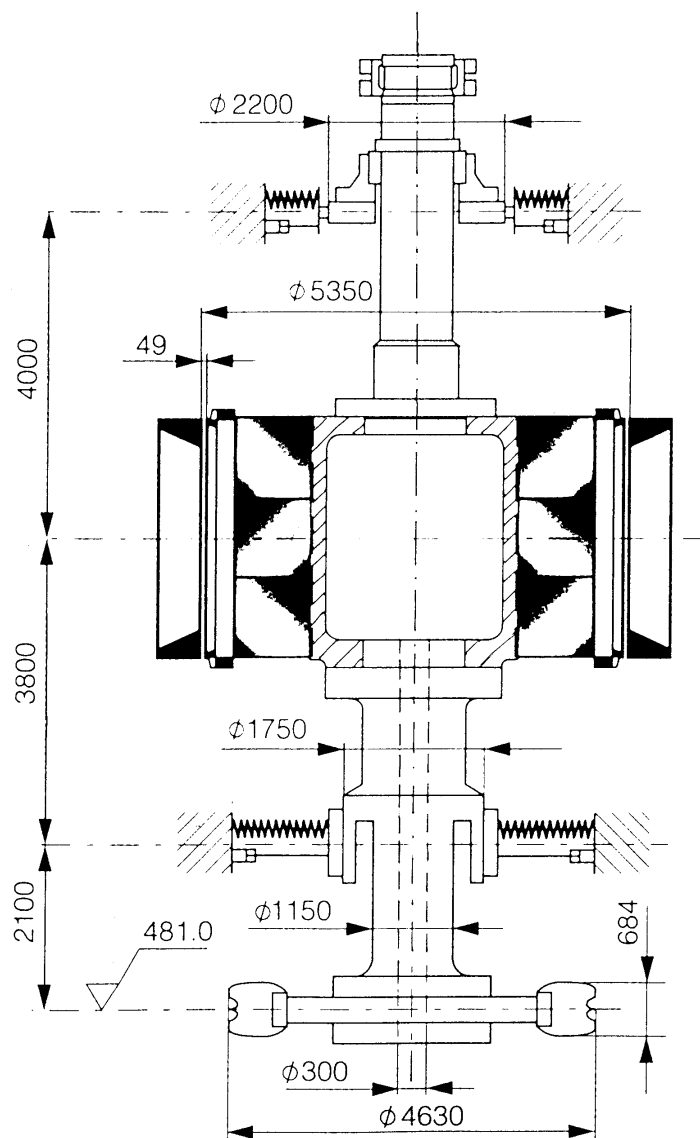


Fig. 4.4 (from [4.3])

Note the small overall height of the machine (only 10 m) imposed by the installation in a cavern of 40 m height. The hydroelectric set has only two guide bearings (while machines with power ratings above 300 MVA have generally three radial bearings). Also, since the weight of the rotating parts (454 tons) does not exceed 600 tons, the axial bearing above the generator stator is designed as a combined guide and thrust bearing.

The rotating train is designed as a three-section rotor, in which the central rotor body is flanged between two shaft ends.

The guide bearings are mounted in an oblique-arm bearing spider. This support ensures a constant bearing clearance during the transition from the cold to the hot state, despite the temperature-related expansion of the arms [4.4]. Thus, no additional compressive forces are exerted on the foundation by temperature variations.

Physical limitations made it impossible to place the lowest critical bending speed above the runaway speed (~ 800 rpm) as in other turbines. For bearing flexibilities 0.5 to 0.7 mm/MN this speed is about 600 rpm, i.e. it was selected to lie with a good margin of safety above the maximum overspeed (~ 500 rpm).

The model from figure 4.4 has been used to compute the dynamic response to disturbances produced by a) residual unbalance, b) one-sided magnetic pull in the generator, c) rotor double earth fault and rapid de-excitation, d) two-pole synchronizing failure, and e) stator two-phase terminal short circuit.

4.3.3 Computation Example

Figure 4.5 illustrates the structural dynamics model of a Pelton hydraulic group [4.5]. Relevant parameters are the following: turbine rotor mass 3500 kg, turbine rotor polar mass moment of inertia 1350 kgm^2 , fan rotor mass 1235 kg, fan moment of inertia 1104 kgm^2 , generator rotor mass 9450 kg, generator rotor moment of inertia 4281 kgm^2 , exciter rotor mass 500 kg, exciter rotor moment of inertia 31 kgm^2 . Calculations have been carried out for constant bearing stiffness

10^9 N/m. The shaft has been modeled with 90 finite elements, considering Young's modulus 210 GPa, Poisson's ratio 0.27 and shaft mass density 7850 kg/m^3 .

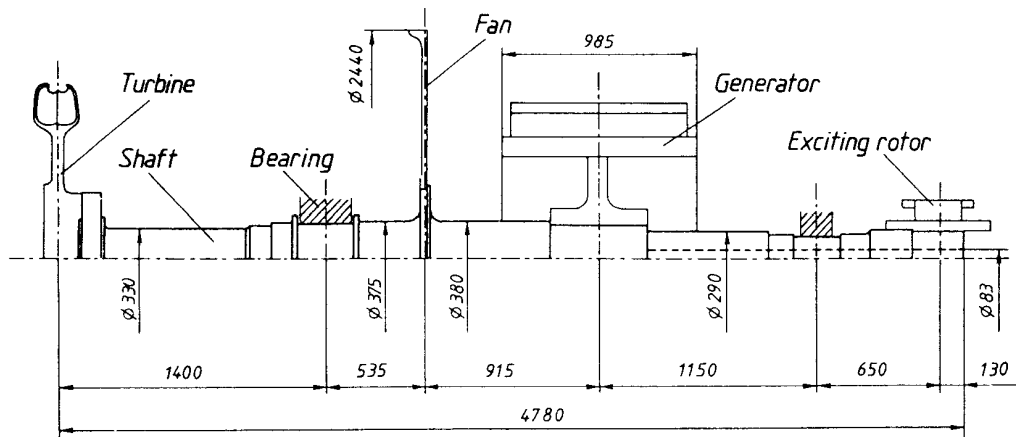


Fig. 4.5 (from [4.5])

The Campbell diagram is shown in figure 4.6. At 1000 rpm spin rate the computed first six natural frequencies are 15.457, 18.589, 30.282, 31.168, 60.730 and 62.735 Hz.

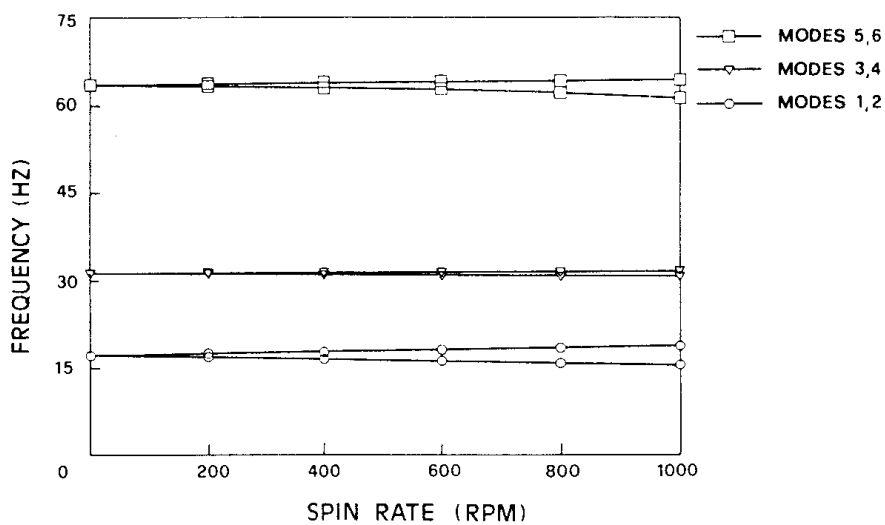


Fig. 4.6 (from [4.5])

Magnetic interactions between stator and rotor as well as speed- and load-dependent bearing coefficients have been neglected.

4.4 Francis Turbines

4.4.1 Design Features

The Francis turbine is a radial-flow reaction machine, much like a centrifugal pump with the flow direction reversed.

Modern Francis turbines have purely radial inlet flow through stationary guide vanes, but the runners are mixed flow devices with a component of the flow in the axial direction. The trend from purely radial inflow device through mixed flow devices to near axial flow devices increases as the specific speed is increased.

The flow channel of a modern Francis turbine with a vertical axis (Fig.4.7) comprises 1 - a spiral inlet case, 2 - stay vanes, 3 - guide vanes, 4 - runner, and 5 - draft tube.

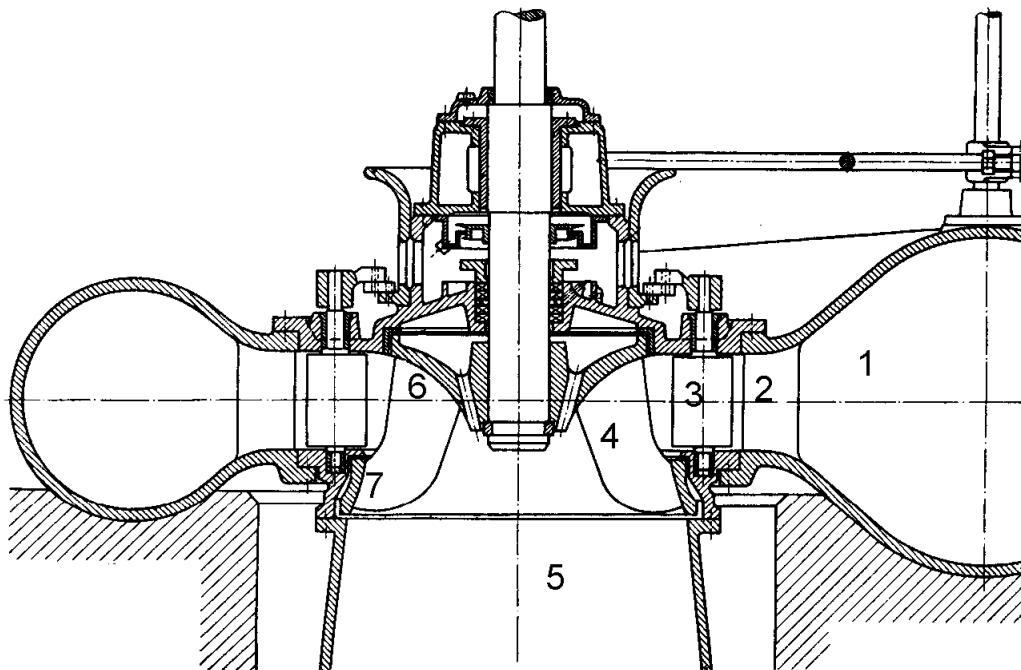


Fig. 4.7

The spiral case 1 is designed such that the velocity distribution in the circumferential direction at the inlet to the stay vanes is uniform and the incidence angle over the height of the stay vanes varies only little. The main function of the stay vanes 2 is to carry the pressure loads in the spiral case and turbine head cover. Their second purpose

is to direct the flow towards adjustable guide vanes 3 with an optimal incidence angle. The adjustable guide vanes are the only device available to control the flow and thus the power output of a Francis turbine.

The runner 4 consists of a crown 6 and a band 7 supporting highly curved blades. To reduce the leakage flow between the runner and the casing, labyrinth seals are provided at the crown and band. The diffuser 5 downstream the runner is usually an elbow-type draft tube, similar to that of Kaplan turbines, used to reduce the exit velocity from the system, improving overall efficiency. The vortices in the draft tube at off-design conditions often give rise to severe vibrations.

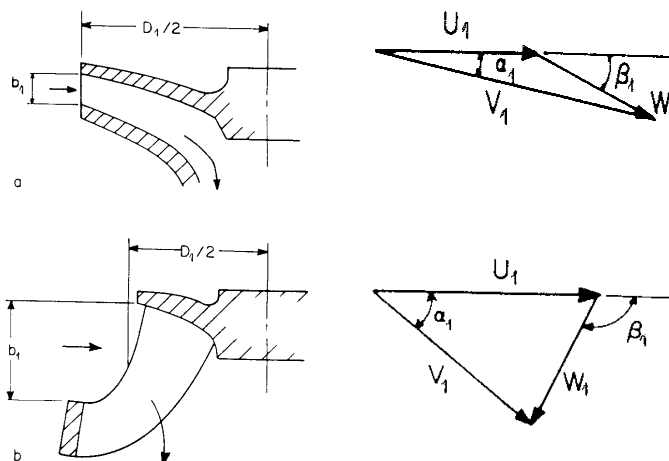


Fig. 4.8

Figure 4.8 illustrates differences in vane design arising from differences in the specific speeds of Francis runners. Low specific speeds imply low flow rates, which result in a smaller axial width b_1 and angle α_1 , as well as a smaller exit diameter at the base of the rotor. Water leaves the high- n_s vane with a large axial component (Fig. 4.8,*b*), in contrast to the large radial component present at the vane exit of a low-specific-speed runner (Fig. 4.8,*a*). The inlet vane angle β_1 is also increased and can be as much as 135° . The lower edge of the high- n_s vane must be twisted to provide axial discharge velocities at varying blade speed. The rotor exit diameter is as large as, or larger than, the mean inlet diameter, to accommodate the higher flow rate associated with larger values of n_s .

Francis turbines are optimally used for medium heads, $H = 70$ to 450 m, and medium flow rates, specific speeds 60 to 350, efficiencies 94% and specific weights 35 to 70 N/kW.

The Corbeni-ARGEŞ hydroelectric power plant has four Francis turbines with nominal speed 428.6 rpm, gross head 250 m, nominal water flow $20 \text{ m}^3/\text{s}$ and individual rated power 50 MW.

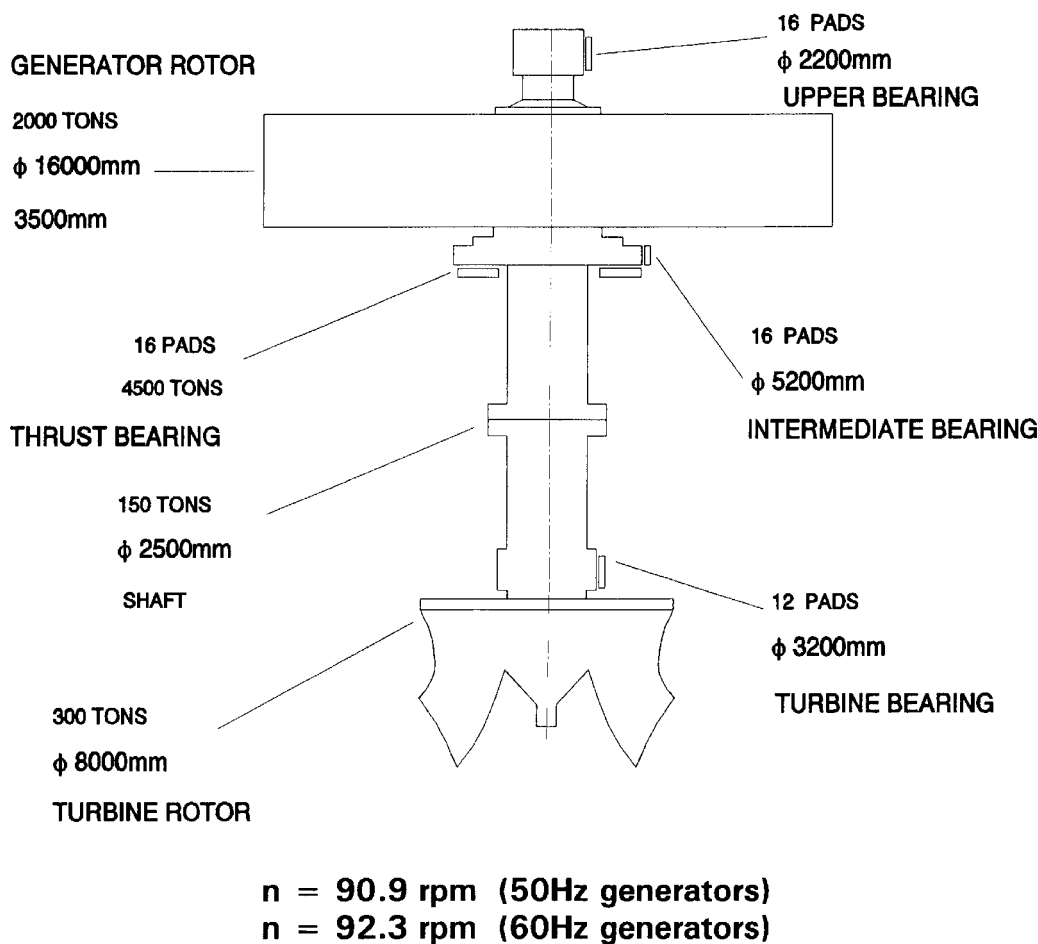


Fig. 4.9

The world's largest hydroelectric plant Itaipu, on the river Rio Paraná, which forms the border between Brazil and Paraguay, near the city of Foz do Iguaçu, consists of 18 generating sets of 824/737 MVA, driven by Francis turbines, with a total rating of 12,600 MW. Turbines have rotors of 300 tons and 8 m diameter, the main shaft has 150 tons and 2.5 m diameter, while the synchronous generator has 2000 tons

and 16 m diameter, running at respectively 90.9 rpm for 50 Hz generators, and 92.3 rpm for 60 Hz generators (Fig. 4.9).

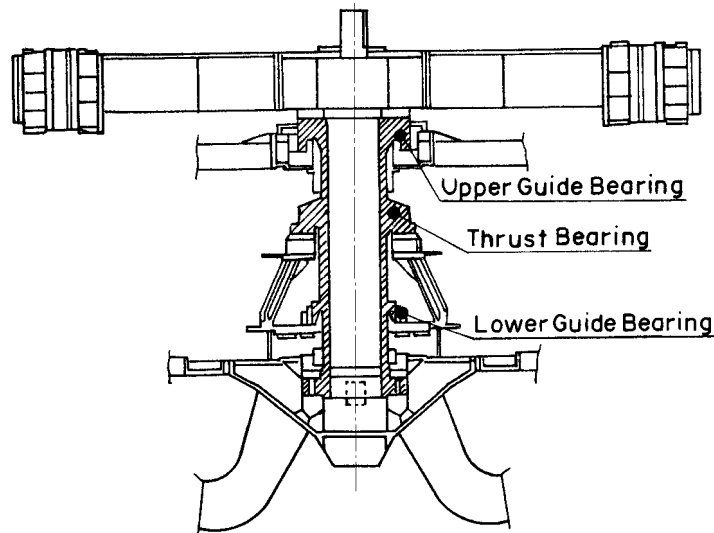


Fig. 4.10 (from [4.6])

The hydroelectric power plant at Ilha Solteira, Brazil, has sets of 160 MW at 85.8 rpm (Fig. 4.10). The vertical distance between generator and turbine is 6.33 m, The shaft has 1.3 m outer diameter and 0.4 m inner diameter. The generator has 495 tons and diameter 13.2 m. The Francis turbine has 145 tons and 12 blades. The first critical speed is about 222 rpm. The effective water head is 46 m, the flow rate is 389.7 m³/s.

4.4.2 Turbine-Generator Rotor Model

The dynamic model of the hydrogenerator from figure 4.10 as presented in [4.6] is shown in figure 4.11.

The hollow shaft is modelled by Timoshenko beam finite elements, with 0.4 m inner diameter, 1.3 m outer diameter, bending rigidity $EI = 2.87 \cdot 10^{10} \text{ Nm}^2$, mass density 7850 kg/m³. The thrust bearing is modelled as a rotational stiffness $K_t = 10^8 \text{ N/rad}$ (not shown). The parameters of the upper and lower guide bearings are their masses $M_u = 0.27 \cdot 10^5 \text{ kg}$, $M_l = 0.3 \cdot 10^5 \text{ kg}$, a linear-elastic oil film

stiffness $K_f=2.2 \cdot 10^{11}$ N/m, and structure stiffnesses $K_u=1.29 \cdot 10^9$ N/m, $K_\ell=0.5 \cdot 10^9$ N/m. All supports are isotropic.

The blade vibrations of the Francis turbine are represented as a mass-spring system $M_b=0.35 \cdot 10^5$ kg, $K_b=5 \cdot 10^9$ N/m, with M_b as a certain fraction (25%) of the total mass inside the turbine which contributes to the blade vibrations. Hydraulic effects between turbine blades and the housing are modelled by a spring $K_h=1.1 \cdot 10^9$ N/m.

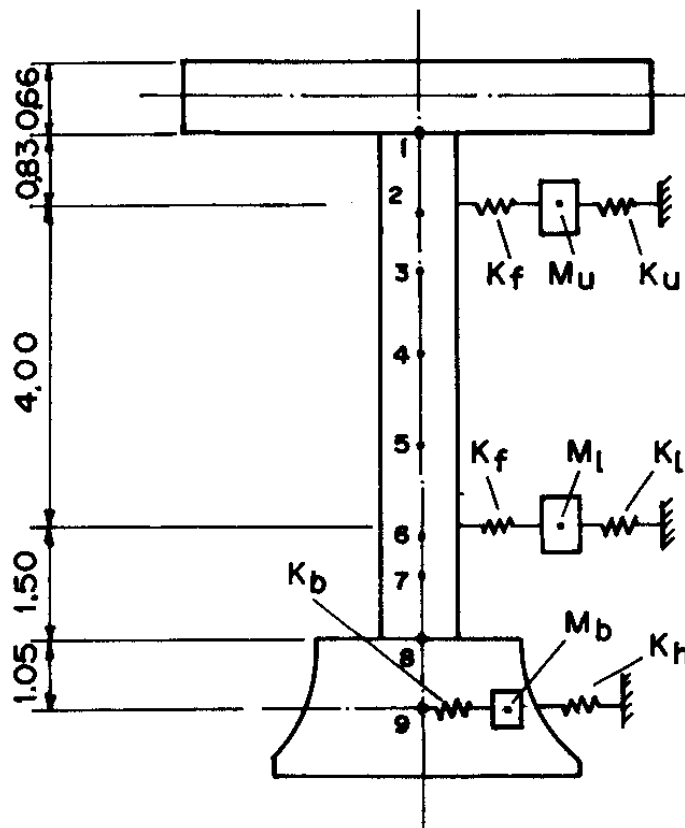


Fig. 4.11 (from [4.6])

The generator is modelled as a rigid disc with mass $4.95 \cdot 10^5$ kg and polar mass moment of inertia $7 \cdot 10^6$ kgm². The magnetic pull is considered by a negative stiffness $K_m = -0.55 \cdot 10^9$ N/m (not shown). The turbine rotor, also modelled as a rigid disc, has a mass $1.45 \cdot 10^5$ kg and polar mass moment of inertia $0.65 \cdot 10^6$ kgm². The water which flows through the turbine ($V \cong 140$ m³) contributes to its overall mass and moment of inertia resulting in a total mass of $2.85 \cdot 10^5$ kg and a total polar moment of inertia $1.11 \cdot 10^6$ kgm².

The calculated first four natural frequencies are 3.8, 9.0, 11.0 and 24.2 Hz, well above the nominal rotational frequency of the runner 1.43 Hz.

Parametric studies have shown that for the first flexural critical speed, the radial bearing flexibilities and the magnetic pull are the determining factors. While masses and polar mass moments of inertia for turbine and generator can be obtained from the manufacturer, the diametral mass moment of inertia is difficult to determine. The effect of water on the turbine blades has to be investigated. The proportion of 25% from the total mass in the turbine added to the runner is rather arbitrary.

4.4.3 Computation Examples

Figure 4.12 illustrates the structural dynamics model of a three-bearing Francis hydraulic group [4.7].

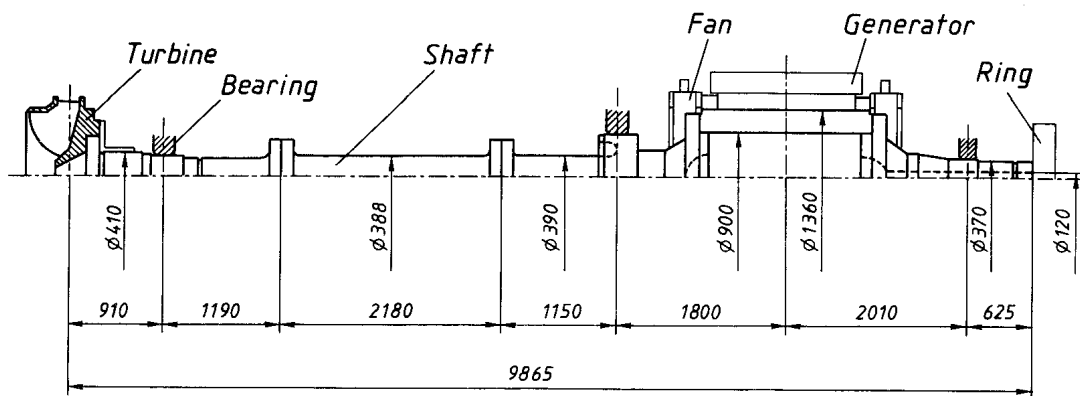


Fig. 4.12 (from [4.7])

Relevant parameters are the following: turbine rotor mass 2500 kg, turbine rotor polar mass moment of inertia 850 kgm^2 , fan rotor mass 1650 kg, fan moment of inertia 950 kgm^2 , generator rotor mass 17,500 kg, generator rotor moment of inertia $15,000 \text{ kgm}^2$, ring mass 1500 kg, ring moment of inertia 350 kgm^2 . Calculations have been carried out for constant bearing stiffnesses of $1.5 \cdot 10^9 \text{ N/m}$. This corresponds to a flexibility of $0.67 \text{ } \mu\text{m/kN}$, which is a good practical approximation.

The shaft was modeled with 55 beam finite elements, considering Young's modulus 210 GPa, Poisson's ratio 0.27 and shaft mass density 7850 kg/m³.

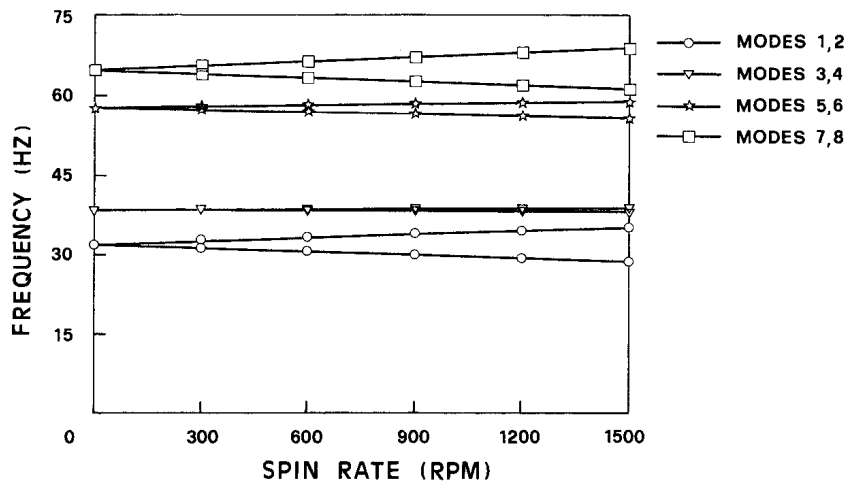


Fig. 4.13 (from [4.7])

The Campbell diagram is shown in figure 4.13. At 900 rpm spin rate the calculated first eight natural frequencies are 29.86, 33.83, 38.33, 38.67, 56.65, 58.40, 62.67 and 67.31 Hz.

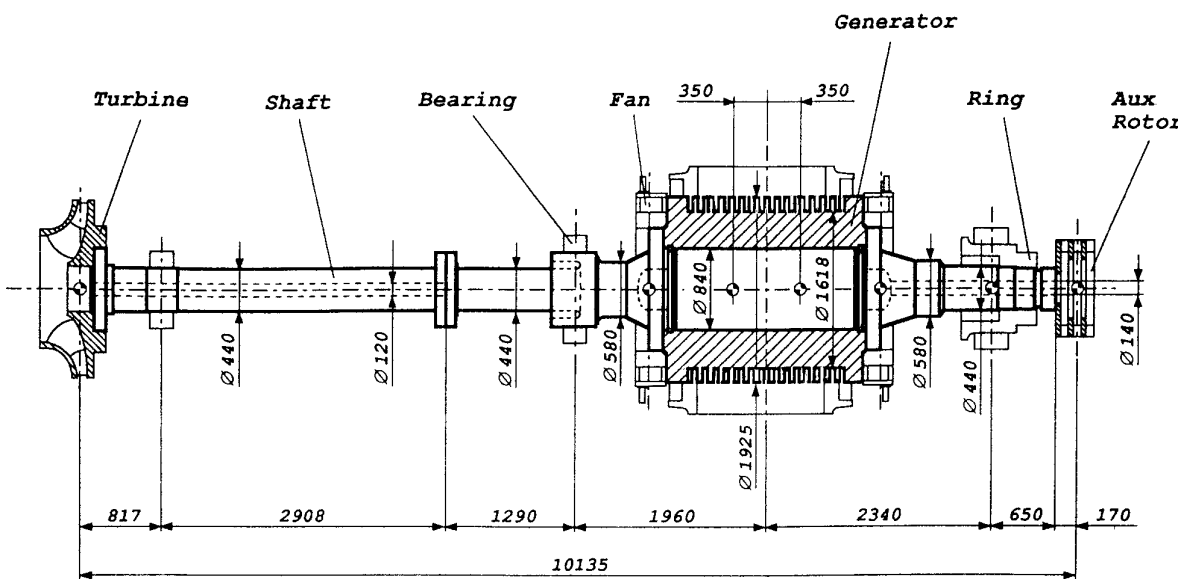


Fig. 4.14 (from [4.8])

A slightly different model is shown in figure 4.14 [4.8]. Relevant parameters are the following: turbine rotor mass 3600 kg, turbine rotor polar mass moment of inertia 1360 kgm^2 , front/rear fan rotor mass 1260/880 kg, front/rear fan moment of inertia $862.5/777.5 \text{ kgm}^2$, generator rotor (2) masses 13,100 kg each, generator rotor (2) moments of inertia $14,500 \text{ kgm}^2$ each, ring mass 1980 kg, ring moment of inertia 250 kgm^2 , auxiliary rotor mass 835 kg, auxiliary rotor moment of inertia 159 kgm^2 .

The front, middle and rear journal bearings have stiffnesses $0.3 \cdot 10^9$, $1.3 \cdot 10^9$ and $0.9 \cdot 10^9 \text{ N/m}$ respectively and damping factors $1.0 \cdot 10^3$, $5.0 \cdot 10^3$ and $2.5 \cdot 10^3 \text{ Ns/m}$. The internal viscous and hysteretic damping factors are $5.0 \cdot 10^{-4} \text{ sec}$ and $1.0 \cdot 10^{-3}$.

The shaft is discretized into 72 shaft cubic elements. The first six natural frequencies computed at 1000 rpm are 24.443, 24.634, 25.844, 27.348, 42.481 and 48.121 Hz.

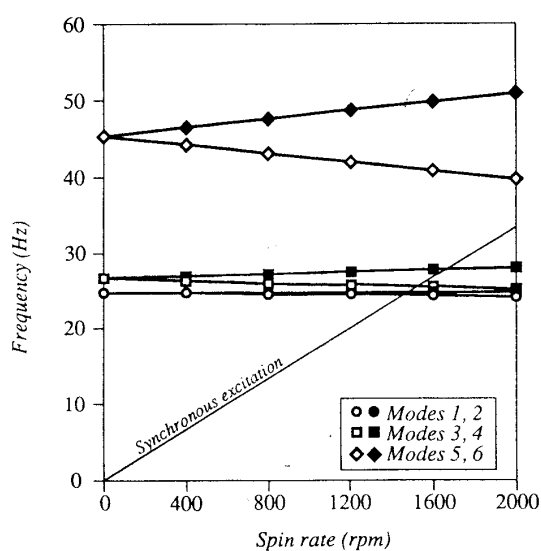


Fig. 4.15 (from [4.8])

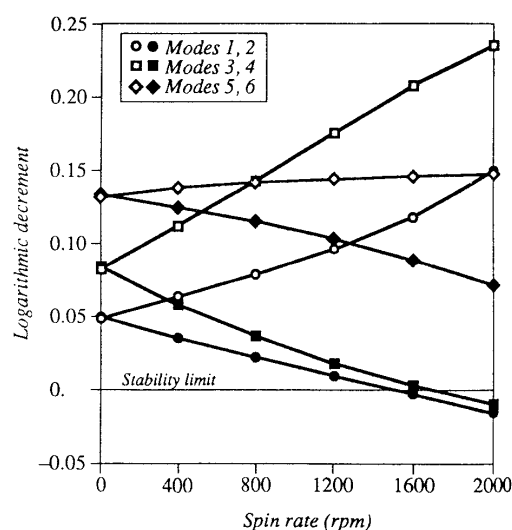


Fig. 4.16 (from [4.8])

The Campbell diagram is shown in figure 4.15 and the logarithmic decrement diagram is depicted in figure 4.16. It is seen that the first forward mode becomes unstable from 1500 rpm upwards.

4.5 Kaplan Turbines

4.5.1 Design Features

Axial turbines are made in different concepts. The most flexible in terms of variation of flowrate and turbine head is the double-regulated turbine with adjustable stator and rotor blades (Fig. 4.17), the so-called full Kaplan concept.

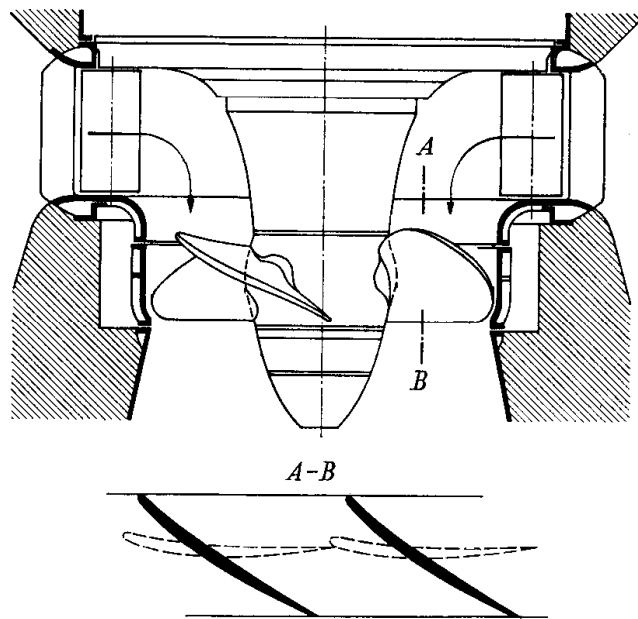


Fig. 4.17

Cheaper but not so flexible concepts are designed as single-regulated turbines. The fixed blade propeller turbine has adjustable stator blades but fixed runner blades. In the so-called semi-Kaplan concept, fixed stator blades and adjustable rotor blades are used.

For classical vertical Kaplan turbines, the inflow and the outflow of the stator is radial, while the inflow and the outflow of the runner is fully axial. In general, steel scroll cases are used for heads between 30 and 60 m, and concrete semispiral casings for heads between 10 and 40 m.

Usually, the blade profiles are different at the root section (large camber and thickness) and at the tip section (small camber and thickness).

An axial cross-section of a vertical axis Kaplan turbine is presented in figure 4.18 where 1 – runner with adjustable blades, 2 – draft tube, 3 – guide vanes, 4 – lower guide bearing, 5 – stay vanes and ring support, 6 – concrete spiral casing, 7 – control ring with servo-motor for the stay vanes, 8 – thrust bearing, 9 – upper guide bearing, 10 – servo-motor for adjustment of runner blades, 11 – runner blades control rod inside the turbine shaft, and 12 – generator.

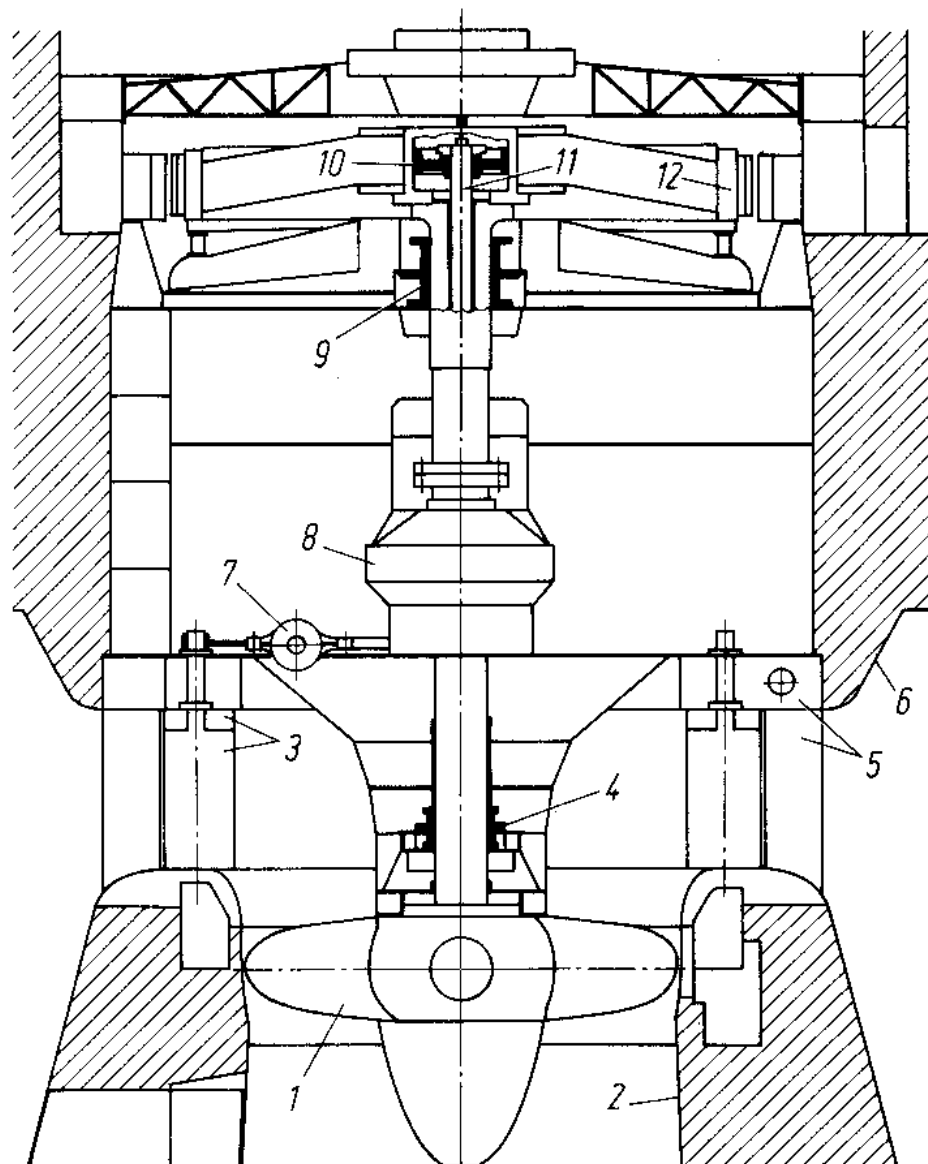


Fig. 4.18 (from [4.17])

A schematic view of a Kaplan runner with a combined guide and thrust bearing is shown in figure 4.19.

Kaplan turbines are efficiently used for low heads 10 to 50 (75) m, very high flow rates up to $800 \text{ m}^3/\text{s}$, specific speeds 300 to 900, specific weights 75 to 140 N/kW and efficiencies 93-93.5%.

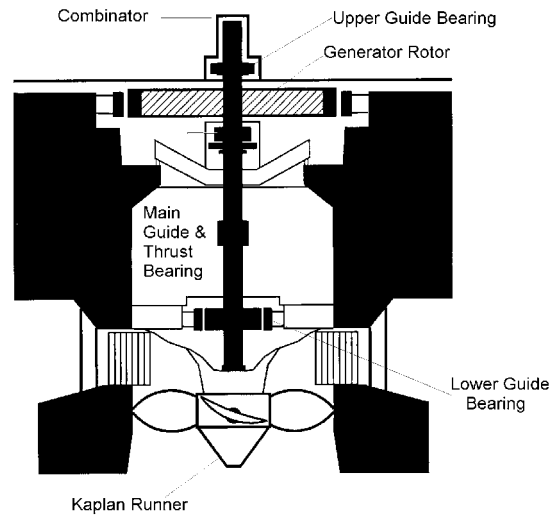


Fig. 4.19

The *Portile de Fier I* hydroelectric power plant has eight Kaplan turbines of 194 MW, head 27 m, nominal water flow $840 \text{ m}^3/\text{s}$, speed 71.43 rpm, 6 blades and rotor diameter 9.5 m.

4.5.2 Computation Examples

Figure 4.21 illustrates the finite element model of the rotating shaft of a Kaplan turbine shown in figure 4.20 [4.9].

The turbine and the generator are modelled by two rigid discs. The shaft is divided into 32 shaft finite elements with four degrees of freedom per node. The three bearings are considered isotropic.

Stiffnesses of bearings 1 and 2 are $0.5 \cdot 10^9 \text{ N/m}$ while bearing 3 has a stiffness $0.1 \cdot 10^{10} \text{ N/m}$. The shaft Young's modulus 210 GPa, Poisson's ratio 0.27 and mass density 7850 kg/m^3 . For discs, turbine mass is 8000 kg, turbine polar mass moment of inertia is 1840 kgm^2 ,

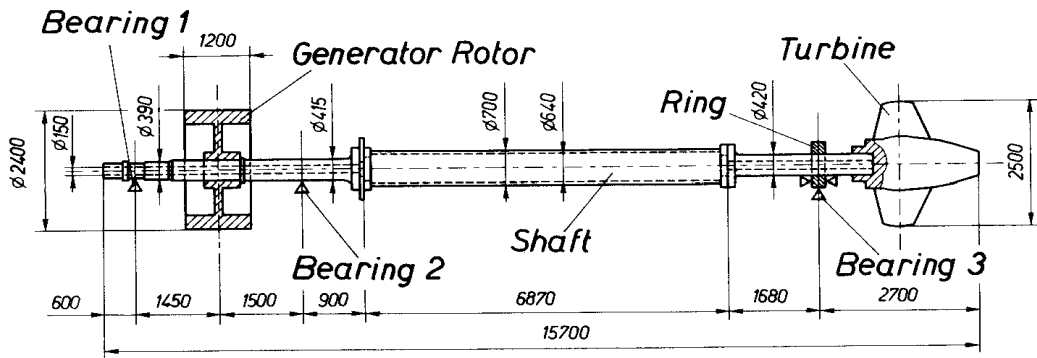


Fig. 4.20 (from [4.9])

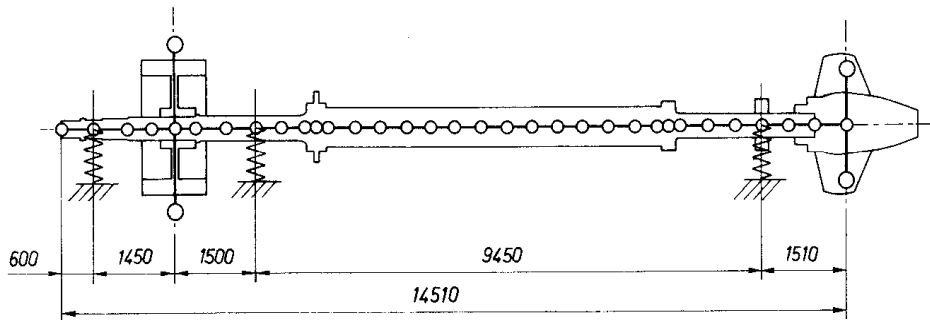


Fig. 4.21 (from [4.9])

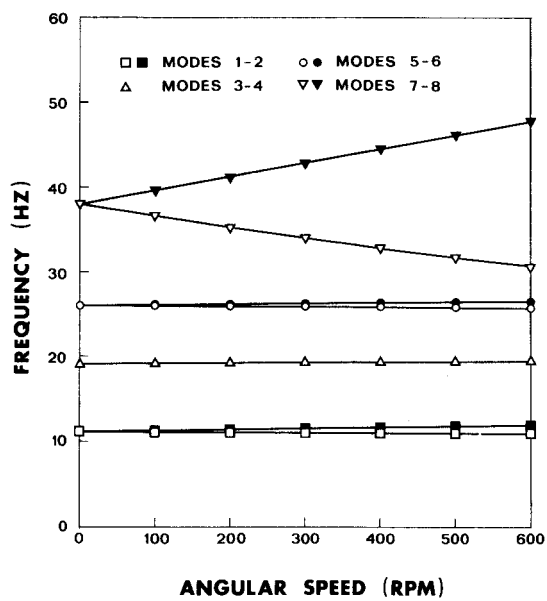


Fig. 4.22 (from [4.9])

generator rotor mass 20980 kg, generator rotor moment of inertia 21330 kgm^2 ; mass of ring at bearing 3 is 910 kg.

The discrete model takes into account the shear deformations, the rotatory inertia of the shaft elements and the gyroscopic effects of the discs and the shaft. The Campbell diagram for the lowest eight modes of precession is shown in figure 4.22. At 300 rpm, the calculated eigenfrequencies are 11.361, 11.801, 19.467, 19.482, 26.130, 26.453, 34.153 and 42.957 Hz. It can be seen that the gyroscopic effects are negligible for the first three pairs of modes, for which the shaft behaves as a rigid body.

Figure 4.23 illustrates the runner of a vertical Kaplan turbine unit [4.10]. The shaft has three guide bearings and a separate thrust bearing dividing the shaft into two different parts.

Relevant parameters of components modelled as rigid discs are the following: turbine rotor mass 28500 kg, turbine rotor polar mass moment of inertia 15400 kgm^2 , middle ring mass 1000 kg, generator rotor part 1 mass 47,700 kg, generator rotor part 1 moment of inertia $49,800 \text{ kgm}^2$, generator rotor part 2 mass 45,700 kg, generator rotor part 2 moment of inertia $47,700 \text{ kgm}^2$, upper ring mass 1260 kg, auxiliary rotor mass 2400 kg.

The shaft is divided into 50 shaft finite elements and has Young's modulus 210 GPa, Poisson's ration 0.27 and mass density 7850 kg/m^3 . The internal viscous and hysteretic damping factors are assumed to be $5 \cdot 10^{-4}$ sec and $1.0 \cdot 10^{-3}$, respectively.

The hydrodynamic guide bearings are assumed to be isotropic with stiffness $0.5 \cdot 10^9 \text{ N/m}$ and damping coefficient $0.75 \cdot 10^5 \text{ Ns/m}$ for the outer bearings. The equivalent values for the inner bearing are, respectively, $0.75 \cdot 10^9 \text{ N/m}$ and $0.25 \cdot 10^6 \text{ Ns/m}$.

The Campbell diagram is shown in figure 4.24 and the logarithmic decrement diagram is shown in figure 4.25. It is seen that the first forward mode becomes unstable from 860 rpm upwards. At 600 rpm, the calculated eigenfrequencies are 9.589, 10.326, 14.757, 14.963, 20.696 and 28.384 Hz.

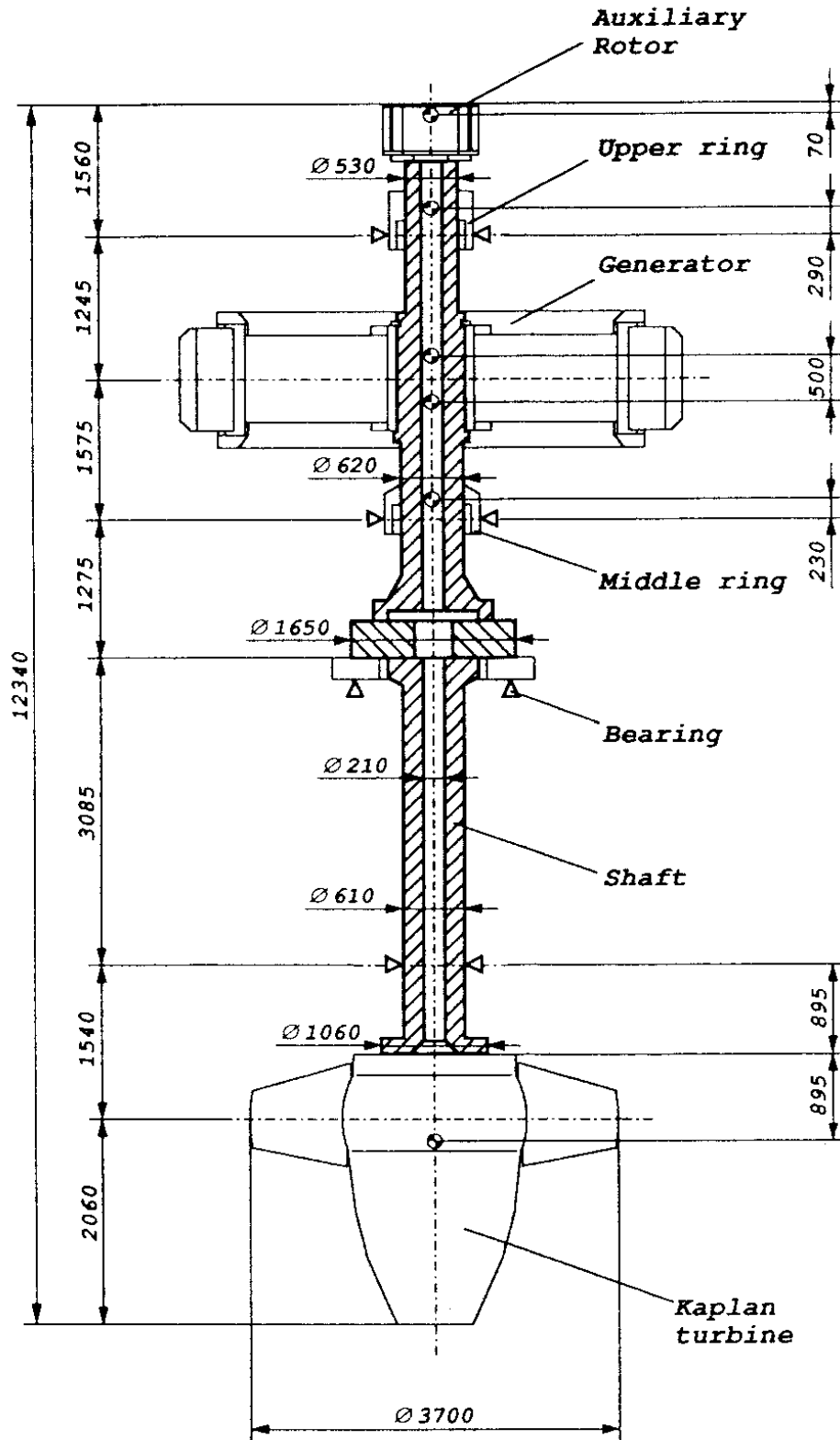


Fig. 4.23 (from [4.10])

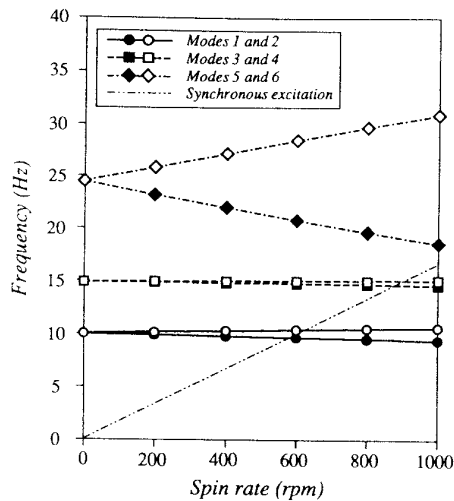


Fig. 4.24 (from [4.10])

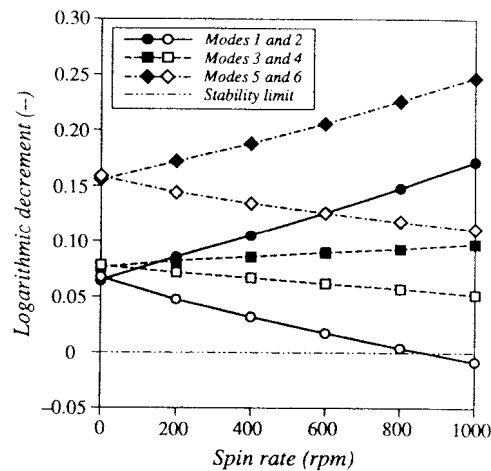


Fig. 4.25 (from [4.10])

Both calculation examples neglect important factors influencing the dynamic response of the turbine runner, such as the magnetic pull in the generator, the effect of entrained water in the turbine runner and the actual properties of radial hydrodynamic guide bearings. However they are instructive and give an idea on the order of magnitude of system parameters. There is no indication on the values of diametral mass moments of inertia of the rigid discs. No comparison with measured data is provided in the references.

4.6 Bulb and Straflo Turbines

For completeness of information, two more axial turbines are presented without any rotordynamic analysis.

The bulb turbines are designed for low pressures and high flow rates, with a horizontal axis. They have the advantage of a more or less straight flow path through the intake and draft tube. The friction losses are considerably lower in these components than in the spiral casing and elbow draft tube of the vertical Kaplan turbine.

In the Straflo (straight flow) turbine design, the generator and the turbine form an integral unit without a driving shaft. The turbine rotor blades are connected to an outer ring which directly carries the generator rotor poles.

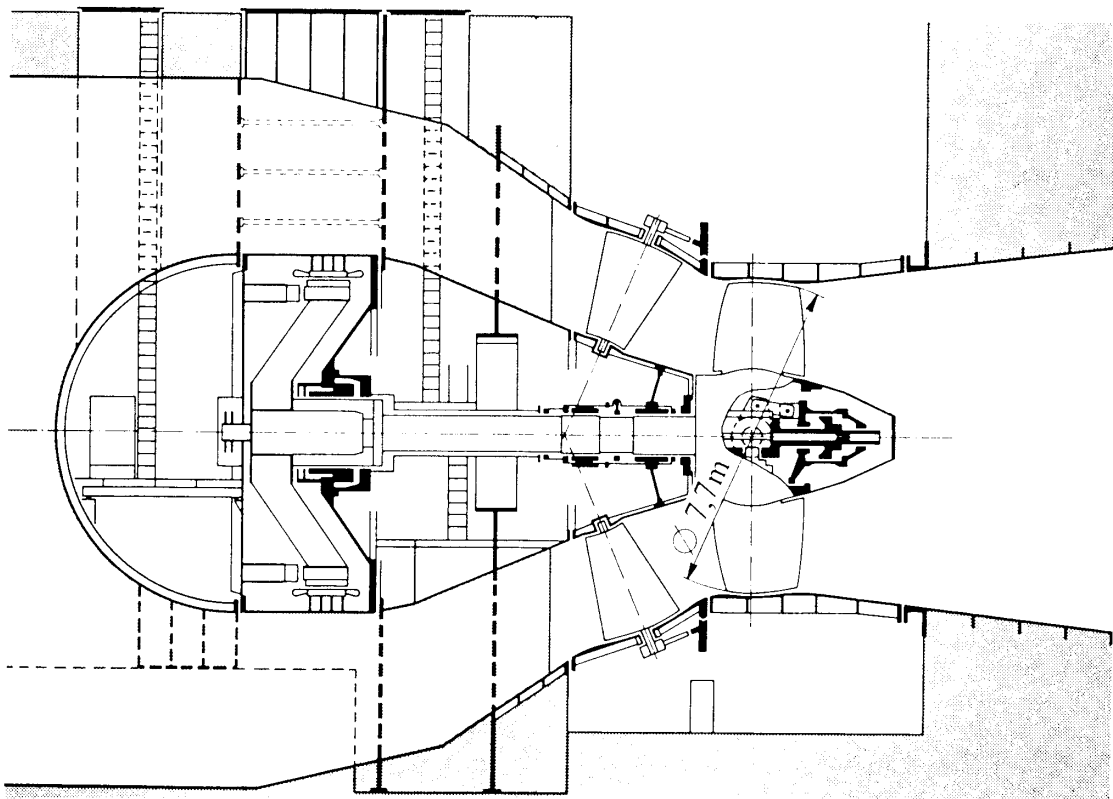


Fig. 4.26

Figure 4.26 shows a bulb turbine of 25 MW, head 6.5 m and 7.7 m rotor diameter, installed at Racine, USA. The generator, located in the middle of the bulb, extends over the whole cross-section.

The *Portile de Fier II* hydroelectric power plant has eight double-regulated bulb units type *KOT 28-7.45*, with the bulb upstream and the turbine overhung downstream. The unit has three guide bearings and a thrust bearing, 16 stator blades and 4 rotor blades, and the following parameters: head 7.45 m, nominal water flow $432 \text{ m}^3/\text{s}$, rated power 27 MW, rotor diameter 7.5 m.

Figure 4.27 shows a schematic diagram of the Straflo turbine installed in the river power station at Andenne, Belgium, on the river Maas. The three Straflo turbines with a diameter of 3.55 m each absorb 80 m^3 of water per second. They have a total rating of 10.2 MW and a speed of 107 rpm.

One can distinguish 1 - stay vanes, 2 - adjustable wicket gates, 3 - fixed-blade runner, and 4 - generator. The generator is arranged

directly around the runner periphery. In comparison with conventional turbines, where the generator or its drive is accommodated in a bulb surrounded by water, it offers advantages in respect to the overall dimensions, generator cooling and operating behaviour.

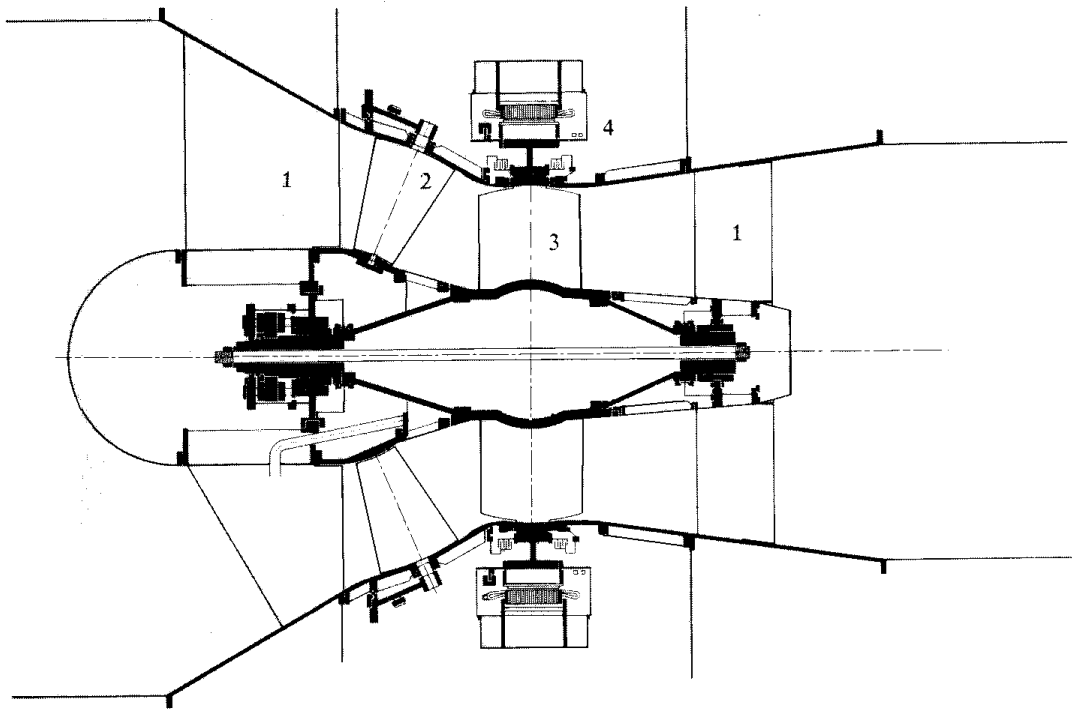


Fig. 4.27

The principle of the turbine with outer rim generator is about as old as the invention of the vertical Kaplan turbine.

4.7 Condition Monitoring of Hydropower Machines

Condition monitoring systems detect vibrations at an early stage and protect machines from consequential mechanical damage.

In order to determine the location of most suitable measurement points and the kind of sensors and signal analysis that is needed to detect the specified faults, information has to be collected about all the common mechanical faults.

A list of the most common faults encountered in hydromachines includes: 1) shaft misalignment; 2) loose brackets and bearing housings; 3) overloading of radial sleeve bearings; 4) wear in

bearings; 5) mechanical unbalance; 6) electrical instability; 7) misshapen rotors; 8) misaligned or misshapen stators; 9) incorrect airgaps; 10) excessive hydraulic load; 11) axial vibration (e.g. caused by Francis turbines at partial load); 12) lost stator core pressure; 13) vibration of coil ends; 14) rotor double-earth faults; 15) two-pole synchronizing failures; 16) two-phase terminal short circuits; 17) operation at inadmissible loads or speeds.

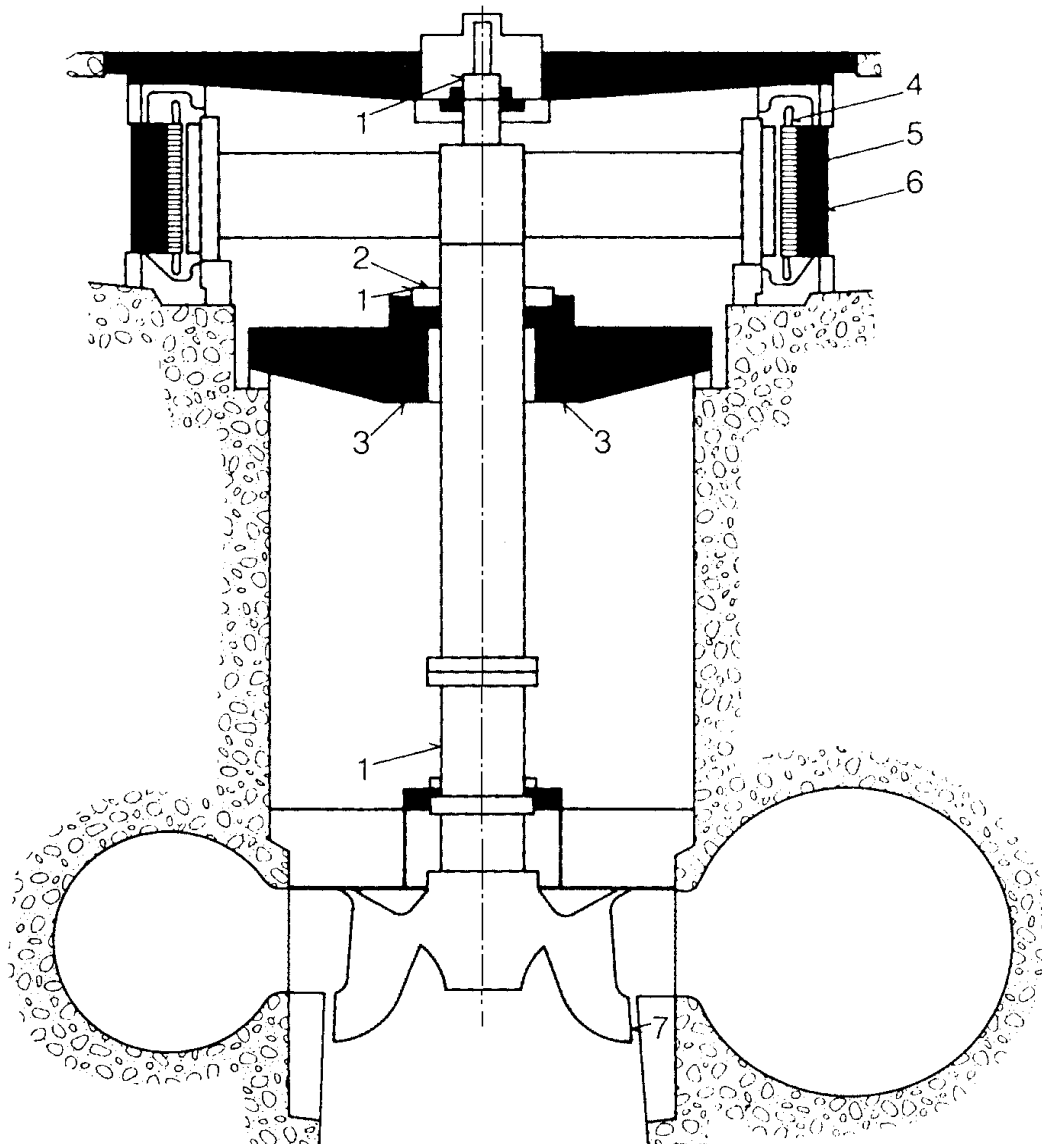


Fig. 4.28 (from [4.11])

To protect a machine from these faults, up to 10 vibration sensors have to be mounted on bearings, shafts, brackets and stator

frames, etc. and other up to 10 sensors are required to measure parameters such as temperature, oil pressure, airgap and load.

Placement of sensors using the *VIMOS* condition monitoring system developed by ABB [4.11] is illustrated in figure 4.28 where:

1 - proximity probes for X and Y directions in radial guide bearings to detect unbalances, rotor winding short-circuits, turbine and bearing problems;

2 - proximity probes in thrust bearing to detect water load, axial vibrations, wrong setting of turbine blade angle;

3 - proximity probes in thrust bearing bracket to detect water load and changes in bracket characteristics;

4 - accelerometers in coil ends to detect coil-end vibrations;

5 - accelerometers on stator core to detect changed core pressure and cracked wedge fixtures;

6 - proximity probes against stator frame to detect stator vibrations due to rotor shape errors, stator movement, changes in stator shape; and

7 - proximity probes on turbine to detect changes in runner clearance.

4.8 Guidelines for Vibration Limits

The standard *ISO 7919, Part 5* [4.12] lists the special features required for measuring shaft vibrations of coupled hydraulic sets. This standard applies to all types of hydraulic machines having nominal speeds between 60 and 3600 rpm, with fluid film bearings and rated powers of 1 MW or more.

The numerical values specified in figure 4.29 represent rotor displacements relative to bearings in micrometers peak-to-peak vs shaft rotational speed in rpm. Zone *A* represents new machines that can be operated without restriction; zone *B* is acceptable for long-term operation; zone *C* represents machines that may be operated for a limited time until a suitable opportunity arises for remedial action to be taken; and, zone *D* is identified as a trip level as these values are considered to be of sufficient severity to cause damage.

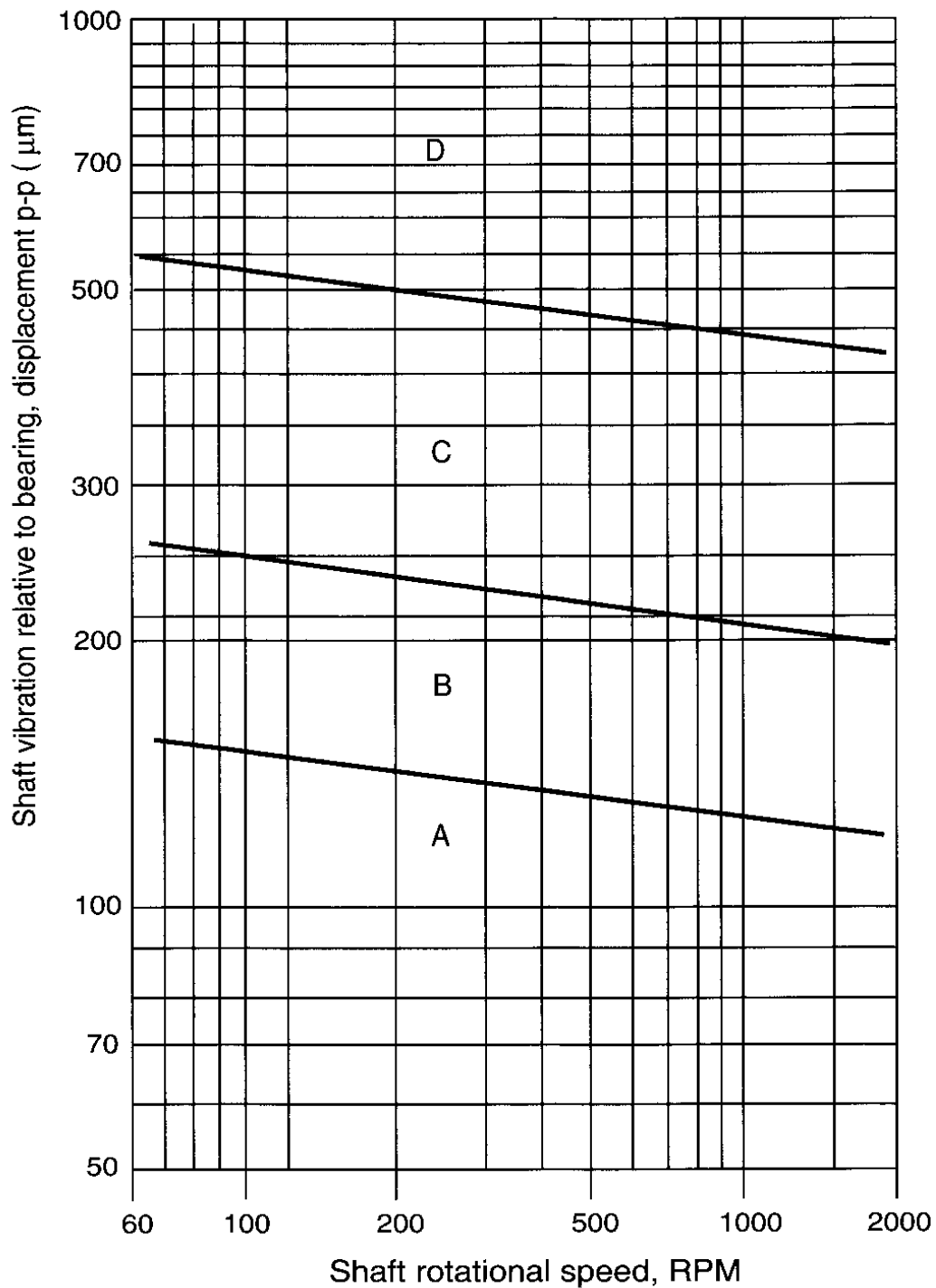


Fig. 4.29 (from [4.12])

In the case of hydraulic machines, the shaft motion seldom displays uniform circular or elliptic orbits. Under stationary operating conditions, the radial forces may lead to cycloidal or polygonal orbits, whose form and size vary statistically within certain limits. In contrast

to thermal turbomachines, here such orbits are not the result of instabilities in the oil film of bearings or self-excitation by clearance flow. At operation at off-design parameters, the radial forces increase strongly, especially during transient conditions.

In contrast to thermal machines, hydraulic machines are normally started up and shut down, or power can be changed quickly and frequently. Larger shaft motion during the transient period can occur at start-up, at each loading or unloading, and at each fill-up or emptying of the hydraulic machine. Such events can, at peak-load or pump-storage equipment, become so frequent that the sum of the time intervals of increased shaft motion amounts to more than 1‰ of the overall operating time.

The published limit curves show that the decrease in the shaft vibration amplitude is proportional to nearly $1/\sqrt{n}$, where n denotes the nominal speed of rotation of the machine. For hydromechanically less problematic turbine types, such as Pelton turbines and double-regulated Kaplan turbines, normally lower shaft vibrations must be expected than presented in figure 4.29.

The standard *ISO 10816, Part 5* [4.13] provides specific guidance for assessing the severity of vibrations measured on bearings, bearing pedestals, or housings of hydraulic machines when measured in situ. It applies to machine sets in hydraulic power generation, and pump plants where the hydraulic machines have speeds from 120 to 1800 rpm, shell- or shoe-type sleeve bearings, and main engine power of 1 MW or more. The position of the line shaft may be vertical, horizontal, or at an arbitrary angle between these two directions.

This Standard refers to turbines and generators, pumps, and electrical machines operating as motors, pump-turbines, and motor generators, including auxiliary equipment. The Standard also includes single turbines or pumps connected to generators or electric motors over gears and/or radially flexible couplings.

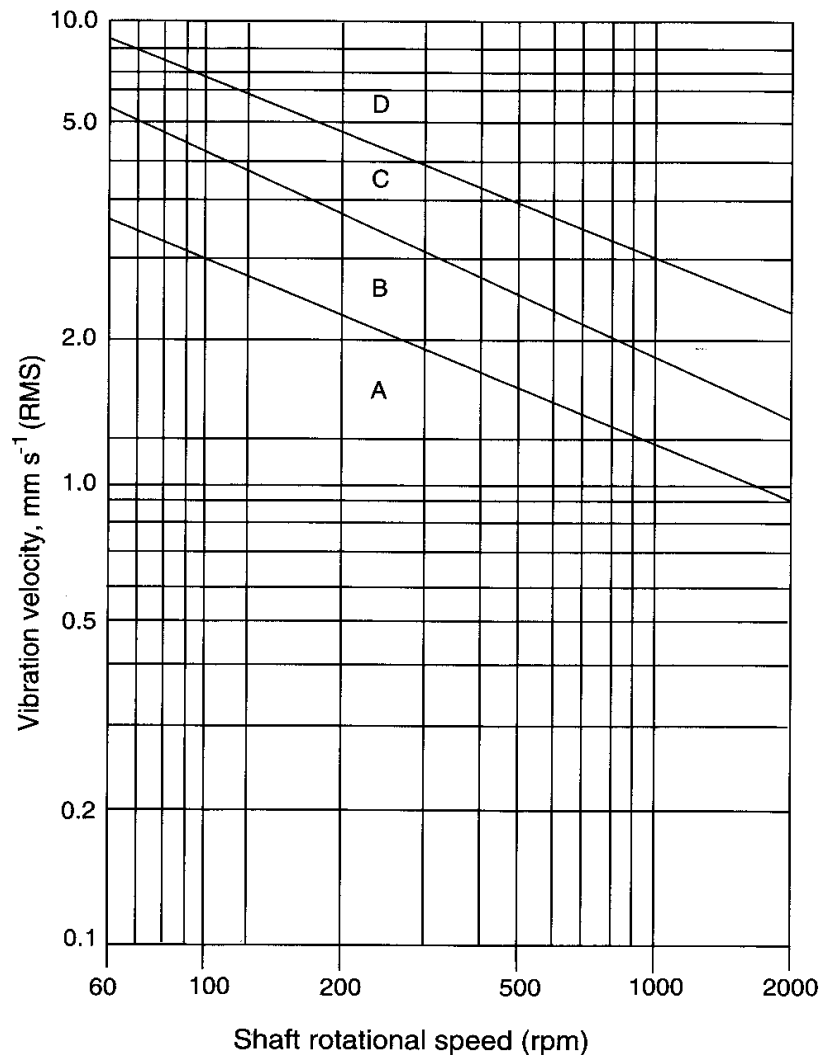


Fig. 4.30 (from [4.13])

The recommended criteria values, in mm/s RMS, vs shaft rotational speed, in rpm, for hydraulic machines with nominal power above 1 MW, and nominal speeds of 120 to 1800 rpm are shown in figure 4.30. The zone descriptions are the same as for figure 4.29.

4.9 Stator Supports for Vertical Generators

Large, vertical hydroelectric generators are mounted on radially flexible supports in order to reduce the thermal stresses and to safeguard the stator and foundations. During operation, the stator laminations become warmer than the casing and the central body of the upper bearing bracket becomes warmer than the foundation or the

stator casing. Compressive stresses occur in the arms and tangential tensile stresses in the foundation or stator casing. These can be relieved by using flexible elements or springs. Spring elements (spiral, Belleville and spring plates) however take up a large space and are expensive. This is particularly true when the short-circuit forces acting on the foundation must also be reduced by means of additional, tangentially acting springs. Skew arms, skew spokes and skew leaf springs patented by BBC provide an elegant solution to these difficulties [4.14].

The generator stator casing is attached to the foundation by a number of separate feet above the bottom ring. When operationally warm, the casing can expand as freely as possible and concentrically with respect to the air-gap, so that the stator core and the foundation are not subjected to additional compression forces.

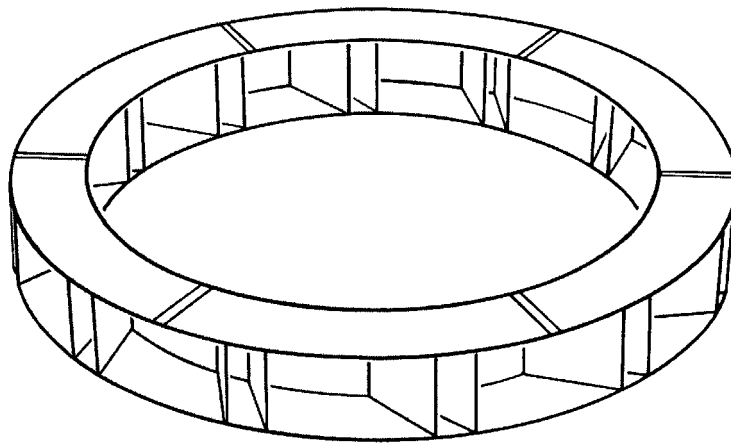


Fig. 4.31 (from [4.15])

The elastic design of the foot with inclined leaf springs converts the radial expansion of the stator into a rotary movement about its own axis. Since this design considerably reduces the forces exerted on the foundation in the event of a short circuit, and also acts against the asymmetrical displacement of the casing, it has significant advantages. From the builders' point of view this enables considerable savings to be made in the reinforcement of the foundations. Figure 4.31 shows a section of the bottom ring with sprung stator feet.

Guide bearings are supported by arms attached at an angle to the rigid central body (Fig. 4.32).

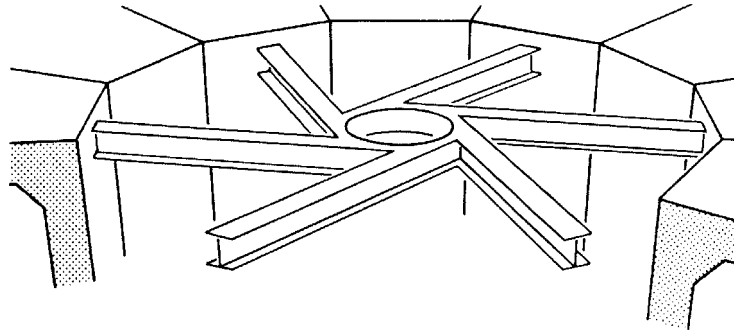


Fig. 4.32 (from [4.15])

The spider structure has obvious advantages over conventional designs. The forces resulting from thermal expansion and acting on the foundations are reduced. Nevertheless, the radial rigidity is quite as good as that of a spider with radially mounted arms. The bearing clearance is not affected by the elongation of the arms.

A first design with skew arms at the top and skew spokes at the bottom has been replaced by a new design with skew leaf springs at the top *and* the bottom [4.14]. The new solution requires less space and enables the arms to be aligned radially.

References

- 4.1 Anton I., **Turbine hidraulice**, Editura Facla, Timișoara, 1979.
- 4.2 Drtina P. and Sallaberger M., *Hydraulic Turbines – Basic Principles and State-of-the-Art Computational Fluid Dynamics Applications*, J. Mech. Engng. Sci., Proc. Inst. Mech. Engrs, vol.213, Part C, pp 85-102, 1999.
- 4.3 Howald W. and Stöckli F., *World's Highest Rated Generators for the Bieudron Hydropower Plant*, ABB Review, nr.10, pp 13-19, 1994.
- 4.4 Wiedemann E. and Kellenberger W., **Konstruktion elektrischer Maschinen**, Springer, Berlin, 1967.
- 4.5 Rodrigues J.F.D. and Gmür T.E.C., *Eigensolution of Large Conservative Gyroscopic Systems by a Subspace Forward Iteration Method*, Proc. 7th Int. Modal Analysis Conference, Las Vegas, Nevada, pp 159-165, 1989.

- 4.6 Sperber A. and Weber H.I., *Dynamic Models of Hydroelectric Machinery*, Journal of the Brazilian Soc. of Mech. Sci., vol.13, nr.1, pp 29-53, 1991.
- 4.7 Rodrigues J.F.D. and Gmür T.E.C., *The Solution of Large Undamped Gyroscopic Eigensystems by a Subspace Iteration Method*, Computers and Structures, vol.32, nr.3/4, pp 591-599, 1989.
- 4.8 Gmuer T.C. and Rodrigues J.D., *A Set of C^0 Finite Elements for Rotor Dynamics Analysis*, Proc. 9th Int. Modal Analysis Conference, Florence, Italy, pp 1255-1262, 1991.
- 4.9 Rodrigues J.F.D. and Gmuer T.E.C., *A Subspace Iteration Method for the Eigensolution of Large Undamped Gyroscopic Systems*, Int. J. Num. Methods in Engineering, vol.28, pp 511-522, 1989.
- 4.10 Gmür T.C. and Rodrigues J.D., *Shaft Finite Elements for Rotor Dynamics Analysis*, J. Vib. Acoustics, Trans. ASME, vol.113, pp 482-493, 1991.
- 4.11 *VIMOS Condition Monitoring for Hydropower Machines*, ABB Review, nr.1, pp 15-22, 1992.
- 4.12 **ISO 7919-5**, Mechanical Vibration on Non-Reciprocating Machines - Measurements on Rotating Shafts and Evaluation Criteria - Part 5: *Machine Sets in Hydraulic Power Generating and Pumping Plants*, 1997.
- 4.13 **ISO 10816-5**, Mechanical Vibration - Evaluation of Machine Vibration by Measurements on Non-Rotating Parts - Part 5: *Machine Sets in Hydraulic Power Generating and Pumping Plants*, 2000.
- 4.14 Kellenberger W., *The Optimum Angle for the Support of Vertical Hydro-Electric Generators with Skew Arms or Skew Leaf Springs*, Brown Boveri Review, vol.67, nr.2, pp 108-116, 1980.
- 4.15 Baltisberger K., Canay M., Vögele H. and Wimmer M., *Motor-Generators for Pumped Storage Schemes*, Brown Boveri Review, vol.65, nr.5, pp 280-291, 1978.
- 4.16 Casey M.V. and Keck H., *Hydraulic turbines*, **Handbook of Fluid Dynamics and Fluid Machinery** (Eds J.A.Schetz and A.E.Fuhs), Wiley, 1996.
- 4.17 Siekmann H., *Wasserturbinen*, **Dubbel. Taschenbuch für den Maschinenbau**, 17. Aufl., Springer, pp R30-R36, 1990.

5. AXIAL COMPRESSORS

5.1 Introduction

An axial compressor is distinguished by the fact that the flow of gas through it is in a direction nearly parallel to the shaft axis. The compressor consists of a rotor of cylindrical or conical form carrying the moving blades (Fig. 5.1), which must run at high speed within the bladed stator casing and accurately maintain small clearances at the blade tips under all operating conditions. Compression results from the summation of the small increases of pressure produced as the air traverses the succeeding stages of rotor and stator blades.

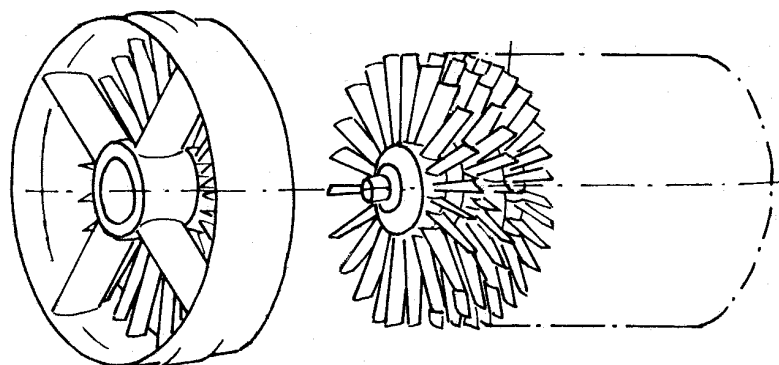


Fig. 5.1

In existing axial compressors, the number of stages has varied between six and twenty-five. The tendency in the latest designs is to limit the number of stages in a single casing to about sixteen, as the desired compression ratio combined with high efficiency can be obtained without exceeding this number of blade rows.

Although patents for axial compressors were taken out as long ago as 1884, it is only in the early 1950's that they become the most versatile form for gas-turbine work. In the aircraft field, where high performance is at a premium, the axial compressor is now used exclusively. It is only for some industrial applications that other compressor types offer serious competition.

The main attraction of the axial compressor is its very high efficiency. Modern designs have stage efficiencies of over 90%, although some efficiency is often sacrificed for other features desirable in specific applications. It is enhanced by the ease with which stages can be compounded to obtain any desired pressure ratio without loss of performance. Further features, important for aircraft engines, are the low frontal area and the low weight, and also the relatively low costs.

The main drawback of the axial compressor would appear to be the large number of blades required. These are both difficult and costly to make; manufacturing techniques are, however, improving rapidly.

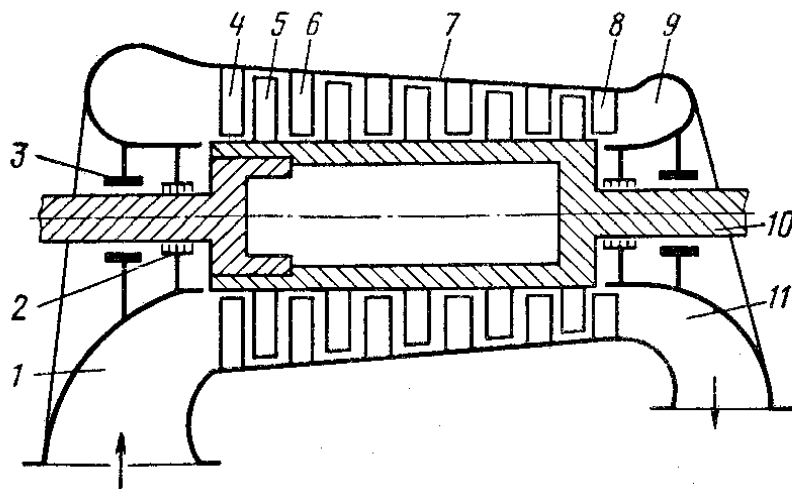


Fig. 5.2 (from [5.1])

5.2 Basic Principles

The axial-flow compressor resembles the axial-flow steam or gas turbine in general appearance. Usually multistage, one observes rows of blades on a single shaft with blade length varying monotonically as the shaft is traversed. The difference is, of course, that the blades are shorter at the outlet end of the compressor, whereas the turbine receives gas or vapour on short blades and exhausts it from long blades.

In figure 5.2: 1 - inlet duct, 2 - end seal, 3 - bearings, 4 - prewhirler stator blades, 5 - rotor blades, 6 - stator blades, 7 - stator casing, 8 - straightener stator blades, 9 - diffuser, 10 - shaft, 11 - discharge duct.

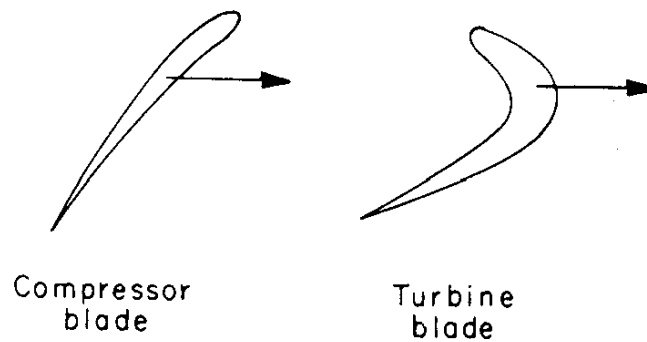


Fig. 5.3 (from [5.2])

A close look at the blades shows that the compressor blade deflects the fluid through only a fraction of the angle that the turbine blade does. This point is illustrated by figure 5.3 which also indicates that the concave side of the blade moves ahead of the convex side; the reverse is true of the turbine blade.

A schematic view of a stage of an axial compressor is shown in figure 5.4. The following notations are used: R – rotor blade, S – stator blade, 1 – inlet to rotor blade, 2 – outlet from rotor blade and inlet to stator blade, 3 – outlet from stator blade, v – absolute velocity, w – relative velocity, u – blade peripheral velocity (transport velocity). In the velocity triangles w_2 is smaller than w_1 and slightly deflected, v_3 is smaller than v_2 and practically equal to v_1 . The figure corresponds to a degree of reaction of 0.85.

In the axial compressor, work is done on the gas through the medium of the rotor. It is converted partly into pressure by reduction of the relative velocity within the blade row, from w_1 to w_2 , and partly into kinetic energy by an increase in the absolute velocity, from v_1 to v_2 . This latter quantity is then converted into pressure by diffusion in the stator, where the absolute gas velocity decreases from v_2 to v_3 .

The proportion of the total energy input converted into pressure in the rotor defines the "degree of reaction", ρ . Thus, if all the pressure rise occurs in the rotor, the design is said to be 100% reaction. If no pressure rise occurs, i.e. if the whole of the energy input appears as kinetic energy, the design is referred to as 0% reaction, or impulse. A very common design criterion is that equal pressure rises should occur in the rotor and stator: this is then known as 50% reaction.

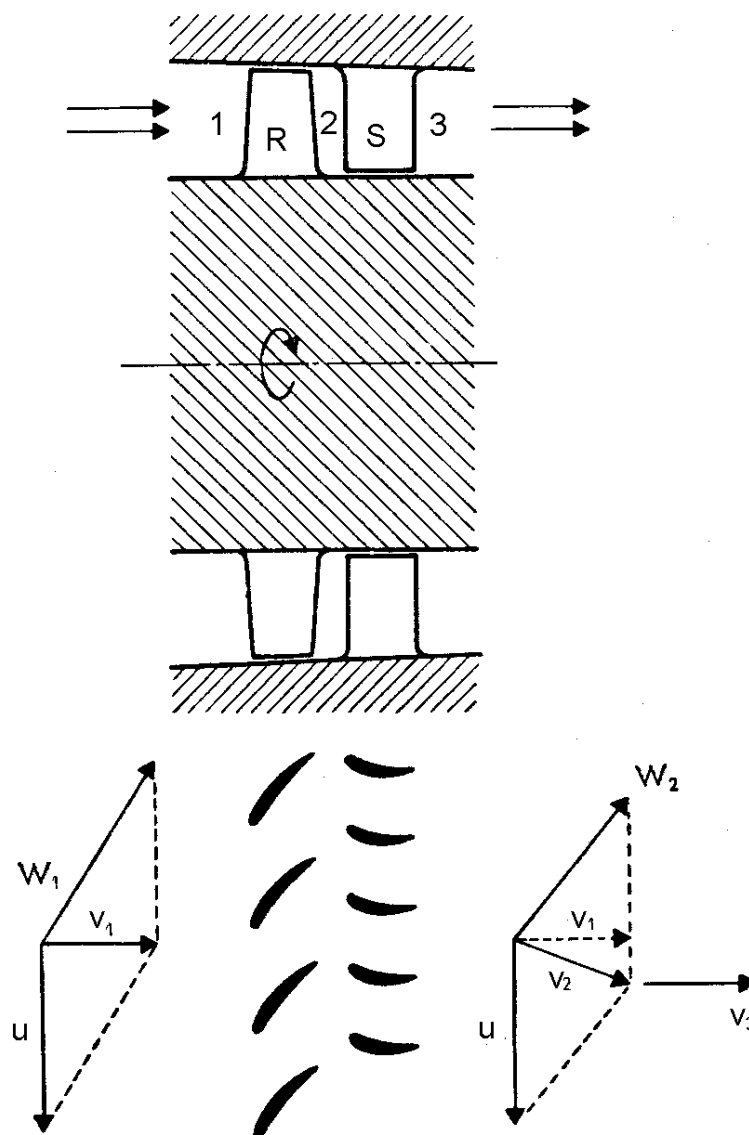


Fig. 5.4 (from [5.2])

Differences in the physical appearance of the blading and in compressor designs arise primarily from the different degrees of reaction.

In figure 5.5 the blading *a* has symmetric rotor and stator blade rows. The velocity triangles before and after the rotor blades are also symmetrical. The stage has 50% reaction, so that the pressure rise in rotor and stator is the same. For this degree of reaction the friction losses are a minimum. The drawback is that with such blading the flow between stages is not axial; to correct this, a row of prewhirler stator blades is placed before the first stage, and a row of straightener stator blades is placed after the last stage. The blading *b* has a degree of reaction of about 0.85. The flow before and after the stage is axial, so that no special diverting blades are necessary.

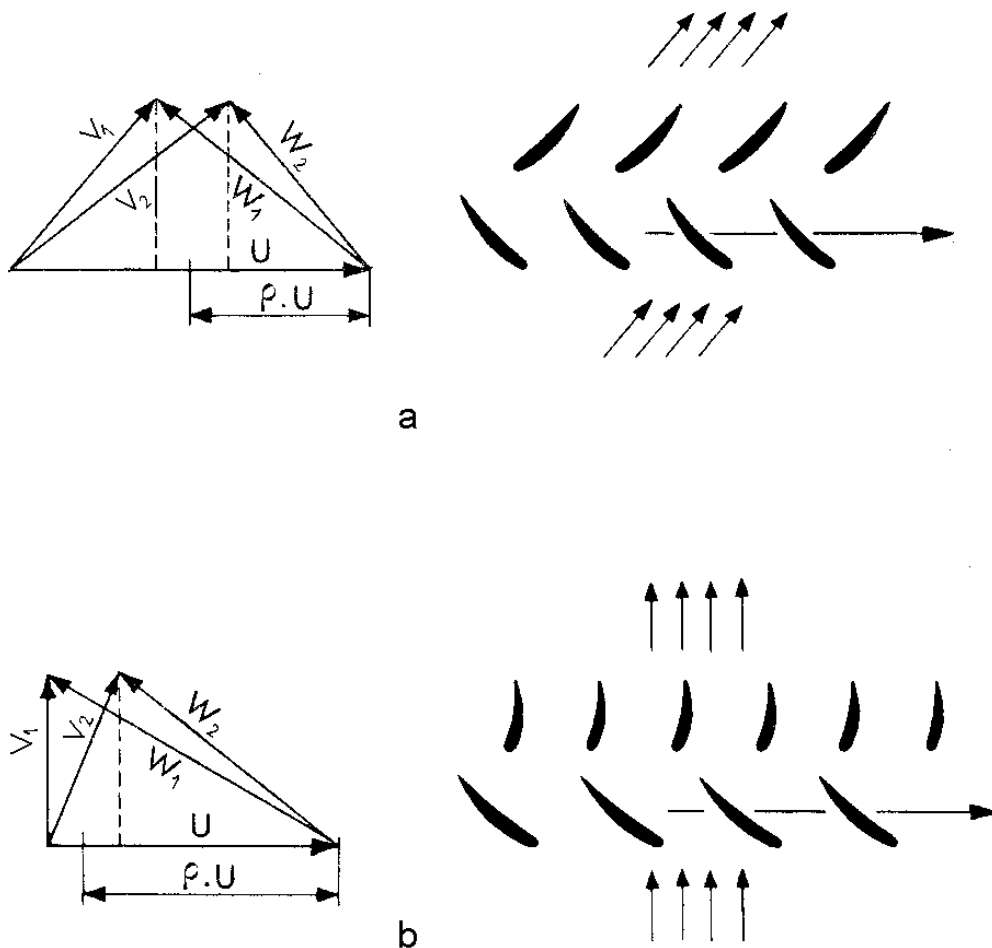


Fig. 5.5 (from [5.2])

Local pressure gradients in a blade passage, and interference effects between adjacent passages induce secondary flows, hence energy losses in a stage.

Aerodynamic analysis must be carried out for compressor blades, since flow in the boundary layer encounters an adverse pressure gradient, which may lead to *separation*, *stall*, and the consequent *surge* phenomenon. To avoid separation, the pressure rise must be small for each stage, in contrast with the very large pressure drops found in turbine stages. Typically, about one-half of the enthalpy rise occurs in the rotor and one-half in the stator.

Surging is an instability associated in some way with *stalling*, which occurs when the flow through the compressor is reduced beyond a certain limit. The flow when surged can take many forms, though some flow reversal is a characteristic feature. Some types are illustrated diagrammatically in figure 5.6 where: a) band of reversed flow (shown shaded) rotating in compressor direction at about half compressor speed; b) band of reversed flow sometimes located by spiders; c) inflow at inside, outflow at outside; and d) whole flow pulsates.

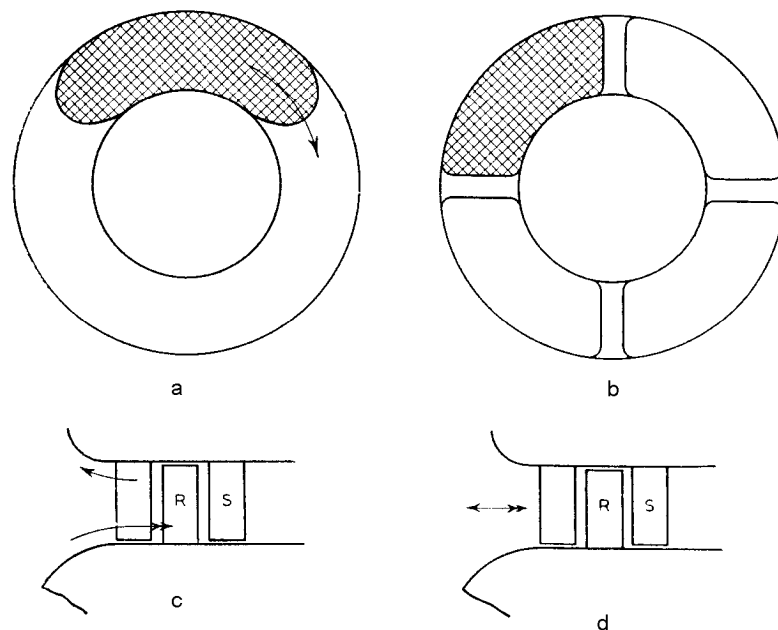


Fig. 5.6 (from [5.3])

The reversed flow bands give rise to alternating loads of considerable magnitude on the blades and bearings, and if allowed to persist, can wreck the machine. It is therefore essential that surging should be avoided in any axial compressor.

5.3 Design Characteristics

The rotor of an axial compressor is essentially a cylindrical or conical body which carries the successive rows of moving blades, and has shaft extensions at each end. For satisfactory operation, safe limits of working stress must be observed, and there should be no whirling criticals in the range of operating speeds.

A compressor design similar to that schematically shown in figure 5.2 is illustrated in figure 5.7.

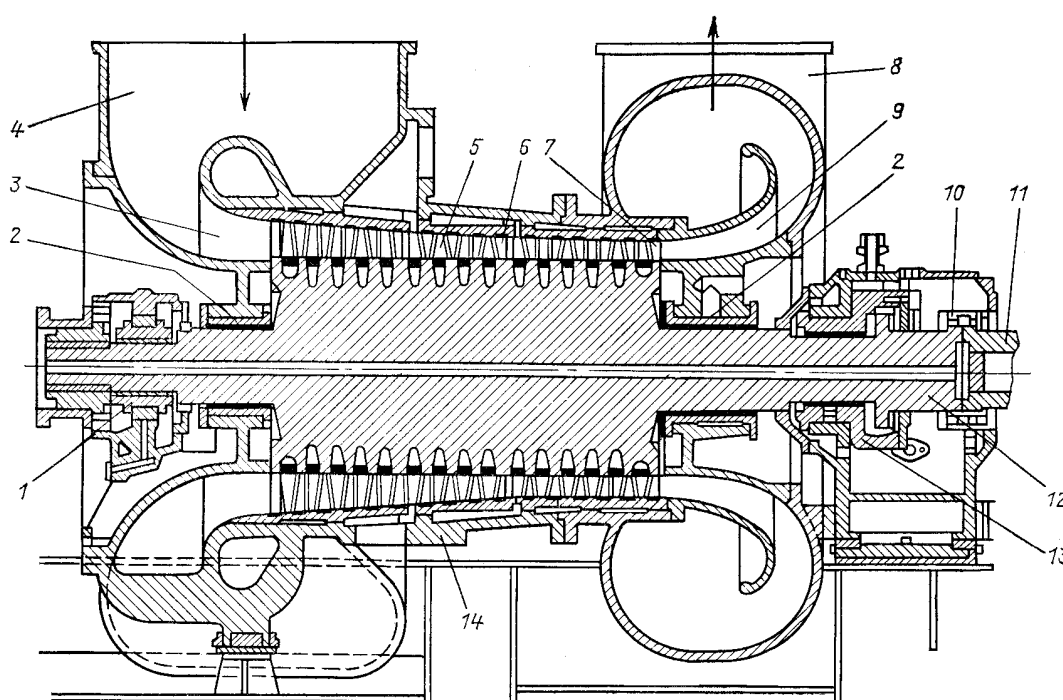


Fig. 5.7 (from [5.4])

In figure 5.7 the numbers have the following designations: *1* and *13* - bearings, *2* - seals, *3* - prewhirler, *4* - intake duct, *5* - rotor blades, *6* - stator blades, *7* - straightener stator blades, *8* - discharge duct, *9* - diffuser, *10* - coupling, *11* - gas turbine shaft, *12* - drum-type rotor, *14* - stator casing.

The size of the various compressors is mainly defined by the first stage. The defining parameters are the rotor diameter, the speed, the number of stages, the degree of reaction, and the blade stagger (outlet angle) or the chord length which together with the number of stages defines the rotor length. The length of the machine increases

markedly with the blade tip to hub diameter ratio, since with a corresponding decrease of the hub diameter, both the number of stages, as well as the chord length, increase rapidly.

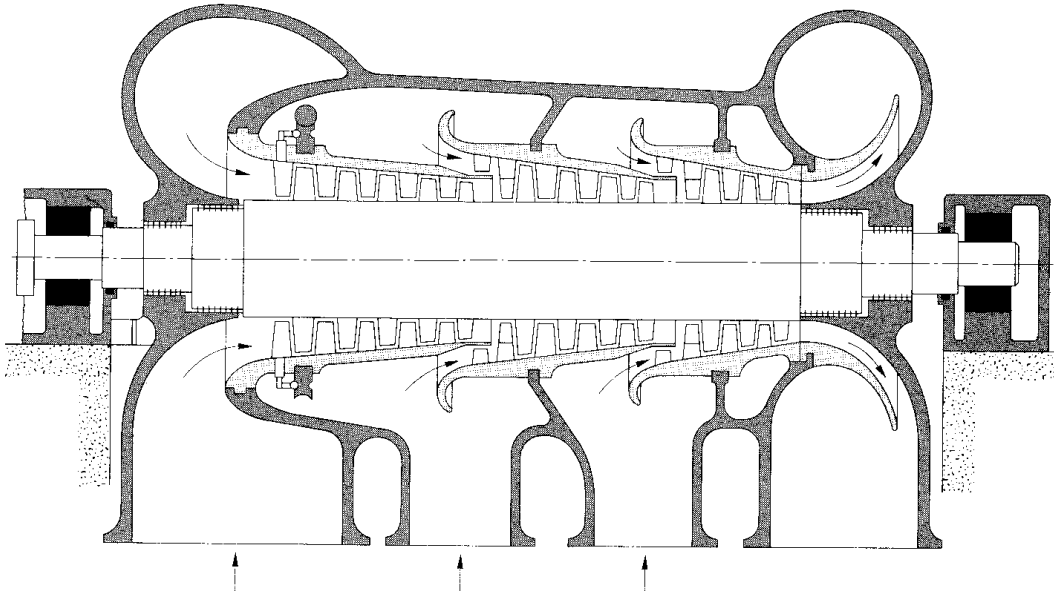


Fig. 5.8 (from [5.5])

Figure 5.8 shows an axial compressor with side streams used for cascaded cryogenic cycles in the liquefaction of the natural gas.

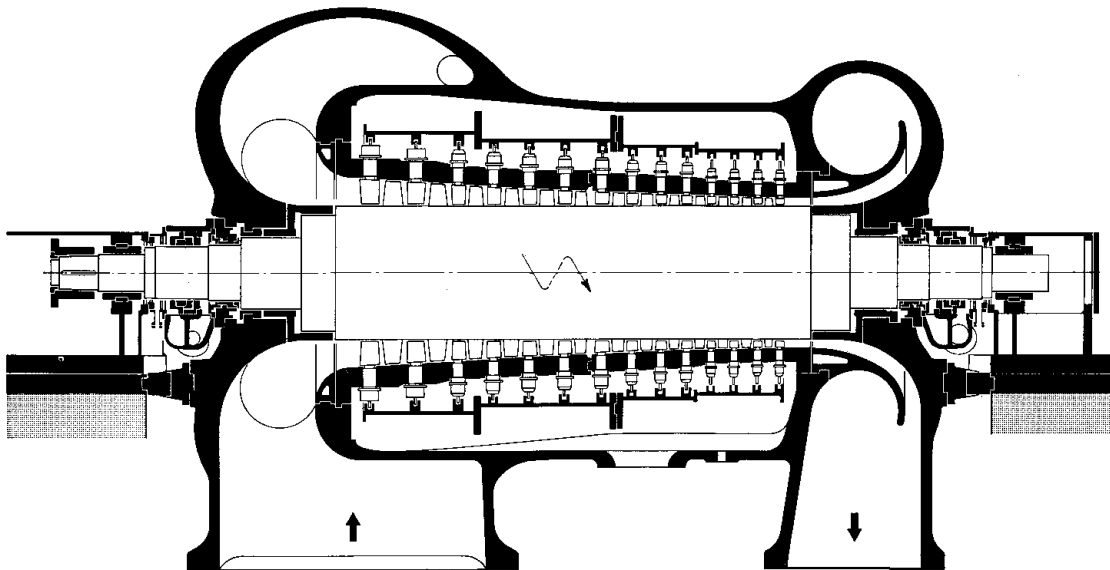


Fig. 5.9 (from [5.6])

Figure 5.9 shows a mixed refrigerant compressor of about 90 MW for a single pressure cryogenic cycle. The movable guide vanes are especially useful for starting with a lighter gas and also to avoid an intense rotating stall during starting at low speed. By closing the first stages more than the last ones, the form of the compressor channel is adapted to avoid surging either at the last stages (for high values of the density ratio) or at the first stages (for low values of density ratio). The overall length of the rotor is determined by bearings, floating contact seals and annular gas seals.

In practically all existing axial compressor designs, the rotor is supported by one bearing at the gas inlet end and by a second bearing at the gas delivery end. In aircraft practice, ball and roller bearings are universally used, on account of their compactness, small lubricating oil requirements, and insensitivity to momentarily cessations of oil flow as may occur during acrobatic flying.

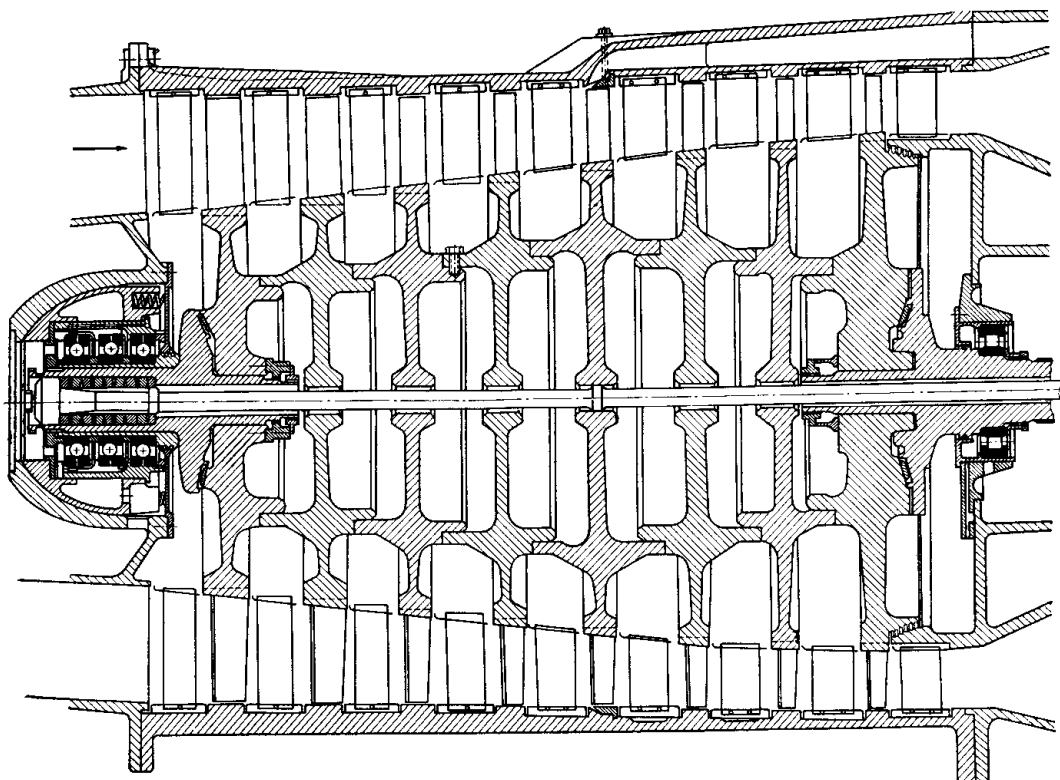


Fig. 5.10 (from [5.7])

In long life gas turbines, plain journal bearings are always used, because the extreme reliability of these types of bearing more than offsets their slightly higher power consumption compared with rolling

bearings. To maintain the necessary close clearances between the tips of the rotor blades and the stator casing, the compressor bearings are as rigidly as possible located relative to the stator structure.

Drum-type compressor rotors have inherently high whirling critical speeds, and present no problem in this direction. Usual designs consist of rings that are flanged to fit one against the other while the entire assembly is held together by through bolts. With built-up disc rotors (Fig.5.10), high whirling speeds can be obtained by providing an annular abutment face between the successive discs at a fairly large radius from the axis, so increasing the rotor's lateral stiffness.

The stress conditions in a compressor rotor favour the adoption of a disc construction as in figure 5.10. This allows the centrifugal load of the blades and disc rim to be carried as a radial stress inwards to a relatively massive boss near the centre of the rotor, where the centrifugal field is small.

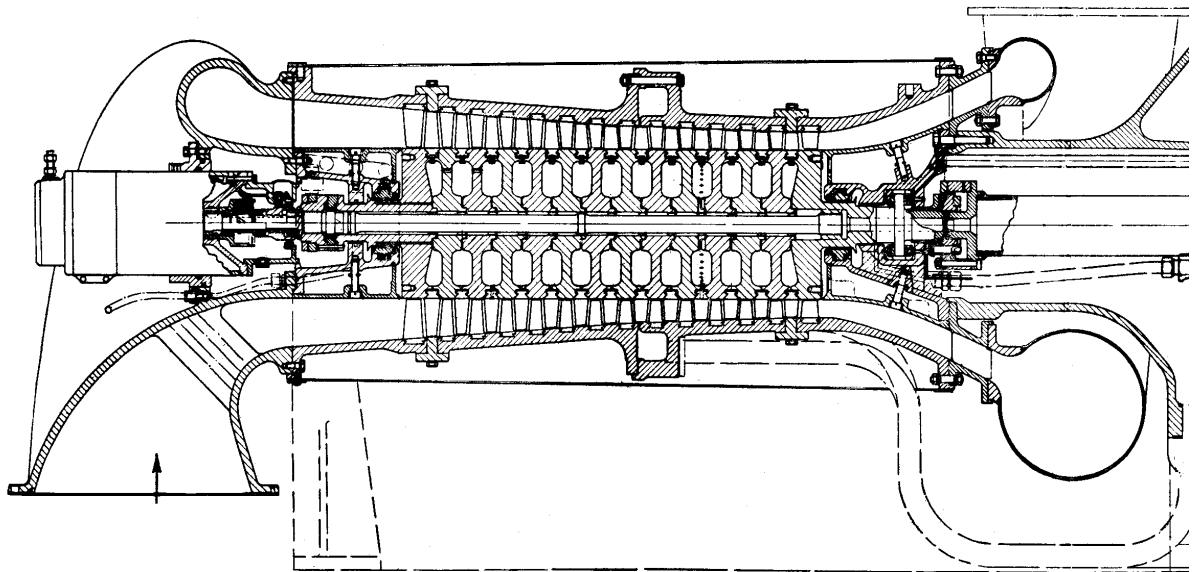


Fig. 5.11 (from [5.3])

Figure 5.11 shows a rotor design where disc construction has been used and the rotor blades are held between the peripherals of adjacent discs, which provides an easy method of assembly. By contrast, when solid forgings or drum-type rotors are used, the blades are usually held in place by circumferential serrations, and some form of "entry slot" must be provided through which the blades are passed during the assembly of the rotor.

If the same maximum stresses are taken, it has been found that a disc rotor of given dimensions is lighter than the equivalent hollow drum rotor, and has a lower mass moment of inertia.

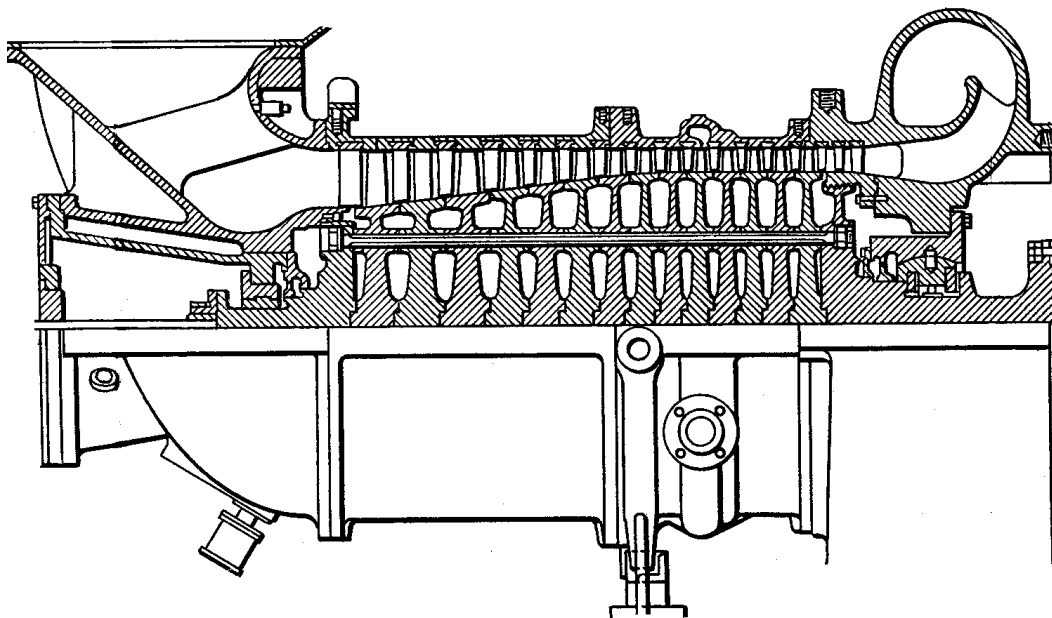


Fig. 5.12 (from [5.3])

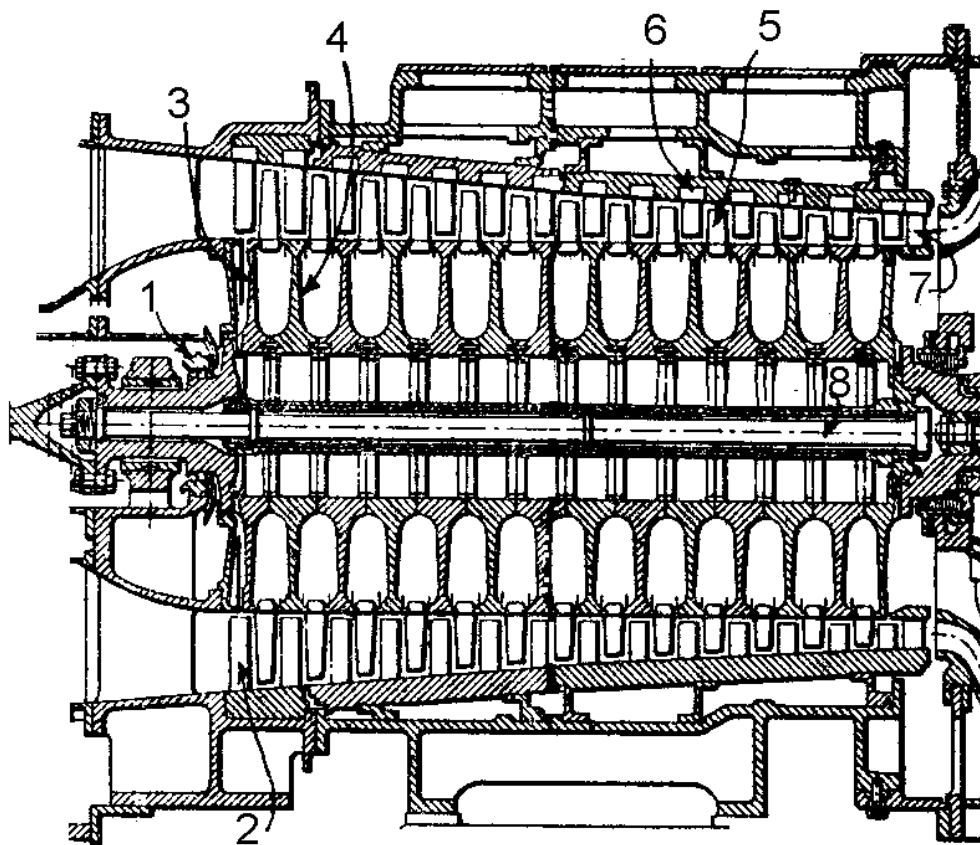


Fig. 5.13 (from [5.3])

For aircraft applications the importance of these considerations is immediately apparent. Advantage has also been taken of the low mass moment of inertia of disc-type rotors in some long life gas turbines which are called upon to respond to rapid load changes involving a quick response of compressor rotational speed to the transient conditions, as in naval gas turbines.

Whilst a drum-type compressor rotor is a self-supporting structure, a disc-type rotor is essentially a number of separate structures connected together. Figure 5.12 shows an arrangement with multiple axial tension bolts used in a gas turbine.

An alternative is to use a single central tension bolt as in figure 5.13 where: 1 - oil baffle, 2 - prewhirler, 3 - rotor wheel, inlet end, 4 - rotor wheel, intermediate, 5 - rotor blades, 6 - stator blades, 7 - straightener stator blades, and 8 - central bolt. Where the construction limits the tension bolt length, it may be necessary to resort to the use of a compound bolt to withstand differential thermal expansions in the rotor.

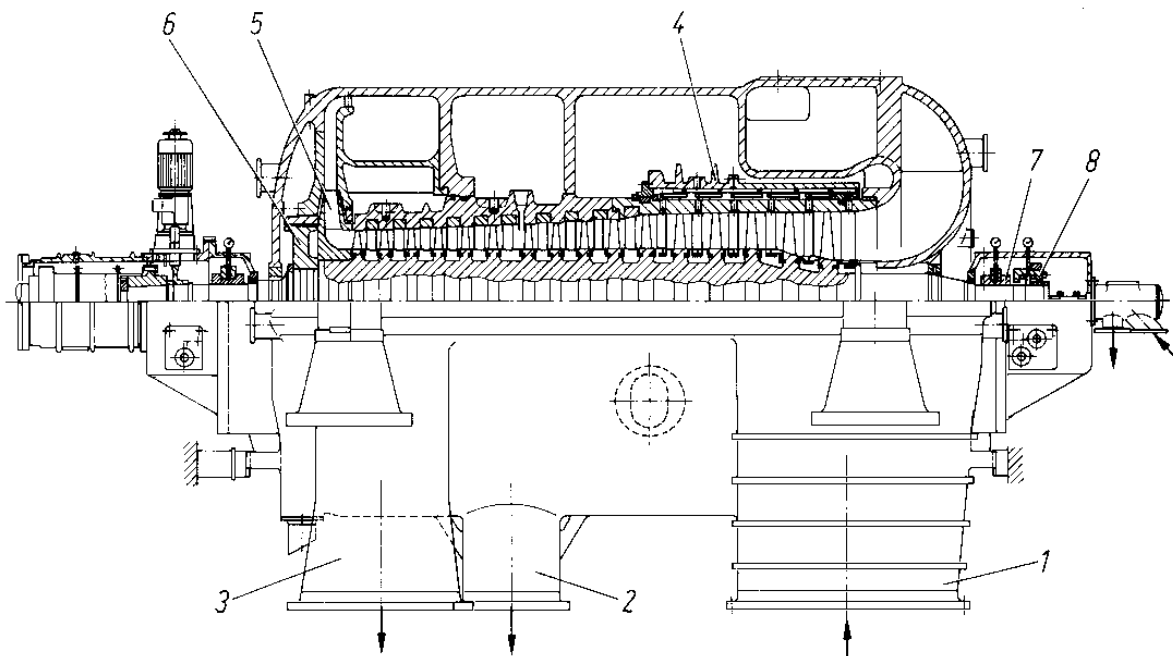


Fig. 5.14 (from [5.8])

A modern design with 16 axial stages and one final radial stage is presented in figure 5.14 where 1 - inlet duct, 2 - extraction duct, 3 - discharge duct, 4 - stator blade adjustment fixture, 5 - final radial stage, 6 - balancing piston, 7 - radial bearing, 8 - thrust bearing. The

compressor built by MAN has a flow rate of 515,500 m³/h, pressure ratio 5.6, absorbed power 36,830 kW and speed 3000 rpm.

5.4 Axial vs Centrifugal Compressor Considerations

A comparison of the relative merits of axial and radial compressors [5.7] is of interest.

In the following, the index *R* is for single inlet radial compressors, *RR* - for double inlet radial compressors and *A* - for axial compressors. Denoting *Q* - intake flow, *n* - rotational speed and *D* - a characteristic diameter, the following equations have been established for usual specific parameters:

$$\frac{n_R}{n_A} = \frac{0.73}{\sqrt{Q_R/Q_A}}, \quad \frac{D_R}{D_A} = 2.19 \sqrt{\frac{Q_R}{Q_A}} \quad (5.1)$$

where *D_R* is the outer diameter of the impeller and *D_A* is the outer diameter of the drum (Fig.5.15).

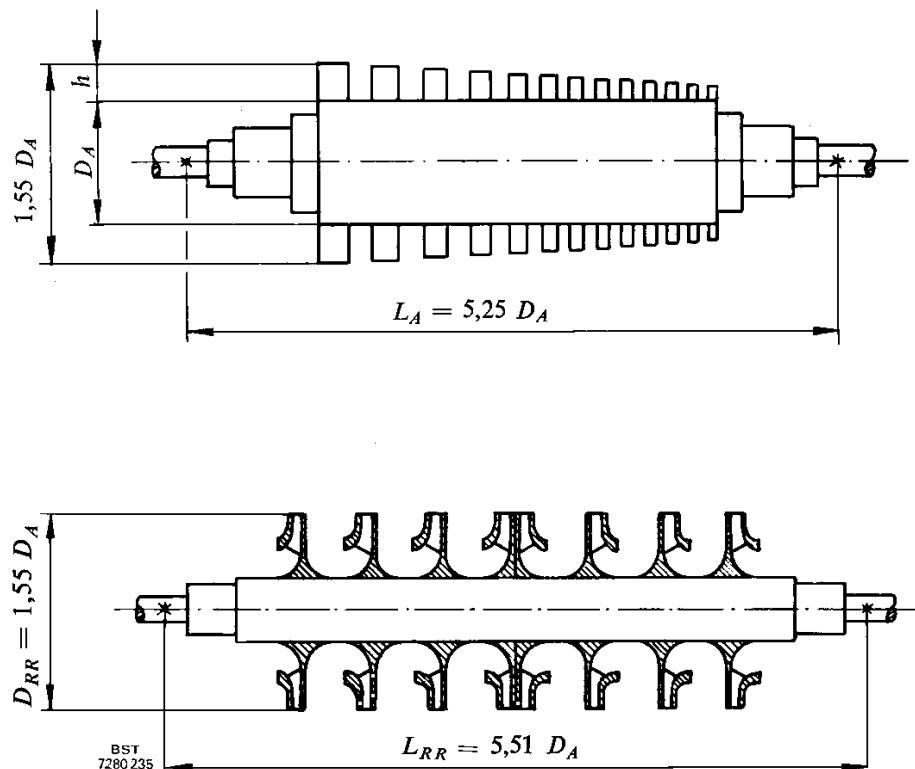


Fig. 5.15 (from [5.6])

Taking into account that, for the same flow, the outer diameter of impellers in double inlet radial compressors is only $1/\sqrt{2}$ of the diameter for the single inlet compressor, the above relations become

$$\frac{n_{RR}}{n_A} = \frac{1.03}{\sqrt{Q_{RR}/Q_A}}, \quad (5.2)$$

$$\frac{D_{RR}}{D_A} = 1.55 \sqrt{\frac{Q_{RR}}{Q_A}}. \quad (5.3)$$

For the same volume flow, the rotational speed of the single inlet centrifugal compressor is about 75% of that of the axial compressor, while the double inlet centrifugal compressor will have almost the same speed as the corresponding axial machine.

For a typical diameter ratio of 1.55 ($h/D_A=0.275$) the diameter of the double inlet centrifugal compressor is identical to the outer diameter of the axial blading. As the hub diameter is much smaller, the rotor of an axial compressor is much stiffer than the rotor of the corresponding centrifugal compressor.

References

- 5.1 Smolenskii A.N., **Steam and Gas Turbines** (in Russian), Mashinostroenie, Moskow, 1977.
- 3.2 Agnet E., *Turboverdichter*, Sulzer Dampfkalender.
- 5.3 Cox H.R. (ed), **Gas Turbine Principles and Practice**, George Newnes Ltd., London, 1955.
- 5.4 Kostyuk A.G. and Frolov V.V., **Steam and Gas Turbines** (in Russian), Energoatomizdat, Moskow, 1985.
- 5.5 Strub R.A., *Axial Compressors for Large LNG Plants or Other Applications*, Sulzer Technical Review, vol.62, nr.4, pp 134-142, 1980.
- 5.6 Naegeli J.P., *Turbocompresseurs frigorifiques pour les installations de liquéfaction de gaz naturel à charge de base*, Revue Technique Sulzer, vol.55, nr.4, pp 213-224, 1973.
- 5.7. Pfeleiderer C. and Petermann H., **Strömungsmaschinen**, 6.Auflage, Springer, 1990.
- 5.8 Lüdtke K., *Turboverdichter*, in **Dubbel. Taschenbuch für den Maschinenbau**, 17.Auflage, Springer, pp R65-R75, 1990.

6. GAS TURBINES

6.1 Introduction

The main application areas of gas turbines are the aircraft engines, the land-based units for power generation, and the turbochargers of large reciprocating engines. Other applications include prime movers for locomotives and automobiles, marine main and auxiliary engines, and industrial applications.

The first gas turbine for aircraft propulsion was developed by Whittle in Britain, and made its initial test run in April 1937. However, the world's first flight of a turbo-jet propelled aeroplane occurred on August 27, 1939 in Germany. It was made by the *Heinkel HE.178* powered by a *HE.S.3b* gas turbine designed by H. J. P. von Ohain. The first British flight was made on May 15, 1941 by the *Gloster E28/39* propelled by a *WI* engine. The first turbo-prop to fly was the Rolls Royce *Trent* on September 20, 1945.

The first land gas turbine was installed by BBC at Neuchâtel, Switzerland, in 1939. It was the result of experience gained with application of axial compressors to *Velox* boilers. In the early designs of stationary gas turbines, a marked influence of axial steam turbine practice was noticeable, except that superior materials of construction were adopted to comply with the higher temperatures.

The new approach introduced by Whittle, especially the concept of few expansion stages and the extensive use of cooling, has been soon accepted in the designs of stationary gas turbines.

6.2 Basic Principles

The simplest gas turbine engine requires at least two major components besides the turbine proper (Fig. 6.1). The gas (usually air) must be compressed by an axial-flow compressor, and then it must be

heated (usually by burning a hydrocarbon fuel) in a combustion chamber. Gas is delivered to the turbine inlet at an elevated pressure and temperature.

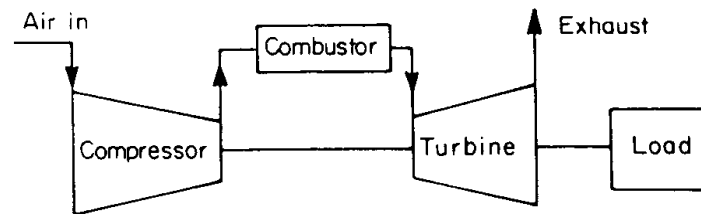


Fig. 6.1

The basic conception of the jet-propulsion engine is best described in Whittle's patent application as "consisting of one or more stages of compression, one or more stages of expansion and a heat addition between the end of compression and the beginning of expansion, part of the work done in expansion being employed to do the work of compression and the remainder to provide" power.

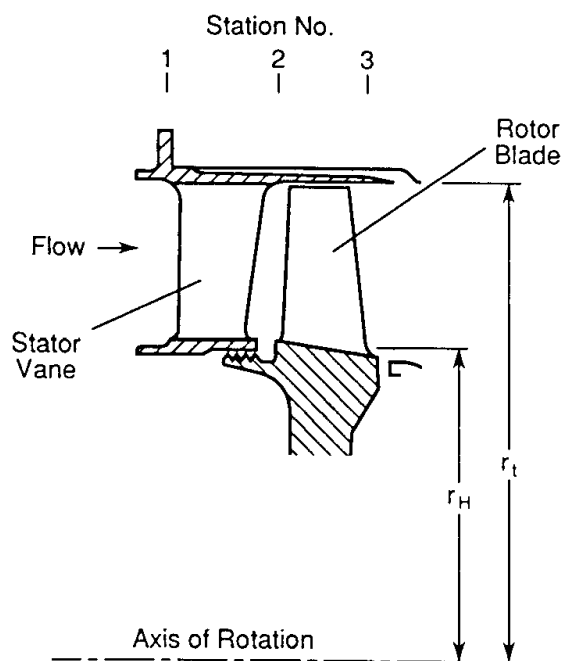


Fig. 6.2

The compressor and the turbine are interdependent. When mounted on the same shaft, the speed of one must be the speed of the other. Furthermore, the pressure ratios and mass flows are also roughly equal. The determination of a point of operation is a process

known as *matching*, and the two machines are matched when speeds, mass flows, and pressure ratios are equal.

In multistage gas turbines used in stationary power plants, as well as in gas turbine engines used to drive ships, trains, and aircraft, a *reaction* turbine is commonly used. It has a non-zero stage reaction. A single stage of a reaction turbine comprises a row of stator vanes followed by a row of rotor blades arranged as in figure 6.2.

Reaction blades of any length are commonly twisted as shown in figure 6.3. Changes in blade profile are made to create a free vortex distribution in the tangential component of the absolute velocity. Each parcel of gas passing through the rotor loses the same energy per unit mass.

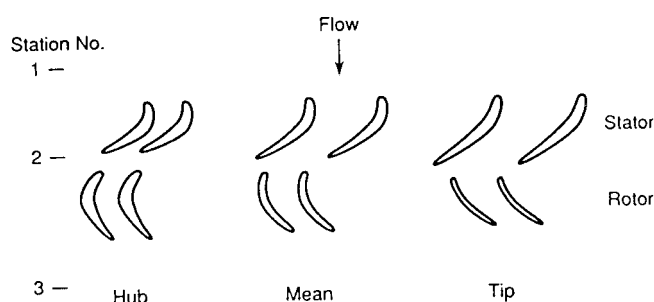


Fig. 6.3

The velocity diagrams at the rms mean radius of a typical stage of gas turbine are shown in figure 6.4.

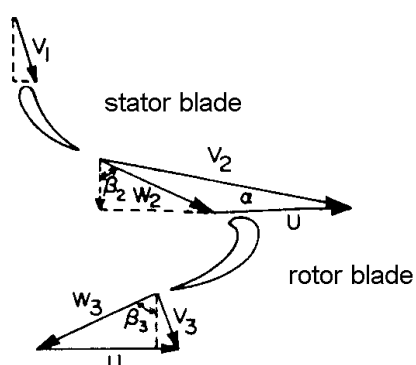


Fig. 6.4

The three-dimensional flow calculations and the design of low-loss profiles for the turbine cascades are key factors in modern gas turbine construction. Figure 6.5 shows the blading of a BBC type *GT8*

gas turbine. The shaping of the end contours, the radial clearance and the blade shrouds are important aspects of the design process.

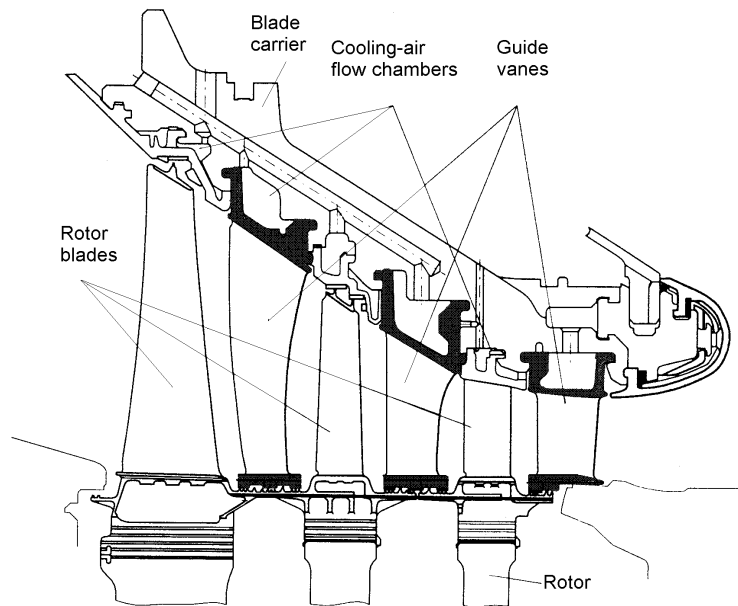


Fig. 6.5 (from [6.1])

Special attention is given to the correct prediction of the outlet angle in the first row of blades, since this has a major effect on the flow characteristic of the turbine.

6.3 Stationary Turbines for Power Generation

Gas turbines are appropriate for standby and peak load service in power station plants, as well as for base-load service in places with natural gas resources. Stationary gas turbines have very good fuel flexibility. Their constructional features have been adapted to the available fuels ranging from residual, crude and light oil, low-Btu blast furnace gas - for peak and base-load applications, to natural gas - for modern base-load plants.

At present, over 35 percent of the power generation capacity installed annually - a total of about 85 GW - is based on gas turbines [6.1]. Ecological as well as economic benefits underline the current preference for operating gas turbines together with steam turbines in combined cycles, involving large and small units as well as

regeneration plants for district heating. Combined cycle power plants can achieve up to 58 percent thermal efficiency, while individual gas turbines have up to 38 percent thermal efficiency.

In the traditional gas turbine process, the unit rating and efficiency is increased via the mass flow, the turbine inlet temperature (*TIT*) and the corresponding pressure ratio.

The *TIT* has been increased beyond 1200°C by increasing the permitted blade temperature from 850°C for conventionally cast blades (e.g. from Inconel 738), to 920°C for direction solidified blades, and to 950°C - using single crystal technology.

In the BBC type *GT11* gas turbine, a pressure ratio of 11:1 at 3600 rpm is obtained with 17 compression stages, while the turbine has 5 stages to obtain a 247.2 kW/kg/s specific output, and a base load of 71.72 MW with a thermal efficiency of 31.1%.

Typical stationary gas turbine installations are schematically shown in figures 6.6 to 6.8.

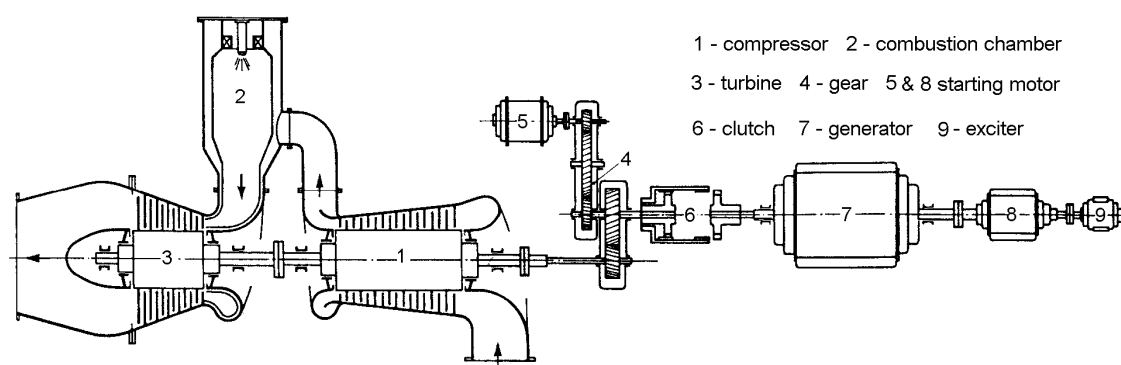


Fig. 6.6 (from [6.2])

The simplest type of open circuit installation comprises a compressor, a combustion chamber, and a gas turbine. In the arrangement from figure 6.6, the compressor and turbine rotors form a single shaft line, while the generator 7 is coupled via a clutch 6. The starter 9 is used to launch the generator when operating as a compensator. The starter 5 is used to launch the turbine while the generator turns.

Part of the compressed air is used for the fuel combustion. The remainder (aprox. 70%) is used for cooling the shell of the combustion chamber and some components of the turbine, and is mixed with the hot gases.

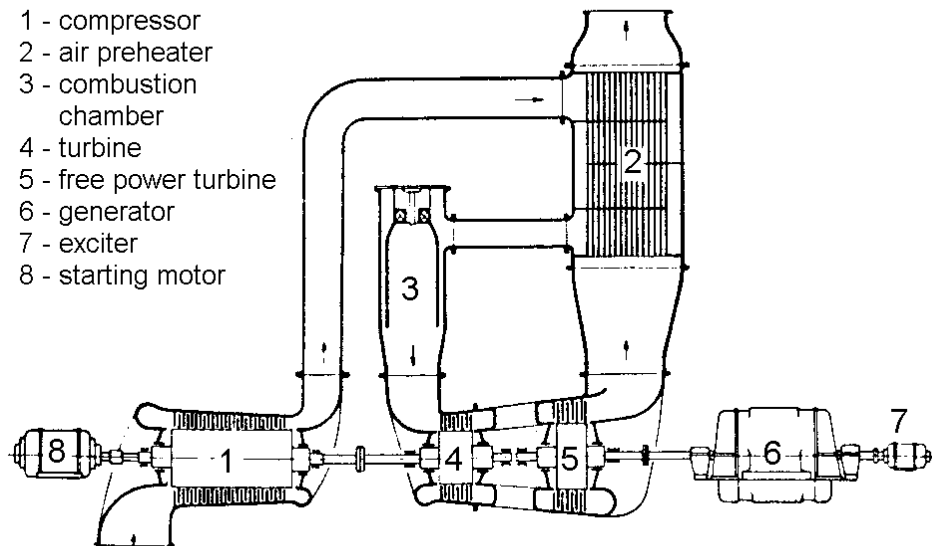


Fig. 6.7 (from [6.3])

The volume of the expanded gas in the turbine is much larger than the volume of the compressed air in the compressor, due to the heating in the combustion chamber. The difference between the work produced by the turbine and the work absorbed by compressor and friction losses is the work supplied to the electrical generator. It is a function of the compressor and turbine thermodynamic efficiencies and the *TIT*.

A 'split-shaft' gas turbine group is shown in figure 6.7. It comprises two distinct gas turbines, one to drive the compressor, the other to drive the generator (free power turbine). The speed of the compressor can be reduced at partial load, while the free power turbine can operate at constant (or variable) speed.

A 10 MW gas turbine installation with two shaft lines is shown in figure 6.8 (installed at Santa Rosa power station, Lima, Peru). It comprises two gas turbines, two combustion chambers, and three compressors with inter-coolers, and an air reheater.

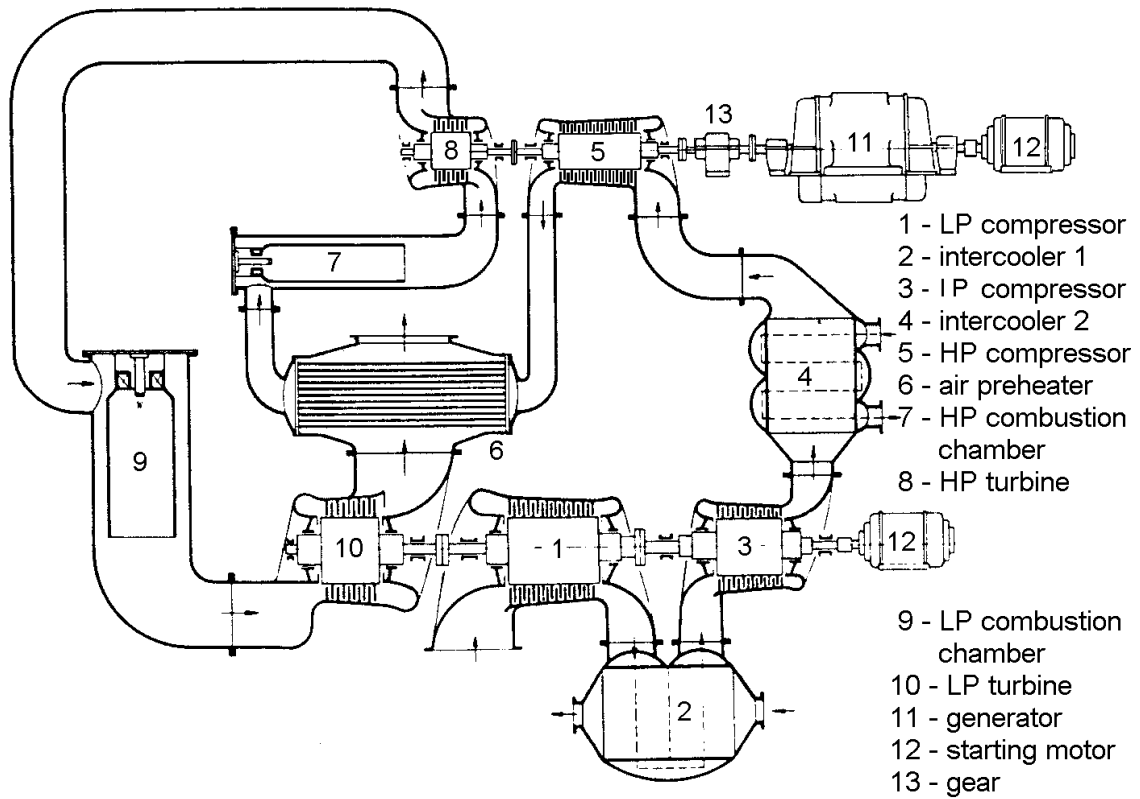


Fig. 6.8 (from [6.3])

The structure of a single shaft gas turbine unit, built in the 1950's, with separate compressor and turbine casings, is shown in figure 6.9. Between the two machines there is a turning gear and a pressure lubricated bearing.

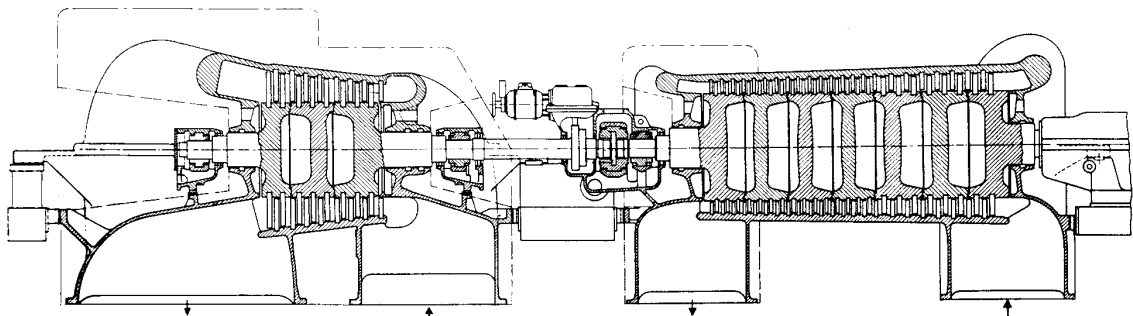


Fig. 6.9 (from [6.3])

Between 1947 and 1960, BBC built dual-shaft gas turbines featuring an intermediate cooler, air preheater and dual heat supply

(with reheat). The advantages of a single shaft were soon recognized and this design was consequently introduced

Figure 6.10 shows an axial section of the BBC type *GT11* gas turbine built in 1969.

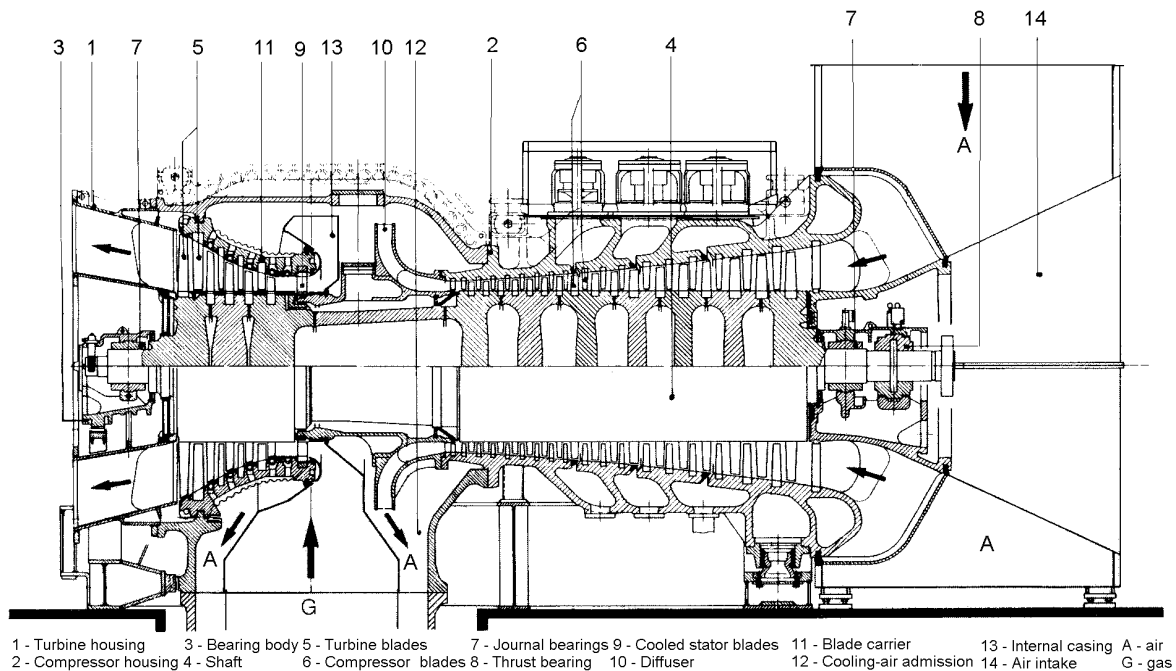


Fig. 6.10 (from [6.4])

The design comprises a single shaft carrying the blading of both compressor and turbine. The shaft is welded from sections of relatively small, homogeneous and easily heat-treated forgings. They are joined together at the circumference by welding in two stages. First the root is welded under argon, then the rest of the joint is filled in by submerged arc welding. Within the highly stressed zones of the sections there are no holes or other grooves likely to cause stress concentration. The rotating blades are held in peripheral slots, except for the final row where they are fixed in axial slots by means of a fir-tree root.

The hot gas flowing from the silo combustion chamber enters the hot-gas casing where it is evenly distributed to the entire periphery of the first row of stationary blades. On flowing through the turbine it expands. To provide the increase in flow area required by the expanding gases, the stator casing is "flared" outwards in the direction

of the flow. In some designs, the diameter of the body of the rotor is also reduced in the later stages, to give a greater rate of increase of blade annulus area through the turbine.

The hot-gas flow through the turbine is lined with a heat shield consisting of separate plates which are free to expand and are thus free from thermal stresses. Cooling air flows beneath these plates, thereby protecting the supporting elements below them – in particular the shaft and blade carriers – against unduly high temperatures. In the blade carrier, the cooling air is conveyed to and fro in peripheral ducts and emerges just before the first row of stationary blades, i.e. it has to perform work in the turbine. The first stationary and revolving blades are cooled. In the first row of stationary blades the cooling air emerges at the trailing edge, in the first rotating row just before the trailing edge on the pressure side. In this manner, the trailing edges are reliably cooled and cracking due to thermal stresses is avoided.

The shaft is supported by two bearings which are accessible from outside while the machine is running. The bearing space in the exhaust-gas duct is cooled by air extracted from the first stage of the compressor and used to seal the turbine gland.

Figure 6.11 shows the main components of the middle section of the *GT24* and *GT26* gas turbines with sequential combustion system built by BBC: 1 - SEV combustor, 2 - fuel injection, 3 - EV combustor, 4 - EV burners, 5 - low-pressure turbine, 6 - high-pressure turbine, 7 - compressor.

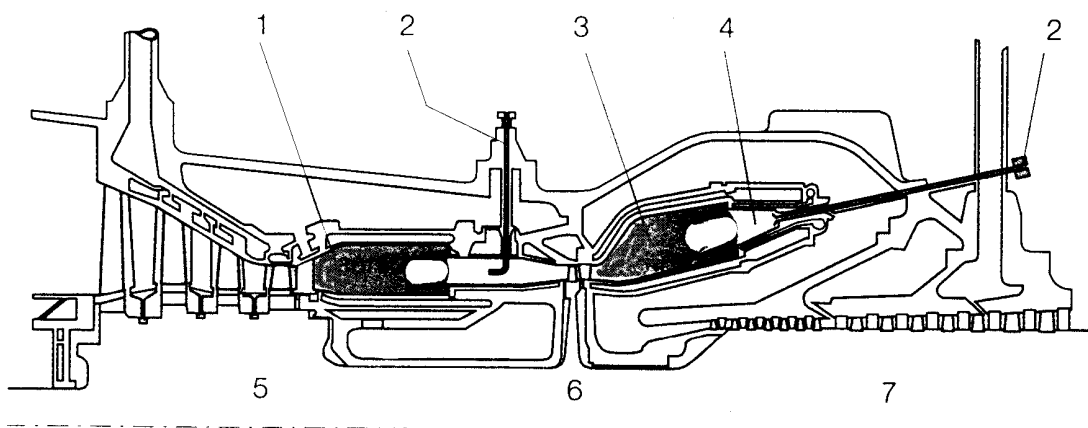


Fig. 6.11 (from [6.1])

A design with concentric shafts, resembling the aircraft gas turbines, is shown in figure 6.12.

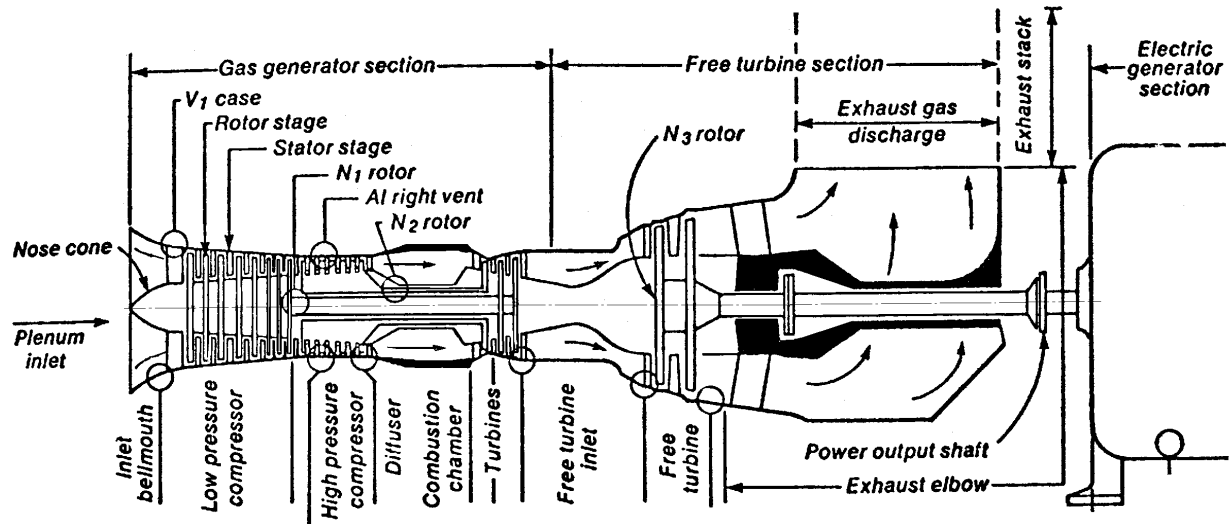


Fig. 6.12 (from *Power*, Jan 1980,p.27)

The type *MS9001FA* gas turbine built by General Electric is illustrated schematically in figure 6.13. Its main technical data are: output 226.5 MW, heat rate 9570 Btu/kWh, exhaust flow 2,212,000 kg/hr, firing temperature 1288°C, exhaust temperature 589°C.

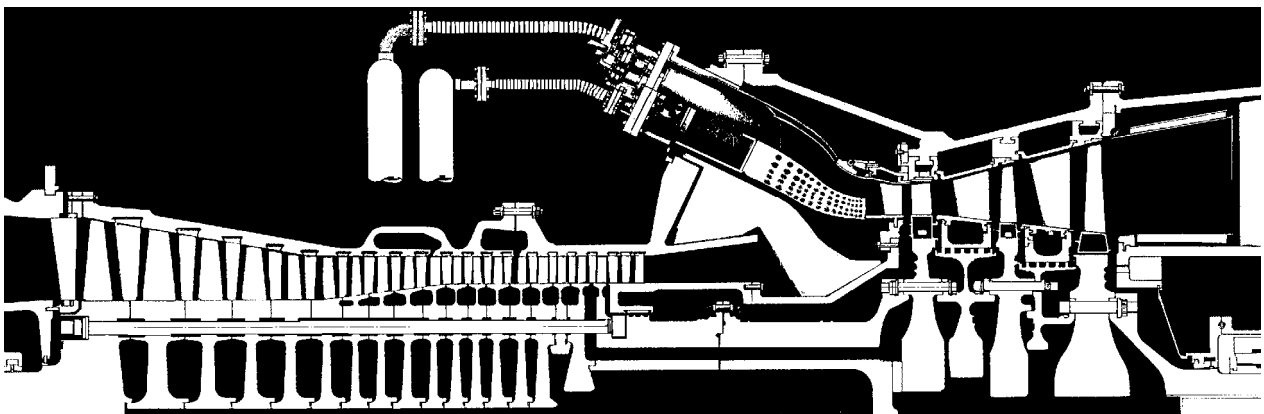


Fig. 6.13 (from [6.5])

Both compressor and turbine rotors are built with discs held together by pretensioned bolts. Generally, mutual slipping of the discs can be prevented either by Hirth-type serrations or by friction between the faces of the discs.

6.4 Gas Turbines for Aero-Engines

Aircraft propulsion is mainly achieved by jet-propulsion engines (turbojets) and propeller turbine engines (turboprops).

The *jet-propulsion engine* inhales air and ejects it, in the form of exhaust gas, at high velocity, rearwards relative to the direction of flight. The *propeller turbine engine* combines the propulsion by the air entrained by the propeller rotating blades with the jet propulsion.

Many variants and combinations are possible within these broad classes, from the single-shaft turbojet (Fig. 6.14,*a*) through the compound turbojet (Fig. 6.14,*b*), by-pass engine (Fig. 6.14,*c*), and turbofan (Fig. 6.14,*d*) to the turboprops (Fig. 6.14,*e*, *f*).

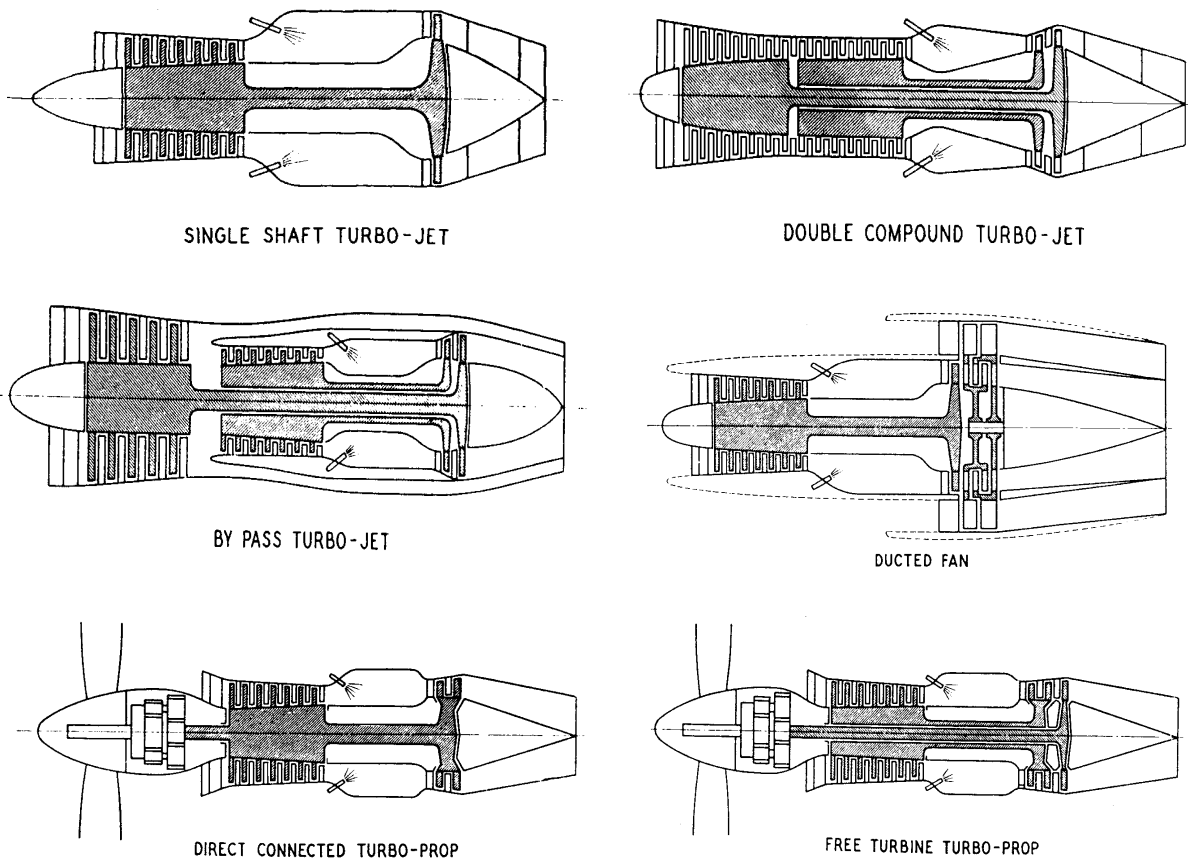


Fig. 6.14 (from [6.6])

6.4.1 Turbojets

Up to pressure ratios of about 8:1 the *single-shaft turbojet* (Fig.6.14,*a*) retains good compressor efficiency, and starting and

handling characteristics. Above this ratio it becomes necessary to consider dividing the engine into two coaxial units and running each at its most suitable speed. Such an engine is called a *double-compound turbojet* (Fig. 6.14,b). It is used mainly in high-speed aircraft where its relatively low frontal area and high thrust are at a premium to enable high speeds, often into the supersonic range, to be achieved.

OLYMPUS 593

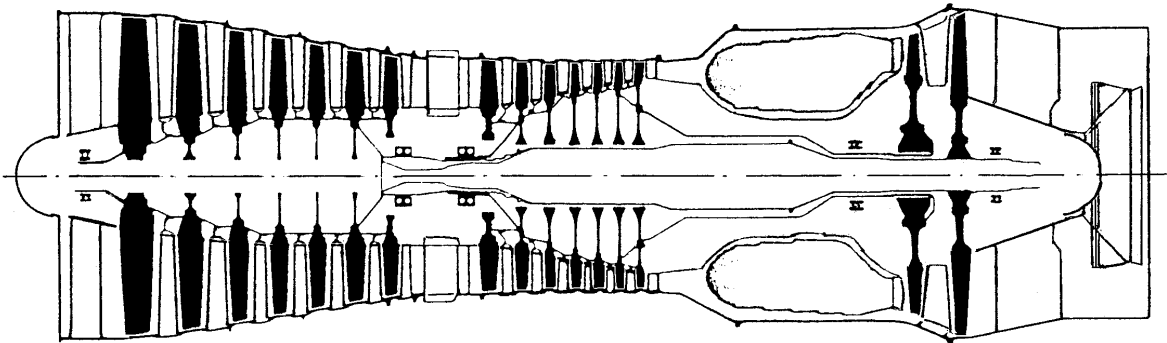


Fig. 6.15 (from [6.7])

A *by-pass turbojet* (Fig. 6.14,c) consists of an engine, possibly compounded, in which only a portion of the compressed air is heated in the combustion chambers, the remainder being ducted past the combustion system and turbine to augment the propulsive jet.

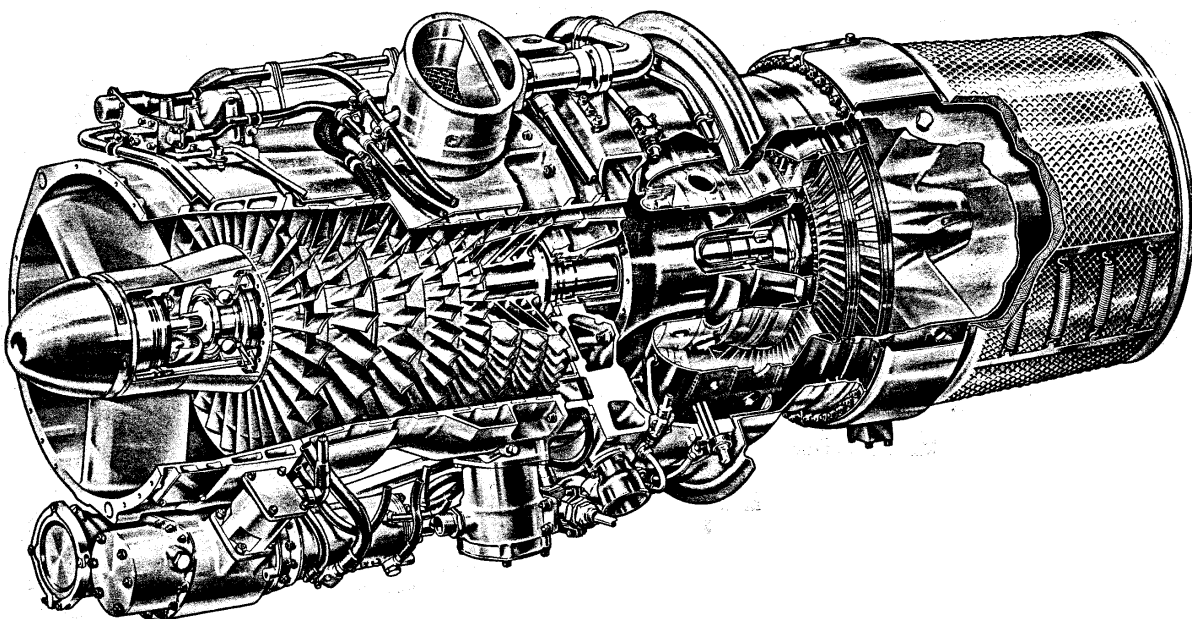


Fig. 6.16 (from [6.8])

Examples of turbo jets are the *Olympus 593* (Fig. 6.15) in Concorde, and the *Viper 600* (Fig.6.16) in military aircraft.

6.4.2 Turboprops

Turboprops can be of various layouts but the most common are the direct-connected and the free-turbine types. In the *direct-connected* turbo-prop (Fig. 6.14,e) the compressor, turbine, and propeller are all mechanically connected, so that the turbine drives both the propeller and the axial compressor. In the *free-turbine* turbo-prop (Fig. 6.14,f) two turbines are used, having their shafts co-axial. The compressor and its turbine form a gas generator feeding a separate power turbine which absorbs the majority of the energy from the exhaust stream to drive a propeller through a reduction gear. Only a small amount of residual jet thrust is available from the exhaust system.

The turboprop is the most efficient power unit for aircraft intended to fly at moderate speeds and altitudes - nominally up to 720 km/h and 10,000 m.

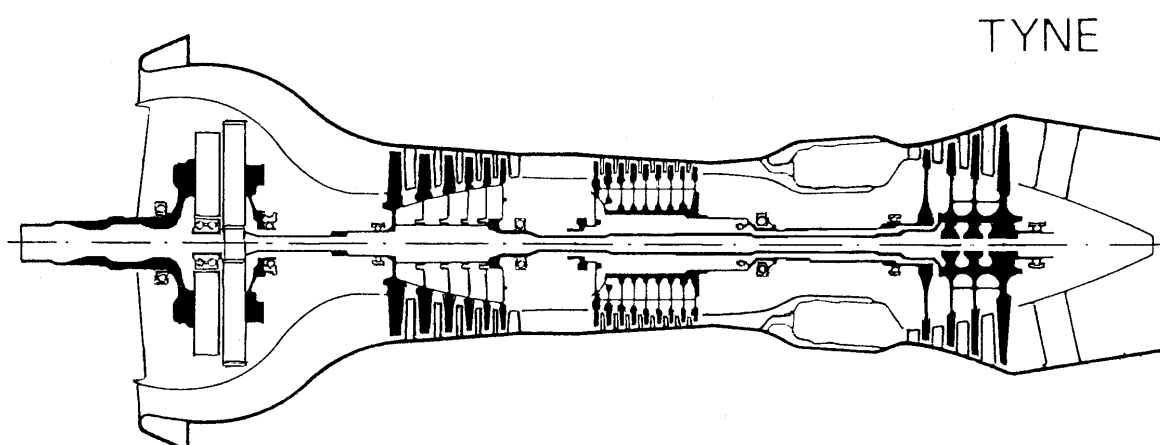


Fig. 6.17 (from [6.7])

Examples are the *Dart* in the HS748, Friendship and Viscount, the *Tyne* (Fig. 6.17) in the Transall C-160 and Antlantic, and the *Proteus* in the Britannia.

6.4.3 Turbofans

In the turbofan (ducted fan) with counter rotating free turbines (Fig. 6.14,d) some of the energy generated by the turbine is used to

drive a fan, which forces air through a streamlined duct to augment the propulsive jet.

The turbofan is the most common derivative of the gas turbine for aircraft propulsion. It combines the advantages of the turbojet and the turboprop. It is a "bypass" engine, where part of the air is compressed fully and passes into the combustion chamber, while the remainder is compressed to a lesser extent and ducted around the hot section.

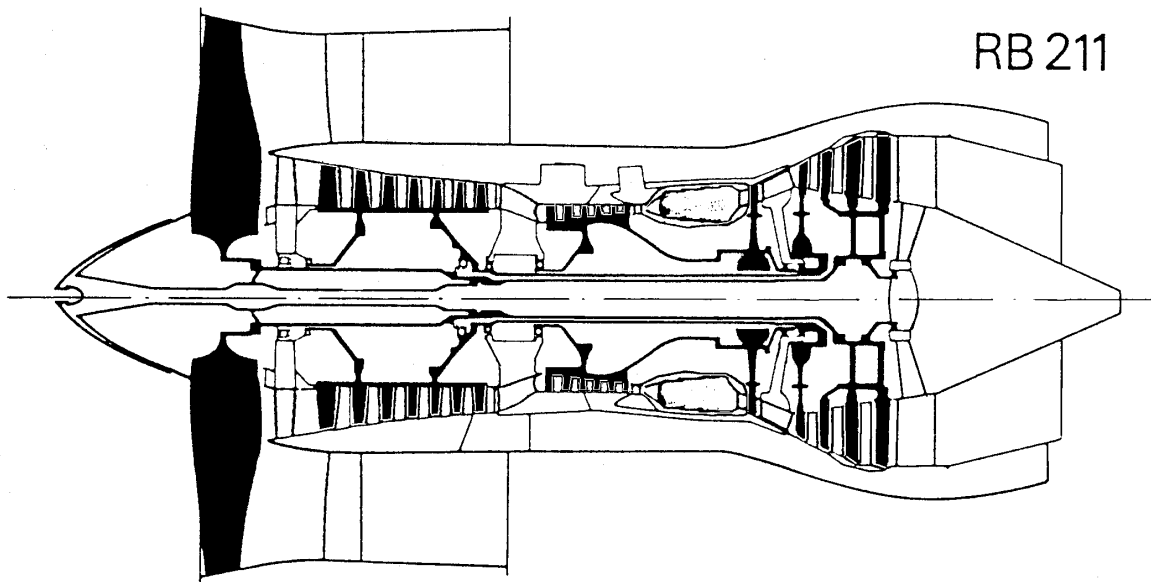


Fig. 6.18 (from [6.7])

This bypass flow either rejoins the hot flow downstream of the turbine, as in the *Spey*, or is exhausted to atmosphere through an annulus surrounding the hot exhaust, as in the *RB211* (Fig. 6.18). In both cases the result is reduced overall jet velocity, giving better propulsive efficiency at lower aircraft speeds, and lower noise levels, features which make the turbofan the obvious choice for modern subsonic airliners.

Examples are the *RB211* in the TriStar and Boeing 747, the *Spey* in the One-Eleven and F28, the *Adour* in the Jaguar and Hawk, and the *RB199* in the Tornado. The *Pegasus* in the Harrier is a variation of the turbofan.

6.4.4. Turboshafths

The turboshaft is virtually a turboprop without a propeller, the power turbine being coupled to a reduction gearbox or directly to an output shaft. As with the turboprop, the power turbine absorbs as much of the remaining gas energy as possible and the residual thrust is very small.

Turboshafts are used in helicopters, where the engine drives both the main and tail rotor, but are also used in ships, locomotives, power stations and pumping equipment, where the engine is a gas generator which drives a separate power turbine carrying an output shaft.

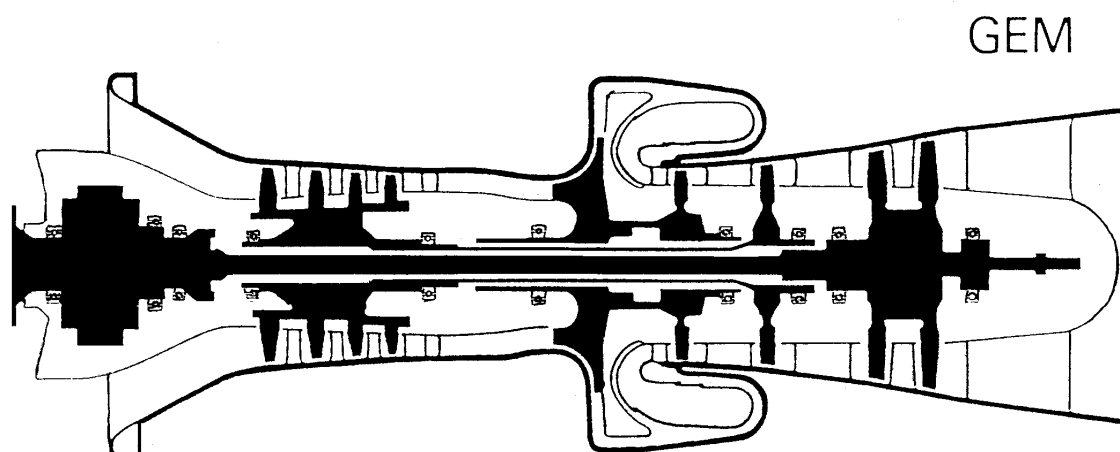


Fig. 6.19 (from [6.7])

Examples are the *Gem* (Fig. 6.19) in the Lynx helicopter and industrial and marine versions of the *RB211* and *Olympus*.

The higher the compression ratio of a modern jet engine the narrower the speed range over which the compressor will run efficiently, if all blades are fixed to the same shaft. To overcome this, the compressor is often split into two or three parts, each part being driven by its own separate turbine.

As a result of this, flexibility of operation is improved, since each section can run at its optimum speed independent of the other. Such arrangements are known as two-spool (or two-shaft) engines typified by the *Olympus*, *Spey* and *Gem* and three-spool (or three-

shaft) engines such the *RB199* and *RB211*. Note that the complete rotating assembly - compressor, shaft and turbine - is known as a 'spool' (Fig. 6.20).

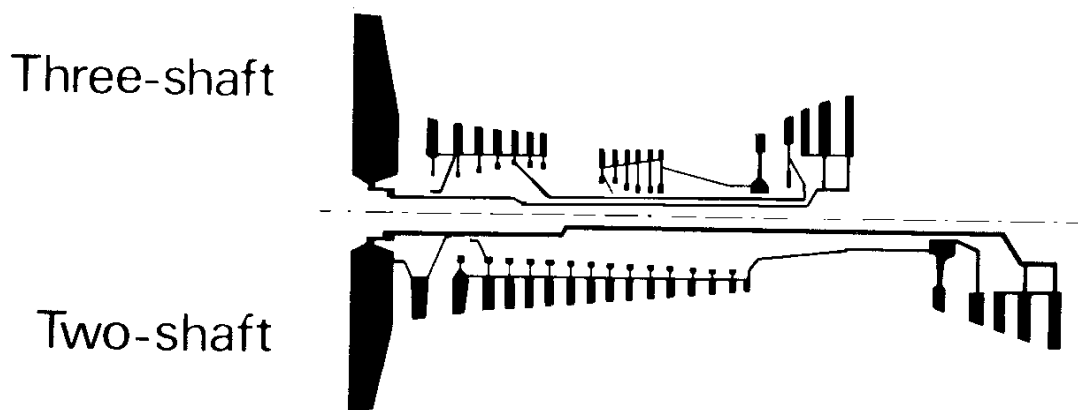


Fig. 6.20 (from [6.9])

Figure 6.21 shows the Rolls-Royce *RB.211* turbofan rotors. The three-stage low pressure (LP) turbine drives the single-stage LP fan which has no inlet guide vanes. The single-stage intermediate pressure (IP) turbine drives the seven-stage IP compressor. The single-stage air-cooled high pressure (HP) turbine drives the six-stage HP compressor.

The eight main bearings are located in four rigid panels (not shown). The three thrust ball bearings are grouped in a stiff intermediate casing. Oil squeeze-film damping is provided between each roller bearing and housing to reduce engine vibration. The short HP system needs only two bearings located away from the combustion zone for longer life.

The single-stage LP fan has 33 blades with mid-span clappers and fir-tree roots. The seven-stage IP axial compressor has drum construction. It consists of seven discs electron beam welded into two drums of five and two stages bolted together between stages 5 and 6. The blade retention is by dovetail roots and lockplates. The six-stage HP compressor consists of two electron beam welded drums bolted

through the stage 3 disc with blades retained by dovetail roots and lockplates.

The three-shaft concept has two basic advantages: simplicity and rigidity. Each compressor runs at its optimum speed, thus permitting a higher pressure ratio per stage. This results in fewer stages and fewer parts, to attain the pressure ratio, than in the case of alternative designs.

The short, large diameter shafts give good vibration characteristics and a very smooth engine. The short carcass and the positioning of the engine mounting points give a very rigid structure. This allows the rotors to run with smaller tip clearances and thus improved efficiency.

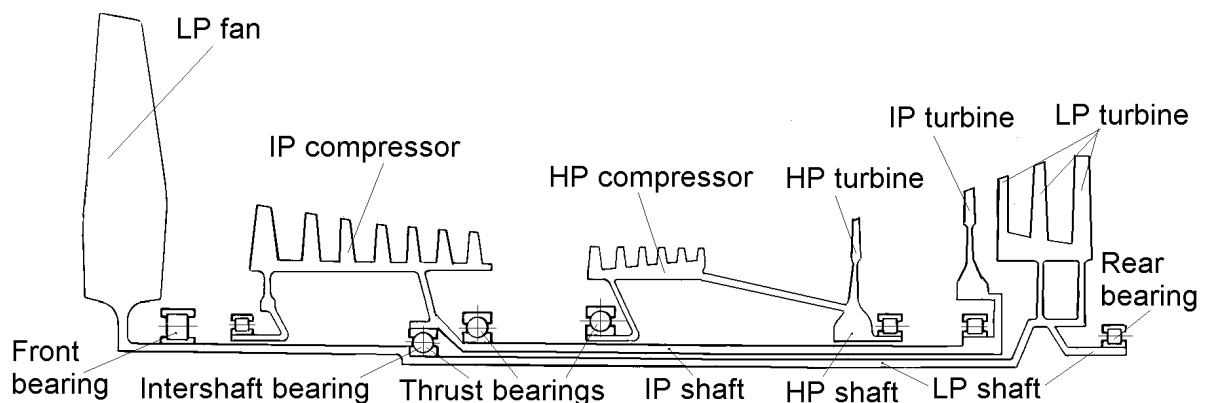
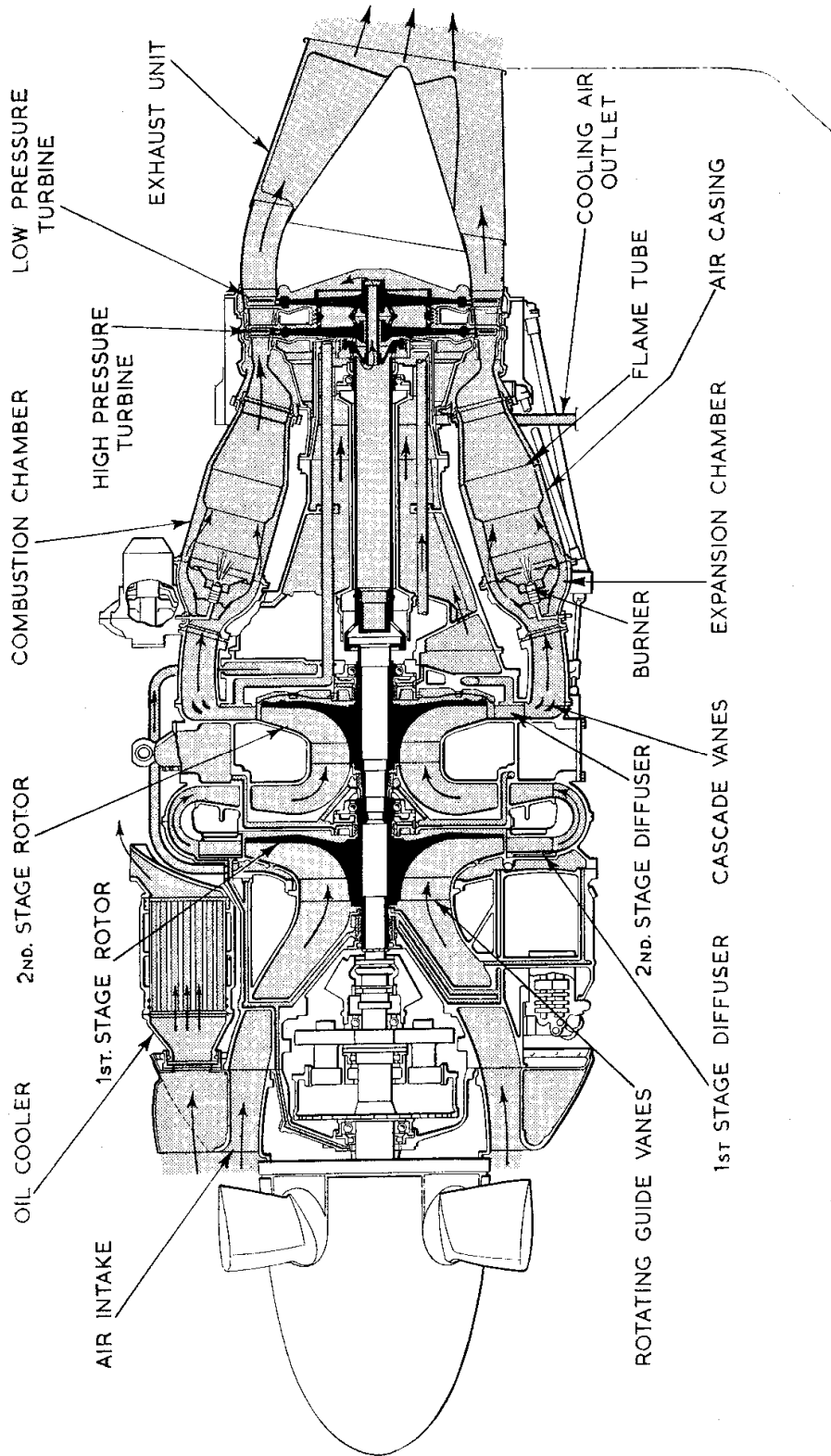


Fig. 6.21 (adapted from [6.9])

Gas turbines manufactured in Romania are: (1) the *Viper 632-41*, Rolls-Royce licence, 8-stage axial compressor and 2-stage turbine at 13,800 rpm; (2) the *Alouette III B*, Turbomeca licence, 422 kW, 33,480 rpm; and (3) the *Turmo IV CA*, Turbomeca licence, 1115 kW.

Note that early turbojets had centrifugal compressors, like the Rolls Royce '*Dart*' engine shown in figure 6.22, but these were replaced by axial compressors, which have higher efficiency, compactness and possibility of developing a high compression ratio in a single casing.



GAS FLOW AND COOLING AIR DIAGRAM OF ROLLS ROYCE DART ENGINE

Fig. 6.22 (from [6.6])

6.5 Exhaust-Gas Turbochargers

Exhaust-gas turbocharging is used to increase the mean effective pressure (m.e.p.) of diesel engines. It has applications in stationary plants for electricity generation, in ships' auxiliary and propulsion machinery and in railway traction.

One of the oldest application was in marine engines. In 1923, BBC and the Vulkan shipyard manufactured turbochargers for the 10-cylinder four-stroke engines from the vessels 'Preussen' and 'Hansestadt Danzig'. The engines, which were designed for an uncharged performance of 1700 HP each at 235 rpm provided, when charged, a cruising power of 2400 HP at 275 rpm and a temporary overload of 4025 HP at 320 rpm (for a m.e.p. = 8.4). Turbocharging of two-stroke marine engines began after 1950.

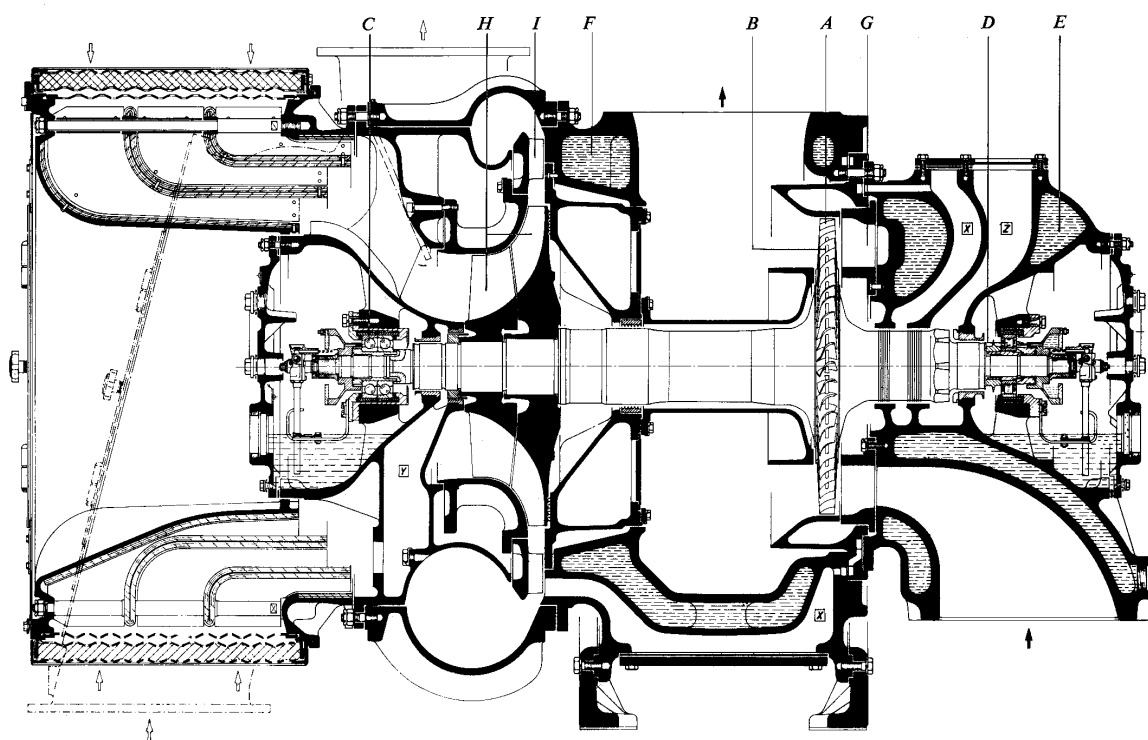


Fig. 6.23 (from [6.10])

Figure 6.23 shows a section of a *VTR400* turbocharger built by BBC. Letters indicate: *A* - turbine blades, *B* - damping wire, *C* - bearing at compressor end, *D* - bearing at turbine end, *E* - gas inlet casing, *F* - gas outlet casing, *G* - nozzle ring/nozzle blades, *H* - inducer and compressor impeller, and *I* - diffuser.

Figure 6.24 shows a cutaway view of the BBC type *VTR501* exhaust-gas turbocharger. The external radial bearings result in minimum loading due to rotor unbalance caused for example by deposits on the turbine blades when using heavy fuel oil.

The calculated first and second critical speeds are about 35 percent and 65 percent of the maximum permitted speed. They are, therefore, passed through any number of times or run through for longish times in the operating range of the turbocharger. But they can only be proved experimentally if particularly significant unbalances are incorporated. With normal amounts of unbalance, the deflections of the shaft are completely damped by the effect of laminations in the bearing assembly. This enables bearings with lower friction to be used, a factor which is important when the engine is run at part load.

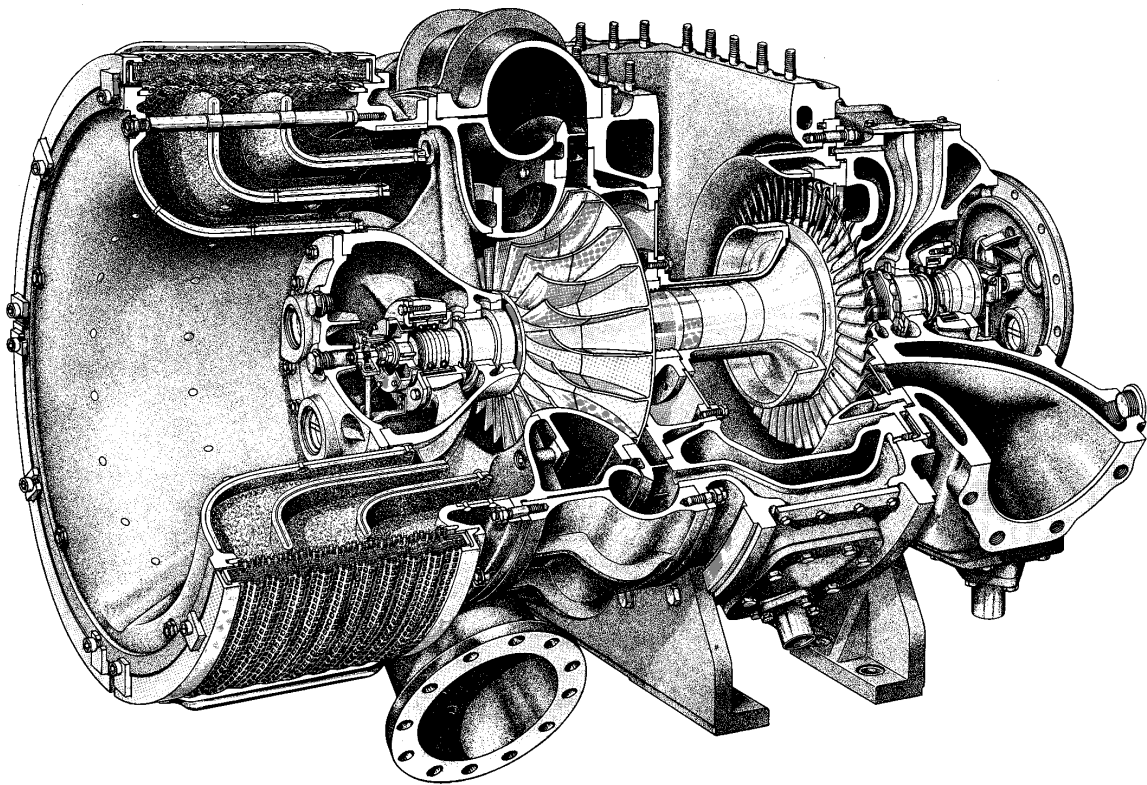


Fig. 6.24 (from [6.11])

The turbine disc and shaft are forged as one piece. The solid design avoids problems with bolted joints and stresses due to discontinuities in composite shafts. This also ensures the maximum possible reliability.

The nozzle ring is designed with a large blade pitch. As a result, it is less susceptible to contamination in service.

Whereas the exhaust-gas turbine produces comparatively little noise, an intensive noise field is produced at the compressor end, particularly in the intake to the diffuser, as a result of the uneven velocity distribution at the outlet from the impeller. The frequency of the so-called 'rotational tone' is given by the product of the angular velocity of the turbocharger and the number of blades on the compressor impeller. The sound energy increases roughly as the fifth power of the speed, so that, as the pressure ratio of compressors increases, anti-noise measures become necessary.

Figure 6.25 shows a longitudinal section through a BBC type *RR* turbocharger where a radial-flow turbine provided with a bladed nozzle ring is used.

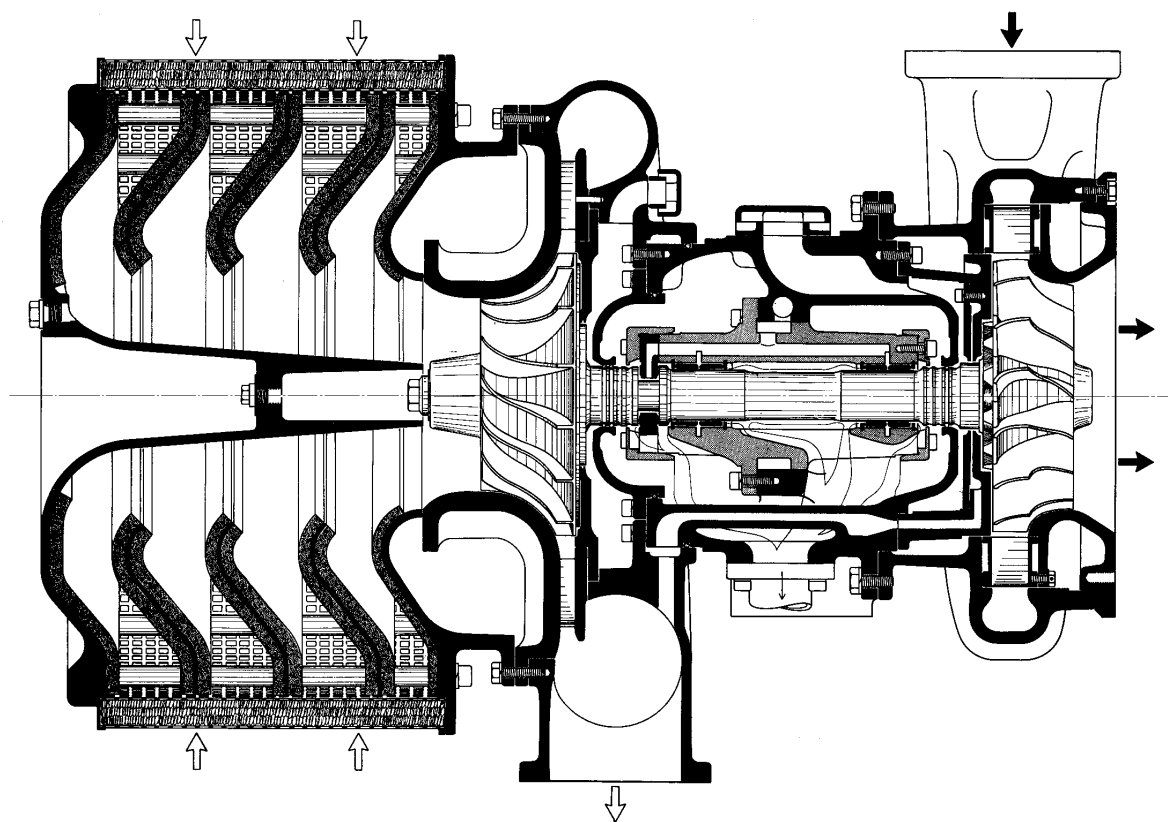


Fig. 6.25 (from [6.12])

For the relatively short turbocharger rotors, which are almost always equipped with single-stage compressor and turbine wheels,

two bearings are sufficient. One of these is a combined radial-axial bearing, the other a pure radial bearing. Two bearing layouts have proved successful on the market: 1) bearings at the shaft ends (external bearings), used predominantly in large machines, and 2) bearings between the compressor and turbine wheel (internal bearings) used mainly for small turbochargers. In both arrangements the axial bearing is located near the compressor wheel, to keep the axial clearance in that region small.

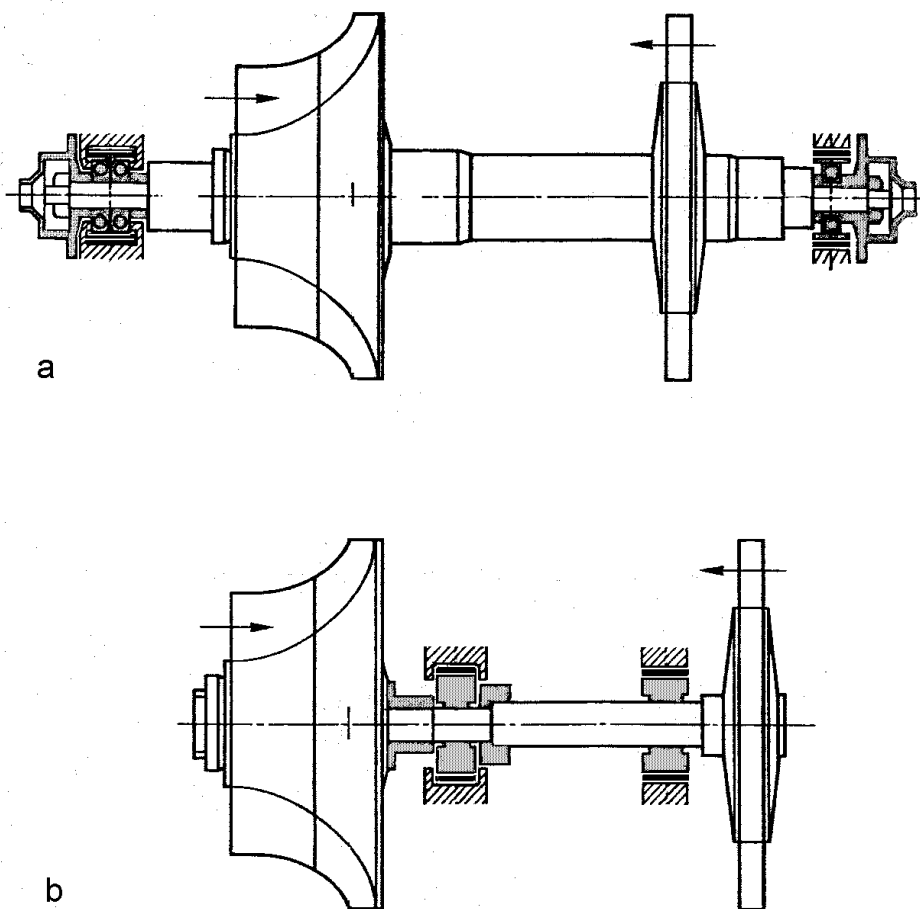


Fig. 6.26

The variant with external bearings (Fig. 6.26,*a*) corresponds to the constructional arrangements from figures 6.23 and 6.24. The large distance between the bearings reduces the radial bearing forces and requires smaller clearances at the compressor wheel and turbine wheel. The frictional losses in the bearings are smaller, particularly at part load. The shaft ends can be kept small in diameter and are simple

to equip with a lubricating oil pump and centrifuge, thus rendering rolling-contact bearings and self-lubrication possible.

The variant with internal bearings (Fig. 6.26,*b*) corresponds to the turbocharger from figure 6.25. Internal bearings offer advantages in fitting a turbocharger with axial air and gas inlets to the engine. Small turbochargers do not, however, have an axial-flow turbine, but a radial-flow turbine with axial gas outlet. For specific applications internal bearings have advantages, which relate mainly to the wider variety of ways of fitting the turbocharger to the engine.

6.6 Gas Turbine Rotor Designs

Early designs of gas turbine rotors are illustrated in figures 6.27 to 6.32. Monoblock rotors used in low power turbines are shown in figures 6.27 and 6.28.

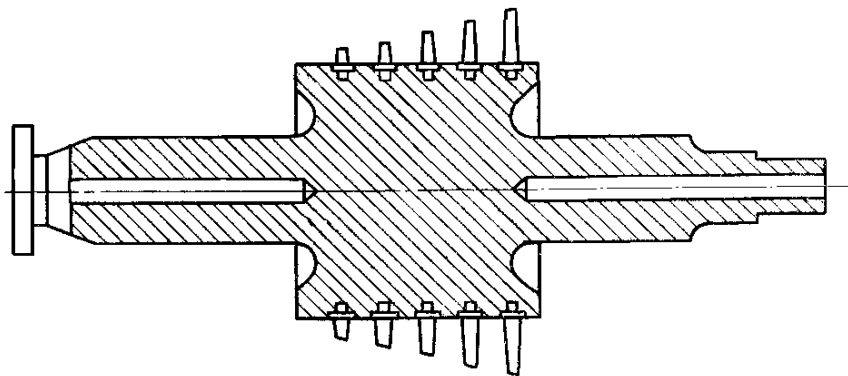


Fig. 6.27 (from [6.13])

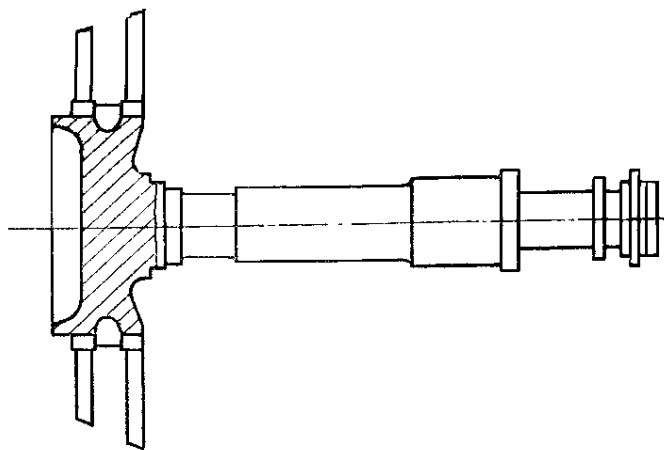


Fig. 6.28 (from [6.13])

The drum rotor from figure 6.27 has a middle section without centre bore to avoid high stresses due to centrifugal loading. The overhung design from figure 6.28 is obsolete, though there are still operating turbines with this design.

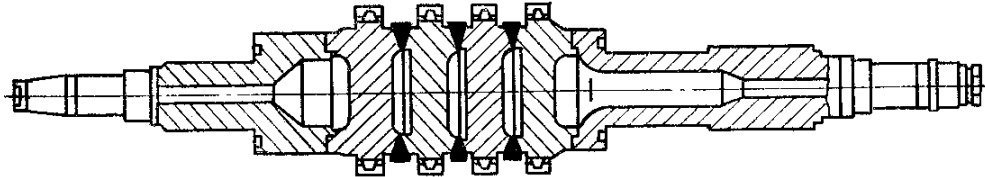


Fig. 6.29 (from [6.13])

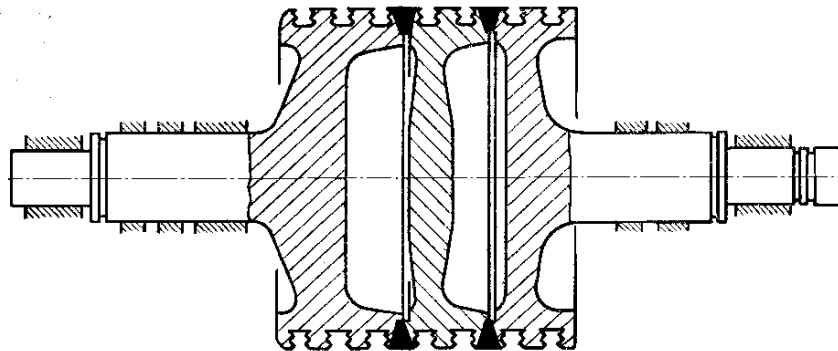


Fig. 6.30 (from [6.13])

Welded rotors are shown in figures 6.29 and 6.30. They have no central bore, hence lower stresses due to centrifugal load, and also lower transient thermal stresses.

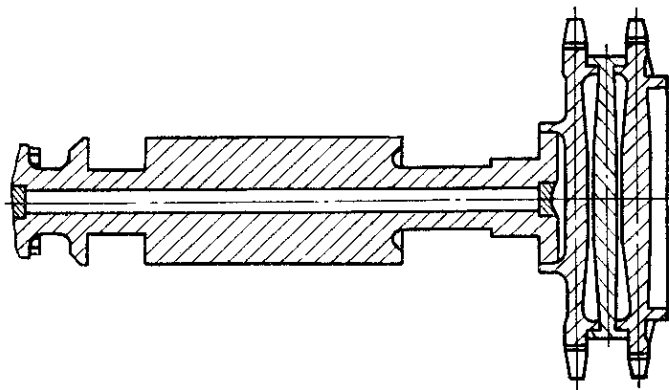


Fig. 6.31 (from [6.13])

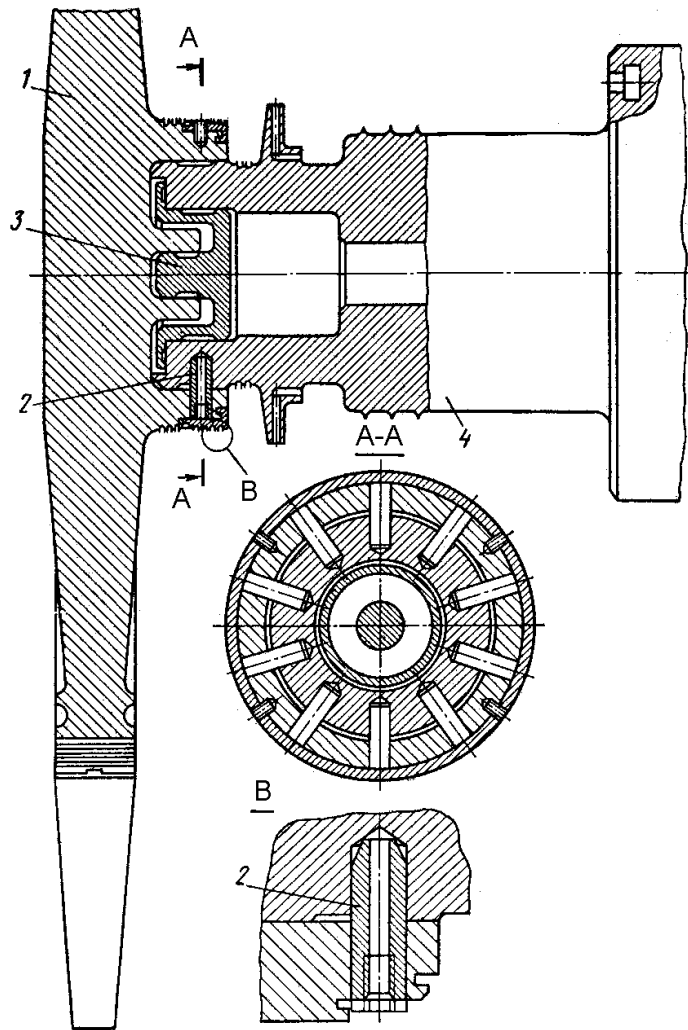


Fig. 6.32 (from [6.14])

Gas turbine rotors with overhung discs are shown in figures 6.31 and 6.32. In the latter design the discs are mounted using radial studs or bolts.

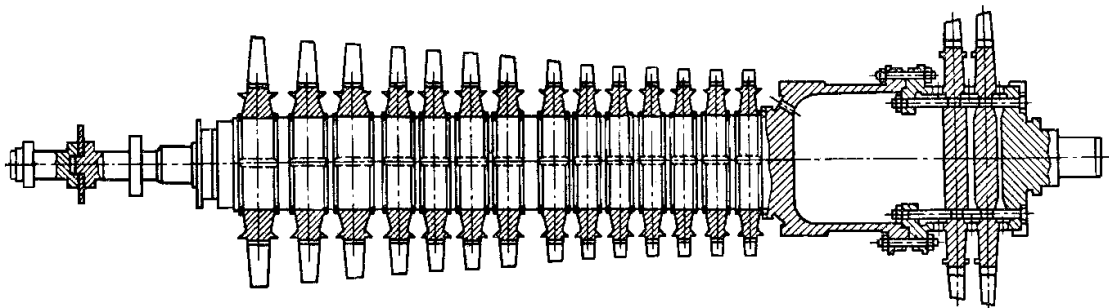


Fig. 6.33 (from [6.14])

The single-shaft rotor of the KTZ type *GTU-9* gas turbine with axial compressor is shown in figure 6.33.

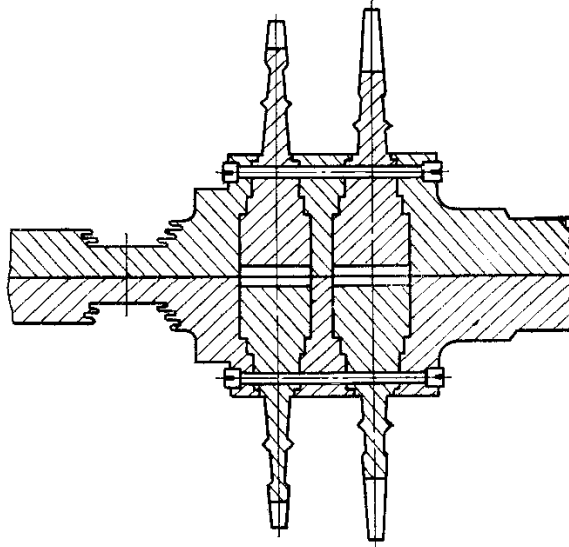


Fig. 6.34 (from [6.13])

Built-up rotors with discs assembled by multiple axial tension bolts are shown in figures 6.34 to 6.36.

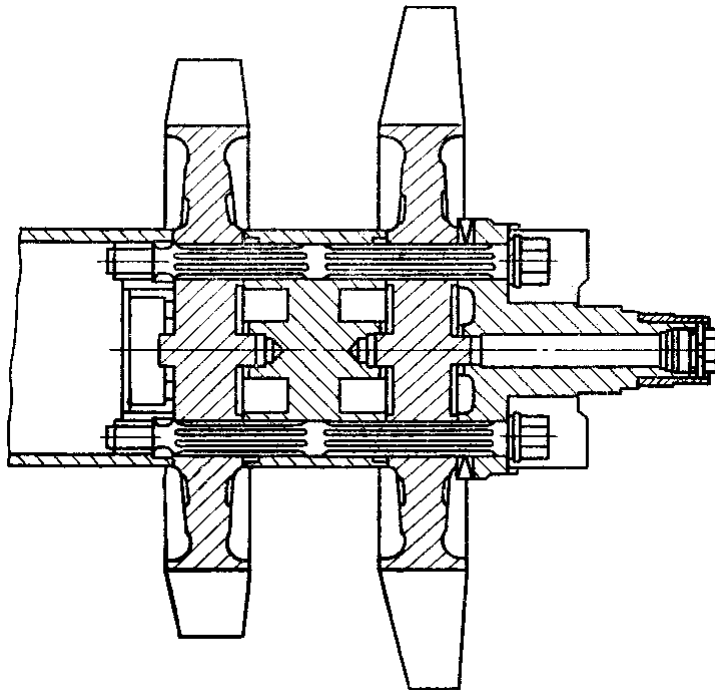


Fig. 6.35 (from [6.13])

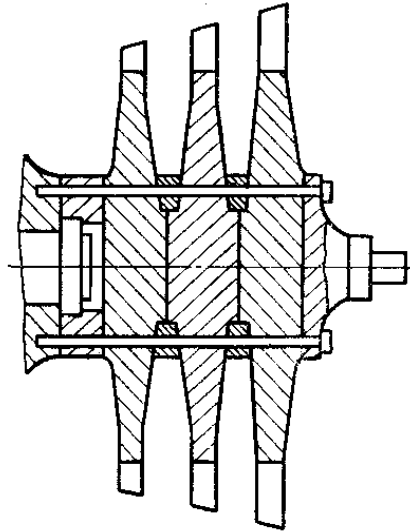


Fig. 6.36 (from [6.13])

Other disc rotors with multiple axial tension bolts are shown in figures 6.37 and 6.39

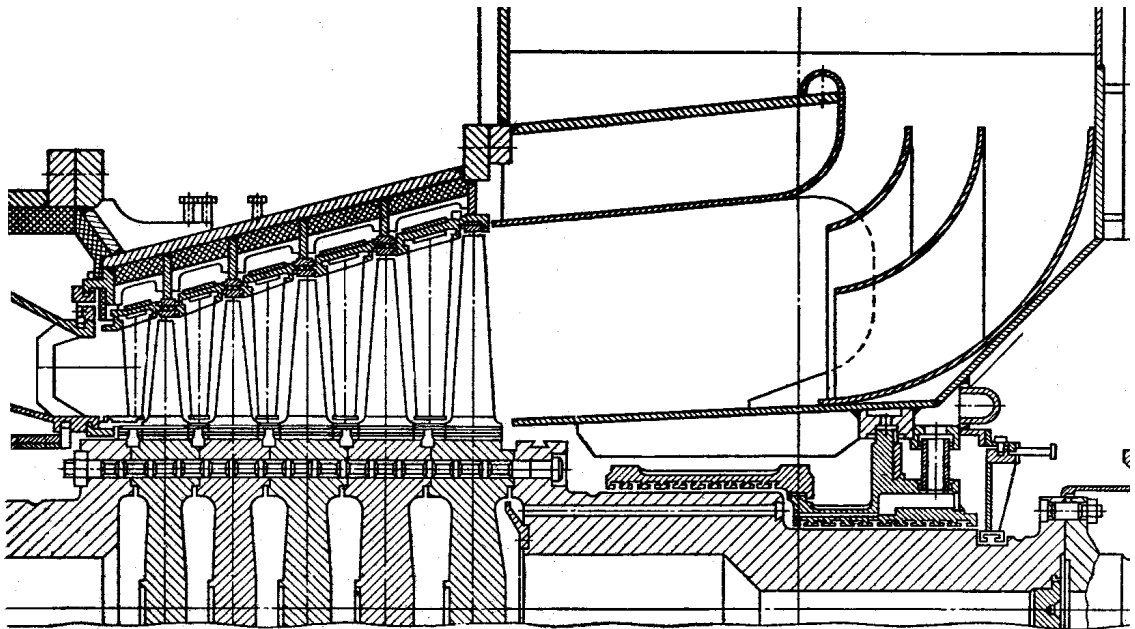


Fig. 6.37 (from [6.14])

The built-up rotor of the KTZ type *GTU-6* gas turbine (Fig. 6.40) has a single central tension bolt and a compensator.

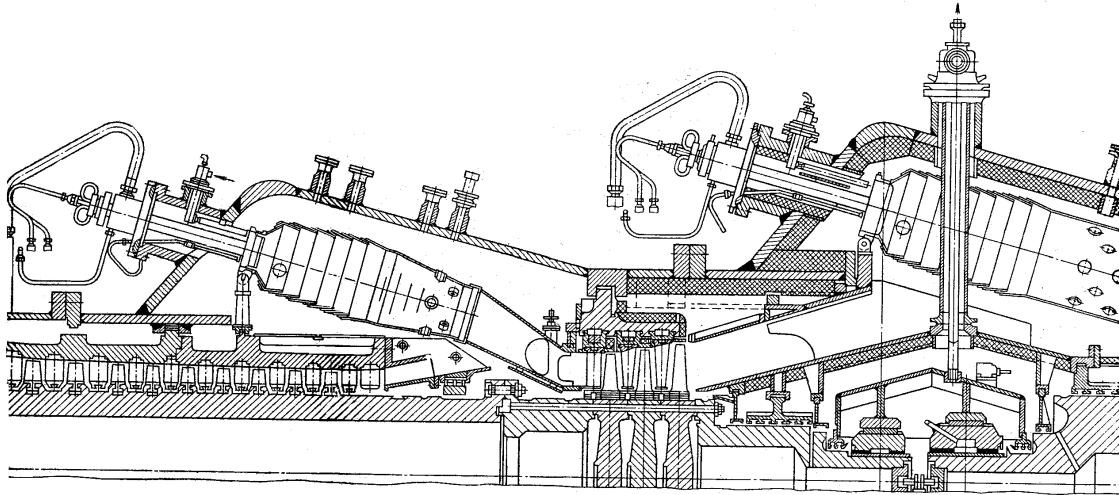


Fig. 6.38 (from [6.14])

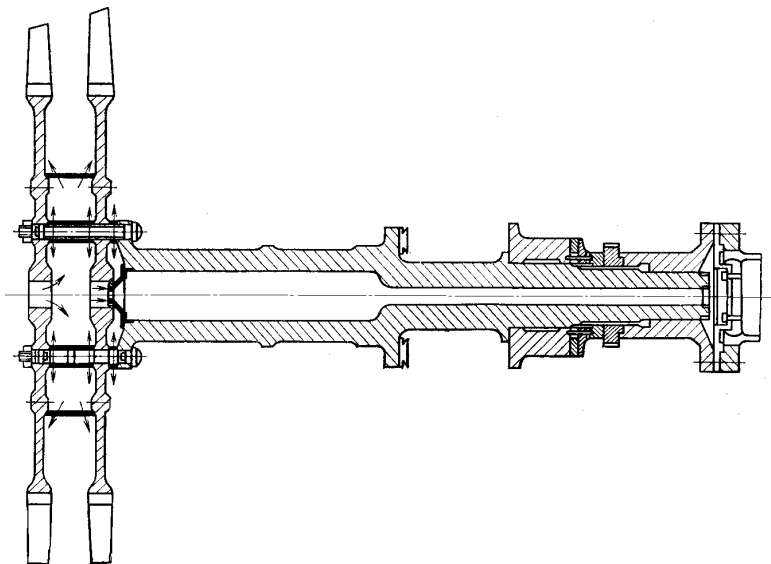


Fig. 6.39 (from [6.13])

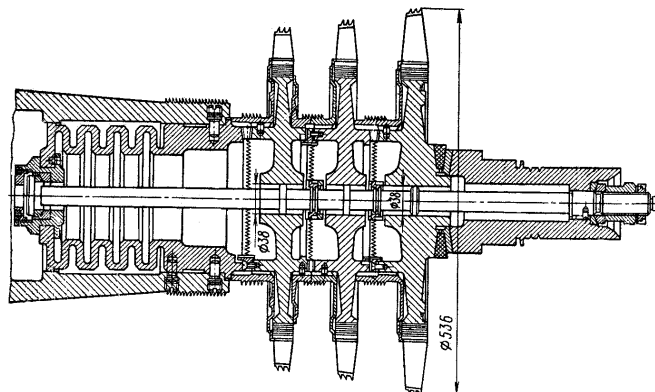


Fig. 6.40 (from [6.14])

A longitudinal section of a modern stationary gas turbine is presented in figure 6.41. The design has two combustion chambers, each with a single burner, a two-stage low pressure turbine and a two-stage high pressure turbine directly coupled with the axial compressor shaft.

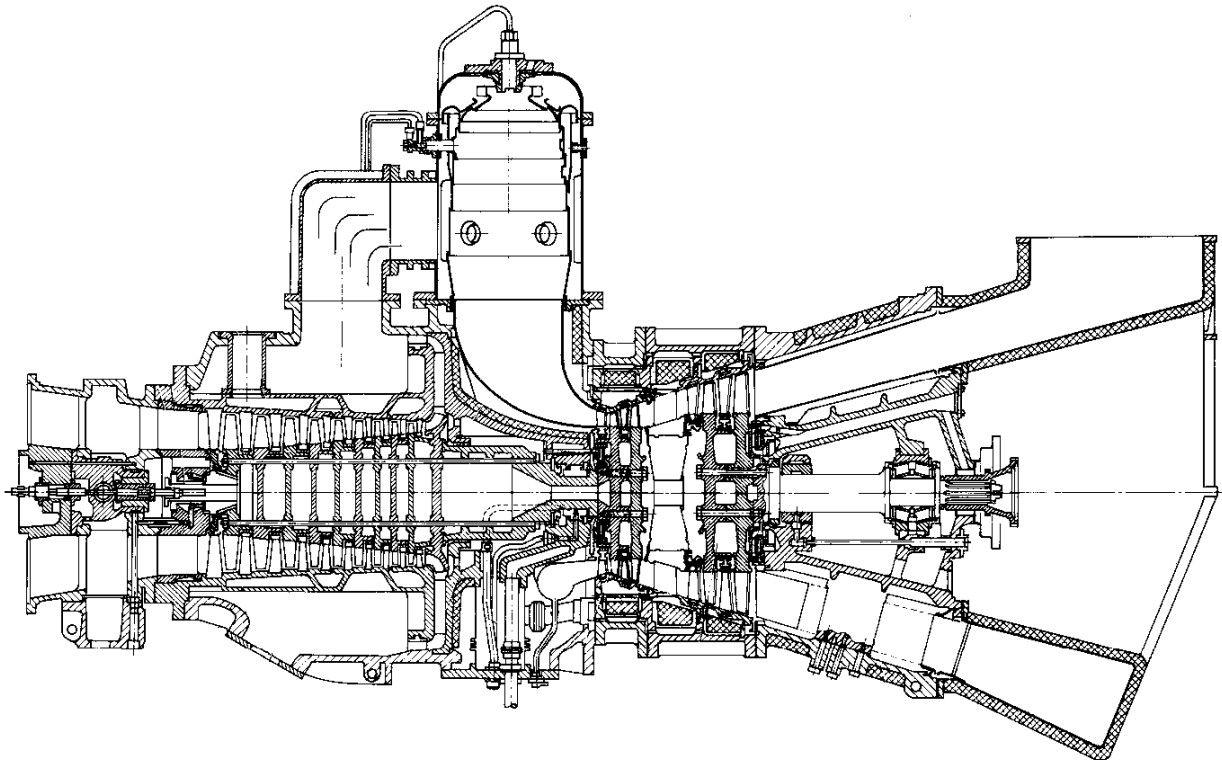


Fig. 6.41 (from [6.15])

6.7 Numerical Example

A two-spool gas engine is shown schematically in figure 6.42 [6.16]. The basic engine consists of an inner rotor, called the power turbine rotor, and an outer rotor, called the gas generator rotor. The inner rotor is supported by two main bearings located near the shaft ends.

The two-stage gas generator turbine rotor, which drives the axial compressor, is supported by four rolling element bearings. There are three intermediate bearings connecting the inner power turbine rotor to the outer gas generator rotor.

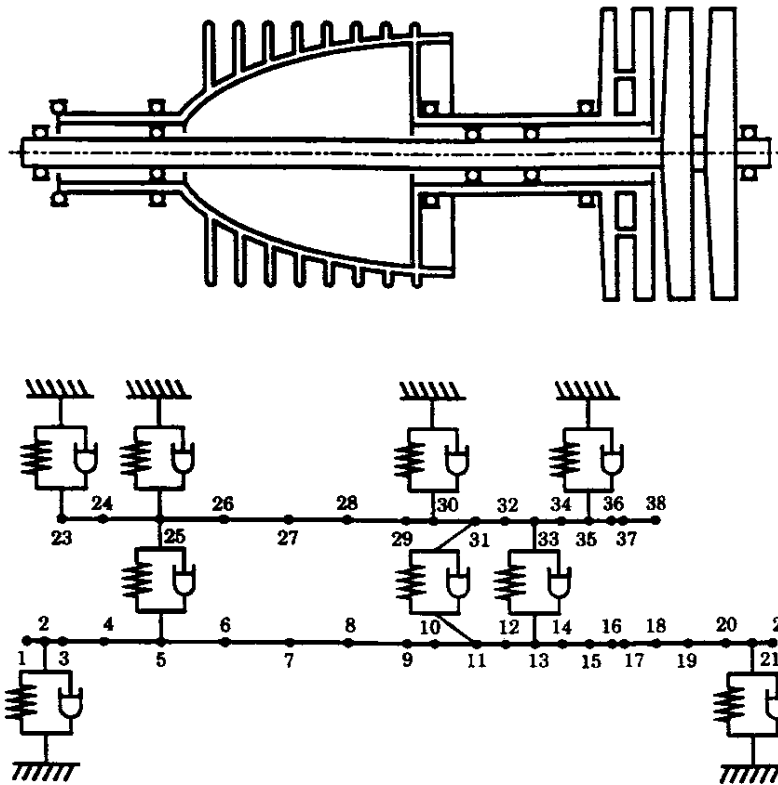


Fig. 6.42 (from [6.16])

The power turbine and gas generator rotors are modelled as 21 and 15 rotating shaft elements, respectively. The whole model has 38 nodes and a total of 152 degrees of freedom. The disc data are given in Table 6.1, the cross-sectional properties of the engine are listed in Table 6.2 and the bearing properties are given in Table 6.3 [6.16].

Table 6.1

Disc data of a two-spool aircraft engine

Disc number	Disc location	M_d (kg)	I_p (kg m ²)	I_d (kg m ²)
1	1	0.227	0.0000	0.0000
2	2	0.454	0.0000	0.0000
3	3	0.454	0.0000	0.0000
4	19	12.26	0.1831	0.0915
5	20	13.62	0.2063	0.1032
6	21	0.908	0.0000	0.0000
7	25	3.387	0.0325	0.0163
8	26	5.235	0.0871	0.0436
9	27	1.693	0.0883	0.0442
10	28	3.482	0.0680	0.0340
11	29	0.000	0.0343	0.0171
12	37	11.35	0.1794	0.0897
13	38	11.35	0.1757	0.0879

The rotor system is by nature divided into two components, the power turbine rotor and the gas generator rotor. The inter-shaft bearings between them act as flexible interface elements.

The natural frequencies of the two components are listed in Table 6.4. Since both rotors have isotropic bearings, only undamped non-rotating modes in one plane need to be calculated.

Table 6.2

Element data of a two-spool aircraft engine ($\rho = 7840 \text{ kg/m}^3$)

Element number	Node number	$E \text{ (N/m}^2\text{)}$	Length (mm)	Inner diameter (mm)	Outer diameter (mm)
1	1-2	2.070×10^{11}	33.020	38.862	53.340
2	2-3	2.070×10^{11}	33.020	38.862	53.340
3	3-4	2.070×10^{11}	76.200	38.862	53.340
4	4-5	2.070×10^{11}	109.22	38.862	53.340
5	5-6	2.070×10^{11}	121.92	45.720	58.420
6	6-7	2.070×10^{11}	121.92	45.720	58.420
7	7-8	2.070×10^{11}	111.76	33.020	45.720
8	8-9	2.070×10^{11}	111.76	33.020	45.720
9	9-10	2.070×10^{11}	53.340	33.020	45.720
10	10-11	2.070×10^{11}	78.740	33.020	45.720
11	11-12	2.070×10^{11}	53.340	33.020	45.720
12	12-13	2.070×10^{11}	53.340	33.020	45.720
13	13-14	2.070×10^{11}	50.800	35.560	66.040
14	14-15	2.070×10^{11}	53.340	35.560	66.040
15	15-16	2.070×10^{11}	43.180	35.560	66.040
16	16-17	2.070×10^{11}	22.860	35.560	66.040
17	17-18	2.070×10^{11}	60.960	39.878	57.150
18	18-19	2.070×10^{11}	60.960	39.878	57.150
19	19-20	2.070×10^{11}	71.120	39.878	57.150
20	20-21	2.070×10^{11}	50.800	38.100	45.720
21	21-22	2.070×10^{11}	38.100	38.100	83.820
22	23-24	2.070×10^{11}	76.200	60.960	71.120
23	24-25	2.070×10^{11}	109.22	62.230	77.470
24	25-26	2.070×10^{11}	121.92	278.64	279.40
25	26-27	1.035×10^{11}	121.92	275.84	279.40
26	27-28	0.883×10^{11}	111.76	274.07	279.40
27	28-29	1.332×10^{11}	111.76	275.84	279.40
28	29-30	1.884×10^{11}	53.340	71.120	97.790
29	30-31	2.070×10^{11}	78.740	73.660	86.106
30	31-32	2.070×10^{11}	53.340	81.280	91.440
31	32-33	2.070×10^{11}	53.340	81.280	91.440
32	33-34	2.070×10^{11}	50.800	81.280	91.440
33	34-35	2.070×10^{11}	53.340	85.090	91.440
34	35-36	2.070×10^{11}	43.180	85.090	93.980
35	36-37	2.070×10^{11}	22.860	95.090	106.68
36	37-38	2.070×10^{11}	60.960	228.60	238.76

Table 6.3

Bearing data of a two-spool aircraft engine

Bearing number	Bearing location	$K_{xx} = K_{yy}$ (N/m)	$C_{xx} = C_{yy}$ (N s/m)
1	2-0	8.7672×10^7	350.69
2	21-0	1.0521×10^7	350.69
3	23-0	1.7534×10^8	350.69
4	25-0	1.7534×10^8	350.69
5	30-0	8.7672×10^7	350.69
6	35-0	2.1567×10^7	17.534
7	5-25	8.7672×10^7	350.69
8	13-33	8.7672×10^7	350.69
9 (squeeze film bearing)	11-31	$K_{xx} = 1.7960 \times 10^6$ $K_{xy} = 1.9817 \times 10^6$ $K_{yz} = -3.5379 \times 10^6$ $K_{yy} = 1.3470 \times 10^6$	$C_{xx} = 1457.1$ $C_{xy} = -590.91$ $C_{yx} = -590.91$ $C_{yy} = 1923.5$

Table 6.4

Damped frequencies of a two-spool aircraft engine

Mode order	FEM, 152 DOF	Damped whirl frequencies (rpm)					
		12 DOF	Error (%)	18 DOF	Error (%)	28 DOF	Error (%)
1b	5 932.36	5 938.86	0.110	5 936.34	0.067	5 933.38	0.017
1f	6 983.12	6 980.81	-0.033	6 983.07	-0.001	6 983.26	0.002
2b	6 175.19	6 190.55	0.249	6 177.00	0.029	6 174.51	-0.011
2f	8 938.09	9 004.05	0.738	8 947.28	0.103	8 935.84	-0.025
3b	10 107.0	10 178.1	0.704	10 126.8	0.196	10 111.2	0.042
3f	20 853.2	21 103.9	1.203	20 864.7	0.055	20 854.8	0.008
4b	18 751.0	18 854.0	0.550	18 750.5	-0.003	18 744.7	-0.034
4f	30 402.9	31 244.7	2.769	30 567.8	0.542	30 429.0	0.086
5b	26 094.3	27 413.1	5.055	26 108.7	0.056	26 083.4	-0.041
5f	33 939.7	35 950.1	5.924	34 080.5	0.415	33 979.0	0.116
6b	33 766.2	41 855.7	23.96	33 771.3	0.015	33 756.0	-0.030
6f	40 776.4	45 546.0	11.70	41 096.6	0.785	40 790.8	0.035
7b	36 913.1			37 278.2	0.989	36 923.5	0.028
7f	58 025.7			58 290.3	0.456	58 003.6	-0.038
8b	51 624.9			54 467.4	5.506	51 610.4	-0.028
8f	60 500.6			62 421.9	3.176	60 494.7	-0.010
9b	61 157.3			63 852.9	4.408	61 032.5	-0.204
9f	66 192.8			69 297.7	4.691	66 221.9	0.044
10b	66 143.5					66 144.4	0.044
10f	71 136.4					71 121.9	-0.020
11b	78 828.1					78 835.8	0.010
11f	82 968.1					83 002.3	0.041
12b	103 763					103 809	0.044
12f	106 718					106 746	0.027
13b	105 147					105 184	0.034
13f	109 009					109 030	0.019
14b	109 182					109 122	-0.054
14f	116 982					116 979	-0.002

6.8 Guidelines for Vibration Limits

Gas turbines may have several modes of vibration in their service speed range. Their responses due to unbalance, misalignments, thermal bows, rubs, and the unloading of bearings can be better observed by measurements on the shafts.

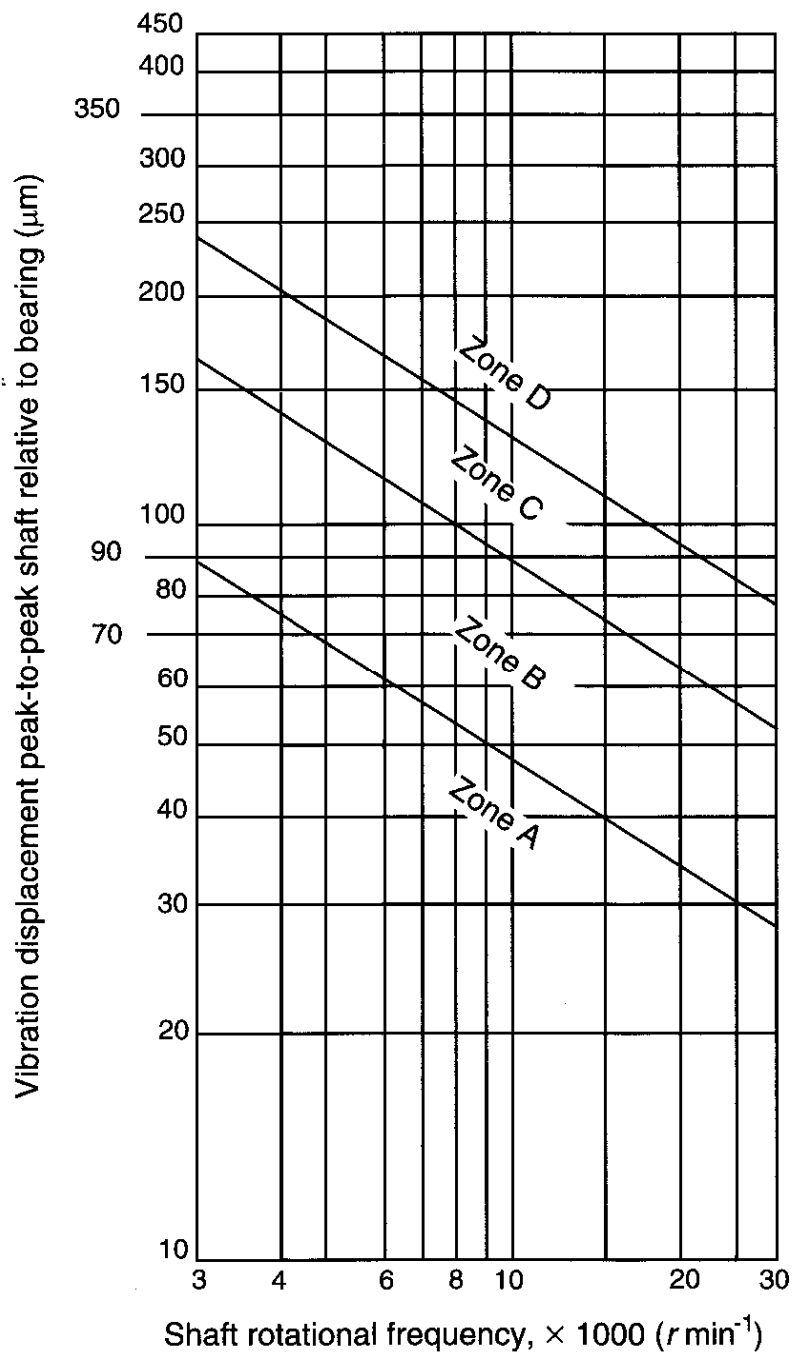


Fig. 6.43 (from [6.17])

The vibration levels specified by *ISO 7919, Part 4* [6.17] apply to industrial gas turbine sets (including those with gears) with fluid film bearings, power outputs greater than 3 MW, and shaft rotational speeds from 3000 to 30,000 rpm. Aircraft type gas turbines are excluded, since they differ fundamentally from industrial gas turbines, both in the types of bearing (rolling element), and in the stiffness and mass ratios of the rotors and support structures. Depending on the construction and mode of operation, three types of industrial gas turbines are considered: 1) single-shaft constant-speed; 2) single-shaft variable-speed; and, 3) gas turbines having separate shafts for hot-gas generation and power delivery.

Guidelines are given in figure 6.43 for the application of shaft vibration criteria measured close to the bearings of industrial gas turbines under normal operating conditions. The numerical values specified in the figure represent rotor displacements relative to bearings in micrometers peak-to-peak vs shaft rotational speed in rpm. Zone *A* represents new machines that can be operated without restriction. Zone *B* is acceptable for long-term operation. Zone *C* represents machines that may be operated for a limited time until a suitable opportunity arises for remedial action to be taken. Zone *D* is identified as a trip level as these values are considered to be of sufficient severity to cause damage.

Specific guidance for assessing the severity of vibrations measured on the bearing housings or pedestals of gas turbine sets are given in *ISO 10816, Part 4* [6.18]. This standard applies to heavy-duty gas turbines used in electrical and mechanical drive applications covering the power range *above 3 MW*, and a speed range under load between 3000 and 20,000 rpm. Generally, the criteria apply to both the gas turbine and the driven equipment. However, for generators above 50 MW, the criteria of *ISO 10816, Part 2* [6.19] should be used.

For compressors in the power range from 30 to 300 kW, the criteria of *ISO 10816, Part 3* [6.20] should be used for assessing vibration severity.

The evaluation of zone boundaries based on bearing housing/pedestal vibration for industrial gas turbines is given in Table

6.5 [6.18]. These criteria assume that the gas turbines incorporate fluid film bearings, and the vibration measurements are broadband values taken *in situ* under normal steady-state operating conditions. This Standard encompasses machines which may have gears or rolling element bearings, but does not address the evaluation of the condition of those gears or bearings. The zone descriptions are the same as in *ISO 7919* described above.

Table 6.5

Shaft	Zone Boundary		
	A/B	B/C	C/D
Rotational			
Speed, rpm	Vibration Velocity, mm/s (RMS)		
3000 – 20,000	4.5	9.3	14.7

For industrial gas turbines with power up to 3 MW the recommended vibration levels are given in the standard *ISO 10816, Part 3* [6.20].

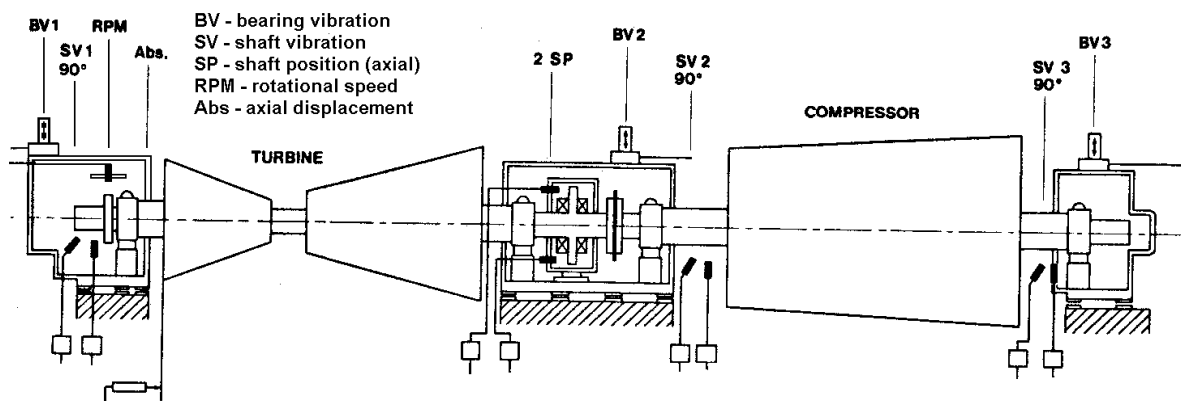


Fig. 6.44 (from [6.21])

A schematic view of the location of sensors for the condition monitoring of a gas turbine set is shown in figure 6.44. Proximity eddy current sensors are used to measure the journal displacement relative to the bearing, while seismic pick-ups are used to measure the absolute rms velocity of bearing housing.

6.9 Final Remarks

Ecological as well as economic benefits, including lower investment and power generation costs, shorter plant construction times, high availability and low emissions, are the reasons for the present upsurge of interest in stationary gas turbines and combined cycle power plants [6.1]. An increase in the unit rating and thermal efficiency, in parallel with acceptable emission levels and a rugged design, will continue to be the main focal points.

Advanced high-temperature gas turbines are characterized by an annular combustor configuration with dual burners and a compressor with rows of variable guide vanes. The design of the gas turbine is based on computer programs and design specifications which have been systematically developed and validated. Tests are performed on models as well as on original parts and components.

For compressors, the design priorities include a) higher stage pressure ratios, b) development of blade profiles with multiple circular arcs and controlled diffusion, and c) reduction of secondary and tip clearance losses. For combustors, the emphasis is on a) low emission levels, b) development of burner technology, and c) better matching of burners with the combustion chamber. For turbines, the priorities are a) higher mass flows and inlet temperatures, b) design of low-loss profiles for the turbine cascades, c) optimization of blade cooling, and d) development of coatings for protection against high-temperature corrosion and oxidation.

As for the gas turbine rotors, continuous development work and years of experience have shown that both the welded construction and the traditional design with discs held together by pretensioned bolts are robust in operation. The rotor cooling, which protects the rotor from the hot gas, and the slow, controlled warm-up during cold starting (to keep the thermal stresses low) are important rotor design criteria. Special heat shields are used to protect the shaft from the high thermal loading. New materials with good behaviour to low cycle fatigue and creep are under development.

Modern high-temperature gas turbines are employed with waste heat recovery boilers in combined cycle plants. Since the generator drive is located on the cold side of the compressor, the entire turbine torque is transmitted via the compressor to the generator. Welded or bolted rotors are used to transmit the torque. Obsolete designs, where the torque was transmitted only by friction via the discs, had caused difficulties in the past.

Combined cycle processes, sequential combustion, flow optimization using computational fluid dynamics codes, further development of high-grade materials and protective coatings are expected to enable gas turbine manufacturers to achieve, in the near future, the goal of 60 percent thermal efficiency without compromising power plant availability.

References

- 6.1 Mukherjee D.K., *State-of-the-Art Gas Turbines - a Brief Update*, ABB Review, vol.84, nr.2, pp 4-14,1997.
- 6.2 * * * *Turbine à gaz de 6000 kW de l'Electricité de France (E.D.F.) à St-Dizier*, Revue Brown Boveri, vol.47, nr.1/2, pp 37-42, 1960.
- 6.3 *Fonctionnement et structure de la turbine à gaz Brown Boveri*, Revue Brown Boveri, vol.44, nr.4/5, pp 190-215, 1957.
- 6.4 Kehlhofer R., *300 MW Combined Cycle Plant with Integrated Coal Gasification*, Brown Boveri Review, vol.72, nr.10, pp 440-448, 1985.
- 6.5 * * * MS9001FA – *The World's Most Powerful 50 Hz Gas Turbine*, GED-7124, GE Industrial & Power Systems.
- 6.6 Cox H.R. (ed), **Gas Turbine Principles and Practice**, George Newnes Ltd., London, 1955.
- 6.7 * * * **How Does a Jet Engine Work?**, Rolls-Royce Publ. TJ427, 1978.
- 6.8 * * * **Military VIPER Turbojet**, Rolls-Royce Publ. TJ 392/5 SSL 1 7058, 1978.
- 6.9 * * * **RB.211 Technology & Description**, Rolls-Royce Publ. TS2100, Issue 18, Nov.1977.
- 6.10 de Pietro W., *Experience in Service with Exhaust-Gas Turbochargers of the VTR Series*, Brown Boveri Review, vol.64, nr.4, pp 247-252, 1977.

- 6.11 Zehnder G. and Meier E., *Exhaust-Gas Turbochargers and Systems for High-Pressure Charging*, Brown Boveri Review, vol.64, nr.4, pp 201-214, 1977.
- 6.12 Muller R., *Experience with the RR Turbocharger*, Brown Boveri Review, vol.64, nr.4, pp 243-246, 1977.
- 6.13 Kostyuk A.G. and Frolov V.V. (eds), **Steam and Gas Turbines** (in Russian), Energoatomizdat, Moskow, 1985.
- 6.14 Smolenskii A.N., **Steam and Gas Turbines** (in Russian), Mashinostroenie, Moskow, 1977.
- 6.15 Gašparović N., Gasturbinen, in **Dubbel. Taschenbuch für den Maschinenbau**, 17.Auflage, Springer, pp R75-R91, 1990.
- 6.16 Wang W. and Kirkhope J., *Component Mode Synthesis for Multi-Shaft Rotors with Flexible Inter-Shaft Bearings*, Journal of Sound and Vibration, vol.173, nr.4, pp 537-555, 1994.
- 6.17 **ISO 7919-4**, Mechanical Vibration of Non-Reciprocating Machines – Measurements on Rotating Shafts and Evaluation Criteria – Part 4: *Gas Turbine Sets. for Gas-Turbines*, 1996.
- 6.18 **ISO 10816-4**, Mechanical Vibration – Evaluation of Machine Vibration by Measurements on Non-Rotating Parts – Part 4: *Gas Turbine Sets Excluding Aircraft Derivatives*, 1996.
- 6.19 **ISO 10816-2**, Mechanical Vibration – Evaluation of Machine Vibration by Measurements on Non-Rotating Parts – Part 2: *Large Land-Based Steam Turbine Generator Sets in Excess of 50 MW*, 1996.
- 6.20 **ISO 10816-3**, Mechanical Vibration – Evaluation of Machine Vibration by Measurements on Non-Rotating Parts – Part 3: *Industrial Machines with Normal Power above 15 kW and Nominal Speeds Between 120 and 15,000 rpm when Measured In-Situ*, 1996.
- 6.21 * * * **Machine Monitoring Systems**, Philips Catalogue 79/80, *Equipment for Electronic Measurement of Mechanical Quantities*, 1979.

7. STEAM TURBINES

7.1 Introduction

Steam turbines, like gas turbines, are predominantly axial-flow units. They are used extensively in power plants to drive electric generators, as are gas turbines, but they are usually much larger than gas turbines. In addition, the large units typically use much higher pressures in the first stages and lower pressures in their later stages than do the large gas turbines.

Steam turbines are used in various industrial sectors such as the papermaking, iron and steel, sugar and foodstuffs industries, the chemical industry including petrochemicals, sea water desalinization plants, refuse combustion plants and in district heating power plants.

An extremely wide range of applications is covered, from the high-speed geared turbine through directly-coupled compressor and pump drives to the standard-speed generator prime mover, from the simple back-pressure turbine through extraction and double extraction machines to the pure condensing turbine [7.1].

7.2 Basic Principles

There are two general types of turbine stages [7.2]. One is the *impulse stage* shown in figure 7.1,*a*. In this stage, all of the pressure energy is converted to velocity in the nozzle, and this resulting high velocity stream impinges on U-shaped blades in the rotor. The purpose of the moving blade is to reduce the kinetic energy of the steam and transfer this energy to work done on the moving blades.

The rotor blades move at half the velocity of the steam jet, and the steam comes out of the rotor blades directed backward with respect to the rotor to leave without significant residual absolute rotational velocity. This design loses up to 8 percent of the available energy in making the U-turn between the rotor blades. Impulse stages

find application in the early stages of large reaction turbines and in impulse small turbines.

A *velocity-compounded*, or *Curtis, stage* is sometimes used when the blade speed is lower than optimum, and it is desirable to extract more kinetic energy from the steam than is possible with a single row of moving blades. An additional row of moving blades is added to the same turbine wheel, and a fixed row of blades is interposed between the moving rows. Additional moving rows may also be added, if required, to reduce the absolute exit velocity to its minimum (axial) value. Velocity compounding implies lower blade speeds for the same nozzle exit velocity.

The *reaction stage*, the second type, shown schematically in figure 7.1,*b*, is more efficient. In its primary (stationary) nozzles, only half the pressure energy of the steam stream is converted to velocity, and the rotor, with a blade speed matching the full jetted stream velocity, receives the latter. In the rotor blades, the other half of the pressure energy is used to jet the steam out of the rotor backward to exhaust.

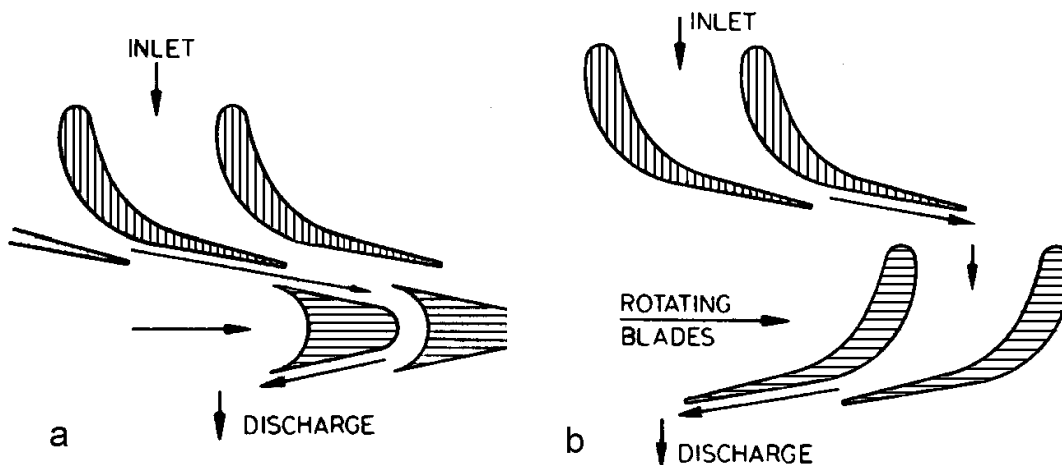


Fig. 7.1

Half the pressure drop is across the rotor so there must be a seal around the periphery of the rotor to contain it. Also, this pressure difference across the rotor acts on the full rotor area and creates a large thrust load on the shaft. A balancing piston and a thrust bearing are provided to compensate it.

For a large steam turbine, the designer could choose to use pressure-compounding, i.e., use a row of nozzles after each row of moving impulse blades. However, a more effective procedure is to allow the expansion to proceed in the moving blades as well as in the nozzles, as in the reaction stage. This results in a higher optimum blade speed, a higher maximum stage efficiency than for the impulse stage, and a broader range of blade speeds corresponding to high efficiency.

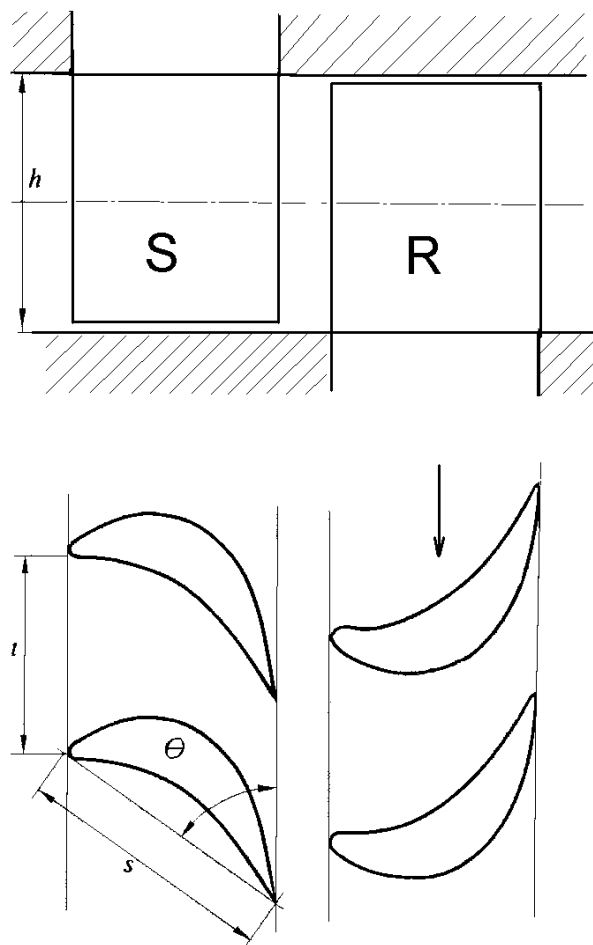


Fig. 7.2

The pressure drop in the moving blades is accompanied by a loss of enthalpy and a gain in the relative kinetic energy, hence an increase of the relative velocity at rotor exit with respect to rotor inlet. This is the reason why the reaction blades have not the symmetry of impulse blades.

A turbine stage with shroudless blades is shown in figure 7.2 to mention the nomenclature: s – chord length of blade, t – pitch, h – passage height, θ – stagger angle, S – fixed blade row (stator), R – moving blade row (rotor).

7.3 Design Characteristics

There are two general types of steam turbines, *condensing* and *back-pressure*, both being either straight or *extraction* turbines.

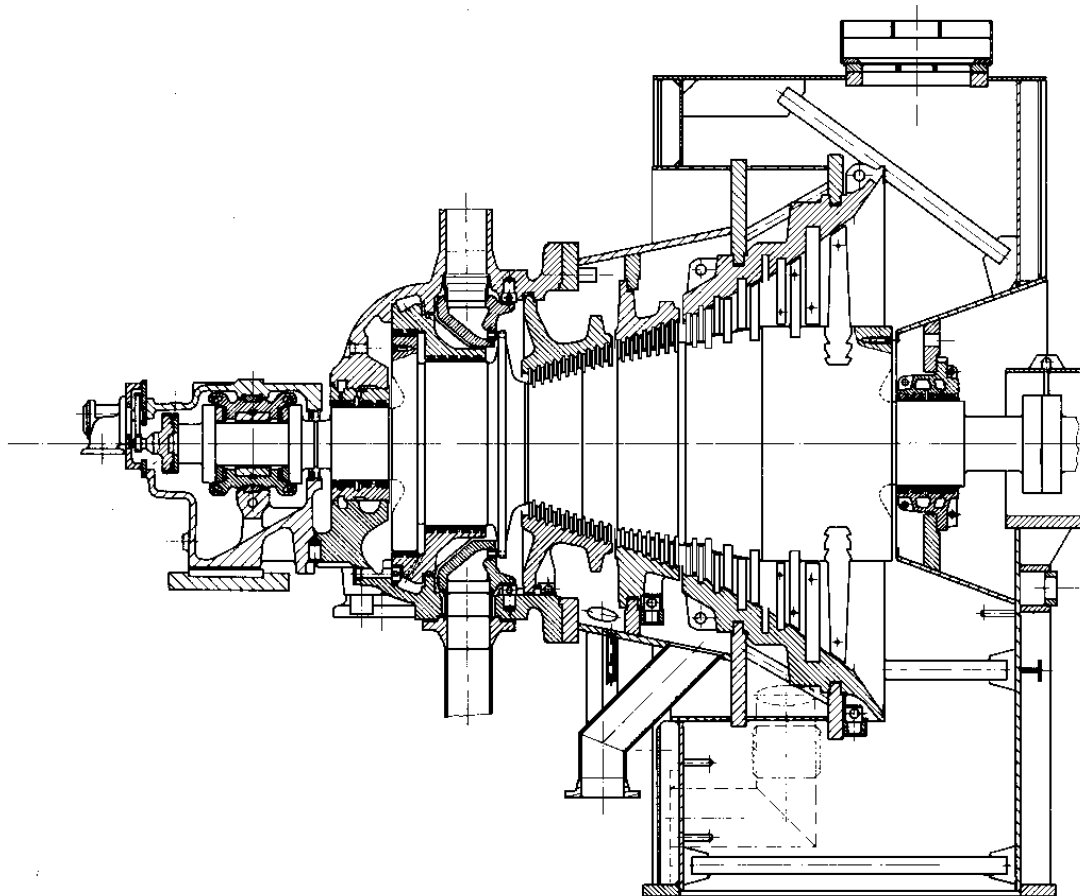


Fig. 7.3 (from [7.3])

7.3.1 Condensing turbines

Condensing turbines are directly connected to a condenser hence they have very low back-pressures. Structurally, they are characterized by a large low pressure section, required by the large volume of flow caused by the low condensing pressure. Usually the

last moving blades have twisted airfoils to accommodate variable reaction along the height.

Figure 7.3 shows the BBC type *DK-m 150* condensing turbine with the following characteristics: output 42 MW, speed 3600 rpm, live steam 42.37 bar/399°C, back-pressure 0.0846 bar. It is used in a refuse incineration plant to drive a generator through a gear.

7.3.2 Back-pressure turbines

Back-pressure turbines have no condenser. The steam is expanded down to pressures higher than the atmospheric one.

In refinery applications they are installed between two steam lines at different pressures; the exhaust steam is generally used for plant requirements. In cogeneration applications, they are sometimes used to expand steam to atmospheric pressure in a hot condenser used as a heat exchanger to produce hot water for district heating.

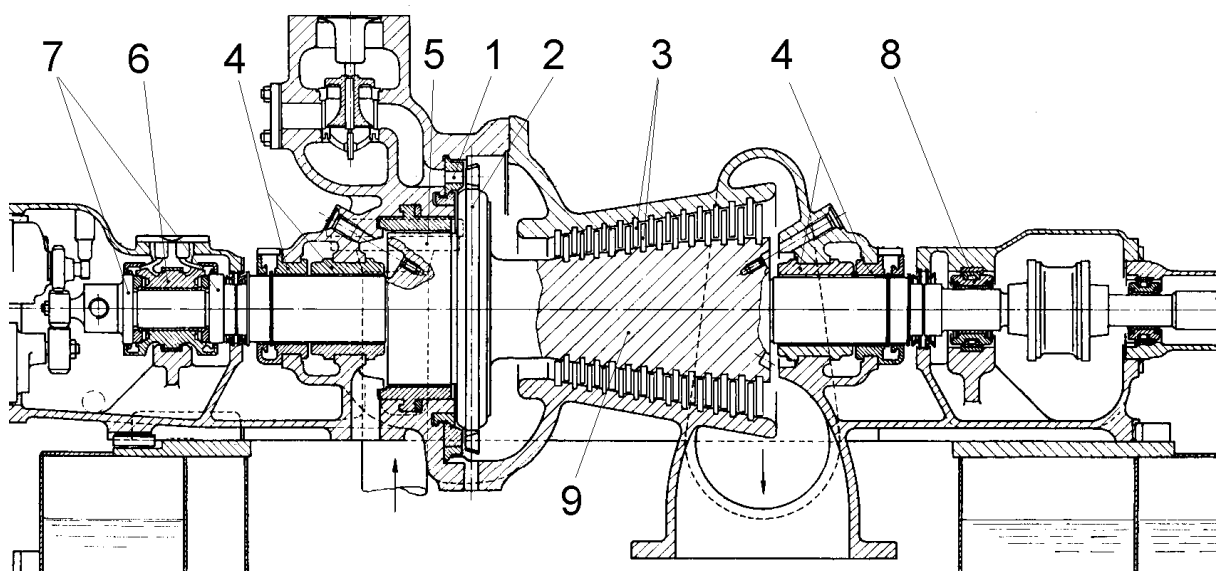


Fig. 7.4 (from [7.4])

Figure 7.4 shows a typical axial section in an industrial back-pressure turbine of an early design. The steam is expanded in the turbine from the live-steam pressure to the exhaust pressure in two principal parts.

In the first part the steam is accelerated in the nozzle segments 1, thus gaining kinetic energy which is utilized in the blades of the

impulse wheel 2. The disc of the impulse stage is integral with the shaft. Usually, the nozzles are machined into several segments fixed into the cylinder by a cover ring. The blades of the impulse wheel are milled from 13 percent chromium steel bars. The roots are fixed into the slot in the impulse wheel with spacers gripping the upset feet of the blades. In some designs the flat outer ends are welded together in groups, thus forming an interrupted shroud.

The second or reaction part consists of stationary and moving rows of blades 3 fixed with suitably shaped spacers into slots in the casing and rotor.

The glands 4 prevent the steam flowing out of the casing along the shaft. Labyrinth seals allow a very small amount of steam to escape into specially provided channels. Due to the turbulence of the steam, the pressure drop is sufficiently high to allow the gland to be made relatively short. The labyrinth strips are caulked into grooves in the rotor shaft whereas the corresponding grooves are machined into a separate bushing of the casing. The risk of damaging the rotor by distortion caused by friction in the seals is avoided, as the heat transfer from the tips of the thin labyrinth strips to the shaft is very small.

The balancing piston 5 is positioned between the impulse wheel and the gland at the steam inlet end. The chamber between is interconnected with the exhaust. Generally the balancing ring is integral with the shaft. In older designs it was shrunk-on but this design can give rise to instability due to rotating dry friction. This arrangement counteracts the axial forces imposed on the rotor by the steam flow.

The bearing 6 at the steam inlet end is a combined thrust and sliding bearing, to reduce the rotor length. The thrust part of it acts in both axial directions on the thrust collars 7 to absorb any excess forces of the balancing piston. Usually tilting bronze pads are fitted on flexible steel rings according to the Mitchell principle.

The journal bearing of the combined bearing and that at the opposite end 8 are lined with white metal cast into separate shells. Tilting pad bearings are used in some designs.

The rotor 9 is machined from high-quality steel forging. After the blades are fitted, the rotor is balanced and subjected to a 20

percent overspeed test for a few minutes. A high-alloy 13 percent chromium steel is used for high pressures and temperatures.

Turbines running at high speeds require reduction gearing to drive alternators with 2 or 4 poles running at 3000 or 1500 rpm (for 50 Hz).

As a rule, the pinion and gear wheel shafts are connected to the driving and driven machines by means of couplings. They must be able to compensate for small errors in alignment and thermal expansion in the machine without affecting the reduction gearing. The coupling hubs are integral with the forged shafts.

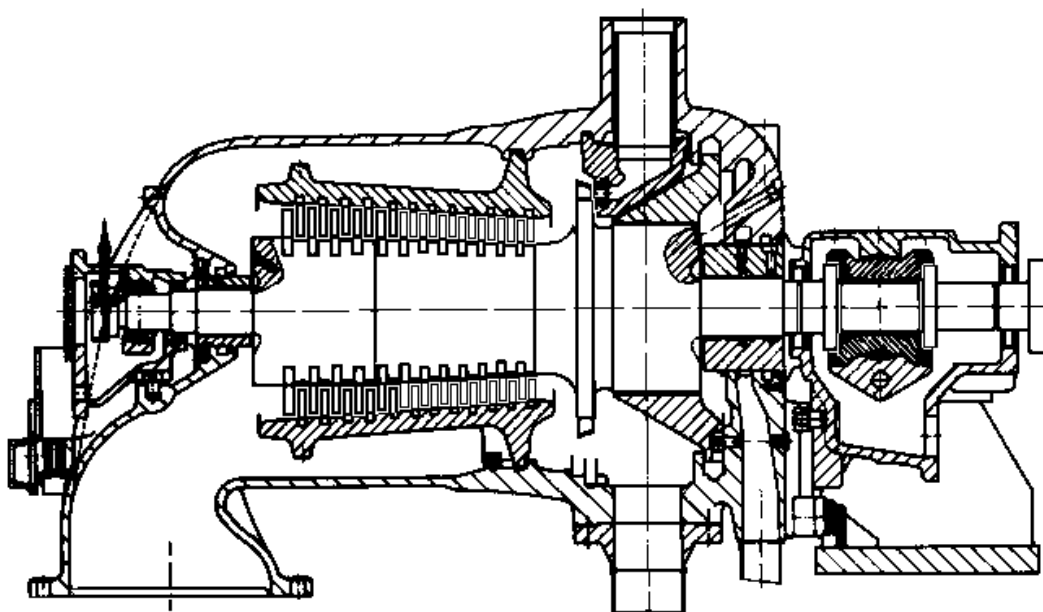


Fig. 7.5 (from [7.3])

Figure 7.5 shows the BBC type *DGX-m 7136* back-pressure turbine with the following characteristics: output 23 MW, speed 5500 rpm, live steam 65 bar/450°C, back-pressure 16.7 bar. It is used in the chemical aromatics production to drive a generator through a gear.

This turbine design is particularly suitable for injecting and/or extracting steam at intermediate pressures, adjusting the number of blade carriers and the number of stages of each blade carrier to match

the injection and/or extraction requirements with the best turbine efficiency.

7.3.3 Extraction turbines

In *extraction turbines*, the inlet steam expands to the intermediate extraction pressure, where part passes into the extraction system, the remaining part being expanded in the condensing section. The design profile of an extraction/condensing turbine constructed on the modular principle is shown in figure 7.6.

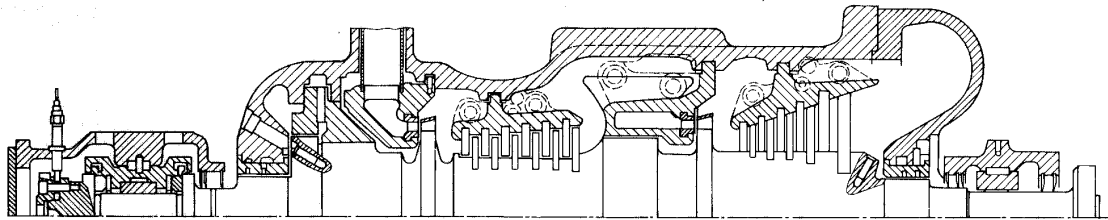


Fig. 7.6 (from [7.3])

Typical cross-sections of *extraction/condensing turbines* are shown in figures 7.7 and 7.8. They can practically be considered as consisting each of two different turbines on the same shaft and in the same casing.

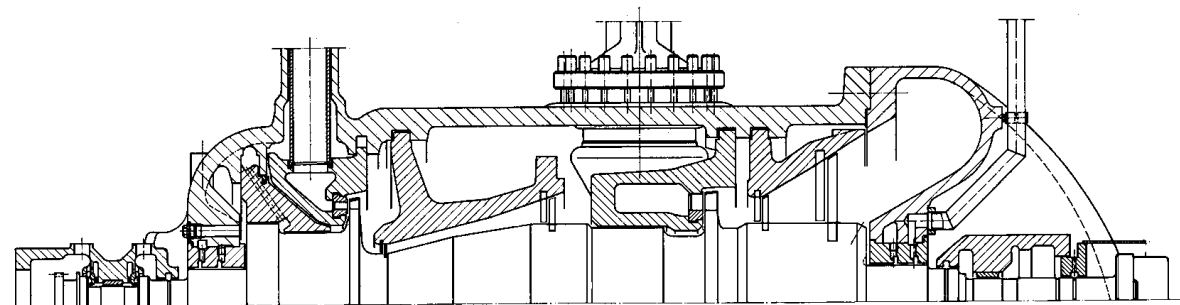


Fig. 7.7 (from [7.5])

The extraction/condensing turbine from figure 7.7 is designed for a live steam pressure of 65 bar at 485°C, an output of 12 MW at 8000 rpm and an extraction pressure of 2 bar. Next to each impulse stage there is a balancing piston with diameter larger than the shaft diameter. There are also end seals.

Figure 7.8 shows a schematic section of a *double-extraction condensing turbine* for an extraction rate of 220 t/h at 45 bar and 270 t/h at 16 bar. The generator output is 50 MW at full load. Note the single-casing design with suspended blade carriers which can easily be adapted to the individual channel geometry as a function of the exhaust pressure. The monoblock rotor is suitable for turbines in the lower output range. The control stages operate on the impulse principle and are of the single or two-stage type, controlled by partial arc admission.

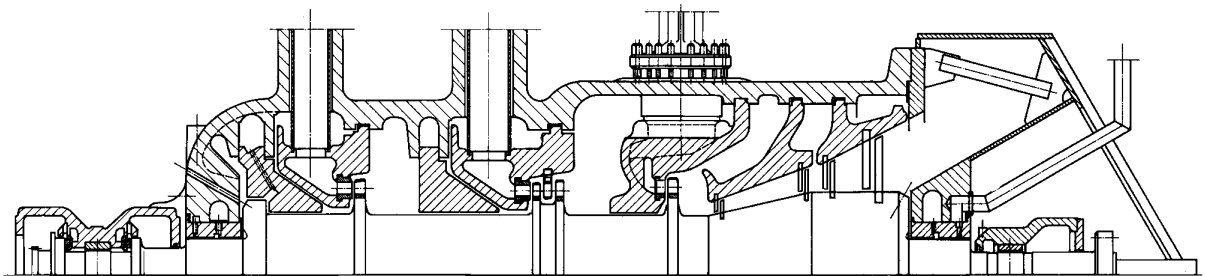


Fig. 7.8 (from [7.5])

Usually, each section consists of an impulse stage, of larger diameter for higher velocities, followed by reaction stages controlled by partial arc admission which give high steam expansion efficiency.

Such models are particularly useful in applications where the steam balance is subjected to large variations due to the process or to the driven equipment. Most of them drive carbon dioxide, ammonia synthesis or cracked gas compressors.

Figure 7.9 shows the sectional arrangement of the BBC type *DEEK-2i 140* turbine with the following characteristics: output 31.25 MW, speed 3600 rpm, live steam 42.4 bar/399°C, extraction pressure 9.287 bar, back-pressure 0.1016 bar. It is used in a paper factory to drive a generator through a gear.

When the extraction pressure is very low and the low pressure section cannot be equipped with an impulse stage, and priority is given to achieving high efficiency rather than flexibility, the low pressure section is equipped with reaction blades only. Its steam flow is controlled by *throttling valves* installed on one or two pipes that

bypass the steam from the high pressure to the low pressure section, as in figure 7.9.

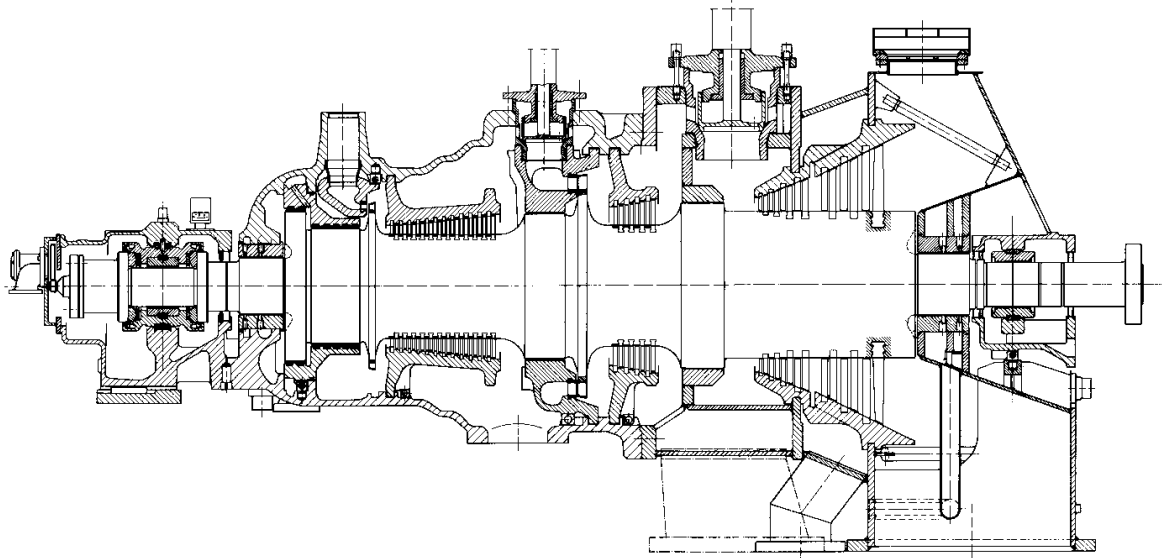


Fig. 7.9 (from [7.3])

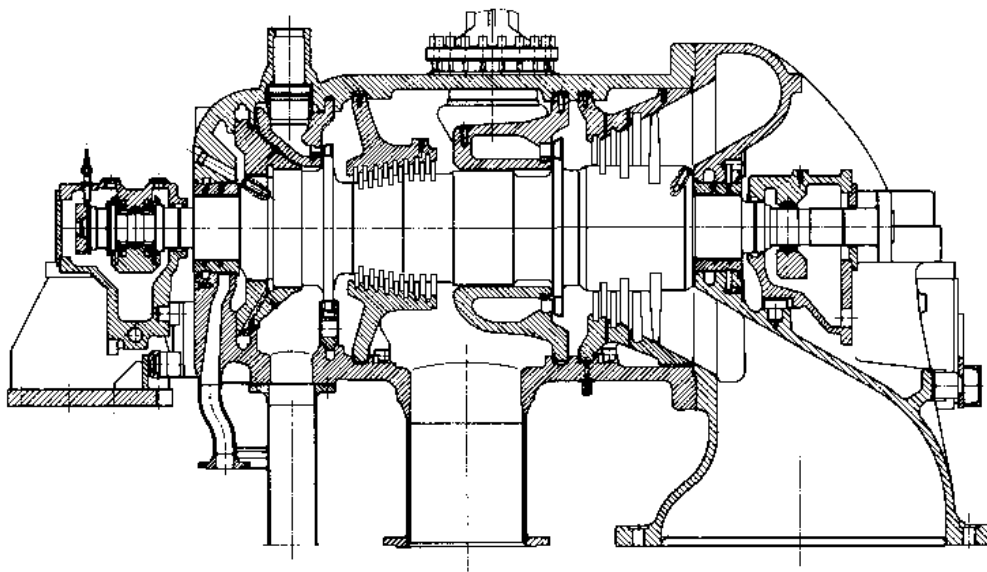


Fig. 7.10 (from [7.3])

Figure 7.10 shows an axial section of the BBC type *DEKX-g 520* turbine with the following characteristics: output 8.66 MW, speed 9600 rpm, live steam 40 bar/390°C, extraction pressure 4 bar, back-pressure 0.14 bar. It is used in a refuse incineration plant to drive a generator through a gear.

Longitudinal sections of *extraction back-pressure turbines* are shown in figures 7.11 and 7.12.

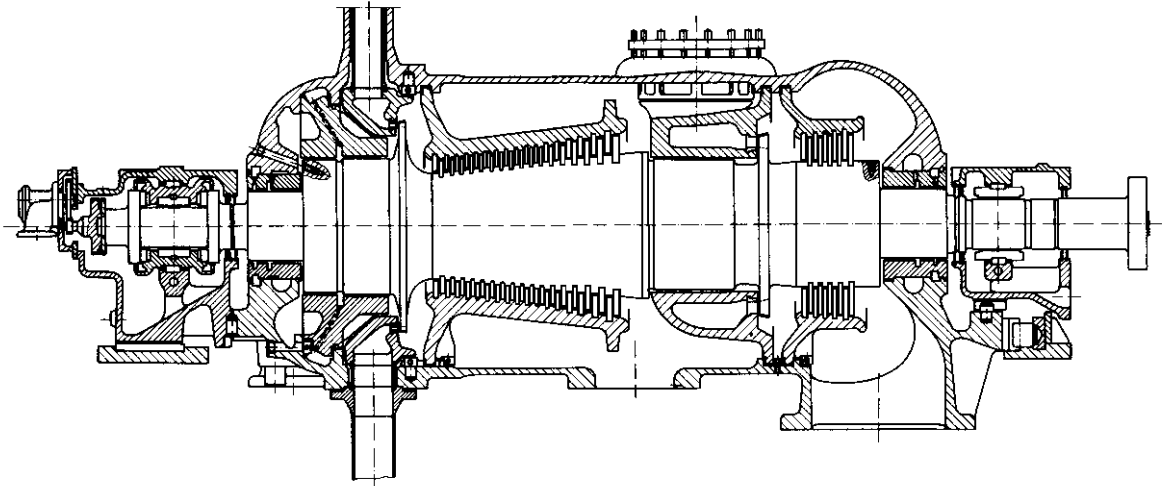


Fig. 7.11 (from [7.3])

Figure 7.11 shows the axial section of the BBC type *DEG-m 10038* turbine with the following characteristics: output 48 MW, speed 3600 rpm, live steam 84 bar/482°C, extraction pressure 12.7 bar, back-pressure 5.1 bar. It is used in paper/cellulose factories to drive a generator.

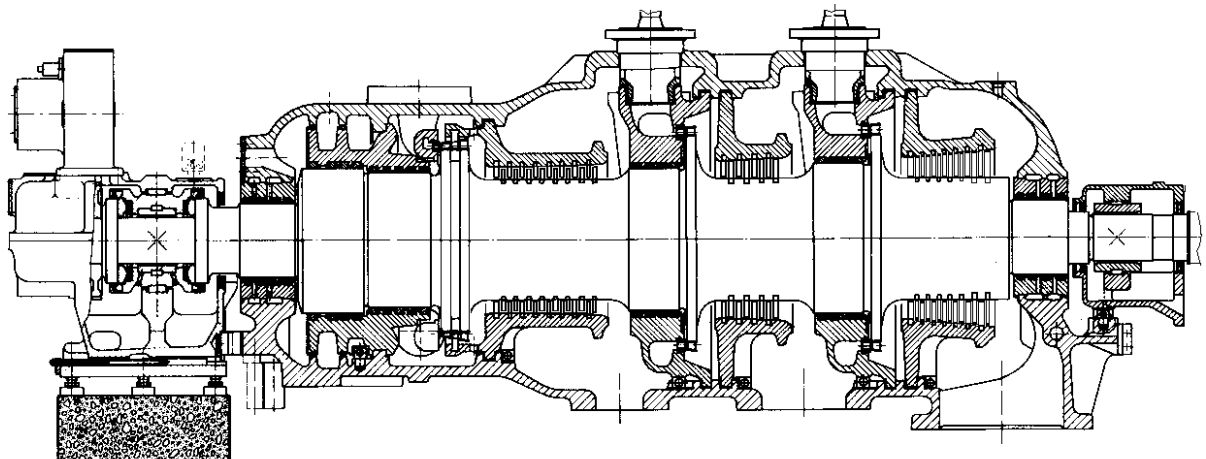


Fig. 7.12 (from [7.3])

Figure 7.12 shows a section of the BBC type *DEEG-2i 10040* double-extraction turbine with the following characteristics: output 64 MW, speed 3000 rpm, live steam 125 bar/535°C, back-pressure 6.4

bar, first extraction pressure 42 bar, second extraction pressure 19 bar. It is used in petro-chemical plants to drive a generator.

7.3.4 Double Flow Condensing Turbines

In high-power high vacuum applications, the ratio between the exhaust volume flow and speed is very high, requiring double flow turbines. They are equipped with reaction stages only. Because of the high steam volumes handled, the blades are tall and therefore a high degree of reaction (variable along the blade) is required to optimize efficiency.

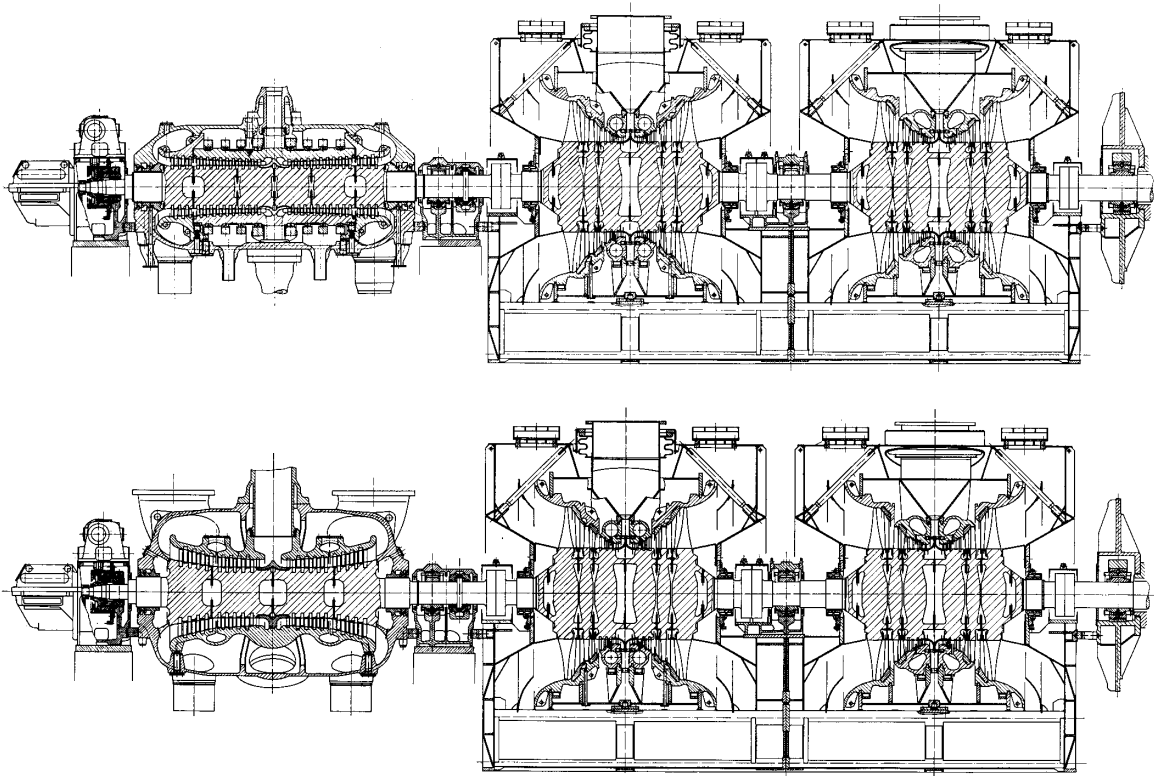


Fig. 7.13 (from [7.6])

In generator driver applications, they are used as the second casing in combined cycle plants.

Figure 7.13 shows a longitudinal section of a 1300 MW cross-compound steam turbine with two shaft lines running at 3600 rpm. The live steam is supplied at 245 bar and 538°C. The double-flow low-pressure (LP) turbines have two welded casings. The inner casings have cast blade-carriers suspended in them. The condenser pressure is 0.068 bar and the last stage blade length is 760 mm.

The intermediate pressure (IP) double-flow turbine, also shown in figure 7.14, has cast double-casing design with bolted flanges.

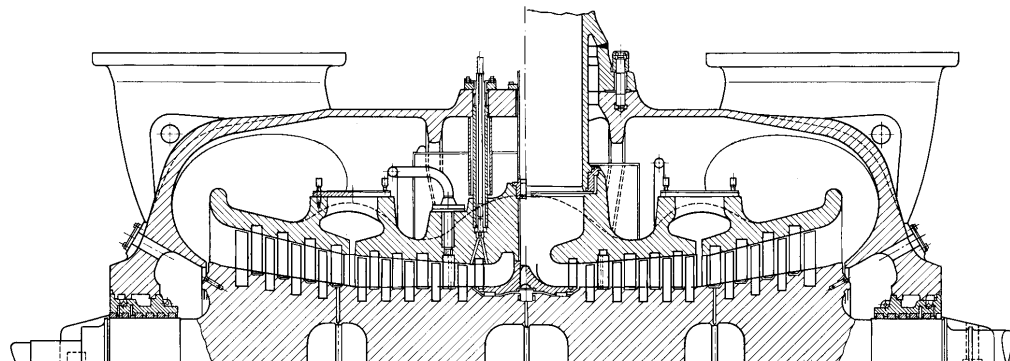


Fig. 7.14 (adapted from [7.7])

The high pressure (HP) double-flow turbine, also shown in figure 7.15, has cast double casings and shrink rings on the inner casing. The live-steam has 538°C and 247 bar.

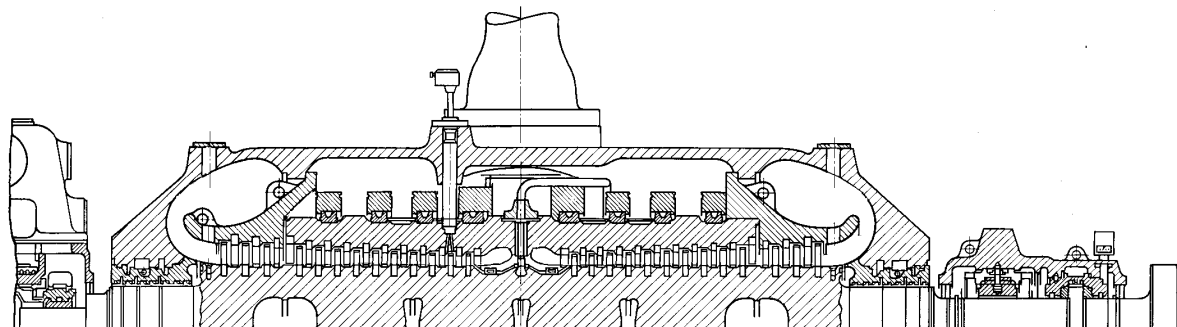


Fig. 7.15 (adapted from [7.7])

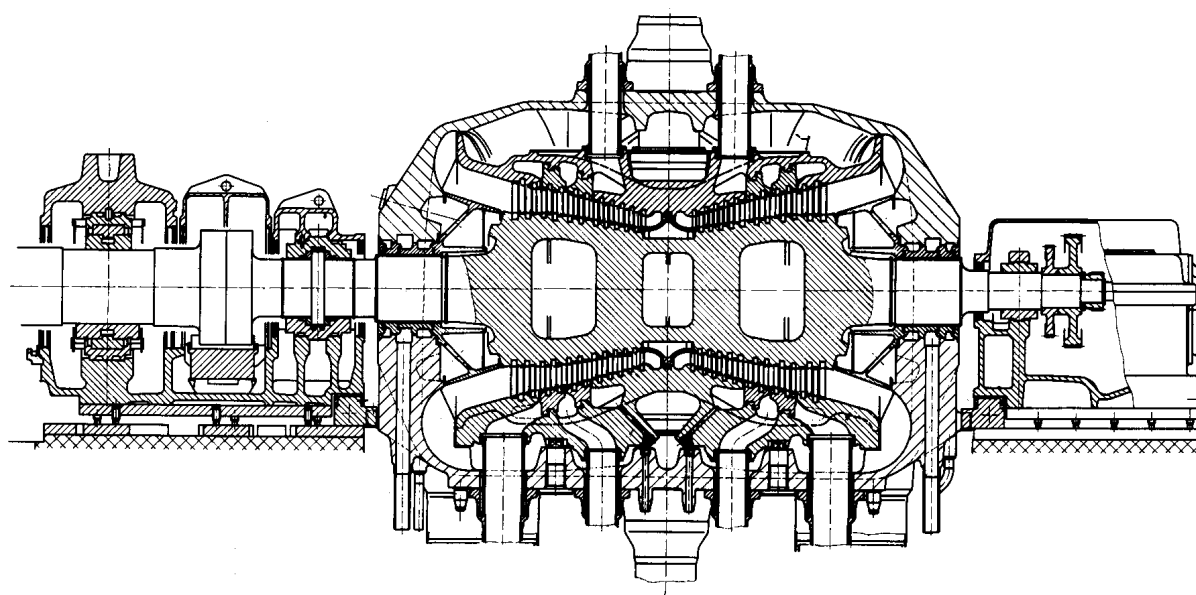


Fig. 7.16 (from [7.8])

Figure 7.16 is a section through a half-speed HP turbine with cast outer casing (1300 MW, 1800 rpm)

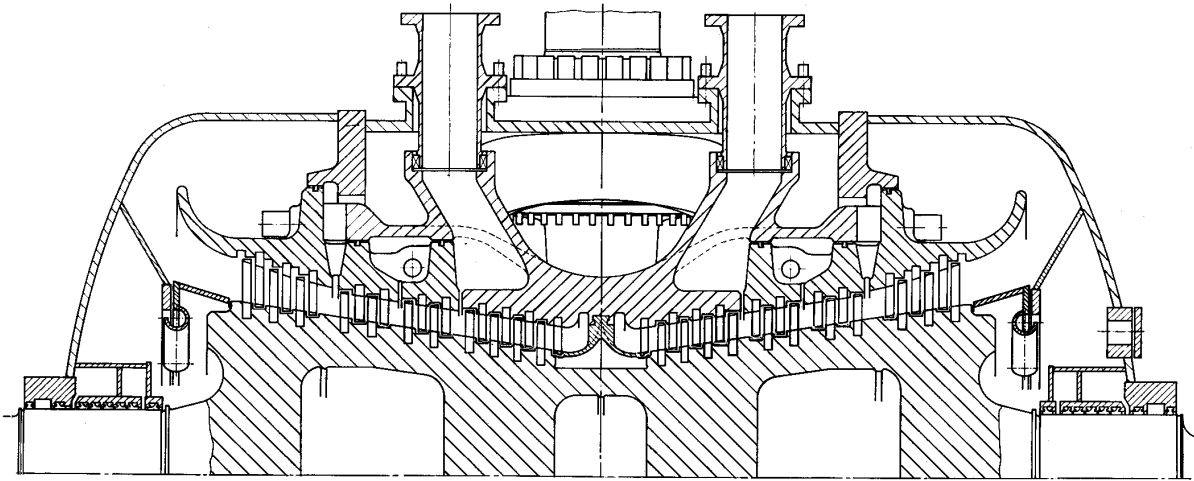


Fig. 7.17 (from [7.8])

Figure 7.17 is a section through a half-speed HP turbine with welded outer casing (1300 MW, 1800 rpm).

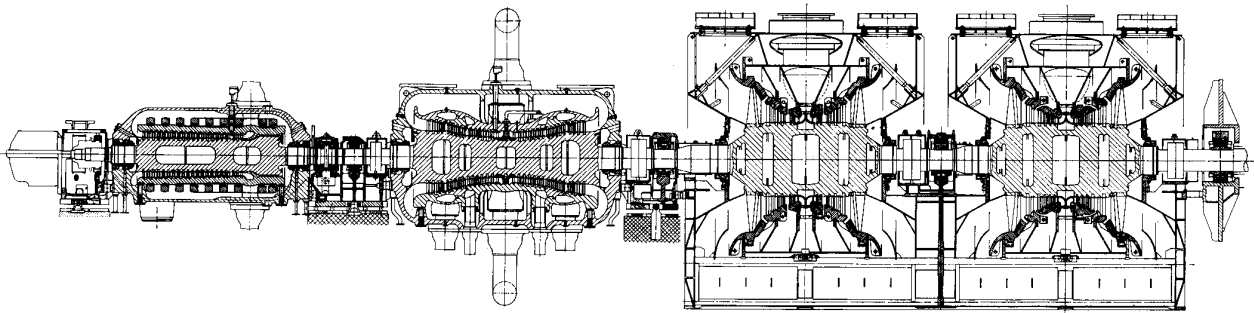


Fig. 7.18 (from [7.7])

Figure 7.18 shows a four-cylinder single-shaft 500 MW turboset with two sets of double-flow low-pressure blading

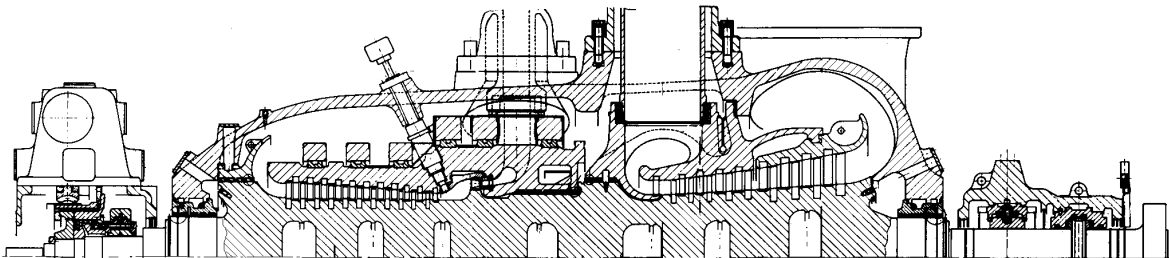


Fig. 7.19 (from [7.8])

The development of the new blading has enabled the number of stages to be reduced in such an extent that both the HP and the IP sections of units with capacities up to 1000 MW can be housed in one

casing. A sectional drawing of the combined HP/IP of a 600 MW, 3600 rpm turbine designed by BBC is shown in figure 7.19. To avoid unnecessary high thermal stresses, the hot inlet sections of both the HP and the IP parts are placed together at the centre of the cylinder.

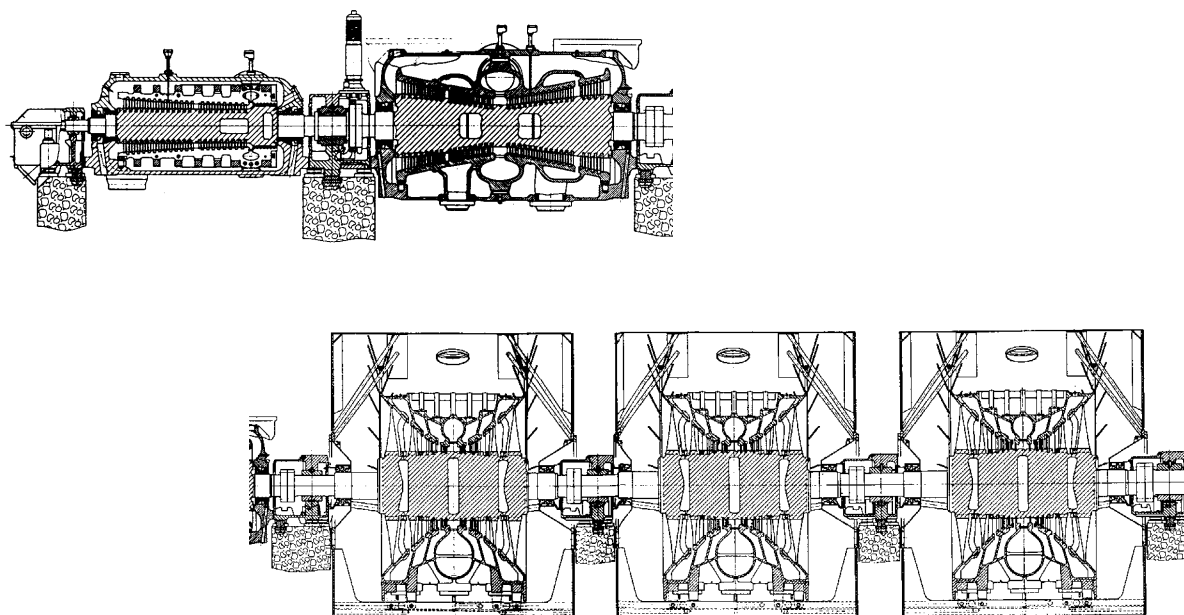


Fig. 7.20 (from [7.9])

Figure 7.20 shows a longitudinal section (split on two rows) of the single-shaft five-cylinder turbosets of the lignite-fired power plant in Lippendorf, Germany. The power capacity of 933 MW per unit and net efficiency of 42.4 percent for the plant make it one of the world's most efficient and largest power plants to be fired with brown coal.

The turboset consists of a single-flow HP turbine, a double-flow IP turbine and three double-flow LP turbines. The shaft system is supported by a single bearing between each pair of casings. The rotors of the turbine sections and the generator are rigidly linked by means of integral expansion sleeve couplings. Axially arranged labyrinth seals with spring backed ring segments prevent the steam from escaping at the gaps between the rotor shaft ends and the casing.

The fixed point for the shaft system is the thrust bearing between the HP and IP turbines. The fixed point for the turbine on the foundation is the bearing pedestal between the IP section and the first LP turbine section.

7.4 Turbine Rotor Designs

Presently used turbine rotor designs are the *monoblock* rotor, with or without (not shown) a central bore, drum-type or with integral discs (Fig. 7.21a), the *built-up* rotor with shrunk-on discs on a central shaft (Fig. 7.21b), and the *welded* rotor (Fig. 7.21c).

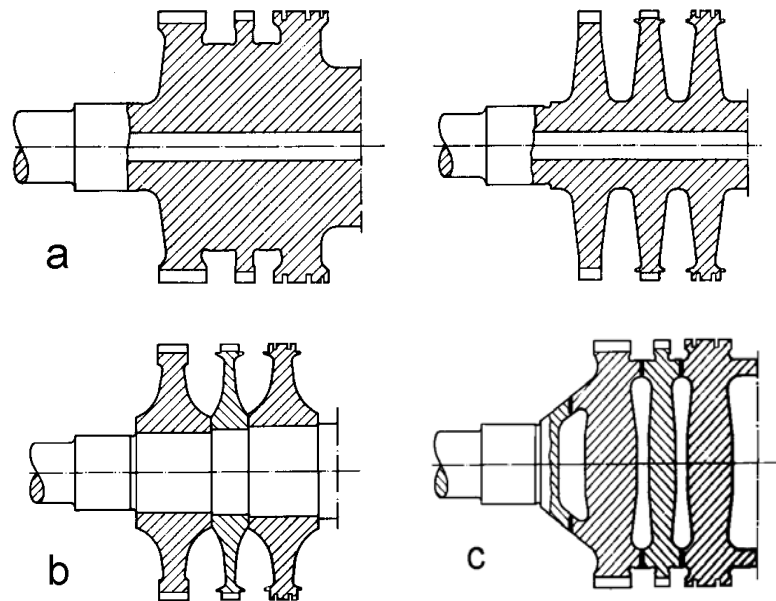


Fig. 7.21 (from [7.10])

7.4.1 Monoblock, Built-Up and Welded Rotors

The oldest type is the built-up rotor with shrunk-on discs (Fig. 7.22). At present it is used mainly in low-pressure turbines.

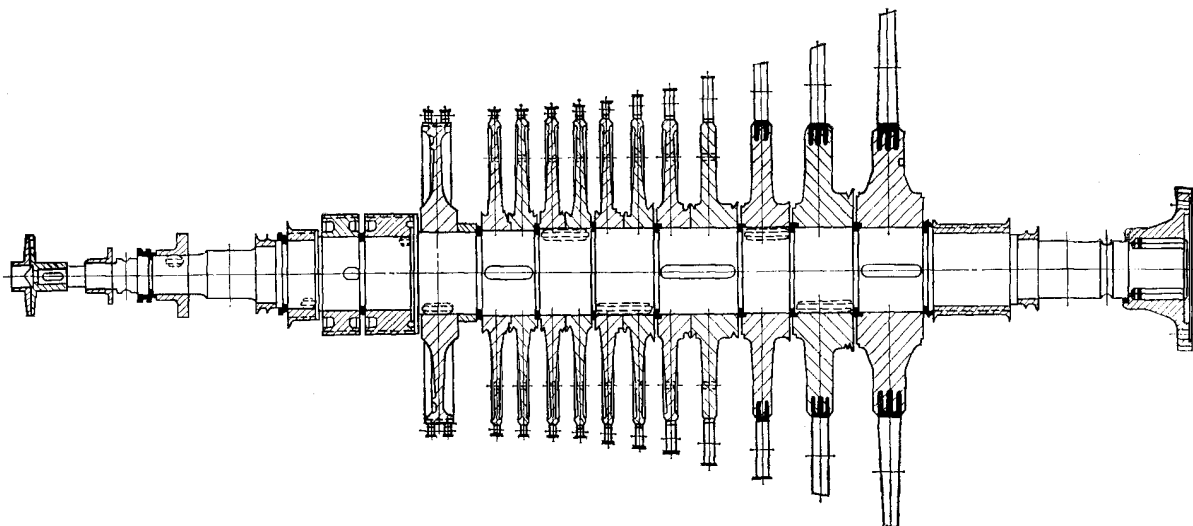


Fig. 7.22 (from [7.11])

The design has to ensure that the last stage disc will not lose its shrink fit at 35 percent overspeed. With this shrink fit, considerable circumferential stresses result at the bore of discs, even at zero speed (about 400 MPa) and at turning gear speed, leading to increased danger of rotor burst due to smaller critical flaw sizes.

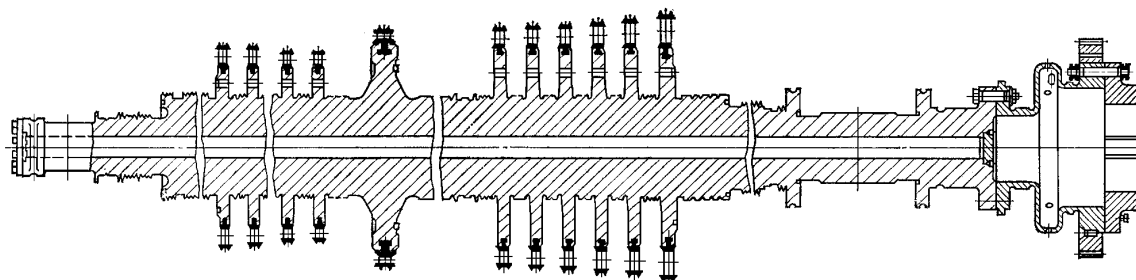


Fig. 7.23 (from [7.11])

In many high-pressure turbines the rotor is monoblock with integral discs (Fig. 7.23). It is generally accepted that the central bore will result in an increase of centrifugal and thermal stresses. The increase of the centrifugal stresses is diminished by creep relaxation in the high temperature region of the rotor but at the cost of creep damage in this region. In the rotor part not subjected to creep, the higher stress level due to the central bore will reduce the critical defect size and therefore will result in an increased risk of brittle fracture. This applies especially to the cold end of IP rotors.

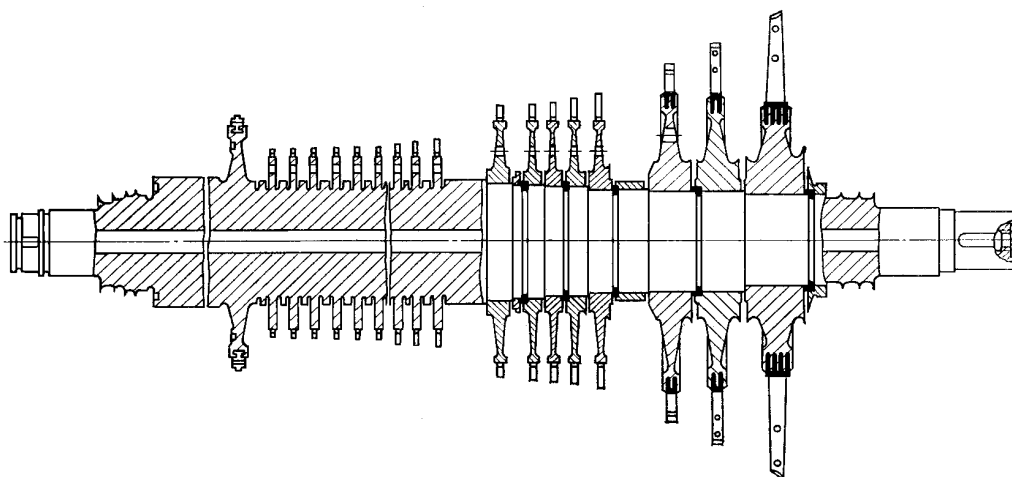


Fig. 7.24 (from [7.11])

A combined rotor design, with both integral discs and shrunk-on discs, is shown in figure 7.24.

A drum-type monoblock rotor is shown in figure 7.25.

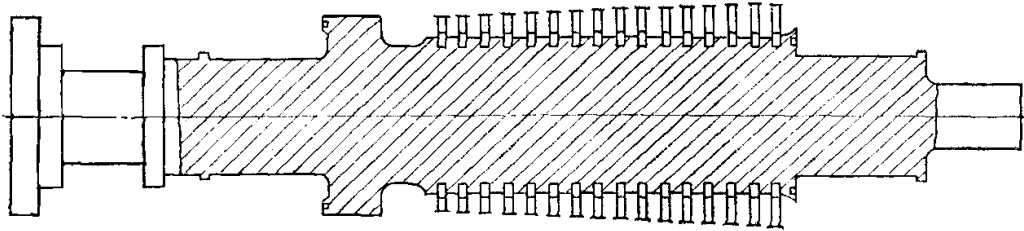


Fig. 7.25 (from [7.11])

Transient thermal stresses occur in such a rotor because the thermal expansion resulting from nonuniform temperature distribution cannot develop freely. Due to the mass concentration and the large temperature differences the strain suppression in a monoblock rotor is relatively pronounced. Significant axial stresses may occur leading to a three-axial state of stress (plain strain condition). Therefore this rotor type is more sensitive to brittle fracture.

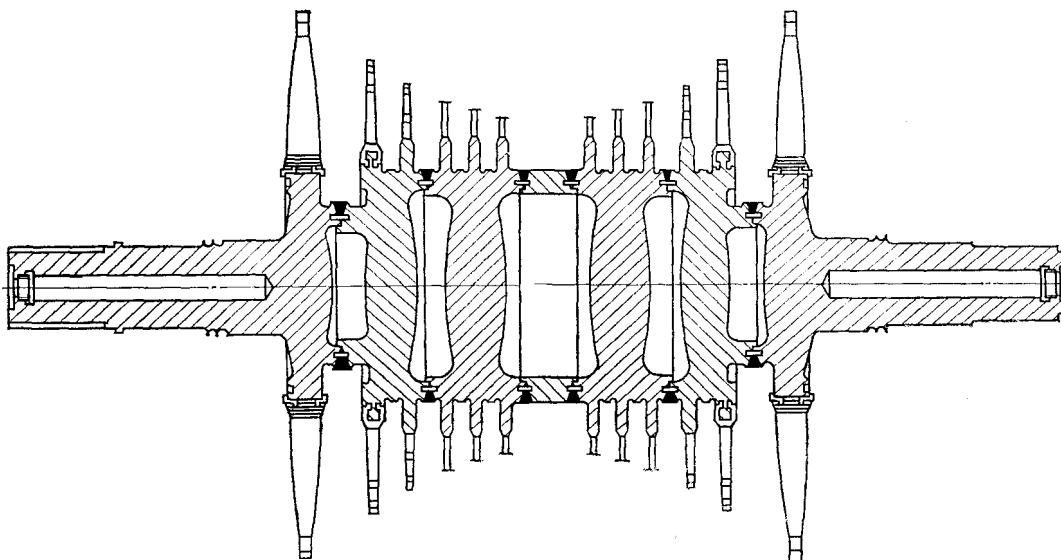


Fig. 7.26 (from [7.10])

A welded rotor is shown in figure 7.26. This design has a series of advantages presented in detail in the following paragraph. Transient thermal stresses which occur during a startup or a shutdown are approximately 43 percent lower in a welded rotor than in a monoblock rotor. The small thickness-to-diameter ratio of each disc in a welded

rotor prevents the formation of significant axial stresses. The welded design enables a thorough ultrasonic test from various directions of the different discs before they are welded together. This ensures that flaws will be found irrespective of their orientation.

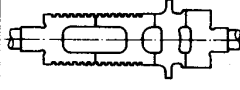
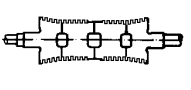

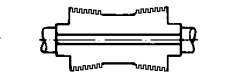
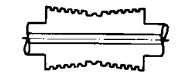

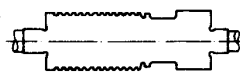
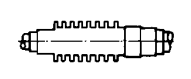
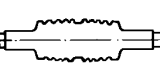
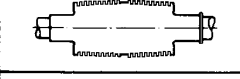



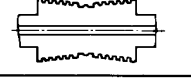
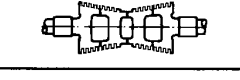
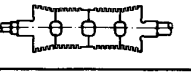

	HP	IP	LP	REMARK
FULLSPEED 3000/3600rpm				WELDED
				MONOBLOCK CENTER BORE
				MONOBLOCK NO CENTER BORE
HALFSPEED 1500/1800rpm				HP/IP: MONOBLOCK WITH OR WITHOUT CENTER BORE LP: BUILT-UP
				
				WELDED

Fig. 7.27 (from [7.12])

A more detailed classification of steam turbine rotor designs at the level of the practice of late seventies is presented in figure 7.27. One has to distinguish between *fullspeed*, i.e. steam turbines for 3000 rpm and 3600 rpm, and *halfspeed* machines, i.e. steam turbines for 1500 rpm and 1800 rpm. A further distinction should be made between *high pressure* (HP), *intermediate pressure* (IP), and *low pressure* (LP) rotors.

Present practice for large HP and IP rotors employs either the monoblock or the welded rotor design for full- and halfspeed machines. Due to limitations of the forging sizes, it has become practice to build monoblock rotors for fullspeed LP rotors and built-up rotors with shrunk-on discs for halfspeed LP's. In the past, built-up rotors have even been used for full-speed machines. With the welded design the same rotor concept can be used for both fullspeed and halfspeed machines.

There is a major difference between American and European manufacturers of monoblock rotors. American manufacturers tend to use a centre bore, while European manufacturers build the monoblock rotor without a centre bore.

Due to the different service temperatures and service loads, different criteria for a comparison of rotors for HP- and IP- and LP-applications must be employed.

For HP- and IP-rotors of fossil fired reheat units, the high-strain thermal fatigue resulting from start-ups, shut-downs and load changes, combined with creep damage, is decisive. HP-rotors for nuclear units operating with low temperature saturated steam are subjected to less severe thermal loading, transient thermal stresses and creep. They may therefore be considered together with the LP-rotors, the conclusions for LP-rotors being also valid for nuclear HP's.

LP-rotors for both fossil fired and nuclear units are subjected to the same loadings and therefore LP-rotors for those two types of units can be treated in the same way.

7.4.2 Rotor Design Stresses

Basically, there are two temperature ranges important for dimensioning steam turbine components (Fig.7.28).

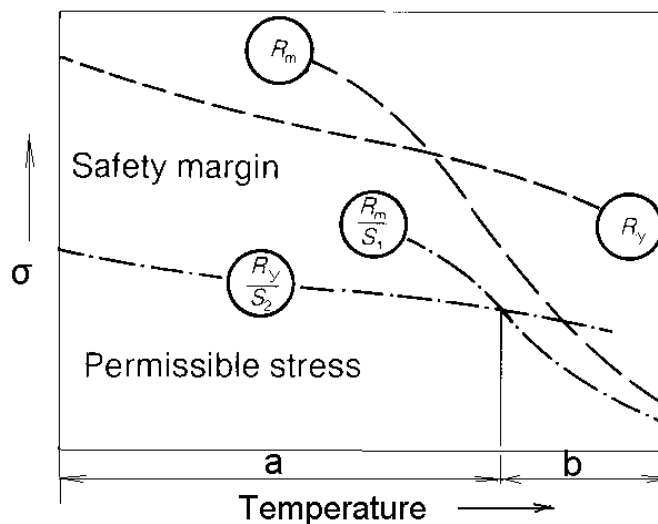


Fig. 7.28 (from [7.13])

At temperatures up to approximately 350°C - range *a* - dimensioning is referred to the high temperature *yield point* R_y . This means that the only stresses permitted in a component are those which exhibit a certain safety margin with respect to the yield point, R_y / S_2 . The yield point is a material characteristic independent of time. Because of the behaviour of their materials, these components have analytically unlimited lifetime.

Above the temperature limit of approximately 350°C - range *b* - dimensioning is referred to the *creep strength*, which depends upon time and lies below the yield point. The creep strength for 10^5 hours (11 years), denoted here R_m , is used as a characteristic value. Permissible stresses are obtained dividing R_m by a safety factor S_1 .

Common practice is to use minimum yield points and creep rupture strengths which represent the lower 99.9% confidence limits of the scatterband. The safety factors applicable to given components and types of stressing allow for parameters that are unforeseeable at the design stage, such as the duration and method of operation. Furthermore, the stress safety factors provide *time safety factors* which, with present-day machines, lead to service lives of more than 200,000 hours (22 years) for normal operation and predictable material behaviour.

Basically, steam turbines operating at high temperatures are designed for a finite service life based on steady-state stresses experienced in service. The safety factors account for non-steady-state phenomena and for changes in the predicted service life and operating mode such as longer operating periods than originally planned or changeover from base load to peak load operation.

In rotors for service temperatures up to 350°C, for example in the LP turbine stages in fossil-fuel or nuclear power plants, the principal loading results from the centrifugal forces, combined with corrosion due to contaminants in the steam supply.

In rotors operating above 350°C, for example in the HP and IP turbine stages under conventional steam conditions, thermal fatigue results from the transient thermal stresses occurring during start-ups, shut-downs and load change. The design must also take care of the

effects of creep due to centrifugal forces and steady-state thermal stresses.

7.4.3 Rotor Material Embrittlement

Certain alloying elements and also the heat treatment can give rise to long-term embrittlement effects. They manifest themselves as low fracture toughness at room temperature and poor ductility and notch sensitivity at operating temperature. The creep-resistant MoV steels are an example of this.

One of the reasons for this embrittlement is that carbides form in the steel during service, resulting in a decrease of its ductility. Embrittlement also alters the value of K_{IC} - the fracture toughness.

Fracture toughness generally increases with temperature. An abrupt change in toughness over a relatively small temperature range occurs in metals with body-centered cubic crystal structure, notably in steels with ferritic-pearlitic and martensitic structures (Fig.7.29).

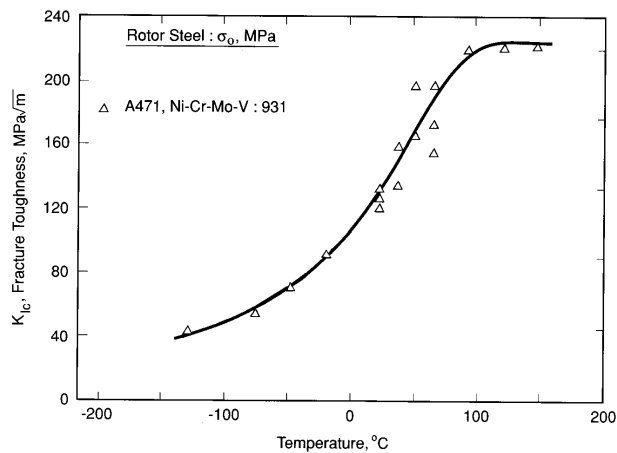


Fig. 7.29 (from [7.14])

The *temperature-transition* behaviour is due to a shift in the physical mechanism of fracture [7.14]. Below the temperature transition, the fracture mechanism is identified as *cleavage*, and above it is *microvoid coalescence*. Cleavage is fracture with little plastic deformation along specific crystal planes that have low resistance. Microvoid coalescence, also called *dimpled rupture*, involves the plasticity-induced formation, growth, and joining of tiny voids in the material, leaving the rough and highly dimpled fracture appearance.

Data on the K_{IC} versus temperature behaviour of rotor steels is useful in selecting specific materials for service. It is important to avoid high-stress use of a material at a temperature where its fracture toughness is low.

A relevant parameter used in turbine rotor design is the *Fracture Appearance Transition Temperature* at 50 percent brittle fracture, denoted $FATT_{50}$.

The Nuclear Regulatory Commission requires for nuclear turbines that $FATT_{50}$ lies below -18°C for LP rotors and below 10°C for HP rotors [7.12]. Although there is no equivalent requirement for fossil-fired units, ASTM specifies $FATT_{50}$ values from -18°C to 20°C for *A471Cl. 1 to 9*. The metal temperature of an LP rotor can, in certain cases, be as low as 10 to 20°C and therefore using a material with $FATT_{50}$ of this magnitude is not recommendable.

In some rotor steels, the $FATT_{50}$ is displaced by about 100°C as a result of service at high temperature. The consequence of this is a reduction in the fracture toughness at the room temperature.

The high transition temperature ($FATT_{50}$) of the low-alloy CrMoV steels used in older high-temperature rotors is accompanied by the danger of brittle fracture when starting up with a cold rotor. Counter-measures involve preheating or sophisticated metallurgical treatments such as forgings with a gradient in the chemical composition or selective zoned heat treatment. A much simpler solution is the welded rotor in which forgings of different materials can be welded together as required.

7.4.4 High Pressure and Intermediate Pressure Rotors

The main requirements for the HP and IP rotors are low levels of transient thermal stresses, good creep and fatigue properties in the steam entrance portion, and low $FATT_{50}$ at the cold end(s).

Transient Thermal Stresses

The circumferential stresses, σ_φ , and the axial stresses, σ_z , resulting from a temperature difference $\Delta\vartheta = \vartheta_1 - \vartheta_m$ between the surface temperature, ϑ_1 , and the mean temperature, ϑ_m , of the section are given in figure 7.30.

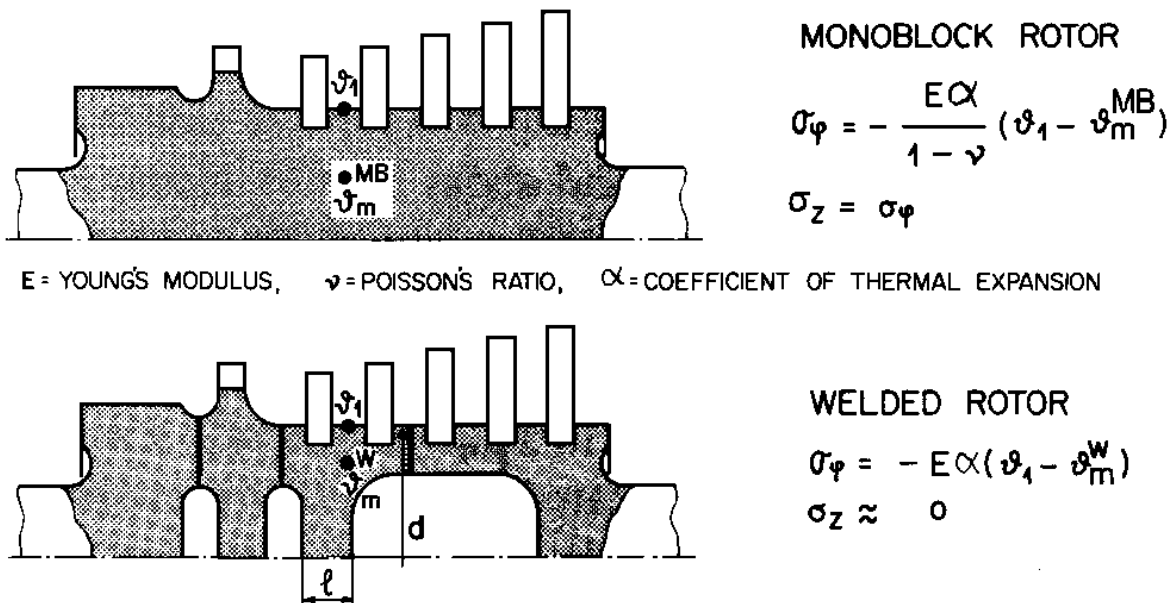


Fig. 7.30 (from [7.12])

The ratio of the circumferential stresses of the monoblock rotor and the corresponding stresses of the welded rotor is $1/(1-\nu) \approx 1.43$.

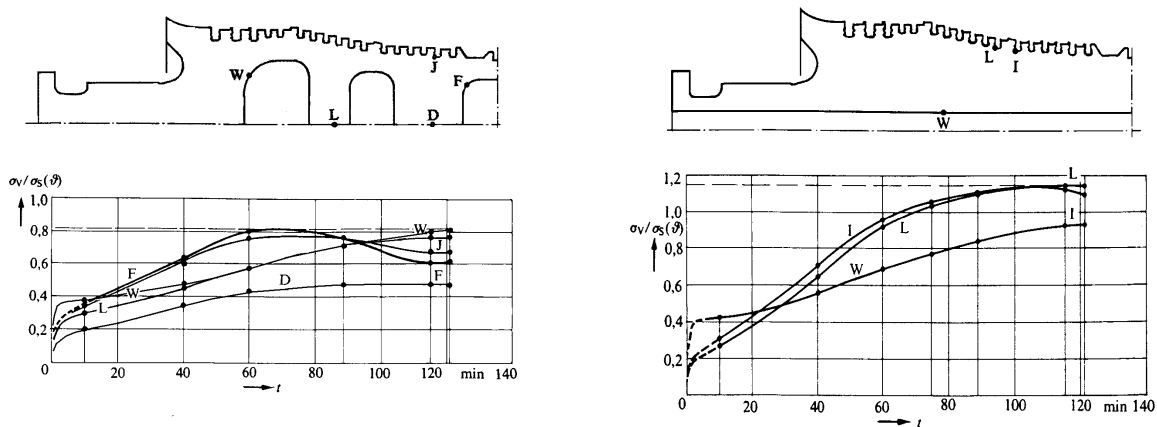


Fig. 7.31 (from [7.15])

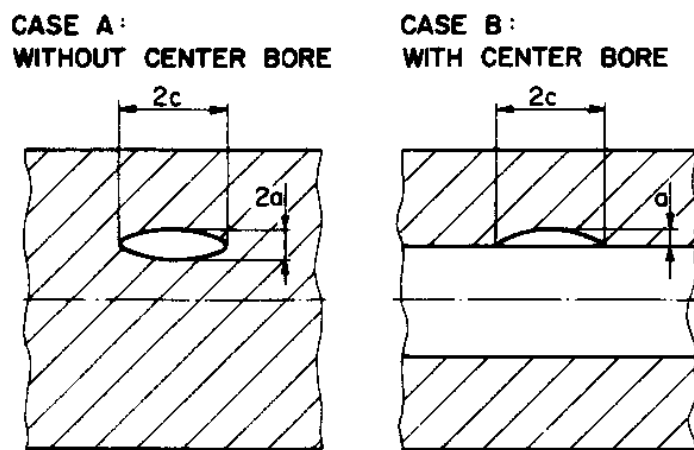
The superior behaviour of the welded rotor can be checked by more exact analyses using finite element methods. The most severe

transient thermal stresses will occur at stress concentrations such as blade grooves and diameter changes.

Figure 7.31 shows the most dangerous thermal stresses which occur during a very quick cold start in two IP rotors of different design for a 500 MW unit. A double-flow welded rotor (left) is compared with a monoblock rotor having a central bore (right). The ratio of the equivalent stress to the yield stress at operating temperature is denoted σ_v / σ_s , and D, F, J, L, W are measuring points for the equivalent stresses. As can be seen, the stresses in the blade root region of the monoblock rotor are approximately 40 percent higher than the corresponding stresses of the welded rotor.

Stationary Stresses

Considering stationary stresses, e.g. centrifugal stresses, there is no major difference between a monoblock rotor without a centre bore and a welded rotor. For a monoblock rotor with a centre bore, the high circumferential stresses at the bore lead to an increased creep damage in the hot region of the rotor and reduced critical defect size in the cold part, hence an increased risk of brittle fracture.



$$\sigma_{CA} = \frac{K}{\pi} \left(\frac{K_{IC}}{\sigma_{\psi A}} \right)^2$$

$$\sigma_{CB} = \frac{K}{1.21} \left(\frac{K_{IC}}{\sigma_{\psi B}} \right)^2$$

$$\sigma_{\psi A} \approx \frac{\sigma_{\psi B}}{2}$$

CIRCUMFERENTIAL STRESS

$$\sigma_{CA} \approx 4.8 \cdot \sigma_{CB} \text{ CRITICAL FLAW SIZE}$$

Fig. 7.32 (from [7.12])

The purpose of the central bore is to remove segregates and non-metallic inclusions in the centre of the rotor, to allow testing the material in the centre for mechanical properties and to enable ultrasonic testing from the central bore.

It must also be considered that a flaw fully embedded near the centre of a rotor constitutes a much smaller danger than a flaw on the surface of a central bore. Figure 7.32 shows the critical flaw size of elliptical embedded flaws and surface flaws in a rotor with and without central bore.

Material Properties

For a welded rotor, an optimized heat treatment of each section is simple and easy to perform. This has been considered as an improvement over a monoblock rotor. Also through-hardening and reduction of forging ratio, both contributing to a uniformity of material properties, are better for the welded rotor than for a monoblock rotor.

With steam inlet temperatures above 540°C, the creep properties of low-alloy CrMoV steels used in older turbines are no longer adequate. High-alloy chromium steels seem to represent a solution. However, these steels have certain distinct disadvantages in that the so-called 'wire-wooling' tends to occur in journal bearings. They have also lower thermal conductivity and hence induce higher thermal stresses than the low-alloy steels. By using the welded design, only those parts subjected to the higher temperatures need to be made of high-alloy CrMoV steel.

In recent years, the efficiency of steam power plants has been improved by increasing the steam parameters (live-steam conditions of 250-300 bar and 580°C, and reheat temperatures of 600°C) which was achieved by choosing appropriate materials. Collaborative European programmes have led to the development and qualification of steels with much improved creep properties at temperatures up to 600°C.

Improved 10% Cr forged steels have a 0.2% yield strength at room temperature of about 700 MPa, a creep strength at 100,000

hours and 600°C of about 100 MPa, and through-hardening to a diameter of at least 1.2 m.

In the HP and IP welded rotors, only the middle rotor section, actually carrying the moving blades, is made of the new 10% chromium steels. The rotor ends are made of a low-alloyed 1% CrMoV steel. Because of the good running properties of this steel, there is no need for overlay welding of the rotor journals. The weld between the high-alloyed and low-alloyed steel is made using conventional methods and filler metal.

Inspection of Forgings

The disc of a welded rotor can be ultrasonic tested from various surfaces and therefore flaws and other nonhomogeneities will be found irrespective of their orientation. After the forgings are welded, the weld areas are inspected by ultrasonic and magnetic particle methods. Monoblock rotors with central bore are inspected boresonic but the accessibility for ultrasonic testing is not as good as for the discs of a welded rotor.

Verification of Material Properties

In a welded rotor, a specimen can be taken near the locations where the most severe stresses are known to occur. For a monoblock rotor without a centre bore, this is only possible with the radial bore method. A monoblock rotor with central bore enables specimens to be taken at the centre of the rotor, where the highest stresses occur. Both radial and axial bores lead to increased stress levels, local or overall.

Based on these considerations, the welded rotor appears to be the HP and IP rotor design offering the highest reliability.

7.4.5 Low Pressure Rotors

The main requirements on LP rotors are low stress levels resulting from the combination of all possible stationary and instationary loads, low sensitivity to environmental effects and integrity at all service conditions.

Stresses from Centrifugal Loads

Due to the large radial dimensions of the LP rotors, the most severe stresses result from centrifugal loads.

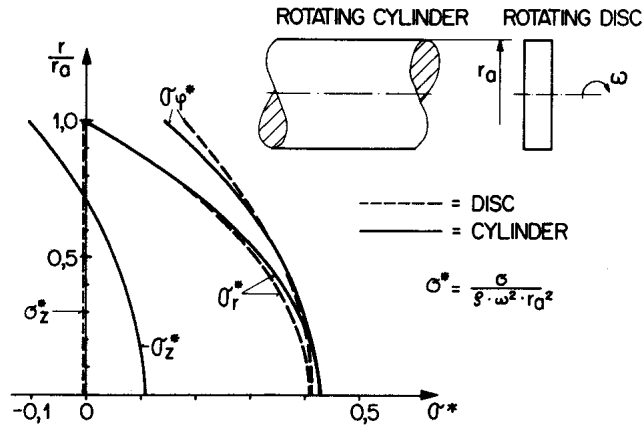


Fig. 7.33 (from [7.12])

As can be seen in figure 7.33, the level of the circumferential and the radial stresses for a welded rotor and a monoblock rotor without central bore is almost identical, due to the fact that the stresses are primarily determined by the outer diameter of the rotor.

In a monoblock rotor, the stress distribution is similar to that in a rotating cylinder. Due to the axial stress component there is a spatial state of stress, which implies higher sensitivity to brittle fracture.

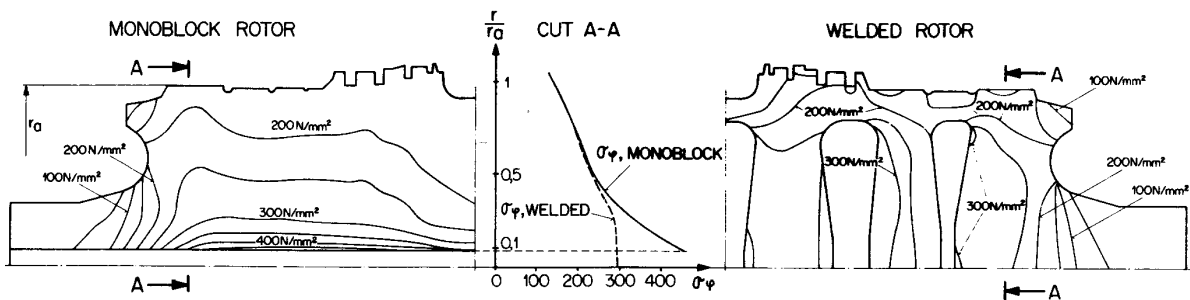


Fig. 7.34 (from [7.12])

If a central bore is employed, the circumferential stresses will be theoretically about twice those for the case without the bore. In figure 7.34 this is illustrated for an LP rotor from a 300 MW power turbine running at 3000 rpm. The calculations are, in both cases, based on the same outer contour, resulting in a stress ratio of 1.6.

The circumferential stresses of the discs due to centrifugal loads are higher in a built-up rotor than in a monoblock or in a welded rotor. A comparison of stresses in a welded rotor (*a*) and in a rotor with shrunk-on discs (*b*) is presented in figure 7.35 where $\sigma_{0.2}$ is the yield stress, σ_ϕ - circumferential stress (elastic), $\sigma_{\phi p}$ - circumferential stress (plastic).

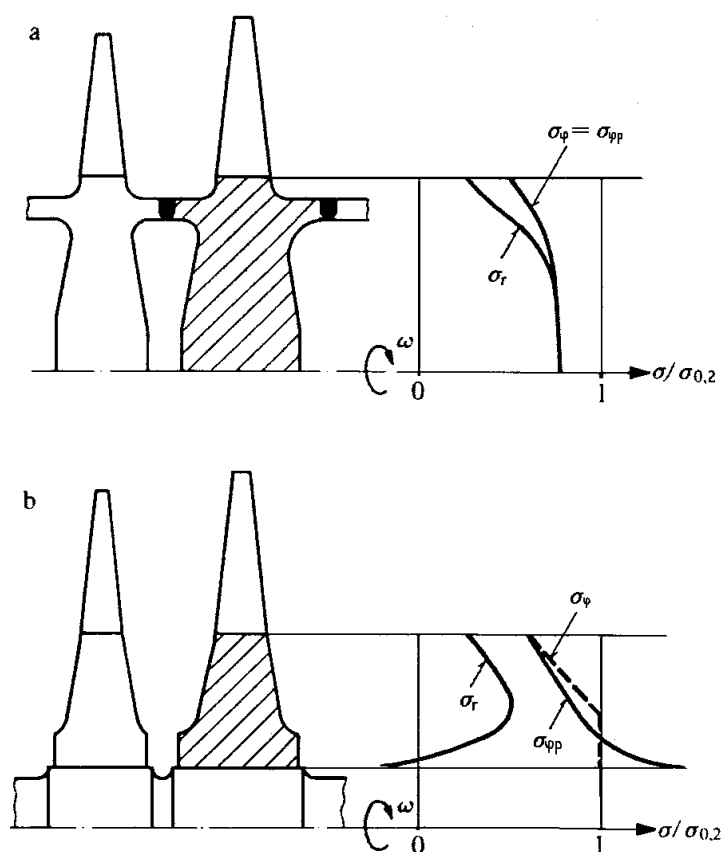


Fig. 7.35 (from [7.16])

Stresses in a shrunk-on disc of an LP rotor for a halfspeed 1300 MW nuclear turbine are presented in figure 7.36, at both zero and nominal speeds. Figure 7.36,*a* right shows that a 2 ‰ shrink fit is needed to ensure that the last stage disc of an LP rotor will not loosen at 35% overspeed. With this shrink fit, considerable stresses at zero speed and at turning gear speed result, as shown in figure 7.36,*a* left.

In figure 7.36,*b* left, the radial and circumferential stresses at nominal speed are shown, illustrating the stress raising effect of the central bore. A comparison with a disc of the same size of a welded LP rotor is given in figure 7.36,*b* right.

It can be concluded that the welded LP rotor and the monoblock rotor without central bore are superior from a stress level point of view. The plane state of stress of the discs in the welded rotors is an additional advantage, considering the danger of brittle fracture.

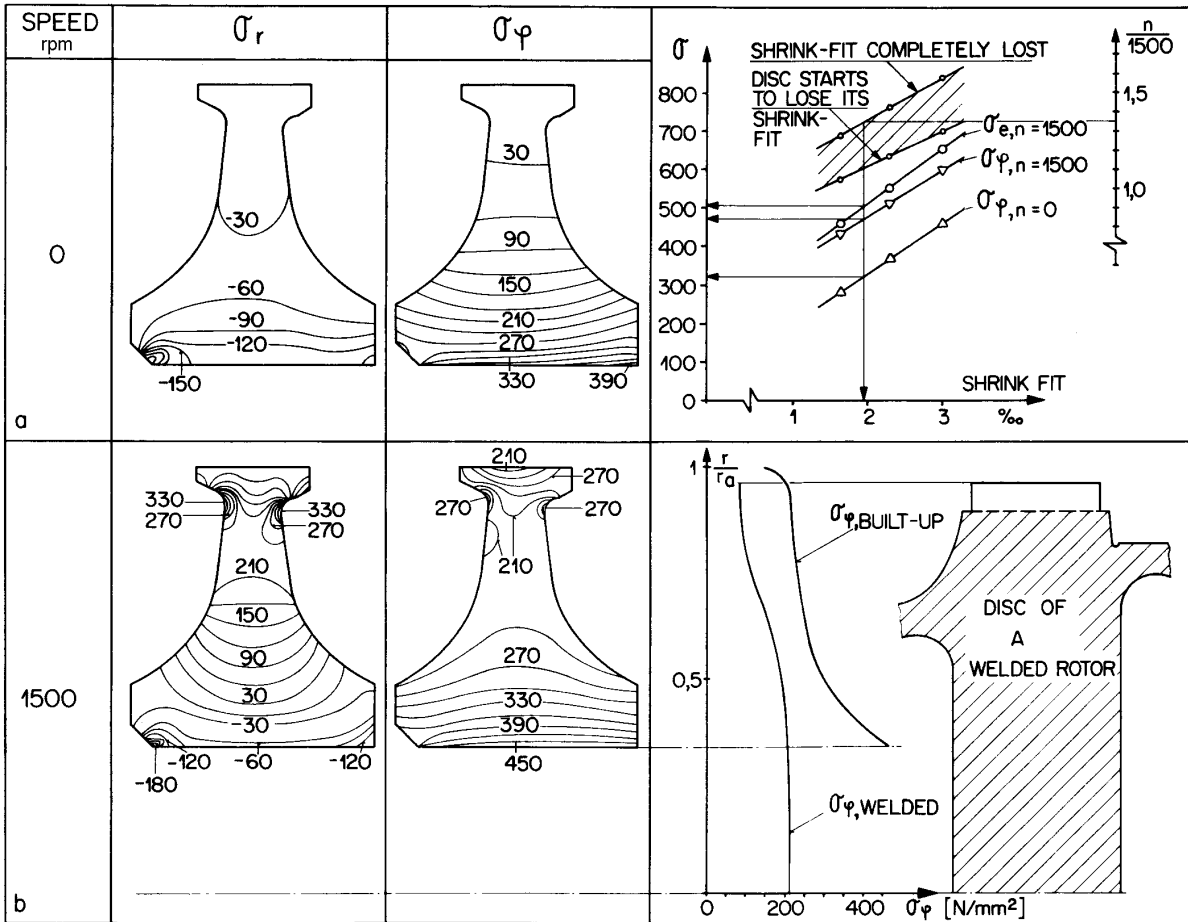


Fig. 7.36 (from [7.12])

Transient Thermal Stresses

The built-up and the welded rotor have low transient thermal stresses. This is not the case for a monoblock rotor.

Rotor Integrity

Due to the low stress level and the high forging quality, the integrity of the welded rotor is ensured under all service conditions. This is confirmed by the operational experience since 1930, when the first welded rotor (Fig.7.37) was placed in operation by BBC, with more than 4000 welded rotors presently in operation with no burst.

Safety requirements imposed upon steam turbines in nuclear power plants specify the assessment of turbine rotor *resistance to bursting*. For a precise analysis, a particular sequence of events must be supposed for the hypothetical case of a load rejection with simultaneous failure of all safety devices.

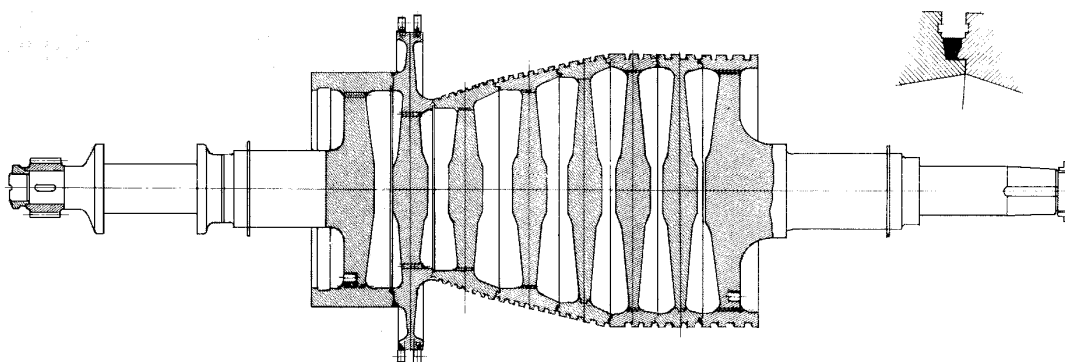


Fig. 7.37 (from [7.16])

Where the safety devices are working normally, the turbine rotor speed will remain well below the overspeed trip set-point in a rejection of full load, as a result of closing of the control valves. If the control system failed, then the first overspeed trip would function at 110% which, while resulting in a speed overswing, would not lead to an overspeed beyond 120%, for which the rotor is designed and tested. Only if the control system and the two safety systems failed simultaneously would the overspeed be exceeded.

The last-stage blades of the LP turbine would be affected first by the large centrifugal force and will fly off. The unbalance effects of the rotor, arising briefly in such a process, can be absorbed by the generously dimensioned bearing pedestals, so that the rotor remains in the bearings.

Upon further increase of speed, the stresses in the rotor become even greater starting the plastic deformation of the rotor disc. When the entire cross-section has attained a plastic condition, the disc bursts. In full-speed LP turbines, the speed at which this occurs - the so-called *bursting speed* - lies below the runaway speed and depends very much upon the design.

The runaway speed is the highest speed which is in any way possible, at which the driving power of the steam and the frictional

losses are in balance. In the reaction blading, it lies theoretically close to twice the rated speed and, in impulse blading, it occurs at approximately three times the rated speed. With half-speed turbines of the reaction type the bursting speed can lie above the runaway speed as a result of the welded rotor having no bore at the center. That is to say that there would be no rupture in this case, but only a partial transition to the plastic state in the rotor discs.

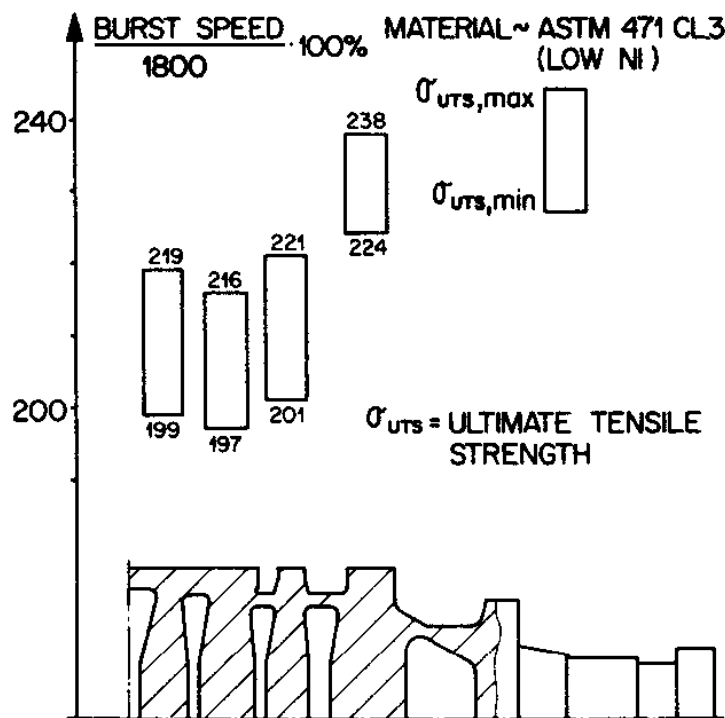


Fig. 7.38 (from [7.12])

In contrast with the LP rotors referred to above, HP rotors have a considerably higher bursting speed, lying far above the runaway speed as a result of smaller diameters, so that bursting is not possible in any way. As examples have shown, discs generally burst into three parts. This effect can be confirmed also by calculation, because the equivalent stress resulting from tangential and shear stresses at the point of rupture then assumes a maximum value.

In the U.S.A., the Nuclear Regulatory Commission has required proof, for every nuclear power turbine, that the probability of rotor bursting is less than 10^{-4} per turbine year, i.e. no more than one corresponding case of extensive damage may occur per 10,000 turbine years.

The burst speed for each disc of a welded rotor, for a halfspeed LP rotor of a 1300 MW nuclear power turbine, is shown in figure 7.38. It can be seen that, considering bearing and ventilation losses, the burst speed of this rotor lies above the maximum theoretical speed if a 50% reaction blading is used.

It can be concluded that, for a halfspeed welded LP rotor with 50 percent reaction type blading, a "destructive overspeed failure" will not occur. This can be achieved with a rotor material having a relatively low strength and, therefore, a high toughness and a low susceptibility to stress corrosion cracking.

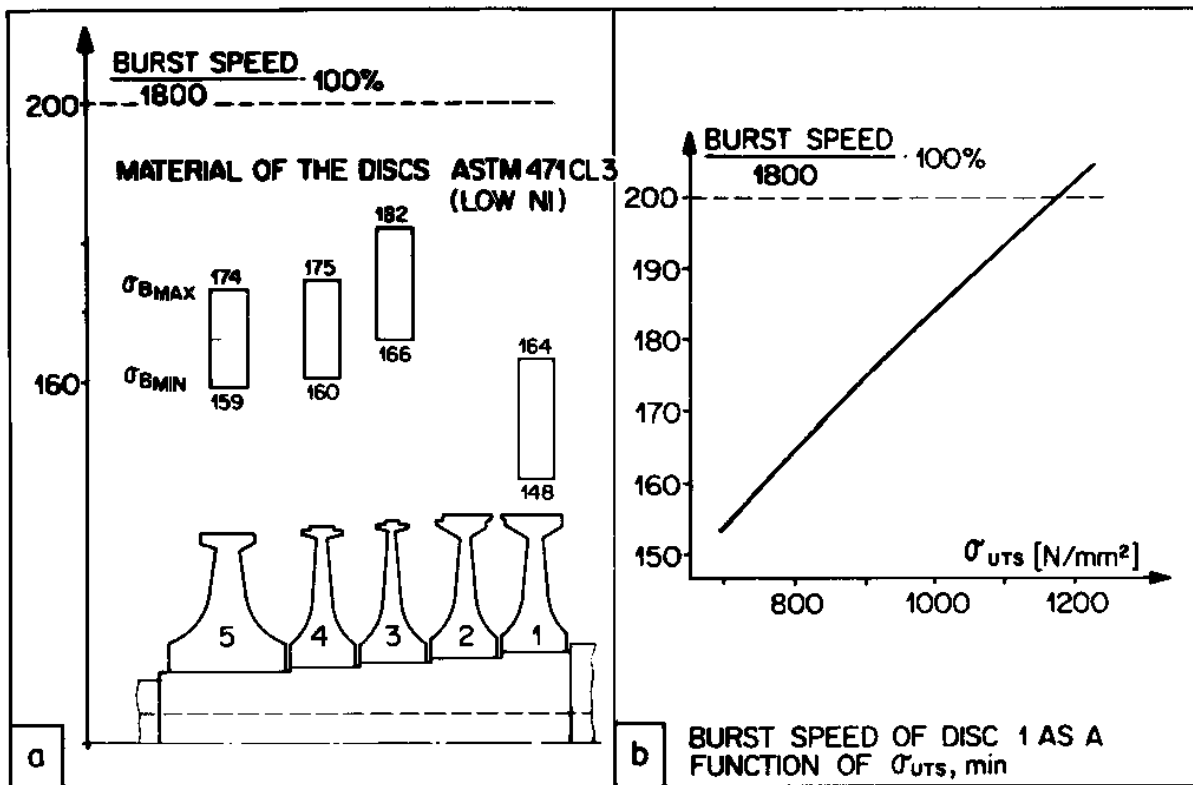


Fig. 7.39 (from [7.12])

The same calculation performed on a rotor of the built-up type is shown in figure 7.39, showing much lower bursting speeds than for the welded one. To ensure the rotor integrity, materials with very high ultimate tensile strength have to be used, resulting in lower toughness which together with the recognized small critical defect size of the shrunk-on disc can worsen the situation.

Sensitivity to Environment

The welded and monoblock rotors are protected from steam at the locations with the highest tensile stresses. This is not the case with a built-up rotor. Figure 7.40,*a* shows an LP steam turbine rotor with shrunk-on discs. These rotors are very sensitive to stress corrosion cracking in keyways, shrink-fit areas, disc rims and blade attachment areas.

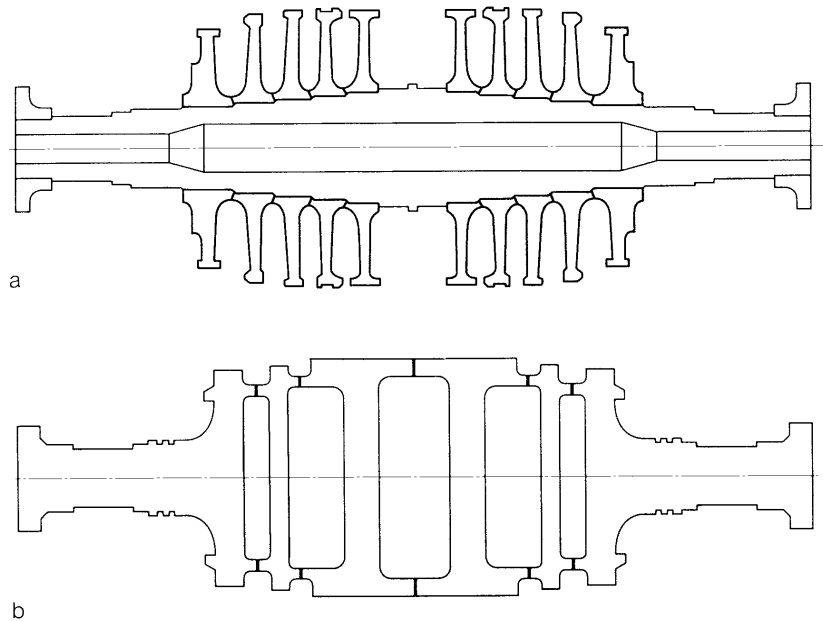


Fig. 7.40 (from [7.17])

The welded design (Fig.7.40,*b*) completely avoids the problem of stress corrosion cracking. The rotor consists of solid discs welded together at their periphery in the region of lowest stress. There are neither crevices for corrosive contaminants to concentrate in, nor regions of higher stress, such as keyways or central bores. As welds are located at a distance from the rotor centre, fatigue due to alternating bending stress is low, vibration is avoided, and the probability of rotor bursting is reduced to an absolute minimum.

The built-up rotor design suffers from a number of inherent disadvantages which make this design vulnerable. These lead to replacements of built-up rotors for halfspeed turbines by monoblock rotors manufactured from ingots up to 500 tons.

Figure 7.41 shows an HP turbine with discs shrunk on the shaft. The design was used in the early 1950's.

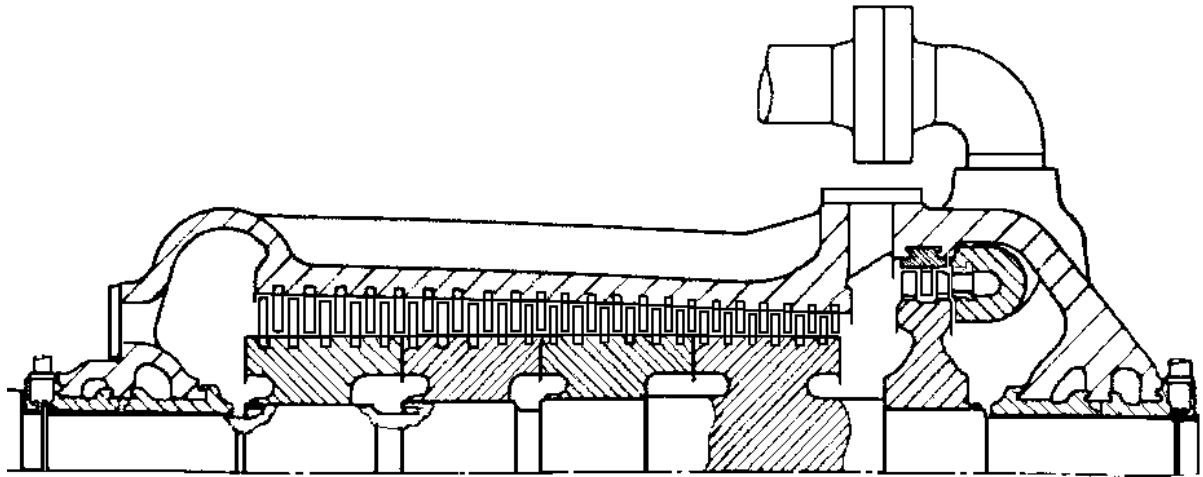


Fig. 7.41 (from [7.18])

A turbine rotor of welded construction is shown in figure 7.42. The welded shaft design results in lower stresses for a given overall diameter. The welded shaft is particularly suitable for non-steady-state thermal stressing

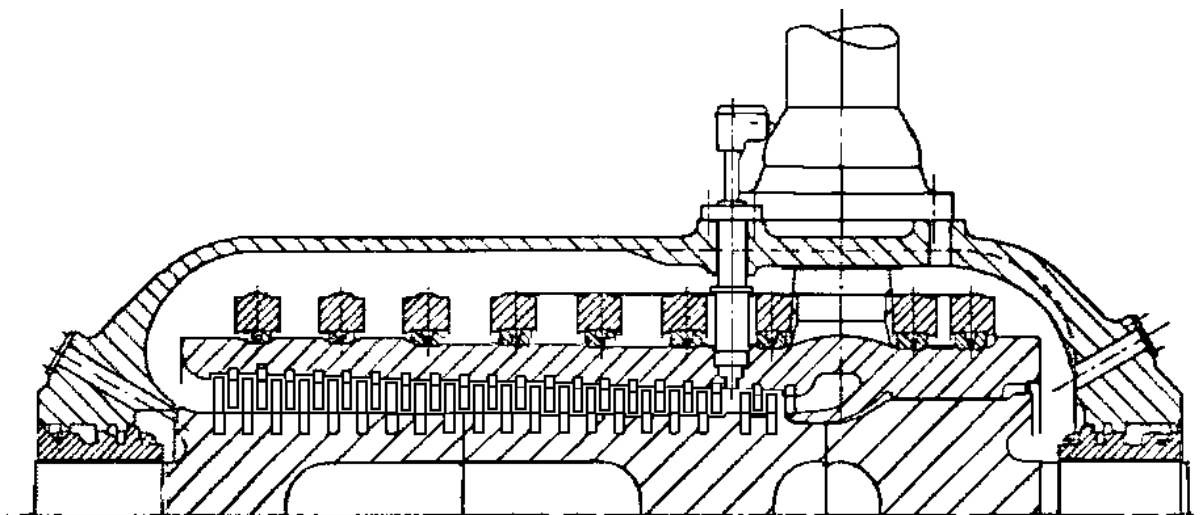


Fig. 7.42 (from [7.18])

It can be concluded that the welded rotor design appears to offer the highest reliability for large steam turbines. Monoblock rotors without central bore are well suited for industrial applications requiring small and medium outputs.

7.5 Rotordynamic Calculations

7.5.1 Critical Speed Map

To illustrate the effect of bearings on the dynamics of the rotor, it is assumed that the pedestal is infinitely rigid, and the bearing may be represented by horizontal and vertical spring coefficients. The natural frequencies of the planar vibration model of the rotor are calculated for different values of the bearing flexibility. The *critical speed map* is a diagram of the rotor 'undamped critical speeds' as a function of bearing flexibility (or bearing stiffness).

Figure 7.43 shows two such curves, corresponding to the cylindrical and conical 'rigid-body' precession modes of a rotor. On each curve, at the crossing point with the bearing flexibility curves (dotted line), the actual critical speed is indicated by a circle, in which the vibration direction is marked by a dash.

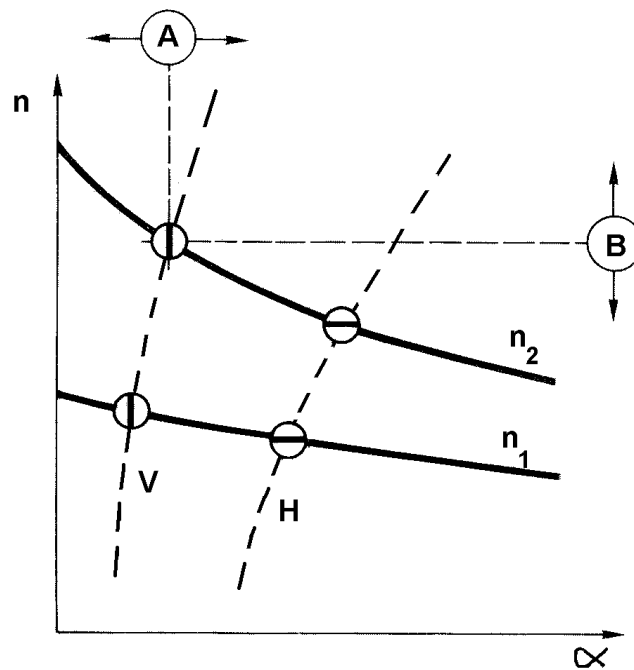


Fig. 7.43 (from [7.18])

If the natural frequencies are within inadmissible limits (10% below to 15% above the operating speed) the draft design of the shaft must be changed within technically feasible limits. A reduced bearing distance, for example, raises the natural frequencies. A similar effect has a reduction in bearing flexibility.

A shift of type *A* is obtained changing the type of bearing, the oil viscosity, the bearing clearance or the bearing pedestal. A shift of type *B* is obtained changing the shaft geometry or material, the bearing spacing or the temperature.

7.5.2 Unbalance Response

All shafts have *residual unbalances* which are continuously distributed along the shaft axis or appear as individual unbalances in various magnitudes and angular positions. In the BBC quality specifications for turbine shaft balancing, the total unbalance for a rotor is limited to a maximum value according to the balance quality grade *Q1* (VDI 2060) or *G1* (ISO 1940 [7.19]).

For the dynamic calculation of the rotor, it is assumed that the operating unbalance increases to a quality grade *Q2.5* (or *G2.5*) as a result of installation of the coupling, bearing configuration, salt deposits, corrosion of shaft components, cavitation and thermal bending. The value $Q=2.5$ mm/s corresponds to a centre of gravity offset

$$e = \frac{Q}{\omega} = \frac{2.5 \cdot 1000}{\frac{\pi n_N}{30}} = \frac{23,885}{n_N} \approx \frac{24,000}{n_N} \quad [\mu\text{m}]$$

where n_N is the operating speed, rpm.

The total unbalance is

$$U = me = \frac{24,000 \cdot m}{n_N} \quad [\text{mm} \cdot \text{g}]$$

where m is the mass of the rotor section between two bearings, kg.

So, for a turbine operating at 3000 rpm, the permissible residual unbalance is $U = 8m$ [mm g].

Using a finite element model of the rotor, the first modes of lateral vibration are calculated, usually all modes below the trip speed and the mode just above the trip speed. Then, the worst unbalance distribution for each mode is considered, as in figures 7.44,*a-d*, subdividing the total unbalance into suitable individual unbalance

components. Apart from the first three modes of vibration, the vibration produced by the overhang half couplings is also considered.

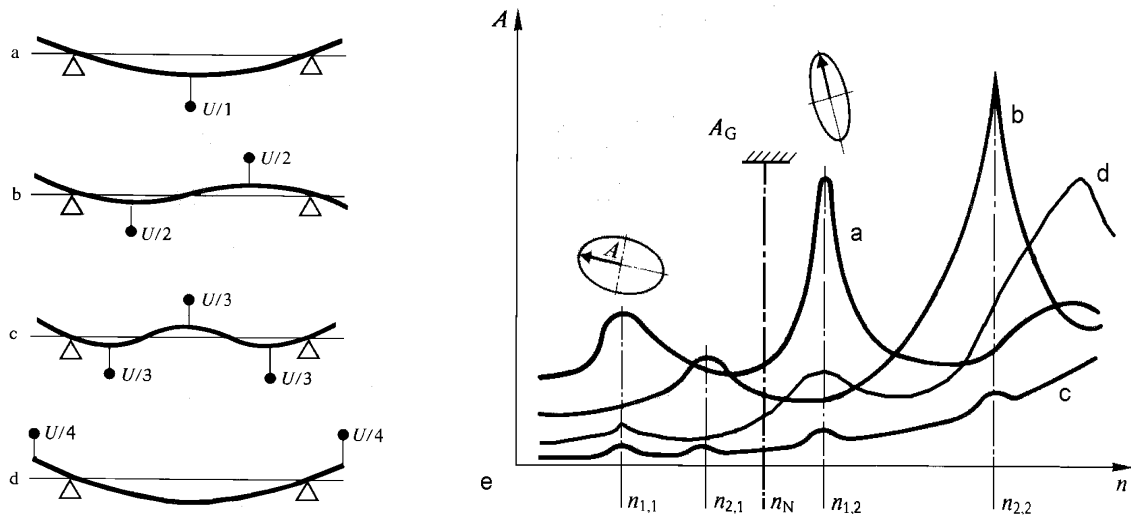


Fig. 7.44 (from [7.18])

The result of the unbalance response calculation at the left bearing location is shown in figure 7.44,e. Each unbalance distribution results in a different amplitude versus speed curve. The amplitude A is calculated as the major semiaxis of the precession elliptical orbit. The positions of the amplitude peaks along the horizontal axis indicate the *unbalance critical speeds*. In figure 7.44,e, $n_{1,1}$ and $n_{1,2}$ are the critical speeds for the first unbalance distribution, $n_{2,1}$ and $n_{2,2}$ are the critical speeds for the second unbalance distribution. The amplitudes of the unbalance response have to be compared with limit values given by guidelines and standards at the operating speed n_N .

The guideline *ISO 7919-2* [7.20] indicates, as a limit of 'good' vibration performance, a maximum value of the journal orbit radius

$$s_{\max A} = \frac{2400}{\sqrt{n_N}} \text{ } [\mu\text{m}] .$$

Taking a safety factor of 1.7, the limit value is established at

$$A_G = \frac{s_{\max A}}{1.7} = \frac{1400}{\sqrt{n_N}} \text{ } [\mu\text{m}] .$$

For a turbine operating at 3000 rpm, $A_G = 26 \mu\text{m}$. The condition $A \leq A_G$ must be satisfied at all speeds up to n_N . In figure 7.44,*e* the peak at $n_{2,2}$ higher than A_G is beyond the operating speed range.

7.5.3 Calculation Example [7.18]

The effectiveness of the unbalance response calculation is illustrated in following by means of an example concerning a turbine rotor used for mechanical drive with variable operating speeds.

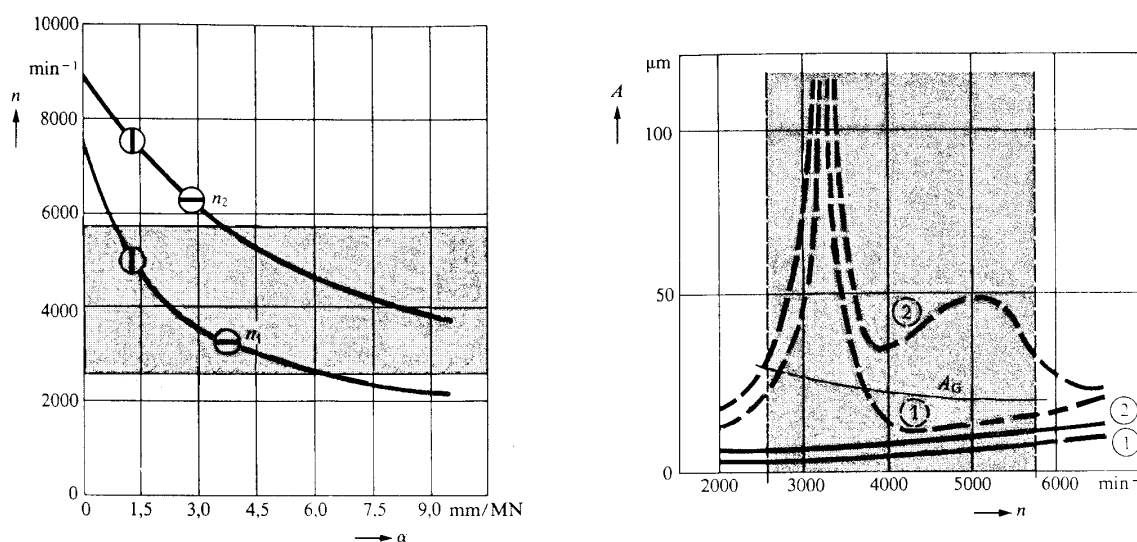


Fig. 7.45 (from [7.18])

The critical speed map for the first two modes of vibration is shown in figure 7.45,*a*. The mean value of oil film flexibilities of both bearings for the first mode is $\alpha_v = 1.3 \text{ mm/MN}$ in the vertical direction and $\alpha_h = 3.7 \text{ mm/MN}$ in the horizontal direction. According to figure 7.45,*a*, there are two undamped critical speeds within the speed range from 2600 to 5800 rpm, the first at 3250 rpm and the second at 5000 rpm. The turbine must therefore be operated at both critical speeds which is inadmissible according to the conventional critical speed design considerations.

The commissioning report, however, stated: "Turbine operating behaviour is very good irrespective of load and speed. Turbine shaft amplitudes are 8-10 μm , bearing housing vibrations are 1-3 μm in

the horizontal and vertical directions. Critical speeds could not be determined".

The unbalance response calculation confirmed the observed operating behaviour. Shaft vibration amplitudes of both bearings show absolutely no resonance peaks near the critical speeds (solid lines in Fig.7.45,b). Despite this, there are two critical speeds in the operating speed range which can be determined if the unbalance response is calculated with the oil film damping reduced to 10% (dotted lines). As shown in figure 7.45,b, there are two unbalance response peaks, the first at 3250 rpm and the second at approximately 5000 rpm.

The operating behaviour of the shaft was smooth, since in this case it was short and quite rigid and was also provided with a soft oil film. The softer the oil film is in relation to the shaft rigidity, the more the shaft moves in its bearing so that oil film damping becomes fully effective.

7.6 Condition Monitoring of Steam Turbines

Figure 7.46 shows a layout of a machine protection system for large steam turbines.

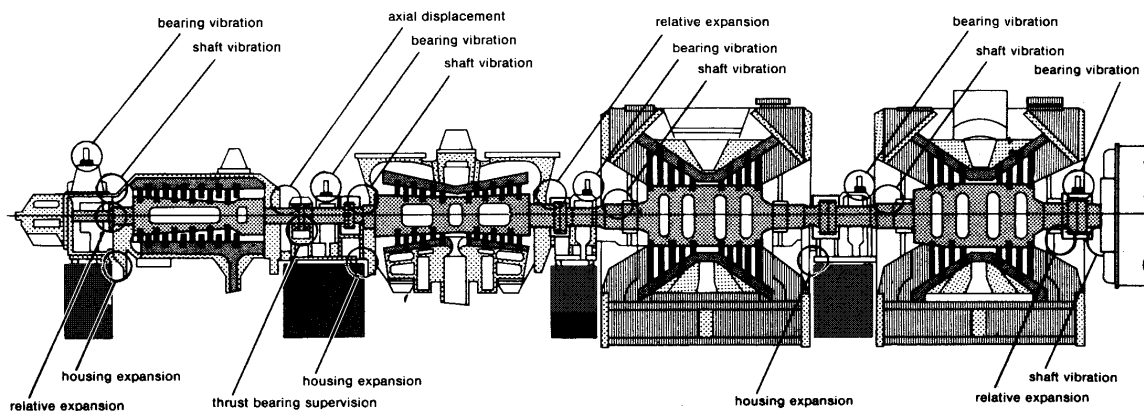


Fig. 7.46 (from [7.21])

A continuous monitoring system of a steam turbine set involves measurement of radial displacement (two proximity sensors 90° apart), axial position (at thrust bearing) and speed (key phasor plus proximity sensor) of the shaft, radial and axial vibration of machine casings and piping (piezoelectric accelerometers), as well as measurement of

housing expansion and relative expansion (casing vs shaft), with provisions for periodic checks of machine alignment and bearing housing vibration (velocity pickups).

7.7 Guidelines for Shaft Vibrations

The guidelines *ISO 7919, Part 3* [7.22] are useful in the evaluation of shaft vibrations measured close to the bearings, under normal operating conditions, for industrial turbines and turbine-generators having powers up to 50 MW and rated speeds up to 30,000 rpm.

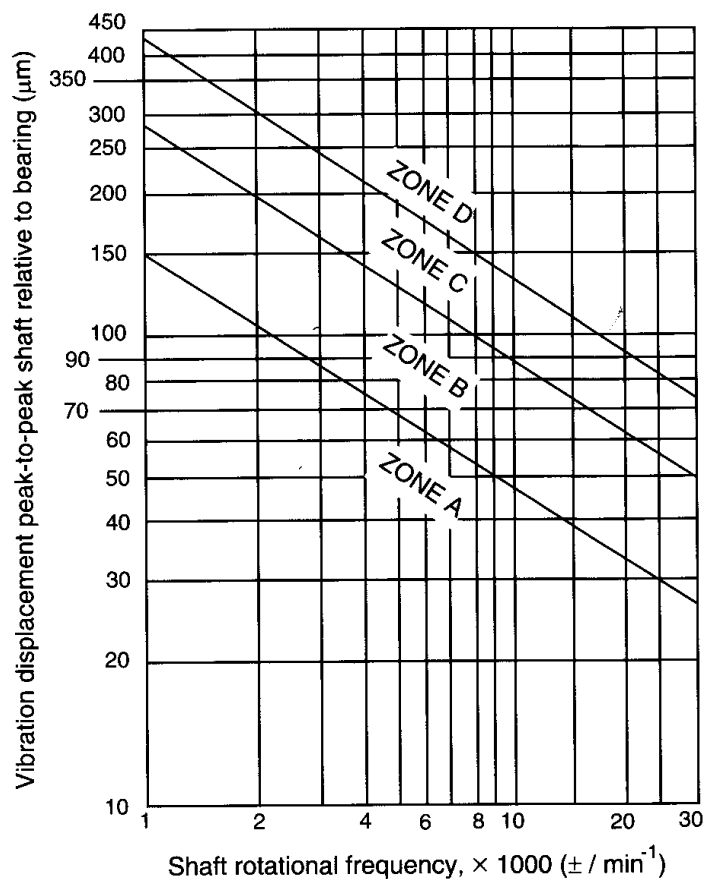


Fig. 7.47 (from [7.22])

In figure 7.47, zone *A* represents new machines that can be operated without restriction. Zone *B* is acceptable for long-term operation. Zone *C* represents machines that may be operated for a limited time until a suitable opportunity arises for remedial action to

be taken. Zone *D* is identified as a trip level as these values are considered to be of sufficient severity to cause damage.

Guidelines for large land-based steam turbine-generator sets with power outputs greater than 50 MW, as given in *ISO 7919, Part 2* [7.20], are presented in Chapter 8.

7.8 Rotor Modelling

Figure 7.48 illustrates the finite element modelling of a low pressure rotor.

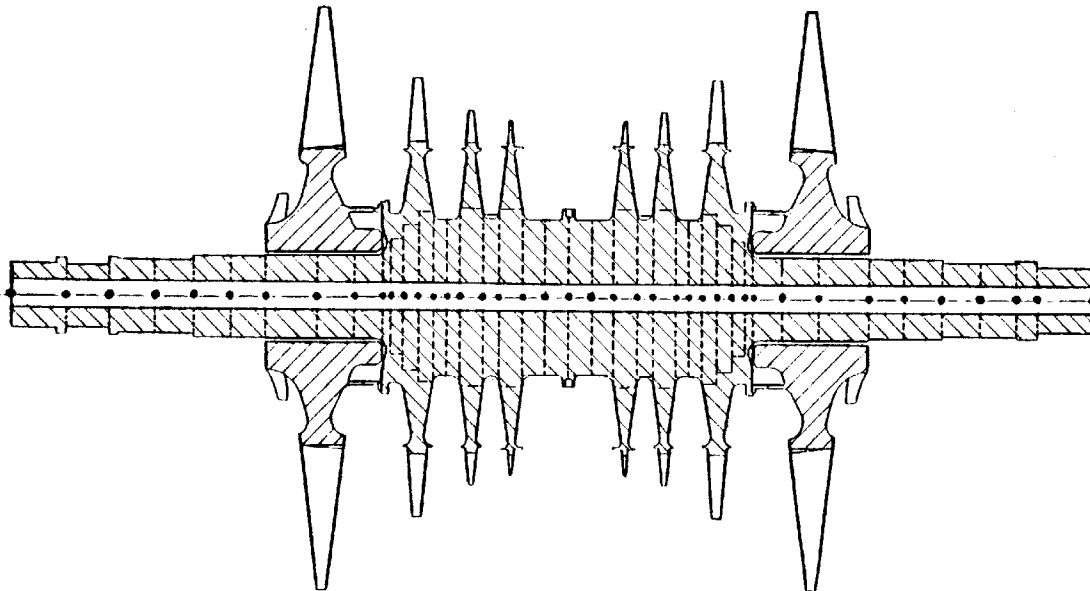


Fig.7.48 (from [7.23])

Usually, Timoshenko beam elements are used to model the shaft. For the discs integral with the shaft, note the way in which the outer diameter of each element is established, in order to ensure a continuous stepwise variation along the rotor length, which is important in the calculation of shaft element stiffnesses. The remaining part of each disc is considered in the calculation of the disc mass moments of inertia. Consistent mass matrices and gyroscopic matrices are normally used for the shaft elements.

References

- 7.1 Grecu T., **Mașini și turbine cu abur**, Litografia Învățământului, București, 1955.
- 7.2 Logan E., **Turbomachinery. Basic Theory and Applications**, 2nd ed., Marcel Dekker Inc., New York, 1993.
- 7.3 Hänsermann A., Hollauf H. and Hosp A., *Steam Turbines of Medium Output in Industry and Power Plants*, Brown Boveri Review, vol.67, nr.5, pp 277-291, 1980.
- 7.4 * * * *Back-Pressure Turbosets for Industrial Use*, Brown Boveri Publication 3090E, 1967.
- 7.5 Zimmermann M., *Steam Turbines for Industry*, Brown Boveri Review, vol.63, nr.6, pp 333-338, 1976.
- 7.6 Reihard K., Vest F. and Vogelsang E., *Experience with the World's Largest Steam Turbines*, Brown Boveri Review, vol.63, nr.2, pp 106-114, 1976.
- 7.7 Cantuniar C., *Accelerated Cooling of High-Output Turbines*, Brown Boveri Review, vol.63, nr.2, pp 141-147, 1976.
- 7.8 Somm E., *Developing Brown Boveri Steam Turbines to Achieve Still Higher Unit Outputs*, Brown Boveri Review, vol.63, nr.2, pp 94-105, 1976.
- 7.9 Busse L. and Soyk K.H., *World's Highest Capacity Steam Turbosets for the Lignite-Fired Lippendorf Power Station*, ABB Review, nr.6, pp 13-22, 1997.
- 7.10 Hohn A., *Les rotors des grosses turbines à vapeur*, Revue Brown Boveri, vol.60, nr.9, pp 404-416, 1973.
- 7.11 Kostyuk A.G. and Frolov V.V. (eds), **Steam and Gas Turbines** (in Russian), Energoatomizdat, Moskow, 1985.
- 7.12 Bertilsson J.E. and Berg U., *Steam Turbine Rotor Reliability*, EPRI Workshop on Rotor Forgings for Turbines and Generators, Palo Alto, California, Sept 13-17, 1980.
- 7.13 Czeratzki A., Heiberger D. and Schmidt J., *Long-Term Recording of Operating Data for Lifetime Evaluation*, Brown Boveri Review, vol.72, nr.4, pp 184-189, 1985.
- 7.14 Dowling N.E., **Mechanical Behavior of Materials**, 2nd ed., Prentice Hall, Upper Saddle River, N.J., 1998.
- 7.15 Hohn A., Brandstätter K. and Cantuniar C., *Large Steam Turbine Generators for Cyclic Operation*, Brown Boveri Review, vol.67, nr.8, pp 492-499, 1980.

- 7.15 Bertilsson J.-E., Faber G. and Kuhnen G., *50 Years of Welded Turbine Rotors*, Brown Boveri Review, vol.68, nr.12, pp 467-473, 1981.
- 7.16 Krämer E., Huber H. and Scarlin B., *Low-Pressure Steam Turbine Retrofits*, Brown Boveri Review, vol.83, nr.5, pp 4-10, 1996.
- 7.17 Berg U., Melton K.N. and Heiberger D., *Determining and Evaluating the Service Life of Steam Turbine Components*, Brown Boveri Review, vol.68, nr.12, pp 486-496, 1981.
- 7.18 Busse L. and Heiberger D., *Aspects of Shaft Dynamics for Industrial Turbines*, Brown Boveri Review, vol.67, nr.5, pp 292-299, 1980.
- 7.19 **ISO 1940**, Balance Quality of Rotating Rigid Bodies, 1973.
- 7.20 **ISO 7919-2**, Mechanical Vibration of Non-Reciprocating Machines - Measurements on Rotating Shafts and Evaluation Criteria - Part 2: *Large Land-Based Steam Generator Sets*, 1996.
- 7.21 Kühl H. and van den Berge H., *Monitoring High-Speed Turbines*, Science and Industry, no.15, pp 30-33, 1974.
- 7.22 **ISO 7919-3**, Mechanical Vibration of Non-Reciprocating Machines - Measurements on Rotating Shafts and Evaluation Criteria - Part 3: *Guidelines for Coupled Machines*, 1996.

8. TURBO-GENERATORS

8.1 Introduction

The turbo-alternator was developed by C.E.L. Brown and first marketed by Brown Boveri in 1901. With a cylindrical rotor having embedded windings, it has proven to be the only possible design for high speeds, as when driven direct by a steam turbine. Such alternators are available for ratings between 500 kVA and 20,000 kVA and higher, but are not normally used below 2500 kW, because salient-pole machines with end-shield bearings are more economical.

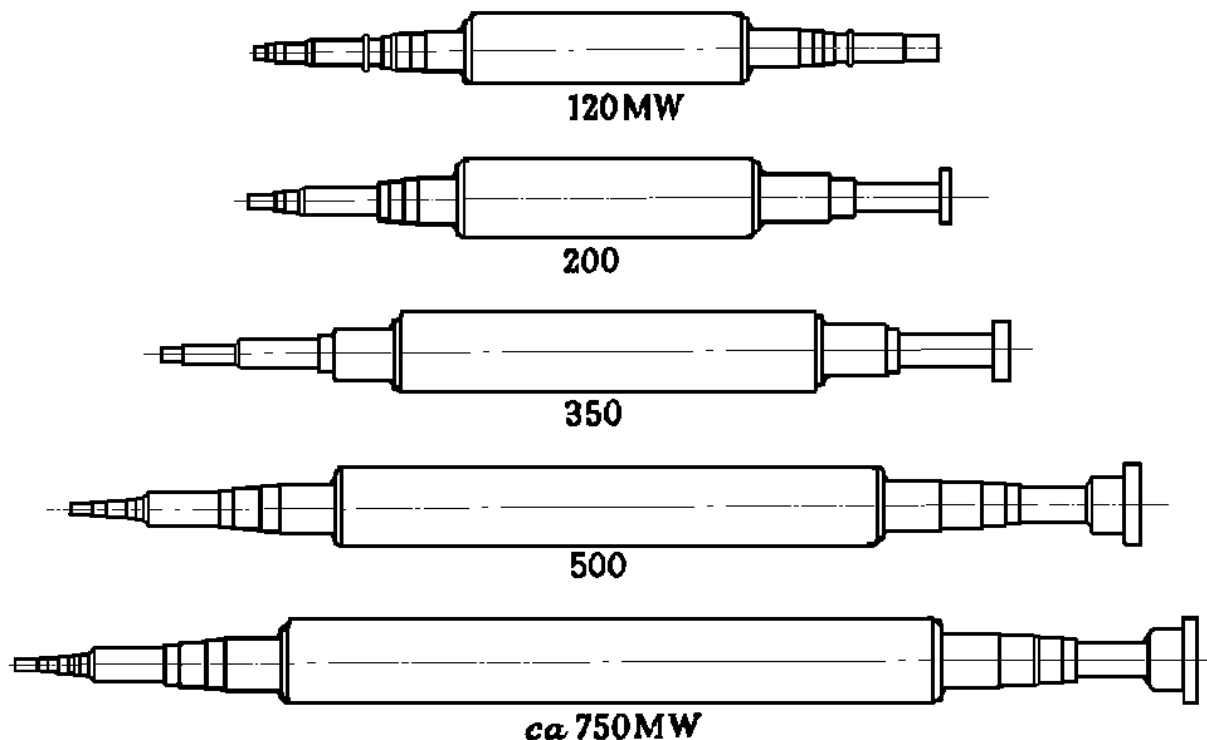


Fig. 8.1 (from [8.2])

Beyond 2500 kW, an alternator running at 3000 (or 3600) rpm permits a more economical gear to be used than a 1500 (or 1800) rpm alternator for the same turbine [8.1].

Between 1940 and 1965, the sizes of turbo-generator rotors have increased dramatically. Figure 8.1 shows the relative sizes of the forgings from which these rotors were cut. The rotors with an output of about 750 MW are 1.7 times longer than the 120 MW rotors that were the largest made in the 1940's. The weight and distance between the bearing centres of the 120 MW rotor are approximately 30 tons and 8 m, respectively, whereas the corresponding parameters for the 500 MW rotor are 70 tons and 12 m. Modern rotors have one or two critical speeds below their operating speed of 3000 rpm.

As the output of these machines has been increased so the length of the rotors has increased, but not the diameters - for increases of diameter are limited by stress considerations. This increase of slenderness has meant that lower critical speeds have to be contended with. This, in turn, has meant that sensitivity to vibration has increased.

8.2 Design Characteristics

The rotor of small units is a solid cylindrical forging of high-quality steel with slots milled in it to accommodate the field winding. For larger units, several hollow cylinders are fitted over a central draw-bolt threaded at both ends, to which the two shaft extensions are fastened by shrinking. The specially formed winding is a single layer of copper strip insulated with glass-fibre which is pressed and baked into the slots. To secure the end sections, end-bells forged from solid-drawn non-magnetic steel with ventilation holes or slots are used.

For large ratings, in the normally preferred tandem arrangement, the mechanical power produced in a number of turbine cylinders has to be converted into electricity in a single machine. The simplest way of attaining a high unit output is to increase the physical size of the machine, but this method has limitations. For the cross-section of the machine there are limits regarding the mechanical stresses and the size of parts that can be transported. The outlook for development of rotor materials of greater strength and stator core-plates with a higher saturation level indicates only a modest increase

in rotor cross-sections. Increasing the active length and thereby the slenderness is restricted by the mechanical stability of the shaft line.

To keep pace with the demand for increased unit ratings one must increase the specific electrical loadings, both on structural materials and on all of the available space. Whereas in 1940 a turbo-generator for 3000 rpm weighed 2 kg per kW of output, its 1975 counterpart weighed only 0.5 kg/kW [8.3].

Up to the end of the Second World War turbo-generators in all countries except the USA were cooled by forced circulation of air. With this technology, machines reached unit ratings of about 80 MVA. Post-war higher unit ratings required hydrogen cooling. Between 1945 and 1975 generator ratings increased from about 100 MVA to 1600 MVA. The most significant steps, summarized below, are connected with removal of losses from the active part of the machine and cooling.

Air-Cooled Generators

Air-cooled turbo-generators have been built for ratings up to 150 MVA. They can be driven by steam or gas turbines, being simple but robust. A longitudinal section of a BBC type *WX* generator is shown in figure 8.2. The rotor body 1 and the rear-end coupling form a single forging. The rotor winding 2, consisting of hard-drawn hollow copper conductors, is mounted in parallel-sided slots. The damping cage is formed by electrically conducting slot wedges in conjunction with short-circuit rings and silver-plated contact fingers located on either side under the rotor end-bells 3. The overhung end-bells of non-magnetic steel which hold the rotor end-coils are shrink-fitted to the rotor body and secured by a bayonet connection. Special labyrinth glands 8 between the casing 9 and the bearing pedestal 7 prevent oil from entering the machine. At the non-driving shaft end 5 an a.c. exciter with rotating diodes or, possibly, sliprings with a cooling fan can be mounted. Other numbered parts are the axial fan 4, bearing 6, laminated core 10, compression rings 11, stator end coil 12, terminals 13 and leakage-air filter 14.

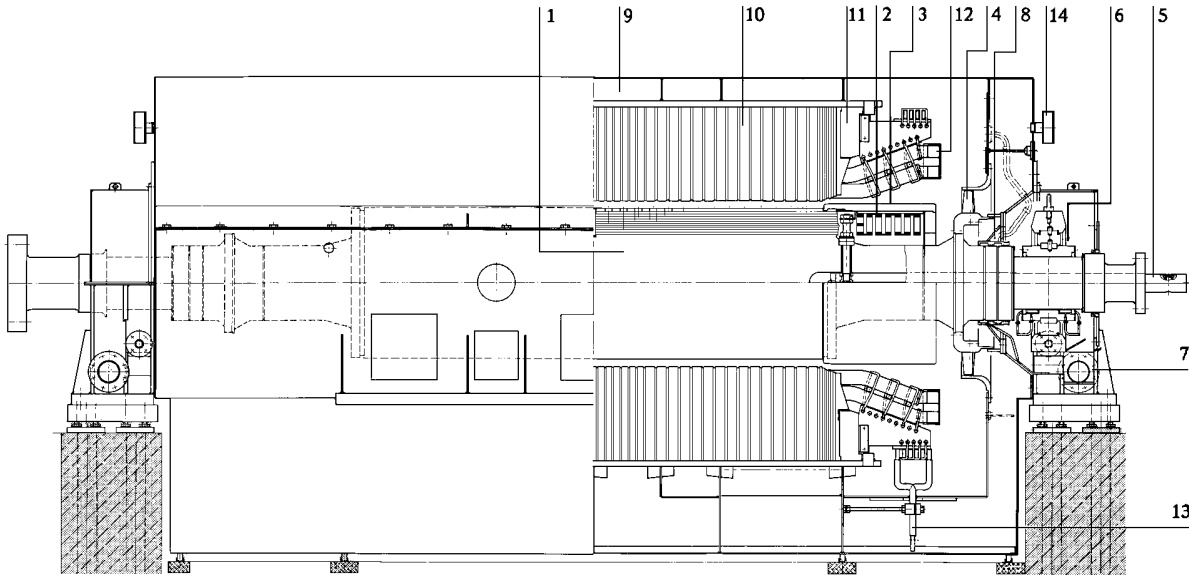


Fig. 8.2 (from [8.4])

The complete rotor is balanced statically and dynamically and run for two minutes at 20% overspeed. This stresses the rotor body and the rotor end bells up to, at the most, 66% of their yield point.

Generators with Direct Hydrogen Cooling of the Rotor

When first introduced for cooling generators, hydrogen was simply substituted for air as coolant since, for the same heat capacity, it has a higher heat transfer coefficient and, due to its lower density (about 1/10 that of air), requires much less pumping power. Hydrogen flows in channels in direct contact with the copper conductors, where the losses are in fact produced. The rotor was the critical component of the generator at that time and these advances secured a major increase in unit ratings.

For rated powers up to 450 MVA, ABB builds hydrogen-cooled turbo-generators. A schematic view of the cooling system is shown in figure 8.3 where: 1 - stator core, 2 - stator winding with indirect cooling, 3 - rotor body, 4 - axial fans, 5 - gas passage, 6 - hydrogen-gas cooler, 7 - casing.

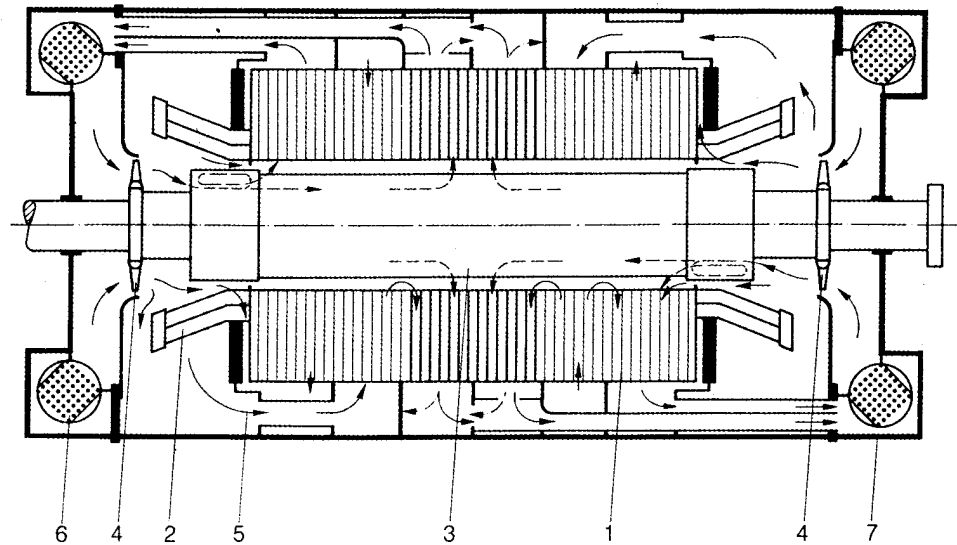


Fig. 8.3 (from [8.5])

Generators with Indirect Cooling of the Stator Winding

This type of generator, illustrated in figure 8.4, is used for ratings between 60 and 250 MVA at 3000 rpm. The rating is limited by loss removal from the stator winding, which ceases to be economical when the current density reaches 3 A/mm^2 .

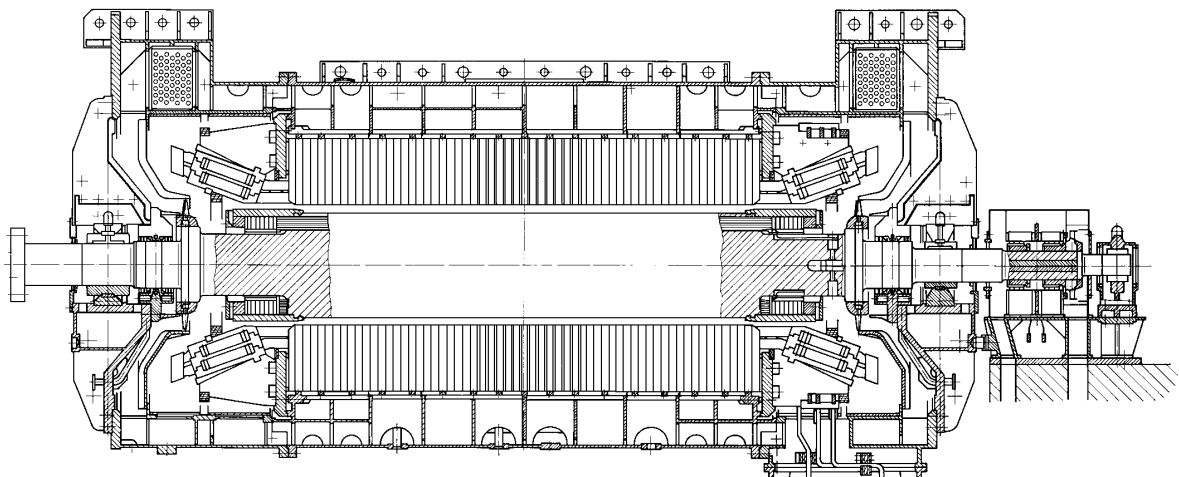


Fig. 8.4 (from [8.3])

Generators with Direct Liquid Cooling of the Stator Winding

Ratings in excess of 250 MVA require more effective stator cooling. After a period of using low-viscosity transformer oil, demineralized water was introduced in hollow *Roebel* bars. Machines with direct, forced rotor cooling can be built up to ratings of 1000 MW and over.

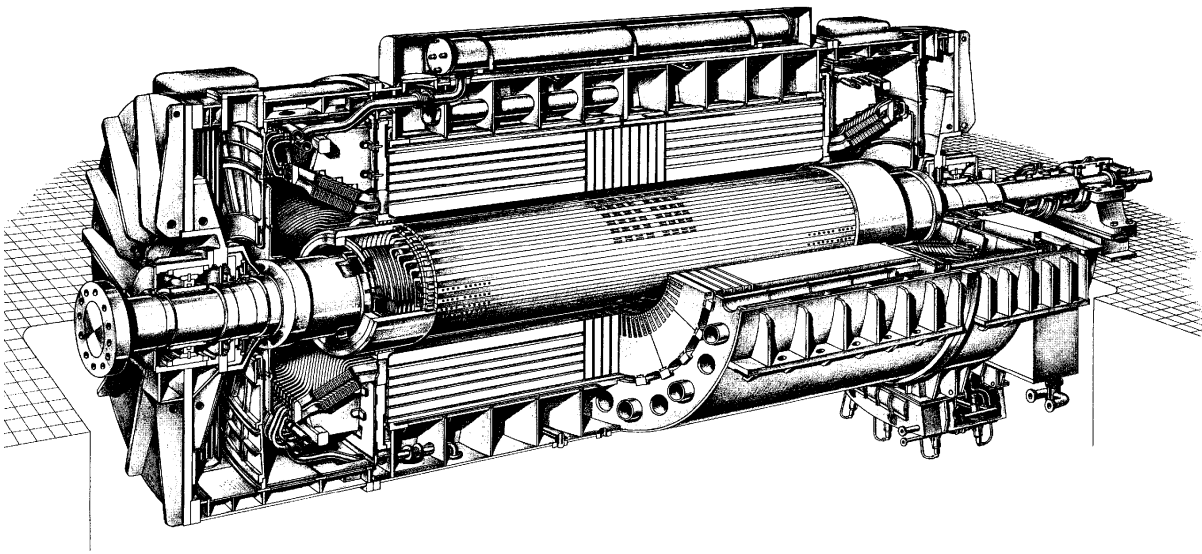


Fig. 8.5 (from [8.3])

Figure 8.5 is a cutaway perspective drawing of a 400 MVA, 3000 rpm generator with water-cooled stator winding and forced hydrogen direct cooling in the rotor. Due to the much-increased flux density and current loadings, generators of over 500 MW employing these cooling methods must have their stator cores mounted in a flexible suspension. This is necessary in order to isolate the foundations from the enormous magnetic vibration forces arising between rotor and stator.

Large Turbo-Generators

Turbo-generators for nuclear power stations are in the rating range 1000 to 1300 MW. Depending on the station's cooling water supply, sets running at either 1500 (1800) or 3000 (3600) rpm have been supplied. Four-pole machines are preferred to two-pole machines because the magnetic forces are more favourably distributed in the former and the flexible stator core suspension may be omitted.

Figure 8.6 shows a two-pole 1185 MVA, 3000 rpm, generator with water-cooled stator and hydrogen-cooled rotor. For sets operating at the optimum speed of 3000 rpm, generator cooling is augmented, especially in the rotor. A two-stage high-head impeller is used to pump the hydrogen gas at a much higher velocity through the hollow copper conductors of the rotor winding.

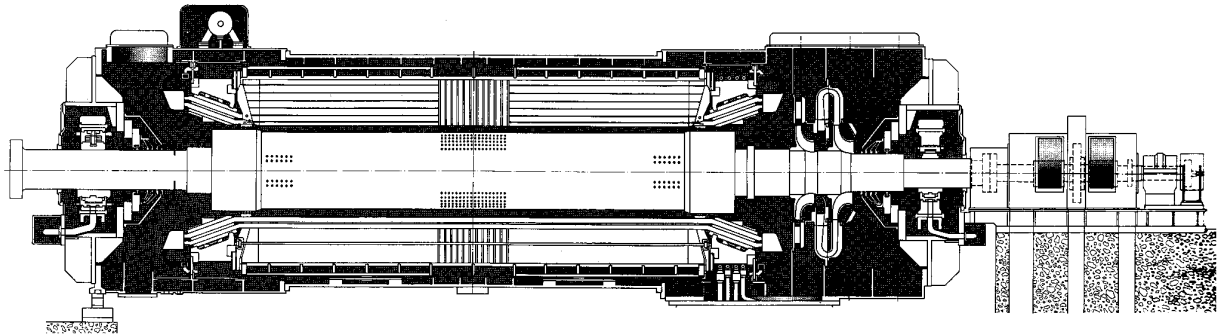


Fig. 8.6 (from [8.3])

Direct, axial hydrogen cooling used for the rotor winding of two-pole ABB generators is schematically shown in figure 8.7, where: 1- stator core, 2 - water cooled stator winding, 3 - water drain ducts, 4 - water passage, 5 - rotor body, 6 - radial blower, 7 - diffuser, 8 - diaphragm, 9 - gas passage, 10 - hydrogen-gas cooler, 11 - casing.

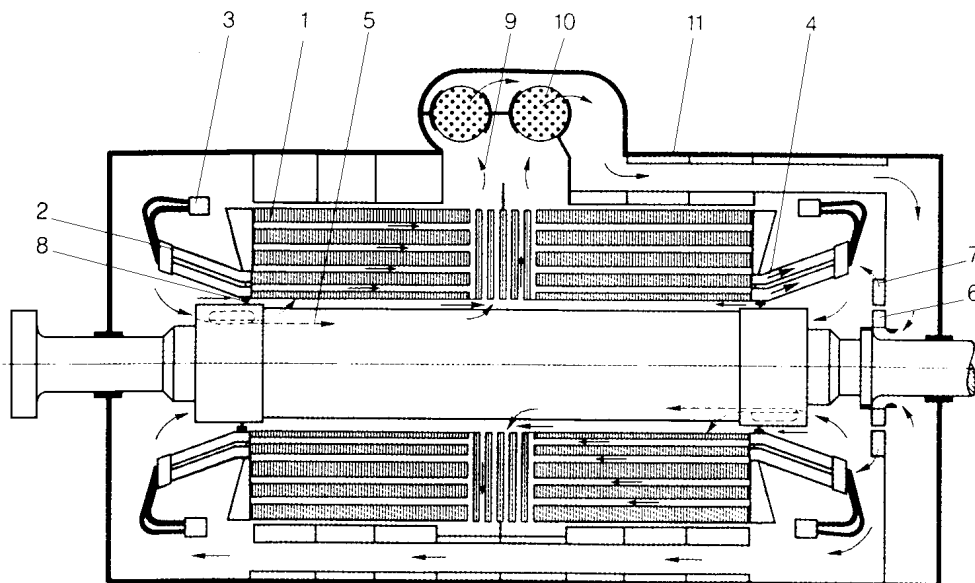


Fig. 8.7 (from [8.5])

The advantage of axial cooling is that the field winding conductors exhibit the same temperature level in every slot cross-section, so there is no relative movement between the hollow conductors. Usually, orifices in the air-gap region enable the blower pressure to be utilized as additional pressure for the rotor on the driven and non-driven sides.

In the world's largest lignite-fired power plant at Lippendorf, Germany, the generators have 1167 MVA rated apparent power, 3000 rpm, and 27 kV rated voltage. The weight of the rotor is 97 tons [8.6].

The slots for the rotor winding are milled along the full length of the rotor body, which is an integral forging made of heat-treated steel alloy with a high magnetic permeability. So-called flexure grooves (cross-cuts) in the pole regions ensure uniform flexibility in all the rotor cross-sectional axes.

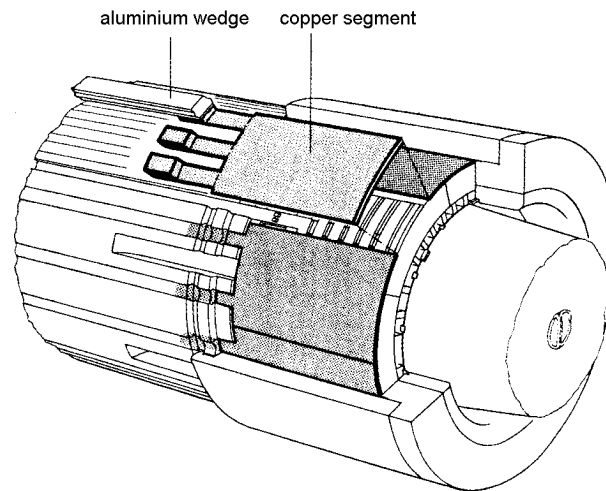


Fig. 8.8 (from [8.5])

The field winding consists of concentric coils of silver-alloyed copper hollow conductors, made up of semi-turns soldered together in the overhang winding. It is stopped from being pulled by the centrifugal forces by the wedges that form the damper winding (Fig.8.8) and by the rotor retaining rings (Fig. 8.9).

The damper winding consists of slot wedges extending over the full length of the rotor, the damper segments and the rotor retaining rings. Additional damper slots with wedges of the same shape are

located in the pole area. The rotor retaining rings, which are made of non-magnetic, austenitic steel which is resistant to stress corrosion cracking, are shrunk-mounted and secured against axial displacement by a bayonet lock and against tangential displacement by wedges.

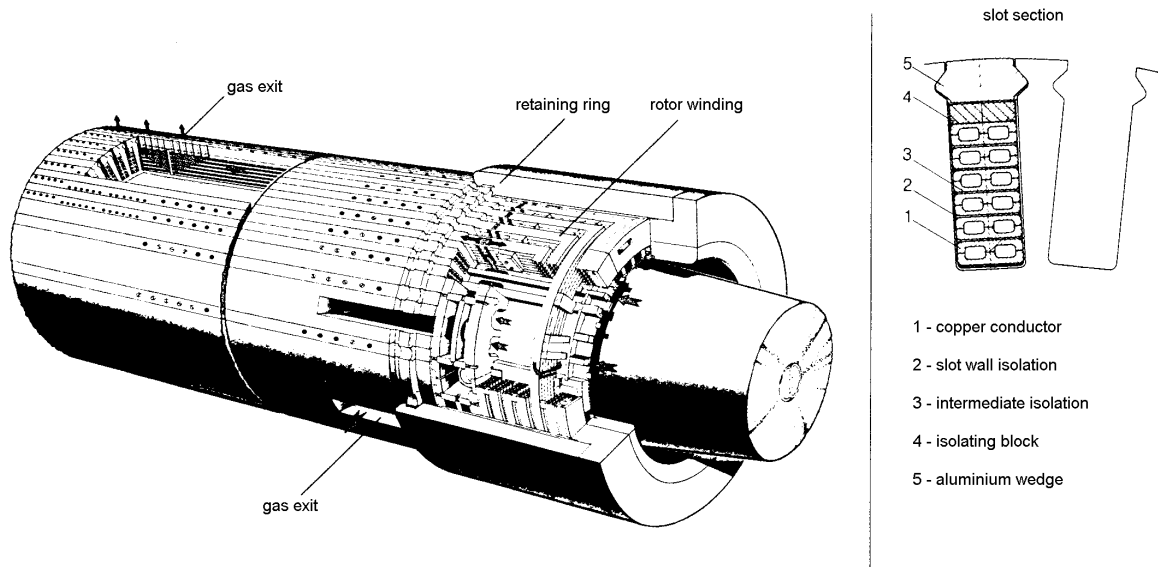


Fig. 8.9 (from [8.5])

8.3 Precession of Non-Symmetric Rotors

Large modern alternator rotors are particularly sensitive to vibration and it has been found that, while accurate balancing is of cardinal importance, it is not sufficient to remove all vibration. There remains, in particular, the second order (or 'twice per revolution') forced vibration which arises from the dual flexural rigidity that is virtually inescapable in a two-pole machine; the motion is excited by the weight of the rotor. This is a source of considerable difficulty, largely because it can be cured only at the design stage and cannot be 'balanced'. Certain 'trimming' modifications can be made but these present problems of their own.

In fact it would be very difficult to design accurately an alternator rotor so as to have axial symmetry in a dynamical sense. The rotor is, in effect, a large rotating electromagnet, having a north pole and a south pole on opposite sides of the rotor and having slots

cut in it, in which copper conductors are embedded to provide the magnetic field.

The cross-section of a 120 MW alternator rotor after slotting is shown in figure 8.10,*a*. It is clear from the figure that the flexural rigidity of the shaft is unlikely to be the same for bending about the horizontal and the vertical neutral axes, even after copper conductors and steel wedges have been placed in the slots.

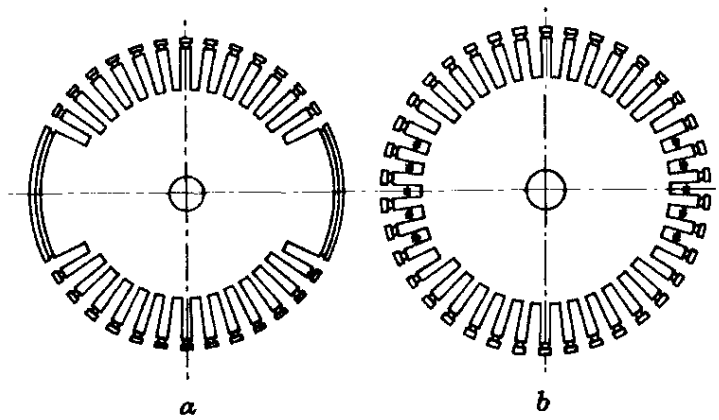


Fig. 8.10 (from [8.2])

In attempts to equalize these rigidities, one of two schemes is usually adopted. In the first, the pole faces are slotted as shown in figure 8.10,*b*. In order to maintain the magnetic flux density, the slots in the pole faces are filled with steel bars that are wedged in. The second technique is to build a rotor in the manner of figure 8.10,*a* and then to cut lateral slots across the poles at intervals along the length of the rotor.

Figure 8.11 shows the different cross-sections in a turbo-generator rotor: *A-A* rectangular slots for field winding and smaller slots in the pole area, and *B-B* cross-cuts to ensure uniform flexibility with respect to the vertical and horizontal cross-section principal axes.

Alternator rotors are supported in plain bearings. These hydrodynamic bearings present unequal dynamical stiffnesses in the vertical and horizontal directions. Asymmetry of the bearings introduces a split of critical speeds but cannot by itself cause second order vibration.

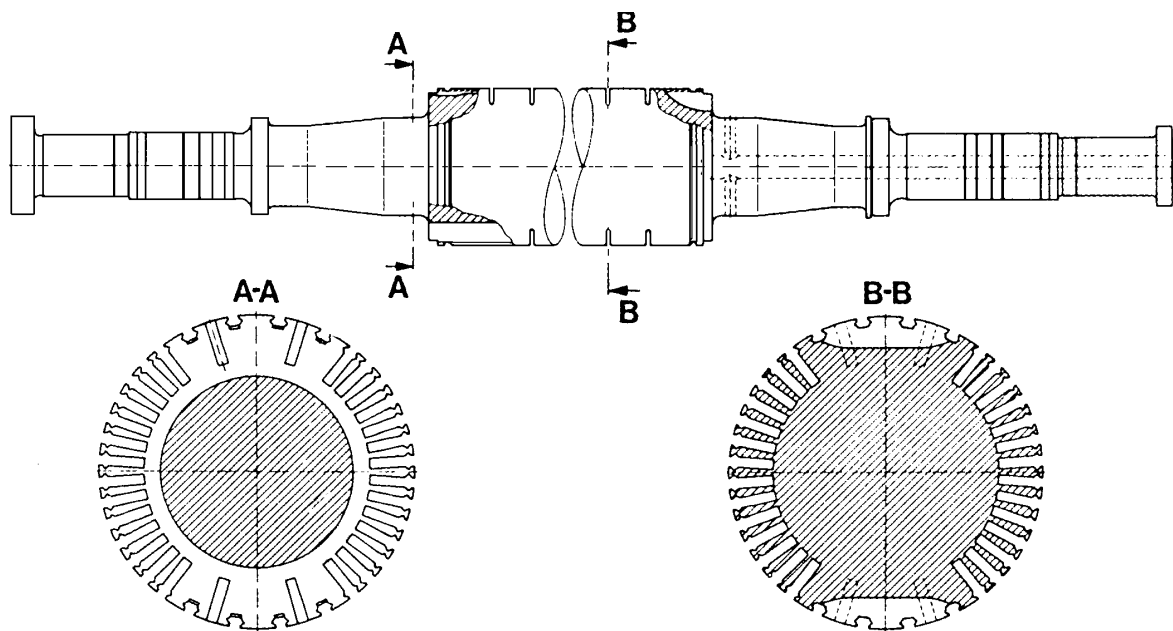


Fig. 8.11 (from [8.5])

Other design features and characteristics of electrical machines are presented in [8.7].

8.4 Guidelines for Vibration Limits

The standard *ISO 7919, Part 2* [8.8] provides the special features required for measuring shaft vibrations on the coupled rotor systems of steam turbine-generating sets for power stations, having rated speeds in the range 1500 to 3600 rpm, and power outputs greater than 50 MW.

Table 8.5

Zone Boundary	Shaft Rotational Speed, rpm			
	1500	1800	3000	3600
Maximum Shaft Relative Displacement, μm				
A	100	90	80	75
B	200	185	165	150
C	300	290	260	240

The recommended shaft vibration amplitude values for large steam turbine-generator sets, in micrometers peak-to-peak, are shown in Table 8.5 for relative shaft to bearing vibrations, and in Table 8.6 for absolute vibrations. In both tables, zone *A* represents new machines that can be operated without restriction. Zone *B* is acceptable for long-term operation. Zone *C* represents machines that may be operated for a limited time until a suitable opportunity arises for remedial action to be taken. Zone *D* is identified as a trip level as these values are considered to be of sufficient severity to cause damage.

Table 8.6

Zone	Shaft Rotational Speed, rpm			
	1500	1800	3000	3600
Boundary	Maximum Shaft Absolute Displacement, μm			
A	120	110	100	90
B	240	220	200	180
C	385	350	320	290

The standard *ISO 10816, Part 2* [8.9], provides specific guidance for assigning the severity of vibrations measured on the bearings or pedestals of large steam turbine-generating sets. Table 8.7 lists recommended vibration velocity levels (mm/s, rms) measured *in situ* on bearing housing/pedestal for turbine-generator sets exceeding 50 MW. The zone descriptions are the same as in *ISO 7919*.

Table 8.7

Zone	Shaft Rotational Speed, rpm	
	1500 or 1800	3000 or 3600
Boundary	Vibration Velocity, mm/s RMS	
A/B	2.8	3.8
B/C	5.3	7.5
C/D	8.5	11.8

Fig. 8.15 (from [8.12])

8.5 Torsional Vibrations

Electrical faults and power system disturbances can create severe transient torques in turbine-generator shafts.

The most important disturbances creating damaging torques in turbosets are: 1) short circuits at the terminals, 2) out-of-phase synchronization, 3) short-circuit clearing, 4) automatic circuit breaker reclosing following fault-clearing on lines leaving power stations, 5) transmission line switching, 6) load rejection, 7) sub-synchronous resonance in series-capacitor compensated systems, and 8) full load trips.

One can add the single-phase operation, such as caused by single pole operation of circuit breakers. This produces alternating torques at twice line frequency. While this frequency is generally above those of the lower modes of the turboset, there are many complex higher modes of vibration which involve internal deflections of the generator and turbine rotors. Further, individual discs and blade groups can respond to such pulsations.

When series capacitors are used in transmission lines situated electrically close to the generator, steady state and transient currents may be generated at frequencies below the normal power system frequency. The existence of such currents causes alternating torques in the generator which can excite the natural vibration modes of the shaft, and cause significant dynamic torques at or near the shaft couplings.

The above mentioned fault conditions typically occur in sequence [8.10]. The first impact on the generator might be a sudden short circuit in a transmission line close to the generator, which in electrical engineering is frequently called *fault application*. In the case of lightning strikes on transmission steel towers, the electric potential of the tower increases because of tower footing resistance, and an arc (or arcs) runs from the tower toward electric wire (or wires), causing a ground fault of the power transmission line. The capacity of power transmission is lost for a moment, partially or completely, depending on the extent of the ground fault. For arc extinction, the faulty phase (or phases) is quickly opened (generally

after about six cycles of system's normal frequency), separated automatically by protective relays and circuit breakers [8.11].

The second impact results from the electrical disconnection of the faulty transmission line, which is called *fault clearing* or *fault removal*. Usually this is all that is needed to extinguish the electrical arc initiated by lightning or by short circuits on the power line. Although the capacity of transmission is recovered in a moment to some extent by the opening operation, in some cases the recovered capacity may not be enough to keep the stability of transmission, and the power station must step out from the power system.

Even if the stability is all right, a second lightning strike on the same tower is very probable. This may cause much larger damage than the first strike on the capacity of transmission, because a part of the capacity has already been lost by separating the faulty phase (or phases). In case all three phases of one of two circuits suffered a ground fault by the first strike, it is quite possible that the second strike may completely stop the power transmission.

For stability and protection against the second lightning strike, it has become a common practice to reclose the separated phase (or phases) automatically by relays and circuit breakers after a very short no-voltage time (about 20 cycles in the case of a 275 kV system) [8.11]. The time required is that necessary for recovery of insulation. After this brief disconnection, the third impact is applied to the generator when the line is electrically re-connected. The technical term for this operation is *high speed reclosing* (HSR).

High speed reclosing can be successful, if the fault is effectively cleared by the disconnection of the line, or unsuccessful if the fault persists after reclosing. In this latter case a fourth impact is applied to the generator by a second clearing attempt.

The maximum number of times the torque fluctuation is repeated is four. HSR is not attempted again even in the unsuccessful case, because the stability of transmission has been so damaged by duplicate ground faults as never to be recovered.

These shocks are applied consecutively. The turbine-generator shaft vibrations result from the initial shock, and the unit is re-shocked from the second, and then the third and the fourth impacts. Depending

strongly on the relative phasing of these shocks, the resulting dynamic strains can result in very high dynamic shaft torques, because rotatory inertia of the turbine is much larger than that of the generator. These torques can be much higher than in the terminal short circuit case, which had been considered the worst design case a long period of time [8.12].

A multi-mass model (Fig. 8.12) simulates the torsionally vibrating mechanical system of a turbine-generator. The number and location of the shaft regions to be investigated and the desired accuracy of the results determine the required number of discrete masses of the model. Six to eight masses, depending on the number of rotors, suffice for routine calculations to determine the mechanical torques that are induced by electrical transients at the shaft couplings and journals of a turbine-generator. The principal determining moments of inertia of this system are those of the bladed rotating components of the turbine and of the generator rotor. The couplings and the reduced-diameter shaft extensions are primarily responsible for the torsional spring characteristics.

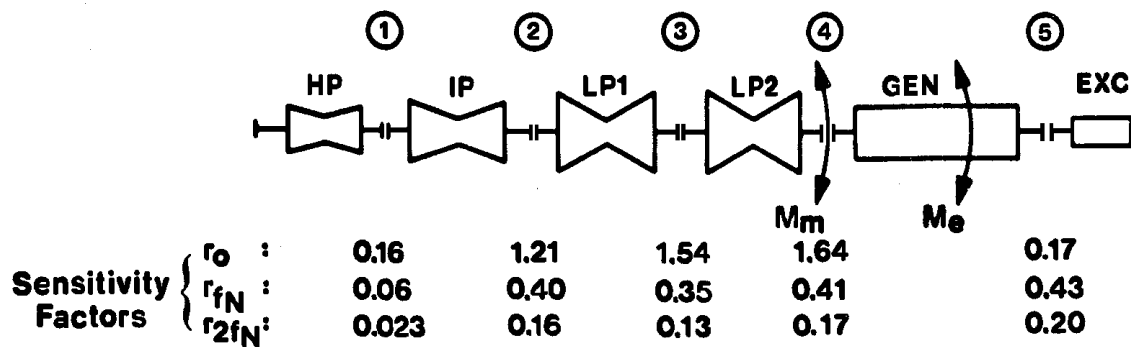


Fig. 8.12 (from [8.13])

When a high degree of accuracy is required, the turbine-generator rotating system is simulated by more than 200 individual masses to determine the torsional natural frequencies. These natural frequency values are then transferred to a modal model with 6 to 20 masses depending upon the objective of the investigation.

If the shaft system is torsionally excited by the generator rotor, each shaft section is subjected to pulsating torques of different magnitude and shape. Figure 8.13 illustrates the mechanical torque

M_m , in the shaft region 4 (see Fig. 8.12) of a 1000 MW turbine with a two-pole generator, as a result of a sinusoidal electrical torque $M_e = M_{e \max} \sin 2\pi ft$ applied to the generator rotor, as a function of the variable frequency f .

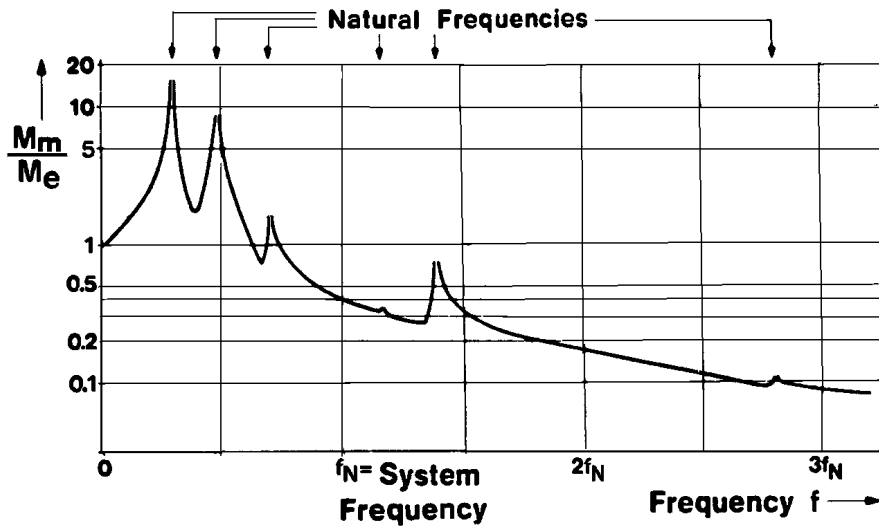


Fig. 8.13 (from [8.13])

Figure 8.14 depicts the mechanical torque reactions, in region 4 of figure 8.12, to three types of electrical disturbing torques (unidirectional, system frequency and double frequency), suddenly applied to the generator rotor:

- 1 $M_{eo} = M_{e \max} \cdot 1,$
- 2 $M_{ef_N} = M_{e \max} \sin 2\pi ft,$
- 3 $M_{e2f_N} = M_{e \max} \sin 4\pi ft.$

All three types of excitation can be present in the electrical torque wave arising from system disturbances.

The sensitivity of the individual regions of the shaft system to the three types of excitation can be characterized by the factors r_o , r_{f_N} and r_{2f_N} , defined as

$$r = M_{m \max} / M_e.$$

These are tabulated in figure 8.12 where it can be seen that the system-frequency and double-frequency electrical torques are reduced in all regions, $r_{f_N} < 1$ and $r_{2f_N} < 1$. On the other hand, the shafts of large turbo-generators, especially four-pole units, are very sensitive to the unidirectional component of torque, $r_o > 1$. High, strongly pulsating torques are created by this direct component, as shown by curve 1 of figure 8.14.

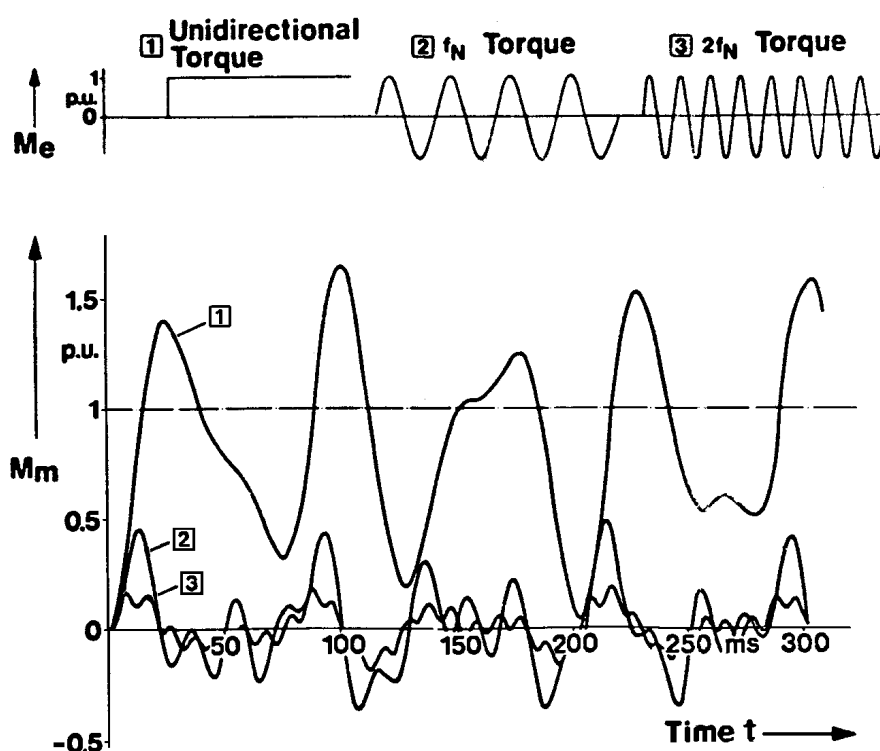


Fig. 8.14 (from [8.13])

Figure 8.15 shows the electrical torque, M_e , and the mechanical torque, M_m , in the shaft of a large two-pole generator when clearing a three-phase network short circuit after 5.5 cycles, followed by (an unsuccessful) reclosing after 37 cycles, at 0 voltage. Extremely high torques of nearly 8 p.u. (per unit) for $M_{m \max}$ and even higher for ΔM_m are reached, which can be far beyond the stress capability of the shafts. If the faulted line is reconnected while it is still shorted, the generator is again subjected to a short-circuit torque plus a subsequent additional sudden clearing torque. Calculations have shown a high dependence of the mechanical torques on the exact

instant of disconnecting the faulted line and of reclosing and, consequently, on chance. Identical switching times could cause entirely different effects with different turbine-generators.

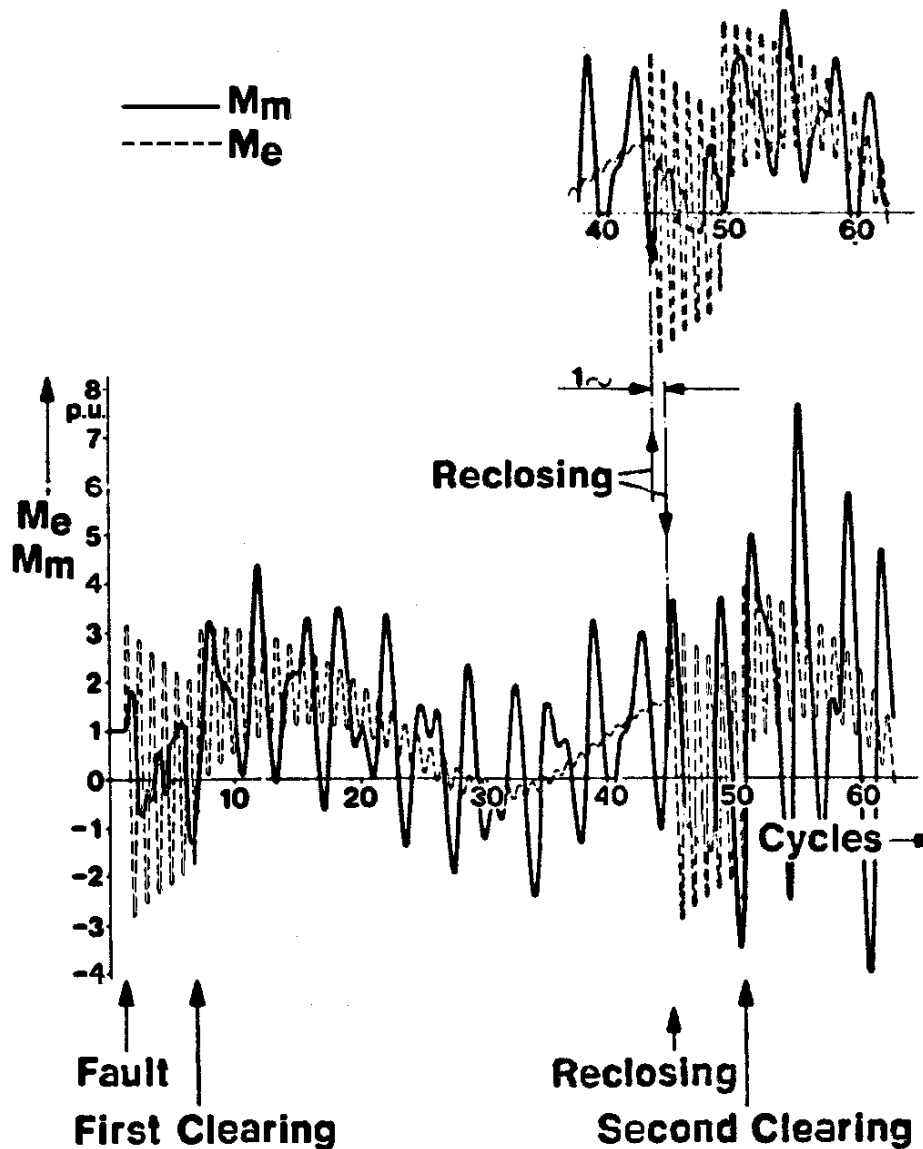


Fig. 8.15 (from [8.13])

The pulsating components of the mechanical torque during most disturbances can cause stresses that exceed the shaft material endurance limit. The mechanical fatigue strength of shafts depends upon the fatigue strength characteristics of the material, local stress concentrations and types of stresses. The effect of repetitive cyclic stressing can be determined from the shaft fatigue resistance curves.

Figure 8.16 illustrates the fatigue resistance for a generator shaft. It expresses the maximum admissible number of disturbances, \bar{Z}_i , with any given pulsating mechanical torque, ΔM_{mi} , after which the safe life cycle of the shaft is spent. With additional disturbances, rotor cracks must be expected.

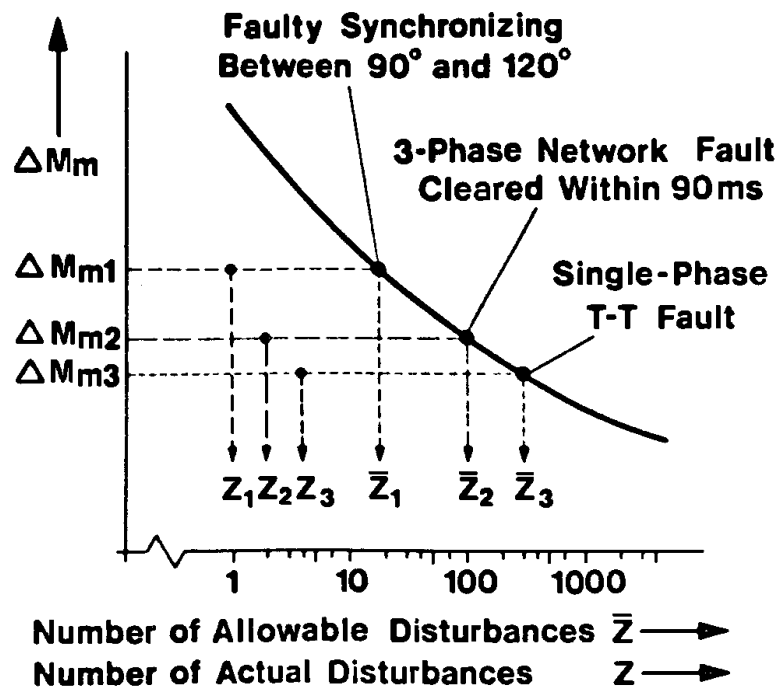


Fig. 8.16 (from [8.13])

If a number of disturbances with different pulsating torques $\Delta M_{m1}, \Delta M_{m2}, \dots, \Delta M_{mn}$ occur, they will have different effects on the life cycle. Each disturbance by itself would be permitted $\bar{Z}_1, \bar{Z}_2, \dots, \bar{Z}_n$ times, in accordance with the fatigue resistance curve. Should they occur in random sequence with the frequency Z_1, Z_2, \dots, Z_n , then the life expenditure (L.E.) can be determined by the Palmgrem-Miner rule of cumulative stresses

$$L.E. = \sum_{i=1}^n \frac{Z_i}{\bar{Z}_i}$$

L.E.<1 means safe life still available. L.E.>1 means safe life exceeded, damage possible.

References

- 8.1 * * * *Back-Pressure Turbosets for Industrial Use*, Brown Boveri Publication 3090E, 1967.
- 8.2 Bishop R.E.D. and Parkinson A.G., *Second Order Vibration of Flexible Shafts*, Phil. Trans. Royal Society, Series A, vol.259, A.1095, pp 1-31, 1965.
- 8.3 Krick N. and Noser R., *The Growth of Turbo-Generators*, Brown Boveri Review, vol.63, nr.2, pp 148- 155, 1976.
- 8.4 Fluhr O., Peyer A. and Richard C., *Air-Cooled Turbo-Generators for 18 – 130 MVA*, Brown Boveri Review, vol.63, nr.6, pp 392-398, 1976.
- 8.5 * * * *Caractéristiques de construction des alternateurs de grande puissance*, Revue ABB, nr.1, 11 pag, 1989.
- 8.6 Busse L. and Soyk K.H., *World's Highest Capacity Steam Turbosets for the Lignite-Fired Lippendorf Power Station*, ABB Review, nr.6, pp 13-22, 1997.
- 8.7 Wiedemann E. and Kellenberger W., **Konstruktion elektrischer Maschinen**, Springer, 1967.
- 8.8 **ISO 7919-2**, Mechanical Vibration of Non-Reciprocating Machines – Measurements on Rotating Shafts and Evaluation Criteria – Part 2: *Large Land-Based Steam Generator Sets*, 1996.
- 8.9 **ISO 10816-2**, Mechanical Vibration – Evaluation of Machine Vibration by Measurements on Non-Rotating Parts – Part 2: *Large Land-Based Steam Turbine Generator Sets in Excess of 50 MW*, 1996.
- 8.10 King D.W. and Rieger N.F., *Problems of Turbine Generator Shaft Dynamics*, **Rotordynamics 2. Problems in Turbomachinery** (Ed. N. F. Rieger), CISM Courses and Lectures No.297, Springer, 1988, pp 307-330.
- 8.11 Hizume A., *Transient Torsional Vibration of Steam Turbine and Generator Shafts due to High Speed Reclosing of Electric Power Lines*, Journal of Engineering for Industry, Trans.ASME, nr.8, pp 968-979, 1976.
- 8.12 Joyce J.S. and Lambert D., *Status of Evaluating the Fatigue of Large Steam Turbine-Generators Caused by Electrical Disturbances*, IEEE Trans. Power Apparatus and Systems, vol.PAS-99, nr.1, pp 111-119, 1980.
- 8.13 Abolins A., Lambrecht D., Jouce J.S., Rosenberg L.T., *Effect of Clearing Short Circuits and Automatic Reclosing on Torsional Stress and Life Expenditure of Turbine-Generator Shafts*, IEEE Trans. Power Apparatus and Systems, vol.PAS-95, nr.1, pp 14-25, 1976.

BIBLIOGRAPHY

Turbomachines

- Baljie O.E., **Turbomachines**, Wiley, New York, 1981.
- Traupel W., **Thermal Turbomachinery** (in German), 3rd ed., Springer, 1977.
- Kostyuk A.G., **Dynamics and Strength of Turbomachinery** (in Russian), Mashinostroenie, Moscow, 1982.
- Arasu A.V., **Turbo Machines**, Vikas Publishing House PVT Ltd., New Delhi, 2001.
- Csanady G.T., **Theory of Turbomachines**, McGraw Hill, New York, 1964.
- Shepherd D.G., **Principles of Turbomachinery**, Mac Millan, New York, 1956.

Centrifugal Pumps

- Cheremisinoff N.P. and Cheremisinoff P.N., **Pumps, Compressors, Fans**, *Pocket Handbook*, Technomic Publishing Co. Inc., Lancaster, 1989.
- Church A.H., **Centrifugal Pumps and Blowers**, Krieger, Huntington, New York, 1972.
- Karassik J.J. et al, **Pump Handbook**, McGraw Hill, New York, 1976.
- * * * **Kreiselpumpen Lexicon**, K.S.B., 1989.
- Pfleiderer C., **Die Kreiselpumpen für Flüssigkeiten und Gase**, Springer, Berlin, 1961.
- Pimsner V., **Maşini cu palete**, Editura tehnică, Bucureşti, 1988.
- Stepanoff A.J., **Centrifugal and Axial Flow Pumps**, Wiley, New York, 1957.
- Wagner W., **Kreiselpumpen and Kreiselpumpenanlagen**, Vogel, Würzburg, 1994.

Hydraulic Turbines

- Daugherty R.L., **Hydraulic Turbines**, McGraw Hill, New York, 1920.
- Esser C. and Sun J.H.T., **Hydraulic Turbines**. *Standard Handbook of Powerplant Engineering*, McGraw Hill, New York, 1989.

Axial Compressors

Eckert B. and Schnell E., **Axial und radial Kompressoren**, Springer, Berlin, 1961.

Horlock J.H., **Axial Flow Compressors**, Butterworths, London, 1958..

Gas Turbines

Bathie W.W., **Fundamentals of Gas Turbines**, 2nd ed., Wiley, New York, 1996.

Boyce M.P., **Gas Turbine Engineering Handbook**, 2nd ed., Gulf Professional Publishing, Boston, 2002.

Horlock J.H., **Axial Flow Turbines**, Krieger, Huntington, New York, 1973.

Kerrenbrock J.L., **Aircraft Engines and Gas Turbines**, MIT Press, Cambridge, Mass, 1977.

Mattingly J.D., **Aircraft Engine Design**, A.I.A.N., New York, 1987.

Vincent E.T., **The Theory and Design of Gas Turbines and Jet Engines**, McGraw Hill, New York, 1950.

Steam Turbines

Church E.F.Jr., **Steam Turbines**, 3rd ed., McGraw Hill, 1950.

Kirillov I.I., Ivanov V.A. and Kirillov A.I., **Steam Turbines and Turbosets** (in Russian), Mashinostroenie, Leningrad, 1978.

Lee J., **Theory and Design of Steam and Gas Turbines**, McGraw Hill, 1954.

Leyzerovich A., **Large Power Steam Turbines**, vol.1, **Design**, vol.2, **Operation**, PennWell Books, Tulsa, Oklahoma, 1997.

Shcheglyayev A.V., **Steam Turbines** (in Russian), 2 vol., 6th ed., Energoatomizdat, Moscow, 1993.

Skrotzki B.G.A. and Vopat W.A., **Steam and Gas Turbines**, McGraw Hill, 1950.

Trojanovsky B.M., Filippov G.A., Bulkin A.E., **Steam and Gas Turbines of Nuclear Power Plants** (in Russian), Energoatomizdat, Moscow, 1985.

Trukhny A.D., **Stationary Steam Turbines** (in Russian), 2nd ed., Energoatomizdat, Moscow, 1990.

Zhiritsky G.S. and Strunkin V.A., **Design and Strength Calculations of Steam Turbines** (in Russian), Mashinostroenie, Moscow, 1968.

Index

A

Aerodynamic cross-coupling, 72
Annular gas seals, 52
API Standard 610, 5
API Standard 617, 73

B

Balancing piston, 47, 49, 186
Blowers, 80
Bulk-flow fluid seal model, 22
Burst speed, 211
Bushing:
 breakdown, 11
 stepped dual, 58
 throttle, 11

C

Campbell diagram, 103, 110, 111, 115, 118
Compressor:
 axial, 129, 135
 back-to-back, 46, 49
 centrifugal, 39, 141
 throughflow, 46, 47
Centrifugal pump, 7
Cross-coupled stiffnesses, 23
Characteristic speed, 8, 81
Coefficients:
 damping, 23, 27, 34, 63, 67
 inertia, 23, 27, 67
 stiffness, 23, 27, 34, 63, 67
Critical speed, 5
Critical speed map, 216

D

Damping force, 18
Destabilizing force, 18, 55

Diffuser, 9, 42
Diffuser/impeller interaction, 49
Ducted fan, 153

E

Embrittlement, 202

F

Fault clearing, 238
Fans:
 centrifugal, 80
 foundation, 89
 induced-draft, 85, 89
 primary air, 85
Flow coefficient, 81
Fracture Appearance Transition
 Temperature, FATT, 203
Friction loss factor, 21

G

Gas seals, 52
Gas turbine:
 described, 143
 aircraft, 153
 rotors, 165
 stationary, 146
Generators:
 air-cooled, 227
 direct hydrogen cooled, 228
 direct liquid cooled, 230
 indirectly cooled, 229
 non-symmetrical rotor, 233

H

Head coefficient, 81
High-speed reclosing, 238
Hydraulic turbines:

discussed, 95
 bulb, 118
 Francis, 104
 Kaplan, 112
 Pelton, 99
 straflo, 120

I

ISO Standard 7919:

Part 2, 218, 235
 Part 3, 221
 Part 4, 176
 Part 5, 122

ISO Standard 10816:

Part 2, 236
 Part 3, 93
 Part 4, 176
 Part 5, 124

Impeller:

cantilevered, 13
 double-suction, 13
 shrouded, 9, 43, 45
 unshrouded, 41, 44

Impeller/casing clearance, 6

Impeller/volute interaction, 30

L

Labyrinth:

balance drum, piston, 53
 centre span, 49
 eye packing, 53
 interlocking tooth, 55
 interstage, 49
 shaft seal, 53

Liquid seal, 56

Lockup of seal ring, 60

Lomakin effect, 18, 20

O

Oil seal, 49

P

Packing gland, 12

Pump:

centrifugal, 5
 multi-stage horizontal, 15, 16
 nuclear reactor main coolant, 13
 single-stage, 12
 three-stage vertical, 14
 two-stage, 10

R

Rotor:

built-up, 138, 168, 196
 design stresses, 200
 disc-type, 138
 drum-type, 135, 140, 165, 198
 high-pressure, 203
 integrity, 210
 intermediate pressure, 203
 low pressure, 207
 monoblock, 196
 non-symmetric, 233
 welded, 166, 196

Rotordynamic coefficients, 22

S

Seals:

annular gas, 52
 annular liquid, 19
 balancing ring, 6
 Black's model, 24
 Child's model, 28
 floating contact, 56
 Jenssen's model, 24
 labyrinth, 52
 neck ring, 11
 oil ring, 39
 wearing ring, 6

Seal ring lockup, 60

Self-excited vibrations, 90

Shroud, 8

Shroud forces, 34

Specific speed, 81, 97

Squeeze film damper, 65

Stability map, 70

Stage:

impulse, 181

reaction, 182

Stall, 134

Stator supports, 125

Steam turbine:

axial-flow, 181

back-pressure, 185

condensing, 184

double-flow, 192

extraction, 188

Stresses:

from centrifugal loads, 208

stationary, 205

thermal, 204

Surging, 134

Swirl brakes, 54

T

Torsional vibrations, 237

Turbocharger, 161

Turbocompressor, 45

Turbofan, 155, 158

Turbo-generators, see Generators

Turbojet:

bypass, 153

double compound, 154

single-shaft, 153

Turboprop:

direct connected, 153

free turbine, 153

Turboshaft, 157

Two-spool gas engine, 172

U

Unbalance response, 217

V

Vanes, 7, 83, 98 105

Vibration limits, 122, 175, 221, 235

Volute, 9, 41

W

Wheel:

axial, 7

diagonal-radial, 7

radial, 7

shrouded, 45

unshrouded, 8